
2 **Consolidation and longevity of the CMS**
3 **Resistive Plate Chamber system in view of the**
4 **High-Luminosity LHC Upgrade**

5



Alexis Fagot

Thesis to obtain the degree of
Doctor of Philosophy in Physics
Academic year 2018-2019



⁷

⁸ Promotors: Dr. Michael Tytgat
Prof. Dr. Dirk Ryckbosch

⁹
¹⁰ Ghent University
¹¹ Faculty of Sciences
¹² Department of Physics and Astronomy
¹³ Proeftuinstraat 86, B-9000 Ghent, Belgium
¹⁴ Tel.: +32 9 264.65.28
¹⁵ Fax.: +32 9 264.66.97

¹⁶



Alexis Fagot

Thesis to obtain the degree of
Doctor of Philosophy in Physics
Academic year 2018-2019



17

Acknowledgements

18

19

XX/XX/2018

Alexis Fagot

Table of Contents

21	Acknowledgements	i
22	Nederlandse samenvatting	vii
23	English summary	ix
24	1 Introduction	1-1
25	2 Investigating the TeV scale	2-1
26	2.1 The Standard Model of Particle Physics	2-1
27	2.1.1 A history of particle physics	2-2
28	2.1.2 Construction and validation of the Standard Model	2-14
29	2.1.3 Investigating the TeV scale	2-15
30	2.2 The Large Hadron Collider & the Compact Muon Solenoid	2-20
31	2.2.1 LHC, the most powerful particle accelerator	2-20
32	2.2.2 Timeline of operation	2-23
33	2.2.3 High Luminosity LHC	2-25
34	2.2.4 The Compact Muon Solenoid experiment	2-25
35	2.2.4.1 The silicon tracker	2-27
36	2.2.4.2 The calorimeters	2-27
37	2.2.4.3 The muon system	2-28
38	3 Muon Phase-2 Upgrade	3-1
39	3.1 Motivations for HL-LHC and the upgrade of CMS	3-1
40	3.2 Description of the muon system	3-5
41	3.2.1 The Drift Tubes	3-5
42	3.2.2 The Cathode Strip Chambers	3-6
43	3.2.3 The Resistive Plate Chambers	3-7
44	3.3 Necessity for improved electronics	3-8
45	3.4 New detectors and increased acceptance	3-10
46	3.4.1 Gas electron multipliers	3-12
47	3.4.2 Improved forward resistive plate chambers	3-15
48	3.5 Impact on Level-1 Trigger and physics performance	3-17
49	3.6 Ecofriendly gas studies	3-20
50	4 Physics of Resistive plate chambers	4-1
51	4.1 Principle	4-1
52	4.2 Rate capability and time resolution of Resistive Plate Chambers	4-3
53	4.2.1 Operation modes	4-3
54	4.2.2 Standard gas mixture for RPCs operated in collider experiments	4-5
55	4.2.3 Detector designs and performance	4-9

56	4.2.3.1	Double gap RPC	4-11
57	4.2.3.2	Multigap RPC (MRPC)	4-13
58	4.2.3.3	Charge distribution and performance limitations	4-16
59	4.3	Signal formation	4-18
60	4.3.1	Energy loss at intermediate energies	4-19
61	4.3.2	Primary ionization	4-23
62	4.3.3	Development and propagation of avalanches	4-27
63	4.3.4	Drift and diffusion of the electron cloud	4-31
64	4.3.5	Space charge effect & streamers	4-33
65	4.4	Effect of atmospherical conditions on the detector's performance	4-37
66	5	Longevity studies and Consolidation of the present CMS RPC subsystem	5-1
67	5.1	Testing detectors under extreme conditions	5-2
68	5.1.1	GIF	5-4
69	5.1.2	GIF++	5-5
70	5.2	Preliminary studies at GIF	5-7
71	5.2.1	RPC test setup	5-7
72	5.2.2	Geometrical acceptance of the setup layout to cosmic muons	5-9
73	5.2.2.1	Description of the simulation layout	5-10
74	5.2.2.2	Simulation procedure	5-11
75	5.2.2.3	Results and limitations	5-12
76	5.2.3	Photon flux at GIF	5-14
77	5.2.4	Results and discussions	5-17
78	5.3	Longevity tests at GIF++	5-20
79	5.3.1	Selection and characterization of CMS RPCs for longevity at GIF++	5-20
80	5.3.2	RPC test setup	5-22
81	5.3.3	GIF++ data flow	5-24
82	5.3.4	Measurements performed during beam periods	5-26
83	5.3.4.1	Efficiency scans	5-26
84	5.3.4.2	Rate scans	5-26
85	5.3.4.3	Offline analysis and Data Quality Monitoring	5-27
86	5.3.5	Measurements performed during irradiation periods	5-28
87	5.3.5.1	Longevity scans	5-29
88	5.3.5.2	Daily rate monitoring scans	5-30
89	5.3.5.3	Weekly noise monitoring scans	5-31
90	5.3.5.4	Weekly source scans	5-31
91	5.3.5.5	Weekly current scans	5-32
92	5.3.5.6	Resistivity measurements	5-32
93	5.3.6	Results and discussions	5-32
94	6	Improved RPC investigation and preliminary electronics studies	6-1
95	6.1	FEE candidate for the production of iRPCs	6-1
96	6.1.1	CMS RPCROC: the RPC upgrade baseline	6-2
97	6.1.2	INFN Front-End Electronics: a robust back-up solution	6-3
98	6.2	Preliminary tests at CERN	6-3
99	7	Conclusions and outlooks	7-1
100	7.1	Conclusions	7-1
101	7.2	Outlooks	7-1

A A data acquisition software for CAEN VME TDCs	A-1
A.1 GIF++ DAQ file tree	A-1
A.2 Usage of the DAQ	A-2
A.3 Description of the readout setup	A-3
A.4 Data read-out	A-3
A.4.1 V1190A TDCs	A-4
A.4.2 DataReader	A-7
A.4.3 Data quality flag	A-10
A.5 Communications	A-12
A.5.1 V1718 USB Bridge	A-13
A.5.2 Configuration file	A-14
A.5.3 WebDCS/DAQ intercommunication	A-17
A.5.4 Example of inter-process communication cycle	A-17
A.6 Software export	A-18
B Details on the offline analysis package	B-1
B.1 GIF++ Offline Analysis file tree	B-1
B.2 Usage of the Offline Analysis	B-2
B.2.1 Output of the offline tool	B-3
B.2.1.1 ROOT file	B-3
B.2.1.2 CSV files	B-5
B.3 Analysis inputs and information handling	B-6
B.3.1 Dimensions file and IniFile parser	B-7
B.3.2 TDC to RPC link file and Mapping	B-8
B.4 Description of GIF++ setup within the Offline Analysis tool	B-9
B.4.1 RPC objects	B-9
B.4.2 Trolley objects	B-10
B.4.3 Infrastructure object	B-10
B.5 Handeling of data	B-12
B.5.1 RPC hits	B-13
B.5.2 Clusters of hits	B-14
B.6 DAQ data Analysis	B-15
B.6.1 Determination of the run type	B-16
B.6.2 Beam time window calculation for efficiency runs	B-17
B.6.3 Data loop and histogram filling	B-18
B.6.4 Results calculation	B-21
B.6.4.1 Rate normalisation	B-21
B.6.4.2 Rate and activity	B-23
B.6.4.3 Correction of muon performance parameters	B-25
B.6.4.4 Strip masking tool	B-27
B.6.4.5 Output CSV files filling	B-29
B.7 Current information extraction	B-31

143

Nederlandse samenvatting
–Dutch Summary–

144

English summary

List of Figures

146

- | | | | |
|-----|------|---|------|
| 147 | 2.1 | Solar spectrum with spectral lines as it visually appeared to Fraunhofer. | 2-2 |
| 148 | 2.2 | Through the gold foil experiment, Rutherford could show that most of the mass of atoms was contained in a positively charged nucleus and could then propose a more accurate atomic model than that of Thomson. | 2-3 |
| 150 | | | |
| 151 | 2.3 | Figure 2.3a: The orbits in which the electron may travel according to the Bohr model of the hydrogen atom. An electron jumps between orbits and is accompanied by an emitted or absorbed amount of electromagnetic energy ($h\nu$). The orbits radius increases as n^2 . Figure 2.3b: Elliptical orbits with the same energy and quantized angular momentum $l = 0, 1, \dots, n - 1$ in the case $n = 5$. Figure 2.3c: Illustration of quantum mechanical orbital angular momentum. The cones and plane represent possible orientations of the angular momentum vector for $l = 2$ and $m = -2, -1, 0, 1, 2$ | 2-5 |
| 152 | | | |
| 153 | | | |
| 154 | | | |
| 155 | | | |
| 156 | | | |
| 157 | | | |
| 158 | 2.4 | Figure 2.4a: The spectral lines of mercury vapor lamp anomalous Zeeman effect without magnetic field (A) and with magnetic field (B - transverse Zeeman effect & C - longitudinal Zeeman effect). Figure 2.4b: Stern-Gerlach experiment: Silver atoms traveling through an inhomogeneous magnetic field and being deflected up or down depending on their spin. | 2-6 |
| 159 | | | |
| 160 | | | |
| 161 | | | |
| 162 | | | |
| 163 | 2.5 | Figure 2.5a: decay of a μ -meson in an emulsion. Figure 2.5b: track of a π -meson in an emulsion signed by Lattes, Powell, and Occhialini. | 2-8 |
| 164 | | | |
| 165 | 2.6 | Figure 2.6a: Meson octet. Figure 2.6b: Baryon octet. Figure 2.6c: Baryon decuplet. | 2-9 |
| 166 | | | |
| 167 | 2.7 | Discovery of the J/Ψ by both SPEAR (SLAC [74]) in Figure 2.7a and AGS (BNL [75]) in Figure 2.7b. In Figure 2.7a, the cross section versus energy is showed for (a) multi hadron final states, (b) e^+e^- final states, and (c) $\mu^+\mu^-, \pi^+\pi^-$ and K^+K^- final states. | 2-10 |
| 168 | | | |
| 169 | 2.8 | Figure 2.8a: the color field of QCD only allows for "white" baryons, particles composed of quarks, to exist. Examples are given for mesons, composed of a quark and its anti-quark, and hadrons, composed of three differently colored quarks or anti-quarks. Other exotic baryons have been predicted and observed, such as tetraquarks and pentaquarks. Figure 2.8b: a crossed analysis performed thanks to the data collected by various experiments at different energies have showed that the coupling constant evolves as predicted by the mechanism of asymptotic freedom [87]. | 2-11 |
| 170 | | | |
| 171 | | | |
| 172 | | | |
| 173 | | | |
| 174 | | | |
| 175 | | | |
| 176 | 2.9 | Energy spectrum of beta particles emitted by a source of ^{210}Bi | 2-12 |
| 177 | 2.10 | As explained through Figure 2.10a, the Wu experiment consisted in measuring the preferred direction of emission of beta rays of a Cobalt source placed in a stable magnetic field aligned, in one case, and anti-aligned, in the other case, with the nuclear spin. The result of Figure 2.10b showed a violation of parity. | 2-13 |
| 178 | | | |
| 179 | | | |
| 180 | | | |

181	2.11	The elementary particles of the Standard Model are shown along with their properties. Their interactions with the strong, weak and electromagnetic forces have been made explicit using color squares. In the left column, the scalar Higgs boson is depicted. The center is focused on the matter particles, the fermions, and the right column on the force carriers, the gauge bosons. The role of the Higgs boson in electroweak symmetry breaking is highlighted, and the corresponding way properties of the various particles differ in the (high-energy) symmetric phase (top) and the (low-energy) broken-symmetry phase (bottom) are shown.	2-15
182			
183			
184			
185			
186			
187			
188			
189	2.12	Figure 2.12a: Total proton-proton cross-section as a function of the collisions center-of-mass energy \sqrt{s} [116] with cosmic-ray data from Akeno Observatory and Fly's Eye Collaboration. Figure 2.12b: Total proton-(anti)proton and interaction channel cross-sections in the TeV scale.	2-16
190			
191			
192			
193	2.13	Rotation curve (points) of the galaxy M33 compared with best fitting model (line). The short-dashed line represents the rotation profile that would be expected from the observation of the stellar disc alone [128].	2-17
194			
195			
196	2.14	Cosmic Microwave Background as measured by the space observatory Planck which mean temperature is $T_\gamma = (2.7255 \pm 0.0006)\text{K}$ with anisotropies of the order of a few μK	2-18
197			
198			
199	2.15	CERN accelerator complex.	2-20
200			
201	2.16	Pictures of the different accelerators. From top to bottom: first the LINAC 2 and the Pb source of LINAC 3. Then the Booster and the LEIR. Finally, the PS, the SPS and the LHC.	2-21
202			
203	2.17	Figure 2.17a: schematics of the LHC cryodipoles. 1: Superconducting Coils, 2: Beam pipe, 3: Heat exchanger Pipe, 4: Helium-II Vessel, 5: Superconducting Bus-bar, 6: Iron Yoke, 7: Non-Magnetic Collars, 8: Vacuum Vessel, 9: Radiation Screen, 10: Thermal Shield, 11: Auxiliary Bus-bar Tube, 12: Instrumentation Feed Throughs, 13: Protection Diode, 14: Quadrupole Bus-bars, 15: Spool Piece Bus-bars. Figure 2.17b: magnetic field and resulting motion force applied on the beam particles.	2-22
204			
205			
206			
207			
208			
209			
210	2.18	The LHC quadrupoles (Figure 2.18a) showed together with the magnetic fields and resulting focussing force applied on the beam by two consecutive quadrupoles (Figure 2.18b).	2-23
211			
212			
213	2.19	Distribution of the four-lepton invariant mass for the $ZZ \rightarrow 4l$ analysis as presented by both ATLAS [112] and CMS [113] in 2012.	2-23
214			
215	2.20	Detailed timeline projection of LHC and HL-LHC operation until 2039 showing the evolution of the instantaneous and integrated luminosity as designed (Figure 2.20a) and in the ultimate case where the instantaneous luminosity is increased to $7.5 \times 10^{34}\text{cm}^{-2}\text{s}^{-1}$ thanks to a new increase of instantaneous luminosity during Run 5 (Figure 2.20b) [175–177].	2-24
216			
217			
218			
219			
220	2.21	Picture of the CMS barrel. The red outer layer is the muon system hosted into the red iron return yokes. The calorimeters are the blue cylinder inside in magnet solenoid and the tracker is the inner yellow cylinder built around the beam pipe.	2-26
221			
222			
223	2.22	View of the CMS apparatus and of its different components.	2-26
224			
225	2.23	Slice showing CMS sub-detectors and how particles interact with them.	2-27
226			
227	2.24	The CMS tracker.	2-27
228	2.25	Figure 2.25a: The electromagnetic calorimeter. Figure 2.25b: The lead tungstate crystals composing the ECAL.	2-28
	2.26	The CMS hadron calorimeter barrel.	2-28

229	2.27	A quadrant of the muon system, showing DTs (yellow), RPCs (blue), and CSCs (green).	2-29
230			
231	3.1	The measured transit time of a HSCP in CMS is compared to the transit time of a particle traveling at near the speed of light [177].	3-2
232			
233	3.2	Slice of the CMS detector showing example of passage of SM particles and R-hadrons. On the one hand, lepton-like HSCPs will appear to behave like slow and heavy muons. On the other hand, R-hadrons are likely to convert into other kind of charged or neutral R-hadrons due to interactions inside the detector volume.	3-2
234			
235	3.3	Distribution of the energy-loss dE/dx as described by Bethe-Bloch formula through the estimator I_h with increasing particle momentum for tracks in the 13 TeV data. The estimator depends on the charge deposition of the particles per unit length in the silicon detectors of CMS which is related to their energy loss as explained in a publication by the CMS Collaboration [181]. The simulated HSCPs are singly or multiply charged particles with masses of 400 and 1000 GeV.	3-3
236			
237	3.4	Distribution of the average number of interactions per crossing (pileup) for pp collisions in 2011 (red), 2012 (blue), 2015 (purple), 2016 (orange), 2017 (light blue), and 2018 (navy blue). The overall mean values and the minimum bias cross sections are also shown [189].	3-4
238			
239	3.5	Absorbed dose in the CMS cavern after an integrated luminosity of 3000 fb^{-1} . Using the interaction point as reference, R is the transverse distance from the beamline and Z is the distance along the beamline [177].	3-4
240			
241	3.6	Figure 3.6a: Barrel wheel with its detector rings and return yokes. Figure 3.6b: CSC endcap disk with the 2 CSC stations. The outer station is made of 10 deg detectors while the inner station is made of 20 deg detectors. Figure 3.6c: RPC endcap disk. The inner station is not equipped and the inner CSC station can be seen.	3-5
242			
243	3.7	Figure 3.7a: Cross section of a DT module showing the two superlayers measuring the ϕ coordinate, perpendicular to the cross section plane, and the superlayer measuring the η coordinate, placed in between the two others with honeycomb and parallel to the cross section plane. The DT detector is sandwiched in between 2 RPCs whose readout strips are perpendicular to the cross section plane, measuring the ϕ coordinate. Figure 3.7b: A DT cell is shown together with its electric field. The path of a muon through a superlayer is shown.	3-6
244			
245	3.8	Figure 3.8a: Cathode strips and anode wire layout of a CSC panel. Figure 3.8b: Avalanche development and charge collection by anode wires and induction on cathode strips inside of a CSC panel.	3-7
246			
247	3.9	Muon track reconstruction through the 6 panels of a CMS CSC using the information of anode wire groups and cathode strip charge distribution combined with comparator bits to decide on which half strip the muon is more likely to have passed.	3-7
248			
249	3.10	Double gap layout of CMS RPCs. Muons passing through the gas volumes will create electron-ions pairs by ionising the gas. this ionisation will immediately translate into a developing avalanche.	3-8
250			
251	3.11	Extrapolated fraction of failing channels of the present DT MiC1 electronics as a function of the integrated luminosity for different scenari until LS4 [177].	3-8
252			
253	3.12	The event loss fractions as a function of the instantaneous luminosity is compared for CFEBs (Phase-1) and DCFEBs (Phase-2) at different CSC locations. HL-LHC luminosity is marked with the dashed brown line [177].	3-9
254			
255	3.13	Comparison of the simulated time residuals in between reconstructed and true muon times without (blue) and with (red) the upgraded RPC link system [177].	3-9
256			

325	3.24	Measured average charge per avalanche as a function of the effective electric field for different gas gap thickness in double-gap RPCs using HPL electrodes [177].	3-17
326			
327	3.25	Level-1 Trigger data flow during Phase-2 operations [177].	3-17
328			
329	3.26	Efficiency of the L1 trigger in the endcap region after Phase-2 upgrade in the case CSC/GEM/RPC hits are requested in at least 2 stations out of four (3.26a) and in all four stations (3.26b) [177].	3-18
330			
331	3.27	Comparison of L1 trigger performances for prompt muons with and without the ad- dition of GEMs in the region $2.1 < \eta < 2.4$ at Phase-2 conditions [177]. GEMs would allow a reduction of the trigger accept rate by an order of magnitude (Fig- ure 3.27a) while increasing the trigger efficiency (Figure 3.27b).	3-19
332			
333	3.28	The angular resolution on reconstructed muon tracks in the GEM overlap region $2.0 < \eta < 2.15$ is compared for Phase-2 conditions in the case CSC are alone (Figure 3.28a) and in the case the GEMs' data, including ME0, is combined to which of CSCs (Figure 3.28b) [177].	3-19
334			
335	3.29	Resolution of the LCT ambiguous events thanks to the combination of CSC and iRPC readout data. Using CSCs only, 2 pairs of hits are possible [177].	3-20
336			
337	3.30	Efficiency (Figure 3.30a) and cluster size (Figure 3.30b) of a standard double-gap RPC operated with CO_2 mixtures for different ratios of SF_6	3-21
338			
339	3.31	Efficiency of a CMS double-gap RPC operated with 30% of HFO , 4.5% of iC_4H_{10} , 1% of SF_6 and 64.5% of CO_2	3-21
340			
341	3.32	The efficiency (solid lines) and streamer probability (dashed lines) of HFO/CO_2 (Figure 3.32a) and CF_3I/CO_2 (Figure 3.32b) based gas mixtures as a function of the effective high-voltage are compared with the present CMS RPC gas mixture represented in black [177]. The detector used for the study is a single gap RPC with similar properties than CMS RPCs. The streamer probability is defined as the proportion of events with a deposited charge greater than 20 pC.	3-22
342			
343	3.33	Efficiency (open symbols) and cluster size (full symbols) of an iRPC as a function of the effective voltage for the standard CMS gas mixture and an environmental- friendly gas mixture. [177].	3-23
344			
345	4.1	Different phases of the avalanche development in the RPC gas volume subjected to a constant electric field E_0 . a) An avalanche is initiated by the primary ionisation caused by the passage of a charged particle through the gas volume. b) Due to its growing size, the avalanche starts to locally influence the electric field. c) The electrons, lighter than the cations reach the anode first. d) The ions reach the cathode. While the charges have not recombined, the electric field in the small region around the avalanche stays affected and locally blinds the detector.	4-2
346			
347	4.2	Movement of the charge carriers in an RPC. Figure 4.2a: Voltage across an RPC whose electrode have a relative permittivity of 5 at the moment the tension s applied. Figure 4.2b: After the charge carriers moved, the electrodes are charged and there is no voltage drop over the electrodes anymore. The full potential is applied on the gas gap only. Figure 4.2c: The streamer discharge initiated by a charged particle transports electrons and cations towards the anode and cathode respectively.	4-4
348			
349	4.3	Typical oscilloscope pulses in streamer mode (Figure 4.3a) and avalanche mode(Figure 4.3b). In the case of streamer mode, the very small avalanche signal is visible.	4-4
350			
351	4.4	Rate capability comparison for the streamer and avalanche mode of operation. An order of magnitude in rate capability for a maximal efficiency drop of 10% is gained by using the avalanche mode over the streamer mode.	4-5
352			
353			

- 372 4.5 Comparison of the charge distribution of signals induced by cosmic muons in an
373 RPC operated with a gas mixture of argon, butane and bromotrifluoromethane (CF_3Br).
374 The Ar/C_4H_{10} is kept constant at 60/40 in volume while the total amount of CF_3Br
375 in the mixture is varied: 0% (Figure 4.5a), 4% (Figure 4.5b) and 8% (Figure 4.5c) [208]. 4-6
- 376 4.6 Comparison of the efficiency and streamer probability, defined as the fraction of
377 events with an induced charge 10 times larger than that of the average avalanche,
378 with and without irradiation by a 24 GBq ^{137}Cs source of an RPC successively
379 operated with a 90/10 mixture $C_2H_2F_4/i-C_4H_{10}$ (Figure 4.6a) and a 70/5/10/15
380 mixture of $Ar/i-C_4H_{10}/CO_2/C_2H_2F_4$ (Figure 4.6b) [209]. 4-6
- 381 4.7 Comparison of the fast charge ratio with and without irradiation by a 24 GBq ^{137}Cs
382 source of an RPC successively operated with a 90/10 mixture $C_2H_2F_4/i-C_4H_{10}$
383 (Figure 4.7a) and a 70/5/10/15 mixture of $Ar/i-C_4H_{10}/CO_2/C_2H_2F_4$ (Figure 4.7b).
384 The results are provided for both single gap and double gap operation [209]. 4-7
- 385 4.8 Efficiency (circles and stars with 30 mV and 100 mV thresholds respectively) and
386 streamer probability (opened circles) as function of the operating voltage of a 2 mm
387 single gap HPL RPC flushed with a gas mixture containing (a) 5%, (b) 2%, (c) 1%
388 and (d) no SF_6 [211]. 4-8
- 389 4.9 Evolution of the efficiency, working voltage, and voltage at 50% of maximum ef-
390 ficiency for CMS Barrel (Figure 4.9a) and Endcap (Figure 4.9b) RPCs obtained
391 through yearly voltage scans since 2011. The working voltage of each RPC is up-
392 dated after each voltage scan to ensure optimal operation [226]. 4-9
- 393 4.10 Comparison of the rate capability of 8 mm and 2 mm wide RPCs. The lines are
394 linear fits on the data [228]. 4-10
- 395 4.11 Distributions of the induced charge of fast signals on 2 mm (Figure 4.11a) and 8 mm
396 (Figure 4.11b) RPCs exposed to a radiation rate of 100 Hz/cm². Average induced
397 charge of fast signals as a function of the high voltage applied on 2 mm and 8 mm
398 RPCs (Figure 4.11c). In the case of the 2 mm RPC, a saturation of the pre-amplifier
399 was observed. The average of the distribution is underestimated and the median is
400 showed together with the average to account for this bias [228]. 4-10
- 401 4.12 Time distributions of the leading, trailing, and average of both leading and trailing
402 edges for 2 mm (top row) and 8 mm (bottom row) RPCs exposed to a 100 Hz/cm²
403 radiation rate. The data was collected with RPCs operated at the voltage correspond-
404 ing to the knee of the efficiency distribution, defined as the point where 95% of the
405 maximum efficiency is obtained [228]. 4-11
- 406 4.13 Possible double-gap RPC layouts: a) "standard" 1D double-gap RPC, as used in
407 CMS experiment, where the anodes are facing each other and a 1D read-out plane
408 is sandwiched in between them, b) double read-out double-gap RPC as used in AT-
409 LAS experiment, where the cathodes are facing each other and 2 read-out planes are
410 used on the outer surfaces. This last layout can offer the possibility to use a 2D
411 reconstruction by using orthogonal read-out planes. 4-12
- 412 4.14 Comparison of performance of CMS double and single gap RPCs using cosmic
413 muons [224]. Figure 4.14a: Comparison of efficiency sigmoids. Figure 4.14b: Volt-
414 age distribution at 95% of maximum efficiency. Figure 4.14c: $\Delta_{10\%}^{90\%}$ distribution. 4-12
- 415 4.15 Representation of different RPC layouts (wide gap on Figure (a), double gap on
416 Figure (b) and multigap on Figure (c)), of the corresponding sensitive volume in
417 gray, and of the associated avalanche size [214]. 4-13

418	4.16 Time distributions of the leading, trailing, and average of both leading and trailing edges for multigap RPCs consisting in two 4 mm (Figure 4.16a) and four 2 mm (Figure 4.16b) exposed to a 100 Hz/cm ² radiation rate. The data was collected with RPCs operated at the voltage corresponding to the knee of the efficiency distribution, defined as the point where 95% of the maximum efficiency is obtained [214].	4-14
419		
420		
421		
422		
423	4.17 Presentation of a study of a possible ALICE MRPC cell using 250 µm gas gaps, 620 µm outer glass electrodes, and 550 µm inner floating electrodes (Figure 4.17a), and of its time resolution performance as a function of the applied high voltage for different radiation levels referred through different filter settings of the 740 GBq ¹³⁷ Cs source the former CERN GIF facility [229].	4-14
424		
425		
426		
427		
428	4.18 Particle identification applied to electrons in the STAR experiment. The identification is performed combining ToF and dE/dx measurements [234].	4-15
429		
430	4.19 Comparison of the detector performance of ALICE ToF MRPC [235] at fixed applied voltage (in blue) and at fixed effective voltage (in red). The effective voltage is kept fixed by increasing the applied voltage accordingly to the current drawn by the detector.	4-16
431		
432		
433	4.20 Ratio between total induced and drifting charge have been simulated for single gap, double-gap and multigap layouts [236]. The total induced charge for a double-gap RPC is a factor 2 higher than for a multigap.	4-17
434		
435		
436	4.21 Charge spectra have been simulated for single gap, double-gap and multigap layouts [236]. It appears that when single gap shows a decreasing spectrum, double and multigap layouts exhibit a spectrum whose peak is detached from the origin. The detachment gets stronger as the number of gaps increases.	4-17
437		
438		
439		
440	4.22 The maximal theoretical efficiency is simulated for single gap, double-gap and multi-gap layouts [236] at a constant gap thickness of 2 mm and using an effective Townsend coefficient of 9 mm ⁻¹	4-18
441		
442		
443	4.23 Mass stopping power as a function of $\beta\gamma = p/Mc$ for positive muons in copper [115]. The total stopping power is indicated with solid line and local components with dashed lines. the vertical bands are used to indicate boundaries between different approximations used at different energy range.	4-18
444		
445		
446		
447	4.24 Mean mass stopping power for liquid hydrogen, as used in bubble chambers, gaseous helium, carbon, aluminum, iron, tin, and lead without the inclusion of radiative effect at higher $\beta\gamma$ necessary for pions and muons in denser materials [115].	4-20
448		
449		
450	4.25 Mean excitation energies normalized to the atomic number as adopted by the ICRU [115, 240, 241].	4-21
451		
452	4.26 Mean mass stopping power at minimum ionization as a function of the atomic number [115].	4-21
453		
454	4.27 Example of straggling function $f(\Delta)$ of particles passing through 1.2 cm of Argon gas with a $\beta\gamma$ of 3.6 and represented with a solid line. The original Landau distribution is showed with a dashed line [242].	4-22
455		
456		
457	4.28 Evolution of straggling functions $f(\Delta)$ of particles passing through a volume of Argon gas with a $\beta\gamma$ of 3.6 with increasing thickness x [242].	4-22
458		
459	4.29 Photo-absorption cross section as computed by HEED for nobles gases with different electric shell numbers [238].	4-24
460		
461	4.30 Photo-absorption cross section as computed by HEED for typical RPC gas mixtures [238]. The RPC mixture with CO ₂ corresponds to the mixture used by CALICE SDHCAL [246] while the other one was foreseen for the experiment ATLAS [247] but has been changed since then.	4-25
462		
463		
464		

465	4.31 Distributions of number of electrons (left) and energy loss (right) for a 5 GeV/c muon passing through 1.2 mm of Helium (Figure 4.31a), Argon (Figure 4.31b) or a typical RPC gas mixture (Figure 4.31c) [238].	4-26
466		
467		
468	4.32 Figure 4.32a: Mean cluster density for muons through different gas volumes [238]. Figure 4.32b: Distribution of the number of electrons per cluster for a 5 GeV/c muon traveling through a mixture of 96.7% $C_2H_2F_4$, 3% i- C_4H_{10} and 0.3% SF_6 [238, 247].	4-27
469		
470		
471		
472	4.33 Townsend and attachment coefficient for a typical 96.7/3/0.3 mixture of $C_2H_2F_4$ /i- C_4H_{10} / SF_6 , at a temperature $T = 296.15$ K and a pressure $P = 1013$ hPa [238, 247].	4-28
473		
474		
475	4.34 Comparison of the distribution law of Furry and the Poisson law for $\bar{n} = 5$ [250].	4-28
476		
477		
478	4.35 Single-electron avalanche size distribution in a proportionnal counter filled with methylal at different E/p values. (a) 70, (b) 76.5, (c) 105, (d) 186.5, (e) 426V/cm torr [251].	4-29
479		
480		
481		
482	4.36 Figure 4.36a: Comparison of avalanche size distributions for different values of Townsend and attachment coefficients. The effective Townsend coefficient is the same for both distributions. Figure 4.36b: Fluctuation in avalanche size for avalanche started by a single electron with $\alpha = 13 \text{ mm}^{-1}$ and $\eta = 3.5 \text{ mm}^{-1}$ [247].	4-31
483		
484		
485		
486		
487	4.37 Figure 4.37a: Electron mean drift velocity v_D in pure $C_2H_2F_4$ and typical RPC gas mixtures. Figure 4.37b: Transverse diffusion coefficient in pure $C_2H_2F_4$ and a typical RPC gas mixture. Figure 4.37c: Longitudinal diffusion coefficient in pure $C_2H_2F_4$ and a typical RPC gas mixture. All results are given with a pressure $P = 760$ Torr and a temperature $T = 296.15$ K [238].	4-32
488		
489		
490	4.38 Comparison of the free charge carriers in the gas after a time $t = 7.90$ ns in the case where no diffusion is taken into account to simulate the avalanche (Figure 4.38a) and in the case where the diffusion is implemented (Figure 4.38b) [238].	4-32
491		
492	4.39 Schematic representation of an avalanche and of the electric field deformation it causes due to the local concentration of charge carriers [220].	4-34
493		
494		
495		
496		
497	4.40 Evolution of the charge induced by an avalanche started by a single electron in a 1.2 mm thick RPC with an applied electric field of 54 kV/cm in the case space charge is not taken into account (Figure 4.40a) and in the case it is implemented into the simulation (Figure 4.40b). The total induced charge is correlated to the size of the avalanche [238].	4-35
498		
499		
500	4.41 Distributions of charge carriers within the gas volume of a 1.2 mm thick RPC and the corresponding deformation of the electric field at different time steps with an applied electric field of 55.5 kV/cm [238].	4-36
501		
502		
503	4.42 Representation of the weighting field in the volume of a RPC and the resulting induced current in the strip placed at 1 V and its neighbour connected to the ground. The induced current corresponds, as can be understood from Formula 4.22 [220].	4-37
504		
505		
503	4.43 Schematics of CMS RPC FEE logic.	4-38
504		
505		
503	4.44 Equivalence in between the charge of the induced signal in input of the CMS FEE and the signal strength on the output of the pre-amplifier.	4-38
504		
505		

506	4.45 Description of the principle of a CFD. A comparison of threshold triggering (left) 507 and constant fraction triggering (right) is shown in Figure 4.45a. Constant fraction 508 triggering is obtained thanks to zero-crossing technique as explained in Figure 509 4.45b. The signal arriving at the input of the CFD is split into three components. 510 A first one is delayed and connected to the inverting input of a first comparator. A 511 second component is connected to the noninverting input of this first comparator. A 512 third component is connected to the noninverting input of another comparator along 513 with a threshold value connected to the inverting input. Finally, the output of both 514 comparators is fed through an AND gate.	4-39
515	4.46 Typical efficiency sigmoid of a CMS RPC detector. The black dots correspond to the 516 data, the blue line to the sigmoid fit and the opened cross to the knee and working 517 extracted from the fit line.	4-40
518	4.47 Effect of the temperature variation on the rate (Figure 4.47a) and the efficiency (Fig- 519 ure 4.47b) of a RPC [252].	4-41
520	4.48 Effect of the pressure variation on the rate (Figure 4.48a) and the efficiency (Fig- 521 ure 4.48b) of a RPC [253].	4-42
522	 5.1 Mean RPC Barrel (left column) and Endcap (right column) rate (top row) and current 523 (bottom row) as a function of the instantaneous luminosity as measured in 2017 p - p 524 collision data.	5-2
525	5.2 Figure 5.2a: The hit rate per region (Barrel, Endcap) is linearly extrapolated to 526 HL-LHC highest instantaneous luminosity ($5 \times 10^{34} \text{ cm}^{-2} \text{ s}^{-1}$) using the rate as 527 a function of instantaneous luminosity recorded by RPCs in 2017 showing a linear 528 dependence. Figure 5.2b: The integrated charge per region (Barrel, Endcap) is ex- 529 trapolated to HL-LHC integrated luminosity (3000 fb^{-1}) using the data accumulated 530 in 2016 in every HV channels.	5-3
531	5.3 CMS RPC mean integrated charge in the Barrel region (Figure 5.3a) and the Endcap 532 region (Figure 5.3b). The integrated charge per year is shown in blue. The red curve 533 shows the evolution of the accumulated integrated charge through time. The blank 534 period in 2013 and 2014 corresponds to LS1. The total integrated charge for the 535 entire operation period (Oct.2009 - Dec.2017) is estimated to be about 1.66 mC/cm^2 536 in the Barrel and 4.58 mC/cm^2 in the Endcap.	5-3
537	5.4 Layout of the test beam zone called X5c GIF at CERN. Photons from the radioactive 538 source produce a sustained high rate of random hits over the whole area. The zone is 539 surrounded by 8 m high and 80 cm thick concrete walls. Access is possible through 540 three entry points. Two access doors for personnel and one large gate for material. 541 A crane allows installation of heavy equipment in the area.	5-4
542	5.5 ^{137}Cs decays by β^- emission to the ground state of ^{137}Ba (BR = 5.64%) and via the 543 662 keV isomeric level of ^{137}Ba (BR = 94.36%) whose half-life is 2.55min.	5-5
544	5.6 Floor plan of the GIF++ facility. When the facility downstream of the GIF++ takes 545 electron beam, a beam pipe is installed along the beam line (z-axis). The irradiator 546 can be displaced laterally (its center moves from $x = 0.65 \text{ m}$ to 2.15 m), to increase 547 the distance to the beam pipe.	5-6
548	5.7 Simulated unattenuated current of photons in the xz plane (Figure 5.7a) and yz plane 549 (Figure 5.7b) through the source at $x = 0.65 \text{ m}$ and $y = 0 \text{ m}$ [262]. With angular 550 correction filters, the current of 662 keV photons is made uniform in xy planes.	5-6

- 551 5.8 Description of the RPC setup. Dimensions are given in mm. A tent containing RPCs
 552 is placed at 1720 mm from the source container. The source is situated in the center
 553 of the container. RE-4-2-BARC-161 chamber is 160 mm inside the tent. This way,
 554 the distance between the source and the chambers plan is 2060 mm. Figure 5.8a
 555 provides a side view of the setup in the xz plane while Figure 5.8b shows a top view
 556 in the yz plane. 5-7
- 557 5.9 RE-4-2-BARC-161 chamber is inside the tent as described in Figure 5.8. In the
 558 top right, the two scintillators used as trigger can be seen. This trigger system has an
 559 inclination of 10° relative to horizontal and is placed above half-partition B2 of the
 560 RPCs. PMT electronics are shielded thanks to lead blocks placed in order to protect
 561 them without stopping photons from going through the scintillators and the chamber. 5-8
- 562 5.10 Hit distributions over all 3 partitions of RE-4-2-BARC-161 chamber is showed.
 563 Top, middle and bottom figures respectively correspond to partitions A, B, and C.
 564 The profiles show that some events still occur in other half-partitions than B2, which
 565 corresponds to strips 49 to 64, in front of which the trigger is placed, contributing to
 566 the inefficiency of detection of cosmic muons. In the case of partitions A and C, the
 567 very low amount of data can be interpreted as noise. On the other hand, it is clear
 568 that a little portion of muons reach the half-partition B1, corresponding to strips 33
 569 to 48. 5-8
- 570 5.11 Signals from the RPC strips are shaped by the FEE described on Figure 5.11a.
 571 Output LVDS signals are then read-out by a TDC module connected to a computer or
 572 converted into NIM and sent to scalers. Figure 5.11b describes how these converted
 573 signals are put in coincidence with the trigger. 5-9
- 574 5.12 Results are derived from data taken on half-partition B2 only. On the 18th of June
 575 2014, data has been taken on chamber RE-4-2-BARC-161 at CERN building 904
 576 (Prevessin Site) with cosmic muons providing us a reference efficiency plateau of
 577 $(97.54 \pm 0.15)\%$ represented by a black curve. A similar measurement has been done
 578 at GIF on the 21st of July with the same chamber giving a plateau of $(78.52 \pm 0.94)\%$
 579 represented by a red curve. 5-10
- 580 5.13 Representation of the layout used for the simulations of the test setup. The RPC
 581 read-out plane is represented as a yellow trapezoid while the two scintillators as blue
 582 cuboids looking at the sky. The green plane corresponds to the muon generation
 583 plane within the simulation. Figure 5.8a shows a global view of the simulated setup.
 584 Figure 5.8b shows a zoomed view that allows to see the 2 scintillators as well as the
 585 full RPC plane. 5-11
- 586 5.14 Geometrical acceptance distribution as provided by the Monte Carlo simulation. . . . 5-12
- 587 5.15 Correction of the efficiency without source. The efficiency after correction gets
 588 much closer to the Reference measurement performed before the study in GIF by
 589 reaching a plateau of $(93.52 \pm 2.64)\%$ 5-13
- 590 5.16 Hit distributions over read-out partition B of RE-4-2-BARC-161 chamber to-
 591 gether with skew distribution fits corresponding to forward and backward coming
 592 muons. 5-14
- 593 5.17 Figure 5.17a shows the linear approximation fit performed on data extracted from
 594 table 5.2. Figure 5.17b shows a comparison of Formula 5.5 with the simulated flux
 595 using a and b given in figure 5.17a in formulae 5.3 and the reference value $D_0 =$
 596 50 cm and the associated flux for each absorption factor F_0^{ABS} from table 5.1 5-16

597	5.18	Efficiency (Figure 5.18a) and cluster size (Figure 5.18b) of chamber RE-4-2-BARC-161 measured at GIF with Source OFF (red) and Source ON using different absorber settings: ABS 5 (green), ABS 2 (blue) and ABS 1 (yellow). The results are compared to the Reference values obtained with cosmics.	5-17
598			
599			
600			
601	5.19	Rates in chamber RE-4-2-BARC-161 measured at GIF with Source OFF (red) and Source ON using different absorber settings: ABS 5 (green), ABS 2 (blue) and ABS 1 (yellow). On Figure 5.19b, the rates of Figure 5.19a were normalized to the measured efficiency and constant fits are performed on Source ON data showing the gamma rate in the chamber.	5-18
602			
603			
604			
605			
606	5.20	Evolution of the voltages at half maximum and at 95% of the maximum efficiency (Figure 5.20a), and of the maximum efficiency (Figure 5.20b) as a function of the rate in chamber RE-4-2-BARC-161. The data is extracted from the fits in Figures 5.18a and 5.19b.	5-18
607			
608			
609			
610	5.21	Presentation of a double-gap endcap RPC with its 3 RPC gaps. Due to the partitioning of the read-out strips into 3 rolls, the TOP layer of gap is divided into 2 gaps: TOP NARROW (TN) and TOP WIDE (TW). The BOTTOM (B) only consists in 1 gap.	5-19
611			
612			
613			
614	5.22	Current density and charge deposition per gamma avalanche, defined as the current density normalized to the measured rate taken from Figure 5.19a as a function of the effective high voltage in chamber RE-4-2-BARC-161 measured at GIF with Source ON using different absorber settings: ABS 5 (green), ABS 2 (blue) and ABS 1 (yellow).	5-20
615			
616			
617			
618			
619	5.23	Characterization of CMS RPC detectors foreseen to be used at GIF++ for longevity studies of the present system. Using cosmic muons, efficiency (Figure 5.23a) and cluster size (Figure 5.23b) were measured as well as noise rate (Figure 5.23c) and current density (Figure 5.23d). For each detector, the working voltage, defined as in Formula 4.25, was extracted from sigmoid fits performed in Figure 5.23a and the values of efficiency, cluster size, noise rate and current density at this voltage are reported using open crosses.	5-21
620			
621			
622			
623			
624			
625			
626	5.24	CMS RPC setup inside of GIF++ bunker during test beam (Figure 5.24a) and ageing periods (Figure 5.24b). The space in between the RPCs and the source is usually used by other detectors while the space in between T1 and the upstream wall is not filled. Due to the presence of the beam pipe, the trolley is moved away from the beam line during irradiation periods and placed further away from the source for less intense irradiation. The position of the trolley can vary due to the use of the space by other setups and is then not exact. In the contrary, the position of the chambers in the trolley is fixed and given in Figure 5.24c.	5-23
627			
628			
629			
630			
631			
632			
633			
634	5.25	Visualtions of the main data flows in GIF++. The yellow flow lines corresponds to the DIP flow used for source, environmental and gas information. The red flow lines are for the CAEN flow through which the WebDCS communicates the voltages to be applied on the detectors using pressure and temperature informformation and retrieves the monitored voltages and currents. Finally, the blue flow lines corresponds to the DAQ flow through which the RPC data is collected from the TDCs by the computer.	5-24
635			
636			
637			
638			
639			
640			
641	5.26	DIP monitoring history accessed through GIF++ WebDCS interface.	5-25
642			
643	5.27	Example of DQM page available on CMS RPC WebDCS in GIF++. Here is presented the rate measured in one of the tracking chabers, namely GT1_20_20-BKL_JUL16_4. The DQM page allows to click on each histogram to extend its view and to navigate through the histograms thanks to the left and right arrows.	5-27
644			
645			

646 5.28 Example of DQM ROOT Browser page available on CMS RPC WebDCS in GIF++. 647 Here is presented the strip activity profile, defined as the rate profile normalized to 648 the mean rate, in one of the tracking chambers, namely GT1_20_20-BKL_JUL16_4. 649 Available ROOT files and histograms can be browsed thanks to the left panel showing 650 the directory and files structures.	5-28
651 5.29 Longevity statistics of chamber RE2-2-NPD-BARC-9 in GIF++. For each month 652 since July 2017, the integrated charge (in blue) as well as the time efficiency of 653 irradiation (in gray) is reported.	5-28
654 5.30 Example of current monitoring (Figure 5.30a) and of corresponding integrated charge 655 (Figure 5.30b) of chamber RE2-2-NPD-BARC-09. The decrease of current are related 656 to a decrease of the voltage due to the daily rate scan procedure or to periods 657 during which the source was turned OFF.	5-29
658 5.31 Example of rate (Figure 5.31a) and current (Figure 5.31b) monitoring of chamber 659 RE2-2-NPD-BARC-09 with increasing integrated charge. The variations of rate 660 and current are correlated and corresponds to change of source irradiation, gas flow, 661 gas humidity, or environmental conditions.	5-30
662 5.32 Example of strip activity of chamber RE2-2-NPD-BARC-09 monitoring through 663 time. The activity of a strip is defined as the rate of the individual channel normalized 664 to the mean rate measured in the corresponding read-out partition.	5-31
665 5.33 Total integrated charge in the irradiated RPCs, RE2-2-NPD-BARC-9 and RE4-2-CERN-165, 666 before starting August 2018 test beam period. The irradiation of the RE2 chamber 667 started in June 2016 while the RE4 chamber couldn't be irradiated before November 668 2016.	5-33
669 6.1 PETIROC 2A block diagram.	6-2
670 6.2 The PETIROC time jitter as a function of the input signal amplitude, measured with 671 and without internal clocks.	6-3
672 A.1 (A.1a) View of the front panel of a V1190A TDC module [263]. (A.1b) View of the 673 front panel of a V1718 Bridge module [264]. (A.1c) View of the front panel of a 6U 674 6021 VME crate [276].	A-3
675 A.2 Module V1190A <i>Trigger Matching Mode</i> timing diagram [263].	A-4
676 A.3 Structure of the ROOT output file generated by the DAQ. The 5 branches (<code>EventNumber</code> , 677 <code>number_of_hits</code> , <code>Quality_flag</code> , <code>TDC_channel</code> and <code>TDC_TimeStamp</code>) are visible on 678 the left panel of the ROOT browser. On the right panel is visible the histogram cor- 679 responding to the variable <code>nHits</code> . In this specific example, there were approximately 680 50k events recorded to measure the gamma irradiation rate on the detectors. Each 681 event is stored as a single entry in the <code>TTree</code>	A-10
682 A.4 The effect of the quality flag is explained by presenting the content of <code>TBranch</code> 683 <code>number_of_hits</code> of a data file without <code>Quality_flag</code> in Figure A.4a and the con- 684 tent of the same <code>TBranch</code> for data corresponding to a <code>Quality_flag</code> where all TDCs 685 were labelled as <code>GOOD</code> in Figure A.4b taken with similar conditions. It can be noted 686 that the number of entries in Figure A.4b is slightly lower than in Figure A.4a due 687 to the excluded events.	A-12
688 A.5 Using the same data as previously showed in Figure A.4, the effect of the quality 689 flag is explained by presenting the reconstructed hit multiplicity of a data file with- 690 out <code>Quality_flag</code> in Figure A.5a and the reconstructed content of the same RPC 691 partition for data corresponding to a <code>Quality_flag</code> where all TDCs were labelled as 692 <code>GOOD</code> in Figure A.5b taken with similar conditions. The artificial high content of bin 693 0 is completely suppressed.	A-12

694	A.6	WebDCS DAQ scan page. On this page, shifters need to choose the type of scan (Rate, Efficiency or Noise Reference scan), the gamma source configuration at the moment of data taking, the beam configuration, and the trigger mode. These information will be stored in the DAQ ROOT output. Are also given the minimal measurement time and waiting time after ramping up of the detectors is over before starting the data acquisition. Then, the list of HV points to scan and the number of triggers for each run of the scan are given in the table underneath.	A-14
701	B.1	Example of expected hit time distributions in the cases of efficiency (Figure B.1a) and noise/gamma rate per unit area (Figure B.1b) measurements as extracted from the raw ROOT files. The unit along the x-axis corresponds to ns. The fact that "the" muon peak is not well defined in Figure B.1a is due to the contribution of all the RPCs being tested at the same time that don't necessarily have the same signal arrival time. Each individual peak can have an offset with the ones of other detectors. The inconsistancy in the first 100 ns of both time distributions is an artefact of the TDCs and are systematically rejected during the analysis.	B-16
709	B.2	The effect of the quality flag is explained by presenting the reconstructed hit multiplicity of a data file without <code>Quality_flag</code> . The artificial high content of bin 0 is the effect of corrupted data.	B-21
718	B.3	Display of the masking tool page on the webDCS. The window on the left allows the shifter to edit <code>ChannelsMapping.csv</code> . To mask a channel, it only is needed to set the 3rd field corresponding to the strip to mask to 0. It is not necessary for older mapping file formats to add a 1 for each strip that is not masked as the code is versatile and the default behaviour is to consider missing mask fields as active strips. The effect of the mask is directly visible for noisy channels as the corresponding bin turns red. The global effect of masking strips will be an update of the rate value showed on the histogram that will take into consideration the rejected channels.	B-28

List of Tables

720

721	3.1	Details of the greenhouse fluorinated gases used in CMS and of their GWP [177]. . .	3-20
722	4.1	Properties of the most used electrode materials for RPCs.	4-3
723	5.1	Total photon flux ($E\gamma \leq 662$ keV) with statistical error predicted considering a 724 ^{137}Cs activity of 740 GBq at different values of the distance D to the source along 725 the x-axis of irradiation field [260].	5-14
726	5.2	Correction factor c is computed thanks to Formula 5.4 taking as reference $D_0 =$ 727 50 cm and the associated flux F_0^{ABS} for each absorption factor available in table 5.1.	5-15
728	5.3	The data at D_0 in 1997 is taken from [260]. Using Formula 5.5, the flux at D , 729 including an error of 1 cm, can be estimated in 1997. Then, taking into account the 730 attenuation of the source activity, the flux at D can be estimated at the time of the 731 tests in GIF in 2014. Assuming a sensitivity of the RPC to $\gamma s = 2 \times 10^{-3}$, an 732 estimation of the hit rate per unit area is obtained.	5-16
733	5.4	Summary of the characterization measurement performed in Ghent on CMS RPC 734 detectors foreseen to be used at GIF++ for longevity studies of the present system. 735 For each detector, the working voltage, defined as in Formula 4.25, was extracted 736 from sigmoid fits performed in Figure 5.23a and the values of efficiency, cluster 737 size, noise rate and current density at this voltage are reported.	5-22
738	A.1	Inter-process communication cycles in between the webDCS and the DAQ through 739 file string signals.	A-18

List of Acronyms

List of Acronyms

742	AFL	Almost Full Level
743	ALCTs	Anode local charged track boards
744	BARC	Bhabha Atomic Research Centre
745	BCS	Bardeen–Cooper–Schrieffer
746	BLT	Block Transfer
747	BMTF	Barrel Muon Track Finder
748	BNL	Brookhaven National Laboratory
749	BSM	Physics beyond the Standard Model
750	BR	Branching Ratio
751	CAEN	Costruzioni Apparecchiature Elettroniche Nucleari S.p.A.
752	CERN	European Organization for Nuclear Research
753	CFD	Constant Fraction Discriminator
754	CFEBs	cathode front-end boards
755	CKM	Cabibbo–Kobayashi–Maskawa
756	CMB	Cosmic Microwave Background
757	CMS	Compact Muon Solenoid
758	CSC	Cathode Strip Chamber
759	CuOF	copper-to-optical-fiber translators
760	DAQ	Data Acquisition
761	DCS	Detector Control Software
762	DMBs	Data acquisition mother boards
763	DQM	Data Quality Monitoring
764	DT	Drift Tube
765	EDM	electric dipole moment
766	ECAL	electromagnetic calorimeter
767	EMTF	Endcap Muon Track Finder
768	FCC	Future Circular Collider
769	FEB	Front-End Board
770	FEE	Front-End Electronics
771	FWHM	full-width-at-half-maximum
772	GEANT	GEometry ANd Tracking - a series of software toolkit platforms developed by CERN
773		
774	GEB	GEM Electronics board
775	GEM	Gas Electron Multiplier
776	GIF	Gamma Irradiation Facility
777	GIF++	new Gamma Irradiation Facility
778	GWP	Global Warming Potential
779	HCAL	hadron calorimeter

780	HEP	High-Energy Physics
781	HL-LHC	High Luminosity LHC
782	HPL	High-pressure laminate
783	HSCPs	Heavy Stable Charged Particles
784	HV	High Voltage
785	ICRU	International Commission on Radiation Units & Measurements
786	iRPC	improved RPC
787	IRQ	Interrupt Request
788	ISR	Intersecting Storage Rings
789	LEIR	Low Energy Ion Ring
790	LEP	Large Electron-Positron
791	LHC	Large Hadron Collider
792	LS1	First Long Shutdown
793	LS2	Second Long Shutdown
794	LS3	Third Long Shutdown
795	LSP	lightest supersymmetric particle
796	LV	Low Voltage
797	LVDS	Low-Voltage Differential Signaling
798	MC	Monte Carlo
799	MCNP	Monte Carlo N-Particle
800	MiC	Minicrate electronics
801	MiC1	first version of Minicrate electronics
802	mip's	minimum ionizing particles
803	MRPC	Multigap RPC
804	MSSM	Minimal Supersymmetric Standard Model
805	mSUGRA	minimal SUper GRAvity
806	NIM	Nuclear Instrumentation Module logic signals
807	OH	Optohybrid Board
808	OMTF	Overlap Muon Track Finder
809	OTMBs	Optical TMBs
810	PAI	Photo-Absorption Ionisation
811	PAIR	Photo-Absorption Ionisation with Relaxation
812	PMT	PhotoMultiplier Tube
813	PS	Proton Synchrotron
814	PU	pile-up
815	QCD	Quantum Chromodynamics
816	QED	Quantum Electrodynamics
817	RADMON	Radiation Monitoring
818	RMS	Root Mean Square
819	ROOT	a framework for data processing born at CERN
820	RPC	Resistive Plate Chamber
821	SC	Synchrocyclotron
822	SiPM	Silicon Photomultiplier
823	SLAC	Stanford Linear Accelerator Center
824	SM	Standard Model
825	SPS	Super Proton Synchrotron
826	SUSY	supersymmetry
827	TDC	Time-to-Digital Converter
828	TDR	Technical Design Report

829	TMBs	Trigger mother boards
830	ToF	Time-of-flight
831	TPG	trigger primitives
832	webDCS	Web Detector Control System
833	WIMPs	Weakly Interacting Massive Particles
834	YETS	Year End Technical Stop

1

835

836

Introduction

837 Grasping an understanding of the world in which they are leaving in has always been part of human
838 life. Beyond the metaphysical questioning of our origins and purpose, curiosity has brought mankind
839 to question its surroundings. Following the philosophy of the ancient Greeks and Indians came
840 the development of the sciences as the systematic experimentation aimed at testing hypothesis and
841 reproducing results obtained by fellow natural philosophers. With the industrial revolution and the
842 organisation of science, it became possible to go always further in the understanding of the universe
843 and of the matter in particular. Investigation on the constituent of matter proved to require more
844 and more powerful machines in order to break apart the bricks of the world into ever smaller pieces,
845 study their behaviour and extract new knowledge to help the development of humanity. So far, the
846 largest and most powerful machine that was built to study the particles composing matter and test
847 the models thought by physicists to explain their behaviour is the Large Hadron Collider (LHC),
848 a circular particle accelerator used to collide protons and heavy ions. After only a few years of
849 investigations conducted thanks to the LHC, several discoveries, predicted by the existing models,
850 have been made. In the future, in order to boost the discovery potential on the LHC and be able to
851 test hypotheses lying beyond the already acknowledged models, the instantaneous luminosity, i.e.
852 the rate of particle interactions, will be slightly increased into a so-called High Luminosity phase to
853 boost its discovery potential.

854 As the Large Hadron Collider will see its instantaneous luminosity be increased, the detectors
855 on the different experimental sites will have to suffer an increased background irradiation due to the
856 byproducts of the interaction of the beams with the infrastructure. This will cause for the detectors
857 a stress which implications need to be understood throughout the High Luminosity LHC (HL-LHC)
858 phase of operations. In the case of the Compact Muon Solenoid (CMS) experiment, it is important
859 to understand if the detectors that will be subjected to the higher levels of radiation will be able to
860 sustain higher detection rates while displaying the same performance they have so far been operated
861 at and if this level of performance of the detectors will stay stable for a period longer than ten years.
862 More specifically, the detectors placed very close to the beam line will be the most subjected to the
863 change of luminosity. In CMS, the endcap detectors will then be particularly affected by the stronger

864 background radiation. The endcap detectors compose a part of the muon system of CMS and among
865 them, the Resistive Plate Chamber (RPC) plays a key role in providing the experiment a reliable
866 trigger on potentially interesting data. This PhD work takes place into this very specific context of
867 muon detector consolidation and certification for the HL-LHC period in order to provide the CMS
868 experiment with robust new detectors and confirm that the present system will survive through the
869 next 20 years.

870 CMS experiment main focus revolves around testing the Standard Model (SM) of particle physics
871 using a multipurpose detector design to detect the interaction products of the protons and ions col-
872 liding along the LHC. Looking at the successive evolution of the theoretical models that gave birth
873 to the SM, the need for very intense particle beams in high energy physics experiment becomes clear
874 in that the higher the center-of-mass energy for each interaction, the greater the probe on very small
875 cross-section processes predicted by the theory, justifying the successive increase in beam energy
876 and intensity at LHC.

877 The implications for LHC experiments and in particular for the CMS detector explain the need for
878 longevity and rate capability studies conducted on the Resistive Plate Chambers which are an impor-
879 tant part of its Muon System as it is needed to certify the quality of operation of the trigger detectors
880 throughout the lifetime of HL-LHC.

881 RPCs are gaseous detectors which physics principles are non trivial and are still being investigated.
882 Nevertheless, key processes driving the electron multiplication in the gas volume, rate capability and
883 ageing have been successfully identified and will define the parameters that will have to be taken into
884 consideration while producing the detectors extending the pseudo-rapidity coverage of RPCs toward
885 the beam line as well as the ones to be monitored during the on-going longevity and rate capability
886 certification campaign.

887 On the one hand, the present RPC sub-system consists in two different RPC productions. Indeed,
888 most of the RPC detectors were produced in view of the start of LHC activities in 2010. These detec-
889 tors were build in between 2007 and 2008 to equip the barrel and the three disks of each endcaps of
890 the CMS apparatus. But during the First Long Shutdown (LS1) of LHC in between end of 2012 and
891 2015, a fourth disk of endcap was added in order to reinforce the redundancy of the endcap trigger.
892 Hence, new RPC detectors using the same technology were built in between 2012 and 2013. These
893 two sets of detector productions only differ in the properties of the High-pressure laminate (HPL)
894 used for their electrodes that could lead to a different ageing rate. This is why spare detectors of
895 both production periods have been tested over the past years to certify their good operation through
896 HL-LHC.

897 On the other hand, producing detectors to equip a highly irradiated region such as the extension of
898 CMS RPC endcaps requires to substantially improve the ageing properties of the chosen technology
899 by reducing the charge deposition per ionizing particle. This can be achieved both by modifying the
900 design of the detector volume or by improving the signal to noise ratio of the Front-End Electron-
901 ics (FEE) used to process the charge collected by the read-out strips making them more sensitive to
902 weaker signals. Two improved RPC (iRPC) designs were selected and tested in order to extend of
903 CMS endcap coverage.

904 Thanks to the study presented in this document, preliminary conclusions will be brought on the pro-
905 duction of iRPCs and on the longevity of the present RPC system, providing with a better understand
906 of the future performance of the RPC sub-system within the CMS experiment.

2

907

908

Investigating the TeV scale

909 Throughout history, physics experiment became more and more powerful in order to investigate finer
910 details of nature to help understanding the building blocks of matter and the fundamental interactions
911 that bind them in the microscopic world. Nowadays, the Standard Model of particle physics is the
912 most accurate theory designed to explain the behaviour of particles and is able to make very precise
913 predictions that are constantly verified. Nevertheless, some hints of new physics are visible as bricks
914 are still missing to obtain a global description of the Universe.

915 To highlight the limits of the SM and test the different alternative theories, evermore powerful
916 machines are needed. It is in this context that the Large Hadron Collider has been thought and built
917 to accelerate and collide particles at energies exceeding anything that had been done before. Higher
918 collision energies and high pile-up imply the use of enormous detectors to measure the properties of
919 the interaction products. The Compact Muon Solenoid is a multipurpose experiment that have been
920 designed to study the proton-proton collisions of the LHC and give answers on various high-energy
921 physics scenarios such as different supersymmetry (SUSY) extensions to the Standard Model or
922 Extra Dimensions models.

923 This Chapter will be the occasion to go through the history of the Standard Model of Particle
924 Physics to understand the research conducted today in High-Energy Physics (HEP) facilities. From
925 the discovery of the atom and of its inner structure to the development of the theories governing
926 the fundamental interactions, all the elements leading to the construction SM will be discussed.
927 Furthermore, highlights on the Physics beyond the Standard Model (BSM) will be given to replace
928 the document in the context of today's research. Finally, a full description of the LHC and of the
929 CMS detector will be provided.

930 2.1 The Standard Model of Particle Physics

931 In the early 21st century it is now widely accepted that matter is made of elementary blocks referred
932 to as *elementary particles*. The physics theory that classifies and describes the best the behaviour and
933 interaction of such elementary particles is the so-called Standard Model. The SM formalizes three of

934 the four fundamental interactions (electromagnetic, weak and strong interactions). Its development
 935 happened since the 1960s thanks to a strong collaboration between theoretical and experimental
 936 physicists.

937 2.1.1 A history of particle physics

938 The idea that nature is composed of elementary bricks, called *atomism*, is not contemporary as it
 939 was already discussed by Indian or Greek philosophers during antiquity. In Greece, atomism has
 940 been rejected by *Aristotelianism* as the existence of *atoms* would imply the existence of a void that
 941 would violate the physical principles of Aristotle philosophy. Aristotelianism has been considered
 942 as a reference in the european area until the 15th century. With the *Rinascimento*, antic text and
 943 history started to be more deeply studied. The re-discovery of Platon's philosophy allowed opening
 944 the door to alternative theories and give a new approach to natural sciences where experimentation
 945 would become central. A new era of knowledge was starting. By the beginning of the 17th century,
 946 atomism was re-discovered by philosophers. The very first attempt at estimating the number of
 947 *particles* in a volume was provided by Magnenus in 1646 by calculating that the number of *particles*
 948 in a stick of incense [1]. He found a value of the order of 10^{18} simply by considering the time
 949 necessary to smell it everywhere in a large church after the stick was lit on. It is now known that this
 950 number only falls short only by 1 order of magnitude.

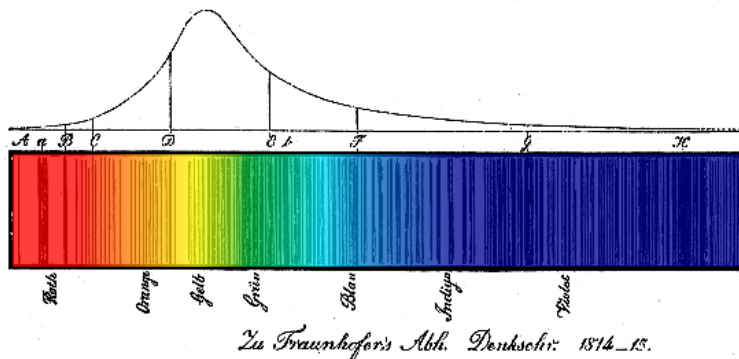


Figure 2.1: Solar spectrum with spectral lines as it visually appeared to Fraunhofer.

951 An alternative philosophy to atomism popularized by Descartes was *corpuscularianism*. Built on
 952 ever divisible corpuscles, contrary to atoms, its principles were mainly used by alchemists like New-
 953 ton who would later develop a corpuscular theory of light. Boyle combined together ideas of both
 954 atomism or corpuscularianism leading to mechanical philosophy. The 18th century has seen the
 955 development of engineering providing philosophical thought experiments with repeatable demon-
 956 stration and a new point of view to explain the composition of matter. Lavoisier greatly contributed
 957 to chemistry and atomism by publishing in 1789 a list of 33 chemical elements corresponding to
 958 what are now called *atoms* [2]. In the early 19th century Dalton summarized the knowledge on
 959 composition of matter [3]. In his atomic model, the atoms are ball-like constituents of the chemical
 960 elements. All atoms of a given element are identical, in size, mass, and other properties while the
 961 atoms of different elements differ. He also considered that atoms cannot be divided into smaller
 962 particles, created nor destroyed and that they combine into chemical compounds. The essence of
 963 chemical reaction was then the combination, separation or rearrangement of atoms. Soon after,

964 Fraunhofer invented the spectrometer and discovered the spectral lines in the sunlight spectrum, as
 965 showed in Figure 2.1 [4]. These were later linked to the absorption by chemical elements present in
 966 the solar atmosphere by Kirchhoff and Bunsen. The rise of atomic physics, chemistry and mathe-
 967 matical formalism unraveled the different atomic elements and ultimately, the 20th century saw the
 968 very first sub-atomic particles.

969 **Discovery of the inner structure of the atom**

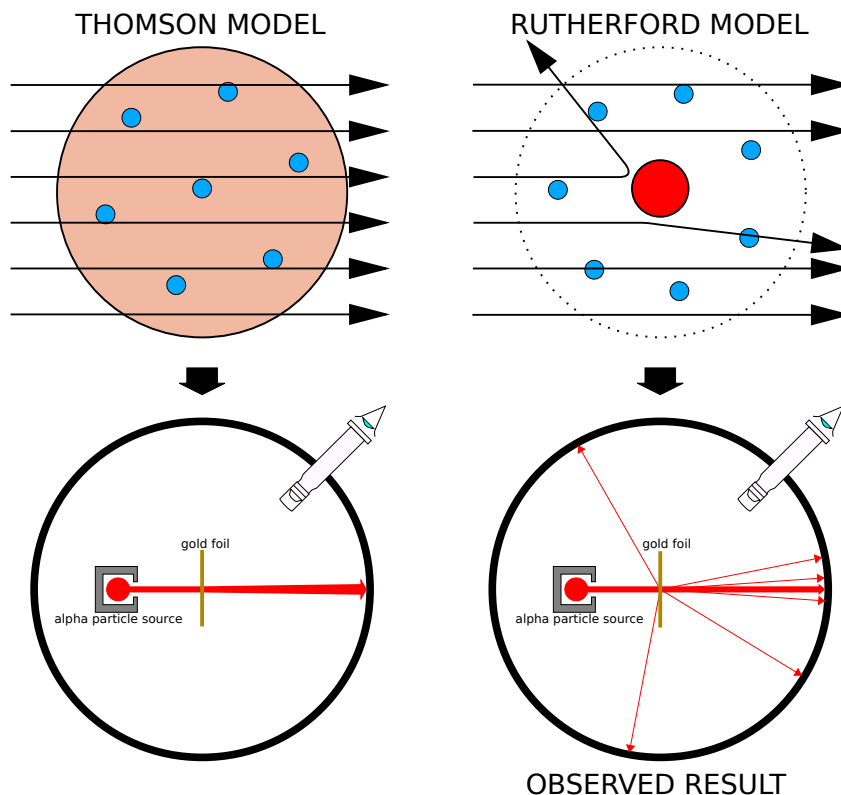
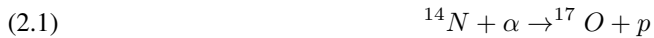


Figure 2.2: Through the gold foil experiment, Rutherford could show that most of the mass of atoms was contained in a positively charged nucleus and could then propose a more accurate atomic model than that of Thomson.

970 The negatively charged *electron* was the first to be discovered in 1897 by Thomson after three
 971 decades of research on cathode rays [5]. He proved that the electrification observed in an elec-
 972 troscope, as reported by Perrin [6], was due to the rays themselves. Hence, they had to be composed
 973 of electrically charged particles. In 1900, Becquerel showed the *beta rays* emitted by radium had the
 974 same charge over mass ratio as was measured by Thomson for cathode rays, pointing to electrons as
 975 a constituent of atoms [7]. This discovery leads to Thomson's plum pudding atomic model in which
 976 electrons are embed into a uniform positively charged atom [8]. In 1907, Rutherford and Royds
 977 showed that *alpha* particles were helium ions [9]. Indeed, once captured in a tube and subjected to
 978 an electric spark causing an electron avalanche, they could combine with two electrons to form a
 979 ${}^4\text{He}$.

This discovery was directly followed by the constraint of the atom structure in between 1908 and 1913 through the Geiger–Marsden gold foil experiments in which the deflection angle of alpha particles fired at a very thin gold foil was measured [10–13]. It highlighted that atoms were mainly empty with nearly all their mass contained into a tiny positively charged *nucleus*. With these two observations, Rutherford could formulate the Rutherford planetary model of the atom in 1911 [14], shown together with the Thomson plum pudding model in Figure 2.2. The link between atomic number and number of positive and negative charges contained into the atoms would fast be understood. Hence, the different kinds of element transmutations appeared to be purely nuclear processes making clear that the electromagnetic nature of chemical transformations could not possibly change nuclei. A new branch in physics appeared to exclusively study nuclei: *nuclear physics*. By studying alpha emission and the product of their interaction with nitrogen gas, Rutherford reported in 1919 the very first nuclear reaction [15]. It leads to the discovery that the hydrogen nucleus was composed of a single positively charged particle that was later baptised *proton* [16]. This idea came from 1815 Prout’s hypothesis proposing that all atoms are composed of “*protyle*” (i.e. hydrogen atoms) [17, 18]. By using scintillation detectors, Rutherford could highlight typical hydrogen nuclei signature and understand that the impact of alpha particles with nitrogen would knock out a hydrogen nucleus and produce an oxygen 17, as showed in Formula 2.1 and would then postulate that protons are building bricks of all elements.



With this assumption and the discovery of *isotopes* together with Aston, elements with identical atomic number but different masses, Rutherford proposed that all elements’ nuclei but hydrogen are composed of both charged particles, protons, and of chargeless particles, which he called *neutrons* [16, 19]. These neutral particles helped maintaining nuclei as one, as charged protons were likely to electrostatically repulse each other. He then introduced the idea of a new force, a *nuclear* force. The first idea concerning neutrons was a bond state of protons and electrons as it was known that the beta decay, emitting electrons, was taking place in the nucleus. However, it was then shown that electrons being confined into the nucleus would hardly be possible due to Heisenberg’s uncertainty principle. Finally, in 1932, following the discovery of a new neutral radiation, Chadwick could discover the neutron as an uncharged particle with a mass similar to that of the proton which would solve the nucleus puzzle [20–24].

1009 Development of the Quantum Electrodynamics

Historically, the development of the quantum theory revolved around the question of emission and absorption of discrete amount of energy through light. Einstein used the initial intuition of Planck about the black-body radiation to develop in 1905 a model to explain the photoelectric effect in which light was described by discrete *quanta* now called *photons* [25, 26]. For this model, Einstein introduced the concept of wave-particle duality as classical theory was not able to describe the phenomenon. With the new understanding of atoms and of their structure, classical theories also proved unable to explain atoms’ stability. Indeed, using classical mechanics, electrons orbiting around a nucleus should radiate an energy proportional to their angular momentum and hence, loose energy through time and the spectrum of energy emission should then be continuous. However, it was known since the 19th century and the discovery of spectral lines that the emission spectrum of material was discrete [4].

In 1913, quantum physics was introduced into the atomic model by Bohr to overcome the electron's energy loss due to orbiting radiation emission [27]. Using the correspondence principle stating that for large enough numbers the quantum calculations should give the same results than the classical theory, he proposed the very first quantum model of the hydrogen atom explaining the line spectrum by introducing the *principal quantum number* n describing the electron shell. The same year, Moseley confirmed Bohr's model through the Moseley's law [28]. Debye and then Sommerfeld extended it by introducing the quantization of the angular momentum [29]. The quantization the z-component of the angular momentum led to the *second and third quantum numbers*, or *azimuthal and magnetic quantum number*, l and m . The second defines the orbital angular momentum of the electrons on their shells and hence, the shape of the orbital, while the third the available orbital on the subshell for each electron as shown in Figure 2.3.

Nevertheless, although the model was not only limited to spherical orbitals anymore, making the atom more realistic, the Zeeman effect couldn't be completely explained by just using n , l and m [30–33] nor could the result of the Stern-Gerlach experiment [34]. Both experiments are shown in Figure 2.4. A solution was brought after Pauli in 1925 proposed together with his exclusion principle the idea of a new quantum degree of freedom in order to resolve the apparent problem [35, 36]. This degree of freedom was interpreted as an intrinsic angular momentum vector associated to the particle itself, not to the orbital [37], and associated to a new quantum number s , the *spin projection quantum number* explaining the lift of degeneracy to an even number of energy levels [38]. The new quantum number helped in theorizing the neutron as a neutral particle rather than a bond state of a proton and an electron confined in the nucleus itself.

The introduction of the *spin* happened one year after another attempt of improvement of the theory was made by De Broglie in his Ph.D. thesis [39]. The original formulation of the quantum theory only considered photons as energy quanta behaving as both waves and particles. De Broglie proposed that *all* matter are described by waves and that

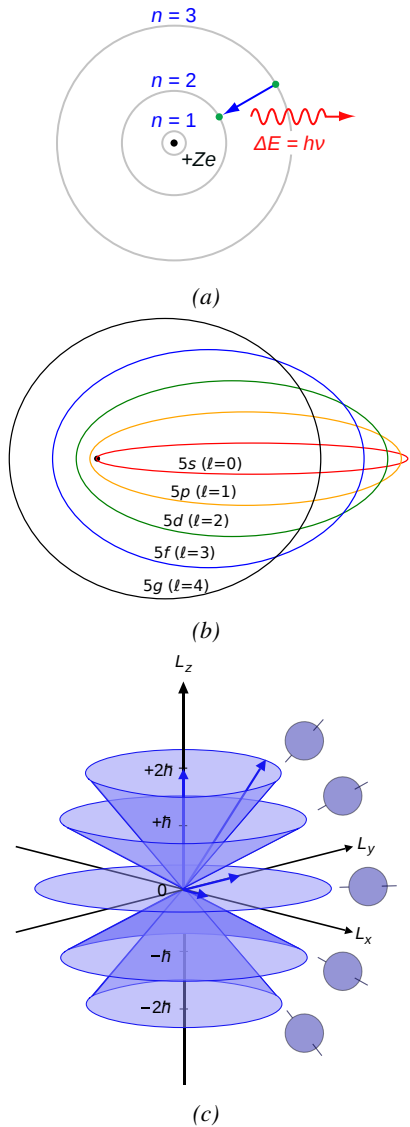


Figure 2.3: Figure 2.3a: The orbits in which the electron may travel according to the Bohr model of the hydrogen atom. An electron jumps between orbits and is accompanied by an emitted or absorbed amount of electromagnetic energy ($h\nu$). The orbits radius increases as n^2 . Figure 2.3b: Elliptical orbits with the same energy and quantized angular momentum $l = 0, 1, \dots, n - 1$ in the case $n = 5$. Figure 2.3c: Illustration of quantum mechanical orbital angular momentum. The cones and plane represent possible orientations of the angular momentum vector for $l = 2$ and $m = -2, -1, 0, 1, 2$.

their momentum is proportional to the oscillation of quantized electromagnetic field oscillators. This interpretation was able to reproduce the previous version of the quantum energy levels by showing that the quantum condition involves an integer multiple of 2π , as shown by Formula 2.2.

$$(2.2) \quad p = \hbar k \Leftrightarrow \int pdx = \hbar \int kdx = 2\pi\hbar n$$

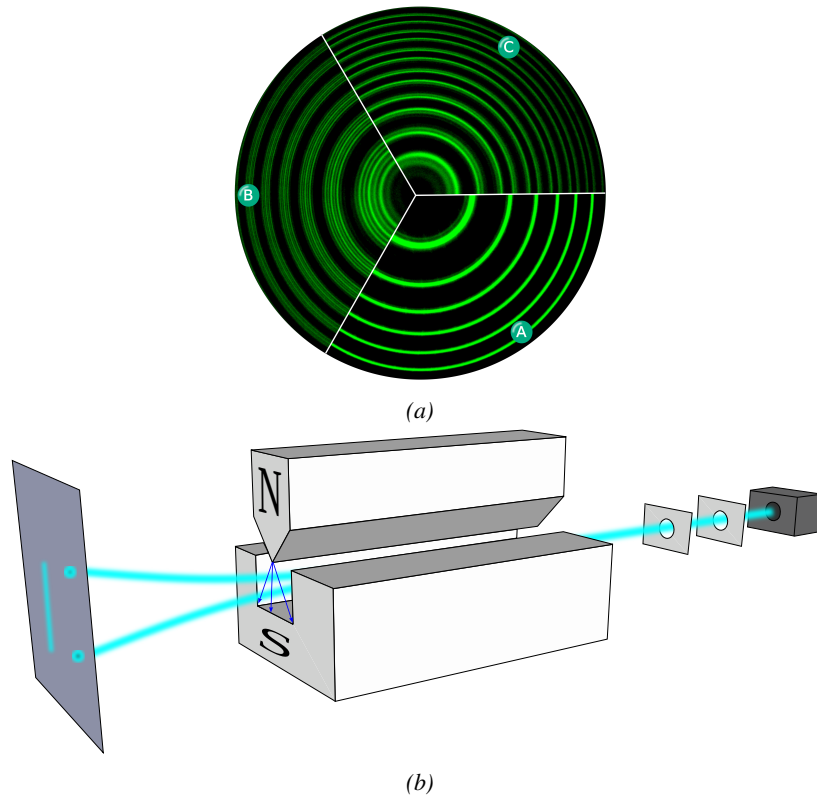


Figure 2.4: Figure 2.4a: The spectral lines of mercury vapor lamp anomalous Zeeman effect without magnetic field (A) and with magnetic field (B - transverse Zeeman effect & C - longitudinal Zeeman effect). Figure 2.4b: Stern-Gerlach experiment: Silver atoms traveling through an inhomogeneous magnetic field and being deflected up or down depending on their spin.

Although the intuition of De Broglie about the wave-particle duality of all matter was a step in the right direction, his interpretation was semiclassical and it is in 1926 that the first full quantum wave equation would be introduced by Schrödinger to describe electron-like particles, reproducing the previous semiclassical formulation without inconsistencies [40]. This complex equation describes the evolution of the wave function Ψ of the quantum system, defined by its position vector \mathbf{r} and time t as an energy conservation law, in which the hamiltonian of the system \hat{H} is explicit, by solving the Equation 2.3.

$$(2.3) \quad i\hbar \frac{\partial}{\partial t} |\Psi(\mathbf{r}, t)\rangle = \hat{H} |\Psi(\mathbf{r}, t)\rangle$$

1077 The spin was then included into Schrödinger equation by Pauli to take into account the interaction
 1078 with an external magnetic field, as shown in Equation 2.4 in which the Hamiltonian operator is a 2×2
 1079 matrix operator due to the Pauli matrices [38]. \mathbf{A} is the vector potential and ϕ is the scalar electric
 1080 potential.

$$(2.4) \quad i\hbar \frac{\partial}{\partial t} |\Psi\rangle = \left[\frac{1}{2m} (\sigma \cdot (\mathbf{p} - q\mathbf{A})^2 + q\phi) \right] |\Psi\rangle$$

1081 Later in 1927, Dirac went further in his paper about emission and absorption of radiation by
 1082 proposing a second quantization not only of the physical process at play but also of the electromagnetic
 1083 field [41]. His equation provided the ingredients to the first formulation of *Quantum Electrodynamics (QED)*
 1084 and the description of photon emission by electrons dropping into a lower energy state
 1085 in which the final number of particles is different than the initial one. Nevertheless, in order to properly
 1086 treat electromagnetism, the incorporation of the special relativity developed by Einstein was
 1087 necessary. Derived in 1928, the Dirac equation, shown as Equation 2.5, similarly to Schrödinger
 1088 equation, is a single-particle equation but it incorporates special relativity in addition to quantum
 1089 mechanics rules [42].

$$(2.5) \quad i\hbar\gamma^\mu \partial_\mu \psi - mc\psi = 0$$

1090 It features the 4×4 gamma matrices γ^μ built using 2×2 Pauli matrices and the unitary matrix,
 1091 the 4-gradient ∂_μ , the rest mass m of any half integer spin massive particle described by the wave
 1092 function $\psi(x, t)$, also called a Dirac spinor and the speed of light c . In addition to perfectly reproduce
 1093 the results obtained with quantum mechanics so far, it also provided *negative-energy solutions* that
 1094 would later be interpreted as a new form of matter, *antimatter* [43, 44]. In the non-relativistic limit,
 1095 the Dirac equation gives a theoretical justification to the Pauli equation that was phenomenologically
 1096 constructed to account for the spin.

1097 The successes of the QED were soon followed with theoretical problems as computations of any
 1098 physical process involving photons and charged particles were shown to be only reliable at the first
 1099 order of the *perturbation theory* [45]. At higher order of the theory, divergent contributions were
 1100 appearing giving nonsensical results. Only two effects were contributing to these infinities.

- 1101 • The self-energy of the electron (or positron), the energy that the particle has due to its own
 1102 interaction with its environment.
- 1103 • The vacuum polarization, virtual electron–positron pairs produced by a background electro-
 1104 magnetic field in the vacuum which is not an "empty" space. These virtual pairs affect the
 1105 charge and current distributions generated by the original electromagnetic field.

1106 Solving this apparent problem was done by carefully defining the concepts of each observable,
 1107 for example mass or charge, as these quantities are understood within the context of a non-interacting
 1108 field equation. From the experimental point of view, they are abstractions as what is measured is
 1109 "renormalized observables" shifted from their "bare" value by the interaction taking place in the
 1110 measuring process. The infinities needed to be connected to corrections of mass and charge as those
 1111 are fixed to finite values by experiment. This was the intuition of Bethe in 1947 who successfully
 1112 computed the effect of such *renormalization* in the non-relativistic case [46]. Full covariant formula-
 1113 tions of QED including renormalization were achieved by 1949 by Tomonaga, Schwinger, Feynman,

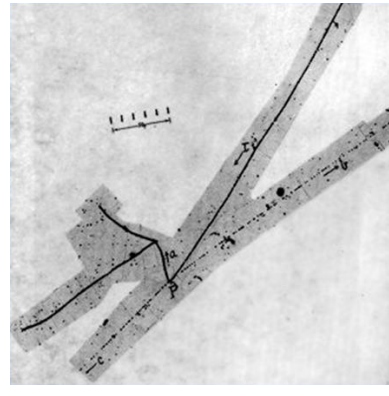
1114 and Dyson [47]. With the resolution of infinities, QED had mostly reached its final form, being still
 1115 today the most accurate physical theory, and would serve as a model to build all other quantum field
 1116 theories.

1117 Development of the quark model and Quantum Chromodynamics

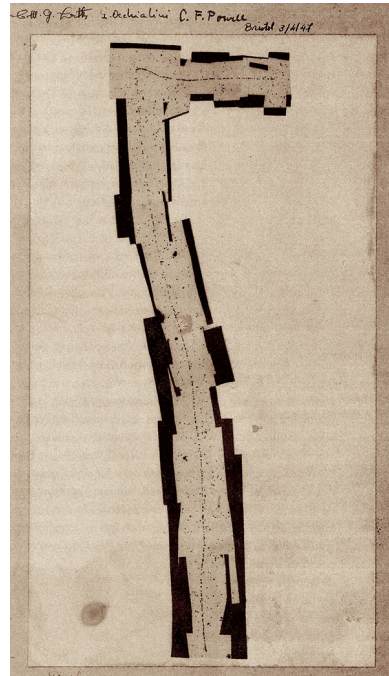
1118 To explain the nuclear force that holds *nucleons*
 1119 (protons and neutrons) together, Yukawa proposed
 1120 in 1934 the existence of a force carrier called *meson*
 1121 due to its predicted mass in the range in between the
 1122 electron and nucleon masses [48]. Discovered in
 1123 1936 by Anderson and Neddermeyer [49, 50], and
 1124 confirmed using bubble chambers in 1937 by Street
 1125 and Stevenson [51], a first meson candidate was ob-
 1126 served in the decay products of cosmic rays. As-
 1127 suming it had the same electric charge as electrons
 1128 and protons, this particle was observed to have a
 1129 curvature due to magnetic field that was sharper
 1130 than protons but smoother than electrons resulting
 1131 in a mass in between the two. But its properties
 1132 were not compatible with Yukawa's theory, which
 1133 was emphasized by the discovery of a new candi-
 1134 date in 1947, again in cosmic ray products using
 1135 photographic emulsions [52–54]. The detections of
 1136 the mu-meson and of the pi-meson in emulsions are
 1137 showed in Figure 2.5.

1138 This new candidate, although it had a similar
 1139 mass than the already believed *meson*, would rather
 1140 decay into it. For distinction, the first candidate
 1141 would then be renamed "*mu meson*" when the sec-
 1142 ond would be the "*pi meson*". The *mu meson* was
 1143 behaving like a heavy electron and didn't partici-
 1144 pate in the strong interaction whereas the pion was
 1145 believed to be the carrier of the nuclear interaction.
 1146 This led to classify the *mu* in a new category of par-
 1147 ticles that shared similar properties called *leptons*
 1148 under the name of *muon* together with the electron.
 1149 The *pi meson* was finally found to be a triplet of par-
 1150 ticles: a positively charged, a negatively charged,
 1151 and a neutral particle. The neutral *pi meson* has
 1152 been more difficult to identify as it wouldn't leave
 1153 tracks on emulsions nor on bubble chambers and
 1154 needed to be studied via its decay products. It was
 1155 ultimately identified in University of California's
 1156 cyclotron in 1950 through the observation of its decay into 2 photons [55].

1157 Also discovered in 1947 but in cloud chamber photographs, the *K meson* has also been an impor-



(a)



(b)

Figure 2.5: Figure 2.5a: decay of a μ -meson in an emulsion. Figure 2.5b: track of a π -meson in an emulsion signed by Lattes, Powell, and Occhialini.

tant step towards the establishment of the Standard Model [56]. A triplet of particles, two charged and a neutral, with a mass roughly half that of a proton, were reported. These particles were baptised *K meson* in contrast to the "light" *pi* and *mu* "L-mesons". The particularity of the *K* is their very slow decays with a typical lifetime of the order of 10^{-10} s much longer than the 10^{-23} s of *pi*-proton reactions. The concept of *strangeness*, a new quantum number was then introduced thanks to an idea of Pais as an attempt to explain this phenomenon as *strange* particles appeared as the pair production of a strange and anti-strange particle [57].

With the development of synchrotrons, the particle *zoo* grew to several dozens during the 1950s as higher energies were reachable through acceleration. In 1961, a first classification system, called *Eightfold Way*, was proposed by Gell-Mann [58]. It found its roots in the Gell-Mann–Nishijima formula, which relates the electric charge Q , the third component of the isospin I_3 , the *baryon* number B and the strangeness S , as showed in Formula 2.6 [59–61].

$$(2.6) \quad Q = I_3 + \frac{1}{2}(B + S)$$

The isospin is a quantum number introduced in 1932 to explain symmetries of the newly discovered neutron using representation theory of SU(2) [62]. The baryon number, was introduced by Nishijima as a quantum number for baryons, i.e. particles of the same family as nucleons [59]. The mesons were classified in an octet and baryons of spin $\pm \frac{1}{2}$ and $\pm \frac{3}{2}$ were respectively classified into an octet and a decuplet, as shown in Figure 2.6. To complete the baryon decuplet, Gell-Mann predicted the existence of baryon Ω^- which would later be discovered in 1964 [63].

Gell-Mann, and independently Zweig, then proposed a full theoretical model in which *hadrons* (strongly interacting particles, i.e. mesons and baryons) were not elementary particles anymore [64–66]. They were rather composed of three flavors of particles called *quarks* and their anti-particles. The three flavors were called *up*, *down* and *strange*. *Up* and *down* were used to explain the nucleons and non-strange mesons, while *strange* came into the composition of hadrons showing strangeness. *Up* and *down* flavors were discovered in 1968 thanks to the deep inelastic scattering experiments conducted at the Stanford Linear Accelerator Center (SLAC) [67, 68], and *strange* could only be indirectly validated even though it provided a robust explanation to *kaon* (*K*) and *pion* (π).

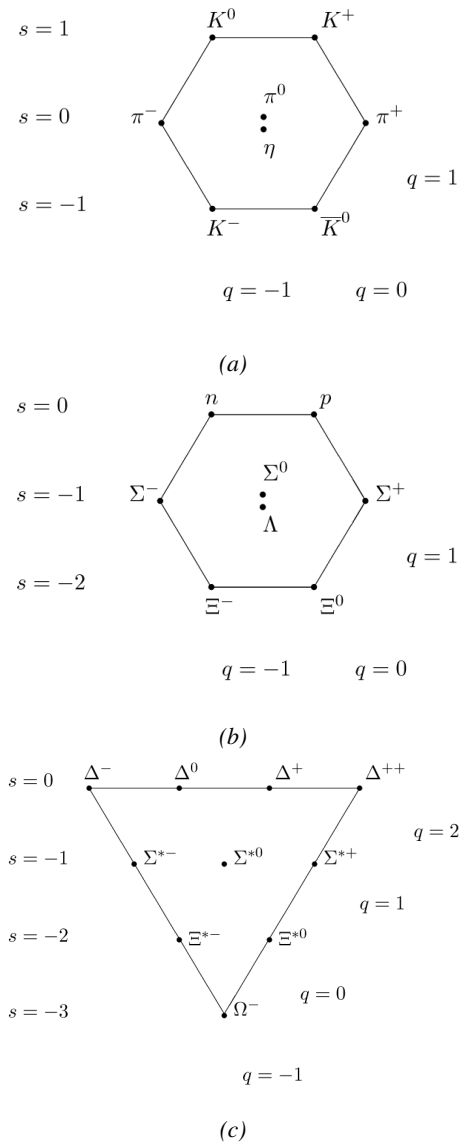


Figure 2.6: Figure 2.6a: Meson octet. Figure 2.6b: Baryon octet. Figure 2.6c: Baryon decuplet.

However, in the decade following the Gell-Mann-Zweig quark model proposition, several improvement to the model were brought. First by Glashow and Bjorken the same year that predicted the existence of a fourth quark flavor, the *charm*, that would equalize the then known number of quarks and leptons [69, 70]. Finally in 1973 by Kobayashi and Maskawa that increased the number of quarks to six to explain the experimental observation of CP violation [71, 72]. These two quarks were referred to as *top* and *bottom* for the first time in 1975 [73]. It's only after these additions to the quark model that finally the *charm* was discovered in 1974 at both SLAC and Brookhaven National Laboratory (BNL) [74, 75]. A meson in which the *charm* is bonded with an *anti-charm*, called J/ψ and presented in Figure 2.7, helped convince the physics community of the validity of the model. The *bottom* was discovered soon after in 1977 in Fermilab [76] and indicated the existence of the *top* that resisted to discovery until Fermilab's experiments CDF and D \emptyset in 1995 due its very large mass and the energy needed to produce it [77, 78].

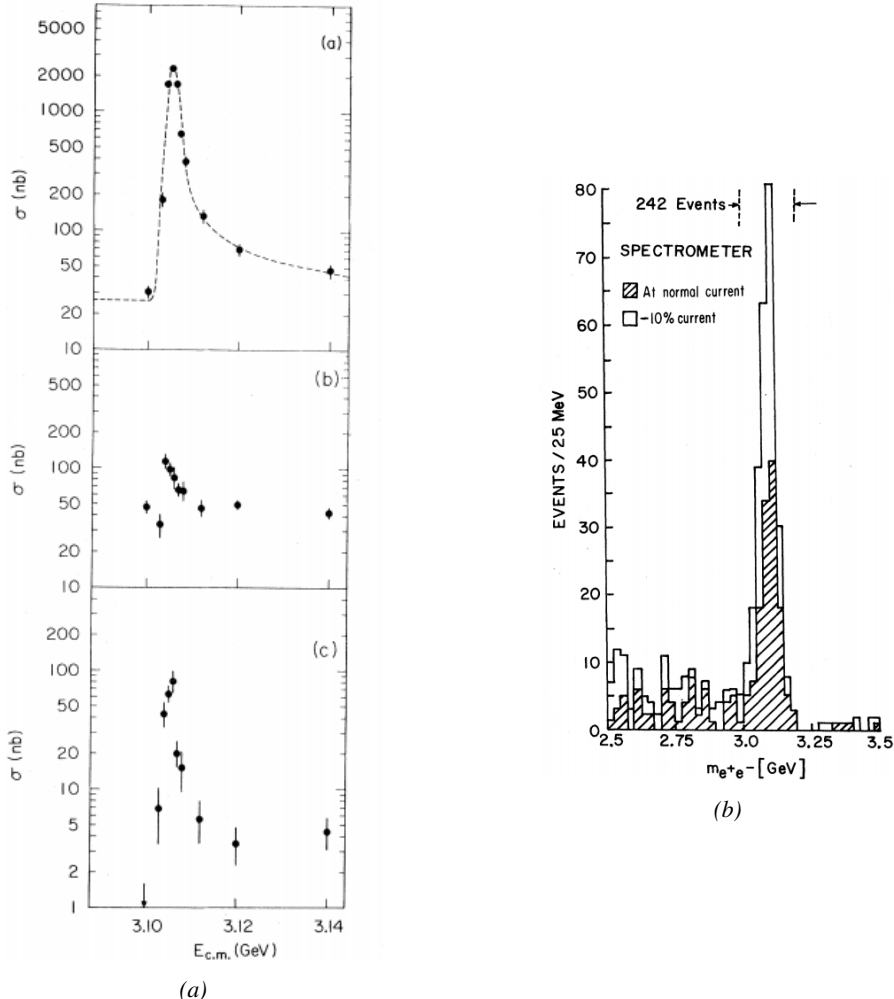


Figure 2.7: Discovery of the J/Ψ by both SPEAR (SLAC [74]) in Figure 2.7a and AGS (BNL [75]) in Figure 2.7b. In Figure 2.7a, the cross section versus energy is showed for (a) multi hadron final states, (b) e^+e^- final states, and (c) $\mu^+\mu^-$, $\pi^+\pi^-$ and K^+K^- final states.

As remarked by Struminsky, due to mesons such as Ω^- or Δ^{++} , the first SU(3) model already should have possessed an additional quantum number [79]. Indeed, these mesons are composed of three identical quarks, respectively three *strange* and *up* quarks, with parallel spins, which should be forbidden by the exclusion principle. Independently, Greenberg, and Han and Nambu proposed an additional SU(3) degree of freedom for the quarks [80, 81]. It was later referred to as *color charge gauge*, that could interact through *gluons*, the gauge boson octet corresponding to this degree of freedom. The color field is presented in Figure 2.8a. Nevertheless, as observing free quarks to prove their existence proved to be impossible, two visions of the quarks were argued. On one side, Gell-Mann proposed to see quarks as mathematical construct instead of real particles, as they are always confined, implying that quantum field theory would not describe entirely the strong interaction. He promoted the S-matrix approach to treat the strong interaction. Opposed to this vision, Feynman on the contrary argued that quarks are real particles, that he would call *partons*, that should be described as all other particles by a distribution of position and momentum [82]. The implications of quarks as point-like particles were verified at SLAC and helped abandon the S-matrix to the benefit of QFT [83]. The concept of *color* was then added to the quark model in 1973 by Fritzsch and Leutwyler together with Gell-Mann to propose a description of the strong interaction through the theory of Quantum Chromodynamics (QCD) [84]. The discovery the same year of asymptotic freedom within the QCD by Gross, Politzer, and Wilczek, allowed for very precise predictions thanks to perturbation theory [85, 86]. The evolution of the gauge constant of QCD with respect to the energy as described by asymptotic freedom is showed in Figure 2.8b.

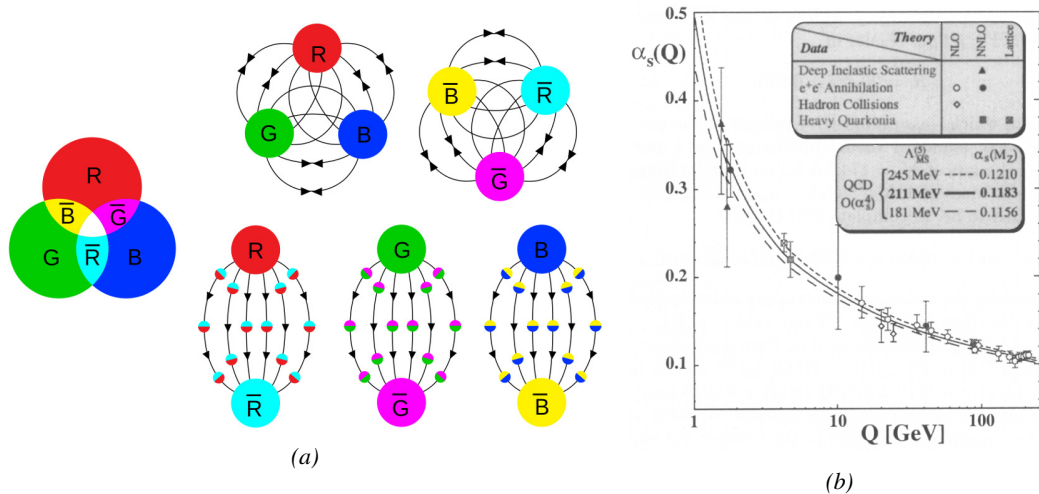
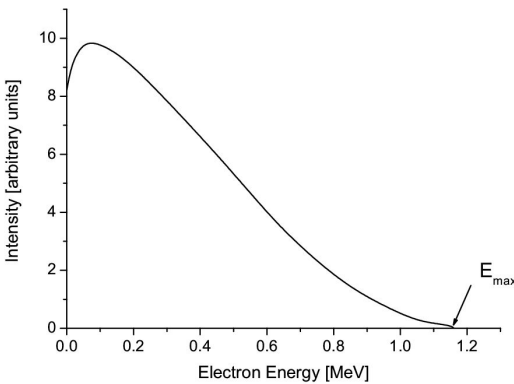


Figure 2.8: Figure 2.8a: the color field of QCD only allows for "white" baryons, particles composed of quarks, to exist. Examples are given for mesons, composed of a quark and its anti-quark, and hadrons, composed of three differently colored quarks or anti-quarks. Other exotic baryons have been predicted and observed, such as tetraquarks and pentaquarks. Figure 2.8b: a crossed analysis performed thanks to the data collected by various experiments at different energies have showed that the coupling constant evolves as predicted by the mechanism of asymptotic freedom [87].

1233 **The Weak interaction, spontaneous symmetry breaking, the Higgs mechanism and the Elec-**
 1234 **troweak unification**

1235 The weak interaction is the process that causes radioactive decays. Thanks to the neutron discov-
 1236 ery [23], Fermi could explain in 1934 beta radiations through the beta decay process in which the
 1237 neutron decays into a proton by emitting an electron [88]. Though the missing energy observed dur-
 1238 ing this process triggered a huge debate about the apparent non-conservation of energy, momentum
 1239 and spin of the process, Fermi, as Pauli before him [89], proposed that the missing energy was due to
 1240 a neutral not yet discovered particle that was then baptised *neutrino*. The impossibility to detect such
 1241 a particle left some members of the scientific community sceptical, but hints of energy conservation
 1242 and of the existence of the neutrino were provided by measuring the energy spectrum of electrons
 1243 emitted through beta decay, as there was a strict limit on their energy, as showed in Figure 2.9.



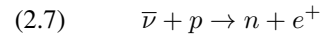
1254 *Figure 2.9: Energy spectrum of beta particles emitted by a source*
 1255 *of ^{210}Bi .*

1256 constraint the beta decay theory of Fermi and extend it to the case of the muon, Konopinski and
 1257 Mahmoud proposed in 1953 that the muon decay would eject a particle similar to the neutrino [91].
 1258 They predicted the existence of a muon neutrino that would be different to the one involved in the
 1259 beta decay, related to the electron. With this, the idea of *lepton number* arised. The *muon neutrino*
 1260 was successfully detected in 1962 by Lederman, Schwartz, and Steinberger [92].

1262 The theory could not be valid though as the probability of interaction, called *cross-section*, would
 1263 have been increasing without limitation with the square of the energy. Fermi had proposed a two
 1264 vector current coupling but Lee and Yang noted that an axial current could appear and would violate
 1265 parity [93]. Gamov and Teller had already tried to account for such parity violation by describ-
 1266 ing Fermi's interaction through allowed (parity-violating) and superallowed (parity-conserving) de-
 1267 cays [94]. The Wu experiment in 1956 confirmed the parity violation [95], as showed by Figure 2.10.
 1268 But the success of QED as a quantum field theory sparked the development of similar theory to de-
 1269 scribe the weak interaction.

1270 As previously discussed, the great success of QED was built on an underlying symmetry, inter-
 1271 preted as a gauge invariance so that the effect of the force is the same in all space-time coordinates,
 1272 and of the possibility to renormalize it in order to resolve infinities. In 1967, Weinberg found a
 1273 way to unite both the electromagnetic and weak interaction into a gauge theory involving four gauge
 1274 bosons, three of which are massive and carry out the weak interaction and the last is a massless bo-

It's only 30 years later in 1953 that it was discovered by the team of Cowan and Reines using the principle of inverse beta decay described through Formula 2.7 [90].



The experiment consisted in placing water tanks sandwiched in between liquid scintillators near a nuclear reactor with an estimated neutrino flux of $5 \times 10^{13} \text{ cm}^{-2} \text{ s}^{-1}$. However, in order to explain the absence of some reactions in the experiment of Cowan and Reines and

son carrying the electromagnetic interaction [96]. Among the three massive bosons, two are charged and one is neutral, similarly to the previously theorized *pi meson* vector of the Yukawa model [48] and all have a mass much greater than nucleons and thus a very short life time implying a finite very short range, contrary to the contact interaction originally proposed by Fermi.

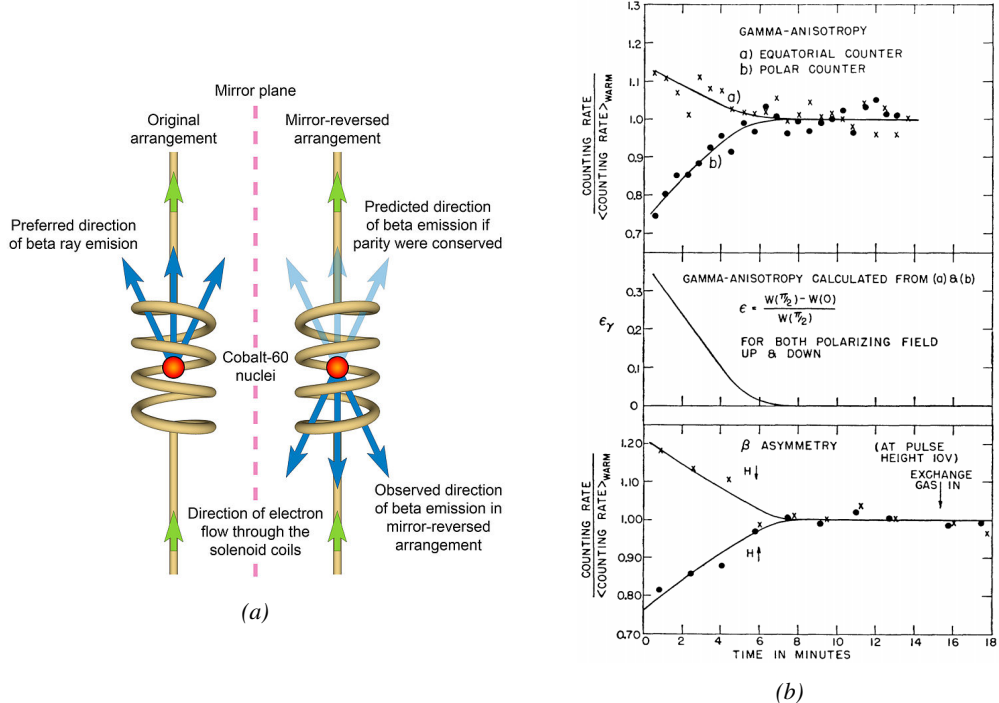


Figure 2.10: As explained through Figure 2.10a, the Wu experiment consisted in measuring the preferred direction of emission of beta rays of a Cobalt source placed in a stable magnetic field aligned, in one case, and anti-aligned, in the other case, with the nuclear spin. The result of Figure 2.10b showed a violation of parity.

Breakthroughs in other fields of physics contributed in giving theoretical support and interpretation to the unified electroweak theory. The stepping stone was the use of spontaneous symmetry breaking that was inspired to Nambu at the beginning of the 1960s [97, 98] following the development of the Bardeen–Cooper–Schrieffer (BCS) superconductivity mechanism in 1957 [99]. Cooper had shown that BCS pairs, pairs of electrons bound together at low temperature, can have lower energy than the Fermi Energy and are responsible for superconductivity. This led to the discovery of Goldstone-Nambu bosons [100, 101] as a result of the spontaneous breaking of the chiral symmetry in a theory describing nucleons and mesons developed by Nambu and Jona-Lasinio in 1961, and now understood as a low-energy approximation of QCD. Similarly to the mechanism of energy gap appearance in superconductivity, the nucleon mass is suggested to be the result of a self-energy of a fermion field and is studied through a four-fermion interaction in which, as a consequence of the symmetry, bound states of nucleon-antinucleon pairs appear and can be regarded as virtual pions. Though the symmetry is maintained in the equations, the ground state is not preserved. Goldstone showed that the bound states correspond to spinless bosons with zero mass [101].

Although the model in itself didn't revolutionize particle physics, spontaneous symmetry breaking was generalized to quantum field theories. As all fundamental interactions are described using

gauge theories based on underlying symmetries, processes such as the chiral symmetry breaking were introduced soon after the publication of Nambu and Jona-Lasinio. In 1962, Anderson, discussed the implications of spontaneous symmetry breaking in particles physics [102]. He did so by following the idea of Schwinger who suggested that zero-mass vector bosons were not necessarily required to describe the conservation of baryons, contrary to the bosons emerging from chiral symmetry breaking [103]. A model was finally independently built in 1964 by Brout and Englert [104], Higgs [105], and Guralnik, Hagen, and Kibble [106], who discovered that combining an additional field into a gauge theory in order to break the symmetry, the resulting gauge bosons acquire a nonzero mass. Moreover, Higgs stated that this implied the existence of at least one new massive, i.e. self-interacting, scalar boson corresponding to this additional field, that is now known as *Higgs boson*. The Higgs mechanism today specifically refers to the process through which the gauge bosons of the weak interaction acquire mass. In 1967, Weinberg could point to the Higgs mechanism to integrate a Higgs field into a new version of the electroweak theory in which the spontaneous symmetry breaking mechanism of the Higgs field would explicitly explain the masses of the weak interaction gauge bosons and the zero-mass of photons [96].

2.1.2 Construction and validation of the Standard Model

The Standard Model of particle physics was built in the middle of the 1970s after the experimental confirmation of the existence of quarks [107]. It is based on the assembly of the models previously introduced and describing the fundamental interactions and their gauge bosons, except for gravitation, as well as the way elementary "matter" particles interact with the fields associated with these force carriers. In this sense, the development of QED and the unification of the electroweak interaction, of the Yukawa interaction and of QCD, and of the Higg mechanism made it possible to explain most of the contemporary physics.

In the SM, "matter" particles, are described by twelve fermion fields of spin $\frac{1}{2}$ obeying the Fermi-Dirac statistics, i.e. subjected to the Pauli exclusion principle. To each fermion is associated its corresponding anti-particle. The fermions are classified according to the way they interact and thus according to the charges they carry. Six of them are classified as quarks (u, d, c, s, t , and b) and are subjected to all interactions and the six others as leptons ($e^-, \mu^-, \tau^-, \nu_e, \nu_\mu$, and ν_τ). Leptons are not subjected to the strong interaction and among them, the three neutrinos only interact weakly as they are neutral particles, which explains why they are so difficult to detect. The gauge boson fields are the gluons g for the strong interaction, the photon γ for the electromagnetic interaction and the weak bosons $W^+, W^-,$ and Z^0 for the weak interaction. Finally, the Higgs field H^0 is responsible, through the spontaneous symmetry breaking, of the mixing of the massless electroweak boson fields $W_1, W_2, W_3,$ and B leading to the observable states $\gamma, W^+, W^-,$ and Z^0 that can gain mass while interacting with the Higgs field. This picture of the SM is summarized through Figure 2.11 where the antifermions are not shown.

When the model was first finalized, the existence of the weak gauge bosons, of the charm, of the third quark generation composed of top and bottom quarks to explain the observed CP violation was not proven but the predictions were measured with good precision in the years following [74–78]. The weak bosons W and Z were discovered during the next decade in 1983 [108–111]. The very last predicted elementary particle of the model that was not observed yet proved to be very difficult to observe. The Higgs boson needed the start of the LHC to finally be observed in 2012 [112, 113]. A few years more of tests were necessary to measure its properties to confirm the observation of a scalar boson compatible with the predicted Higgs boson H^0 [114].

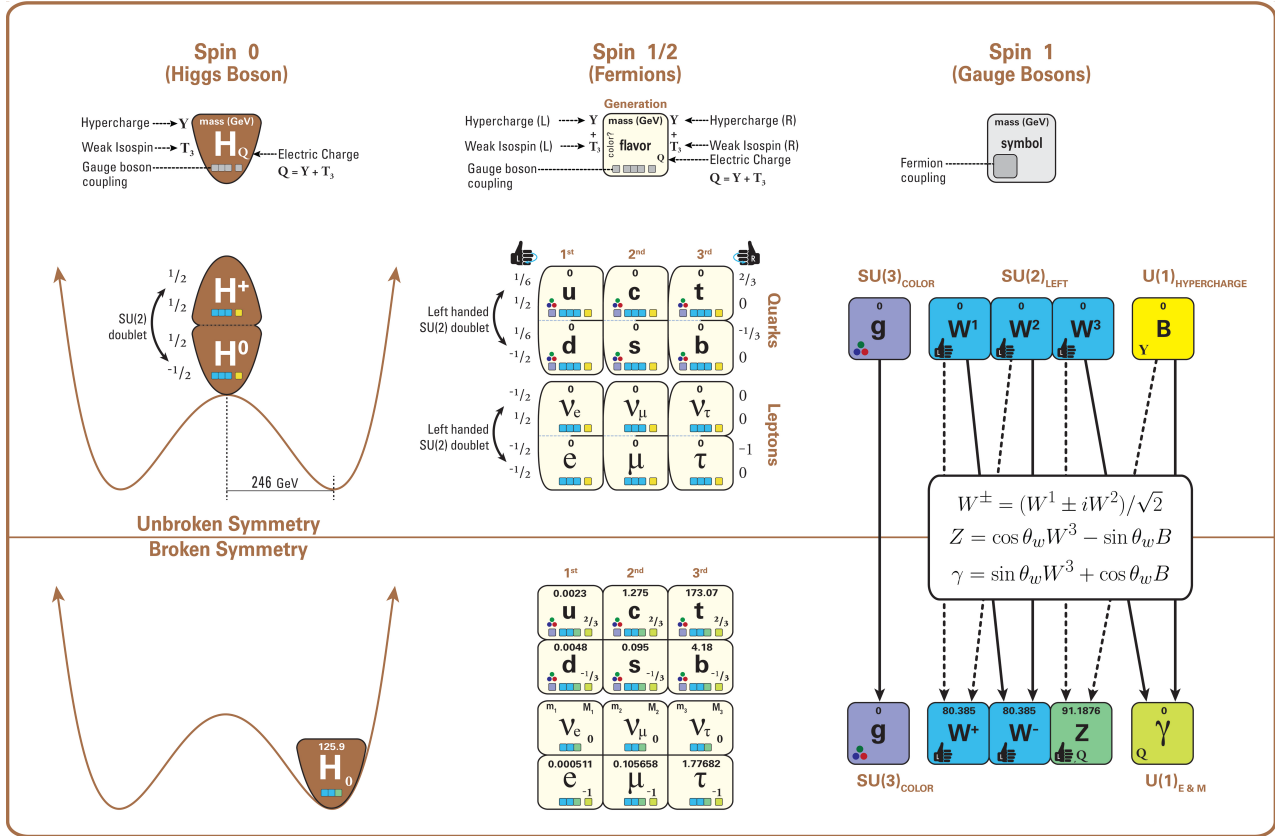


Figure 2.11: The elementary particles of the Standard Model are shown along with their properties. Their interactions with the strong, weak and electromagnetic forces have been made explicit using color squares. In the left column, the scalar Higgs boson is depicted. The center is focused on the matter particles, the fermions, and the right column on the force carriers, the gauge bosons. The role of the Higgs boson in electroweak symmetry breaking is highlighted, and the corresponding way properties of the various particles differ in the (high-energy) symmetric phase (top) and the (low-energy) broken-symmetry phase (bottom) are shown.

1339 2.1.3 Investigating the TeV scale

1340 In High-Energy Physics, the number of experimental events depends on the total interaction cross-
 1341 section of the colliding particles and of the *instantaneous luminosity* [115]. The luminosity is a
 1342 quantity providing an information on the interaction rate normalised to the interaction cross-section.
 1343 The relationship between number of events N , cross-section and instantaneous luminosity \mathcal{L} is given
 1344 in Formula 2.8.

$$(2.8) \quad \mathcal{L} = \frac{1}{\sigma} \frac{dN}{dt} \Leftrightarrow N = \sigma \int \mathcal{L} dt = \sigma \mathcal{L}_{int}$$

1345 The integral of the luminosity over time is referred to as the *integrated luminosity* \mathcal{L}_{int} . In fact,
 1346 the instantaneous luminosity can be deduced from the beam parameters. New colliders now use
 1347 bunched beams. The instantaneous luminosity then depends on the bunch crossing frequency f_{BX} ,
 1348 on the number of particles contained in each bunch n , and on the RMS transverse beam sizes in the

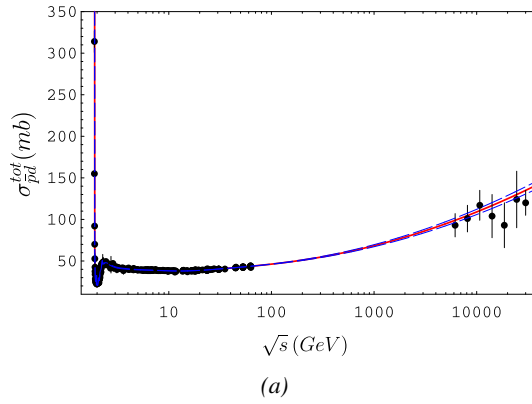
horizontal, σ_x^* , and vertical directions, σ_y^* , at the level of the interaction point. The beam sizes can be assumed to be identical, leading to the relation of Formula 2.9.

$$(2.9) \quad \mathcal{L} = f_{BX} \frac{n^2}{\sigma^*}$$

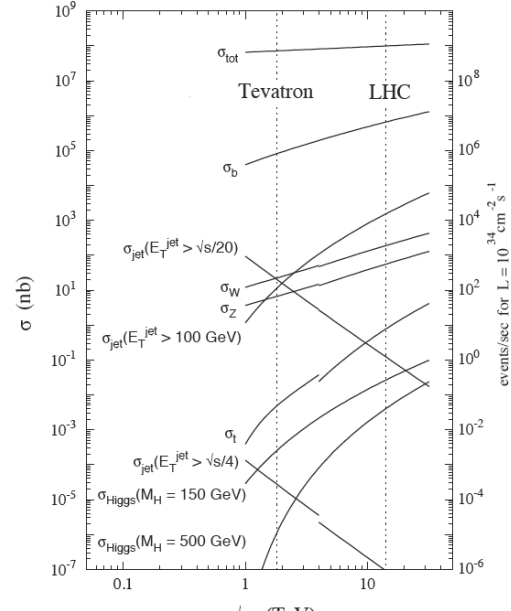
This expression doesn't depend on time anymore and leads to a simple estimation of the integrated luminosity and hence, knowing the cross-section of each available physics channel, to the expected number of events in each channel. The total interaction cross section is the sum of all the different output channels allowed by the interaction process. In the case of highly relativistic protons, the proton-proton (pp) total cross-section increases with the center-of-mass energy of interactions, as can be seen from Figure 2.12.

Enhancing rare processes that allow to finely test the Standard Model is then achieved through an increase in both energy and luminosity. At the energy range that were scanned thanks to high-energy colliders, the SM has so far been a well tested theory. Nevertheless, several hints of physics going beyond its scope have been observed.

Dark matter and gravity: The discrepancy of velocity dispersion of stars in galaxies with respect to the visible mass they contain is known since the end of the 19th century where Kelvin proposed that this problem could be solved if a great majority of the stars would be dark bodies, idea strongly criticized by Pointcaré [117]. Throughout the 20th century, physicists like Kapteyn [118] or Zwicky [119, 120], showed the first hints of a *dark matter* by studying star velocities and galactic clusters, followed by robust measurements of galaxy rotation curves by Babcock which suggested that the mass-to-luminosity ratio was different from what would be expected from watching the visible light [121]. Later in the 1970s, Rubin and Ford from direct light observations [122] and Rogstad and Shostak from radio measurements [123] showed that the radial velocity of visible objects in galaxies was increasing with increasing distance to the center of



(a)



(b)

Figure 2.12: Figure 2.12a: Total proton-proton cross-section as a function of the collisions center-of-mass energy \sqrt{s} [116] with cosmic-ray data from Akemo Observatory and Fly's Eye Collaboration. Figure 2.12b: Total proton-(anti)proton and interaction channel cross-sections in the TeV scale.

the center of

the galaxy. An example of galaxy rotation curve is provided in Figure 2.13. Finally observation of lensing effect by galaxy clusters, temperature distribution of hot gas in galaxies and clusters, and the anisotropies in the Cosmic Microwave Background (CMB), showed in Figure 2.14, kept on pointing to a *dark matter* [124]. From all the data accumulated, the visible matter would only account to no more than 5% of the total content on the visible universe [125]. Alternative theories have tried to investigate modified versions of the General Relativity as this theory is only well tested at the scale of the solar system but is not sufficiently tested on wider ranges or even theories in which gravitation is not a fundamental force but rather an emergent one [126, 127]. But so far, such theories have difficulties to reproduce all the experimental observations as easily as through dark matter.

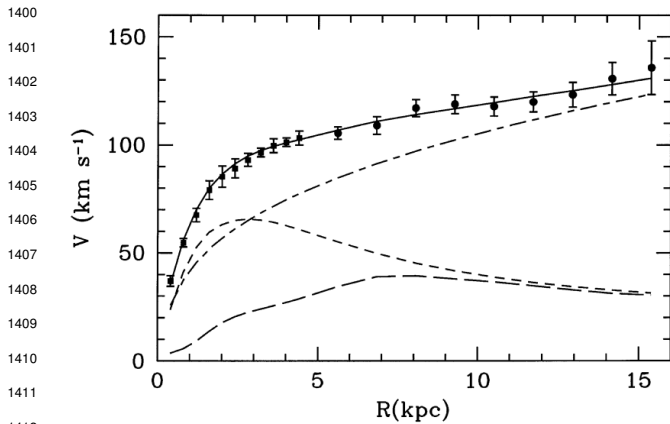


Figure 2.13: Rotation curve (points) of the galaxy M33 compared with best fitting model (line). The short-dashed line represents the rotation profile that would be expected from the observation of the stellar disc alone [128].

into a light Higgs boson compared to the *Planck Mass*. In the SM, the Higgs mass is left to be a measured parameter rather than a calculated one even though the model requires a mass in between 100 and 1000 GeV/c² to stay unitary. Nevertheless, quantum corrections to the Higgs mass coming from its interactions with virtual particles should make the scalar boson much heavier than what measured [130]. Through the MSSM, the stability of fermion masses would provide stability to the Higgs boson mass via the introduction of a fermionic super partner.

On top of providing a solution to the Hierarchy Problem, the model comes with heavy dark matter candidates in the TeV scale [131]. Indeed, in the case *R-parity* is not violated, the lightest supersymmetric particle (LSP) cannot decay and could then explain the dark matter. The LSP in the model is neutral and can only interact through the weak and gravitational interactions. Typical candidates are the *neutralino*, the *sneutrino* or the *gravitino*.

Finally, gravity is not explained through the SM, and huge difficulties are encountered when trying to include it. The strength of gravitational interaction is expected to be negligible at the scale of elementary particles, nevertheless, adding gravitation in the perspective of developing a "theory of everything" leads to divergent integrals that could not be fixed through renormalization. Extensions to the MSSM, and in particular minimal SUper GRAvity (mSUGRA), include general relativity as mediator of the symmetry breaking. mSUGRA gives access to the hidden sector in which the MSSM only interacts gravitationally and suppresses the infinities arising from attempts to include gravity into the SM thanks to possible renormalization [132].

Signatures for the MSSM would come from the super partners of quarks and gluons that can

A possible theory to offer dark matter candidates would be *supersymmetry* (SUSY) which proposes a relationship in between bosons and fermions in the frame of the Minimal Supersymmetric Standard Model (MSSM). In this model, each elementary particle, through a spontaneous space-time symmetry breaking mechanism would have a *super partner* from the other family of particles, pairing bosons and fermions together. The model was first introduced as a way to solve the *Hierarchy Problem* [129]. The discrepancy between the strength of the weak force and gravity translates

decay into an LSP that could then be identified as missing energy as it escapes the detectors undetected. But even in the case MSSM predictions are not to be seen, the other models treating dark matter also propose Weakly Interacting Massive Particles (WIMPs) that could be observed in similar ways than LSPs [133]. Moreover alternative models exist to provide solutions to the Hierarchy Problem. The most investigated models are extra dimensions such as Arkani-Hamed Dimopoulos Dvali [134, 135], Kaluza–Klein [136, 137] or Randall-Sundrum models [138, 139] that usually also include gravitation. Finally, alternative models also exist for the production of dark matter candidates. Models with a hidden valley that would unravel the existence of a new group of light particles through the extension of the SM with a new confining gauge group [140].

1446

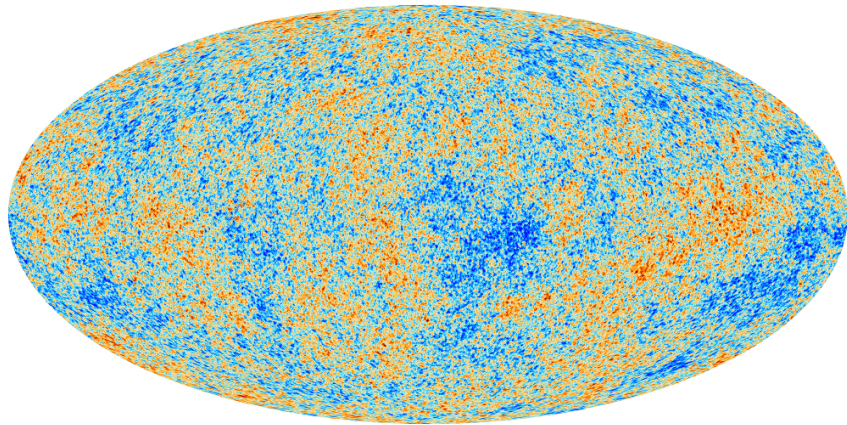


Figure 2.14: Cosmic Microwave Background as measured by the space observatory Planck which mean temperature is $T_\gamma = (2.7255 \pm 0.0006)\text{K}$ with anisotropies of the order of a few μK .

1447 **Baryon asymmetry:** Another intriguing fact is that the universe is dominated by matter. However,
 1448 the SM predicted that matter and antimatter should have been created in equal amounts. For an inter-
 1449 action to produce matter and antimatter at different rates within the SM, three necessary conditions
 1450 were highlighted by Sakharov[141]. First of all, there must be a violation of the baryon number B .
 1451 Then, there must be a C-symmetry and CP-symmetry violation. The C-symmetry violation must
 1452 happen to make sure that the processes creating more baryons than antibaryons are not compensated
 1453 by processes creating more anti-baryons and similarly, the CP-symmetry violation makes sure that
 1454 there are not equal numbers of left-handed baryons and right-handed anti-baryons produced. Fi-
 1455 nally, the interactions must happen out of thermal equilibrium to make sure that CPT-symmetry does
 1456 not balance the processes increasing the baryon number with processes doing otherwise [142]. An
 1457 out-of-equilibrium interaction implies a new unstable heavy particle.

1458 The favoured model to explain this imbalance is the *baryogenesis* that requires electroweak sym-
 1459 metry breaking to be first order phase transition to fall within the scope of SM [143, 144]. This
 1460 means that the symmetry breaking process must involve the absorption or release of a fixed latent
 1461 heat. Through the baryogenesis, the phase transition breaks P-symmetry spontaneously and allows
 1462 for CP-symmetry violation. In turn, the CP violation makes the amplitude of interactions involving
 1463 quarks different than the ones involving anti-quarks leading to the greater creation rate of baryons
 1464 with respect to anti-baryons. The key to this baryon net creation would be found into the *sphaleron*.
 1465 A sphaleron is a particle-like saddle point of the energy functional that appears at the top of the

transition barrier and that could be created if a sufficiently large amount of energy is brought as the tunneling effect through the barrier is largely suppressed for electroweak interactions. The existence of the sphaleron would allow violation of the conservation of B but also of the leptonic number L while conserving $B - L$. The detection at $p - p$ -colliders of such a transition is foreseen to be made through processes with high-multiplicity final states such as $u + u \rightarrow e^+ \mu^+ \tau^+ t\bar{t} b\bar{c} c\bar{s} d\bar{d} + X$ [145]. To be probed, the sphaleron transition requires an energy $E_{sph} \approx 9$ TeV. Nevertheless, if such transition cannot be observed, other BSM models such as the WIMP baryogenesis could be then observed thanks to the detection of displaced vertices, featuring the decay of a WIMP leading to violation of B [146].

Another possibility to explain the apparent asymmetry would be the existence of an electric dipole moment (EDM) in any fundamental particle that would permit matter and antimatter particles to decay at different rates [147]. Indeed, the presence of an EDM violates in itself both P and T symmetries. Experiments are able to probe for the EDM of various fundamental particles such as the electron [147], the charm and strange quarks [148] or even a heavy neutrino EDM [149].

1480

Neutrino mass and sterile neutrino scenario: The SM considers neutrinos to be massless. But it was showed in the late 1960s by the Homestake experiment that the flux of solar neutrinos (i.e. ν_e) measured didn't match the predicted values [150]. The mechanism of neutrino oscillations as a solution to the discrepancy was proposed by Pontecorvo [151] and confirmed in the early 2000s by the Sudbury Neutrino Observatory [152]. This oscillation implies that neutrinos that can be observed are a superposition of massive neutrino states. The research on neutrino oscillation is already quite advanced with experiments looking at atmospheric, reactor or beam neutrinos in order to determine the elements of the mixing matrix (Pontecorvo–Maki–Nakagawa–Sakata matrix [153]) similar to the Cabibbo–Kobayashi–Maskawa (CKM) matrix describing the mixing of quarks [72]. Nevertheless, no answer to the origin of neutrino mass is yet provided.

Explaining the light non-zero mass of the neutrinos ν_l ($l = e, \mu, \tau$) of the order of the eV can be done through the Seesaw mechanism [154, 155]. This model features heavy Majorana counterparts N_l ($l = e, \mu, \tau$) to the ν_l . The masses of the light and heavy neutrinos are linked through a 2×2 mass matrix A with eigenvalues λ_{\pm} expressed as in Equation 2.10.

$$(2.10) \quad \begin{aligned} A &= \begin{pmatrix} 0 & M \\ M & B \end{pmatrix} \\ \lambda_{\pm} &= \frac{B \pm \sqrt{B^2 + 4M^2}}{2} \end{aligned}$$

The Majorana mass term B is assumed to be comparable to the Grand Unified Theory scale (10^{16} GeV) while the Dirac mass term M is of the order of electroweak scale (246 GeV). In these conditions, the eigenvalue λ_+ is almost B while λ_- is close to the ratio $-M^2/B$ compatible with very light neutrinos with masses of the order of 1 eV. Studying the left-right symmetric model seeking for the parity violation in weak interactions leads to the incorporation of three additional gauge bosons W_R and Z' as a result of the spontaneous symmetry breaking. The processes that are predicted by the model and can be probed at colliders are processes such as $pp \rightarrow W_R \rightarrow l + N_l + X$ and $pp \rightarrow Z' \rightarrow N_l + N_l + X$ where the heavy neutrinos decay as $N_l \rightarrow l + j_1 + j_2$, j_i being jets [156]. Other version of seesaw mechanisms exist to account for the neutrino mass that can also be explained thanks to supersymmetric models [157].

1505 2.2 The Large Hadron Collider & the Compact Muon Solenoid

1506 Throughout its history, CERN has played a leading role in high-energy physics. Large regional facil-
 1507 ities such as CERN were planned after the second world war in an attempt to increase international
 1508 scientific collaboration and to allow scientists to share the forever increasing costs of experimental
 1509 facilities. Indeed, it is necessary to use always more powerful tools to improve the fine understanding
 1510 of our Universe. The construction of the first CERN accelerators at the end of the 50s, the Synchro-
 1511 cyclotron (SC) and the Proton Synchrotron (PS), was directly followed by the first observation of
 1512 antinuclei in 1965 [158]. The very first proton-proton collider showing hints of protons not being
 1513 elementary particles was the Intersecting Storage Rings (ISR). From this experience, the Super Pro-
 1514 ton Synchrotron (SPS) was built in the 70s to investigate the structure of protons, the preference
 1515 for matter over antimatter, the state of matter in the early universe or exotic particles, and led to
 1516 the discovery in 1983 of the W and Z bosons [108–111]. These newly discovered particles and the
 1517 electroweak interaction were then studied in detail by the Large Electron-Positron (LEP) collider
 1518 that proved that there only are three generations of elementary particles in 1989 [159]. The LEP was
 1519 then dismantled in 2000 to allow for the LHC to be constructed in the existing tunnel.

1520 2.2.1 LHC, the most powerful particle accelerator

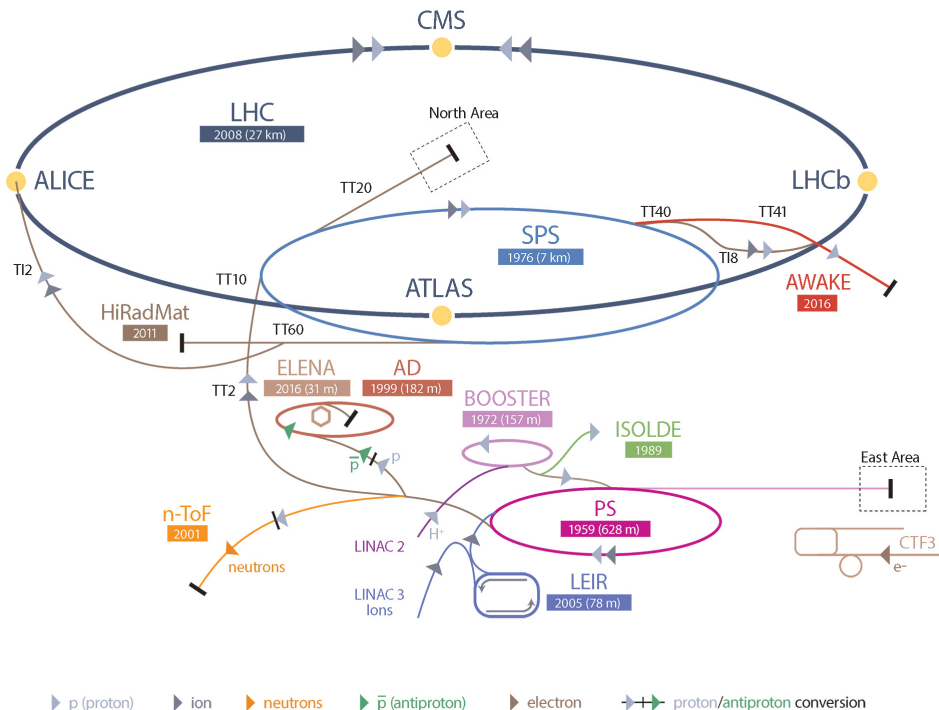


Figure 2.15: CERN accelerator complex.

1521 The different aspects of physics beyond the Standard Model of particle physics and the Standard
 1522 Model itself can be tested through the use of very energetic and intense hadron and ion colliders.
 1523 Powerful hadron colliders are suited for searching for strongly interacting particles. The LHC at

1524 CERN is a perfect tool to seek answers to these open questions and the experiments build along its
 1525 beam lines already started investigating further into the SM and BSM physics.

1526 The LHC has always been considered as an
 1527 option for the future of CERN. At the moment
 1528 of the construction of the LEP beneath the border
 1529 between France and Switzerland, the tunnel was
 1530 built in order to accommodate what would be a
 1531 Large Hadron Collider with a dipole field of 10 T
 1532 and a beam energy in between 8 and 9 TeV [160].
 1533 In 1985, the creation of a 'Working Group on the
 1534 Scientific and Technological Future of CERN'
 1535 took place to investigate such a collider [161].
 1536 The decision was finally taken almost ten years
 1537 later, in 1994, to construct the LHC in the LEP
 1538 tunnel [162] and the approval of the 4 main ex-
 1539 periments that would take place at the four inter-
 1540 action points came in 1997 [163] and 1998 [164]:

- 1541 • ALICE [165] has been designed for the
 1542 purpose of studying the confinement of
 1543 quarks through exploration of the quark-
 1544 gluon plasma that is believed to have been
 1545 a state of matter that existed in the very first
 1546 moment of the universe.
- 1547 • ATLAS [166] and CMS [167] are general
 1548 purpose experiments that have been de-
 1549 signed with the goal of continuing the ex-
 1550 ploration of the Standard Model and the in-
 1551 vestigation of new physics.
- 1552 • LHCb [168] has been designed to investi-
 1553 gate the preference of matter over antimat-
 1554 ter in the universe through CP violation.

1555 These large-scale experiments, as well as the
 1556 full CERN accelerator complex, are displayed in
 1557 Figure 2.15. The LHC is a 27 km long hadron
 1558 collider and the most powerful accelerator used
 1559 for particle physics since 2008 [169]. The LHC
 1560 is designed to collide protons at a center-of-
 1561 mass energy of 14 TeV and luminosity of 10^{34}
 1562 $\text{cm}^{-2}\text{s}^{-1}$, as well as Pb ions at a center-of-mass
 1563 energy of 2.8 TeV/A with a peak luminosity of
 1564 $10^{27} \text{ cm}^{-2}\text{s}^{-1}$. The collider is the last of a long
 1565 series of accelerating devices. Indeed, before be-
 1566 ing accelerated by the LHC, the particles need to pass through different acceleration stages. All

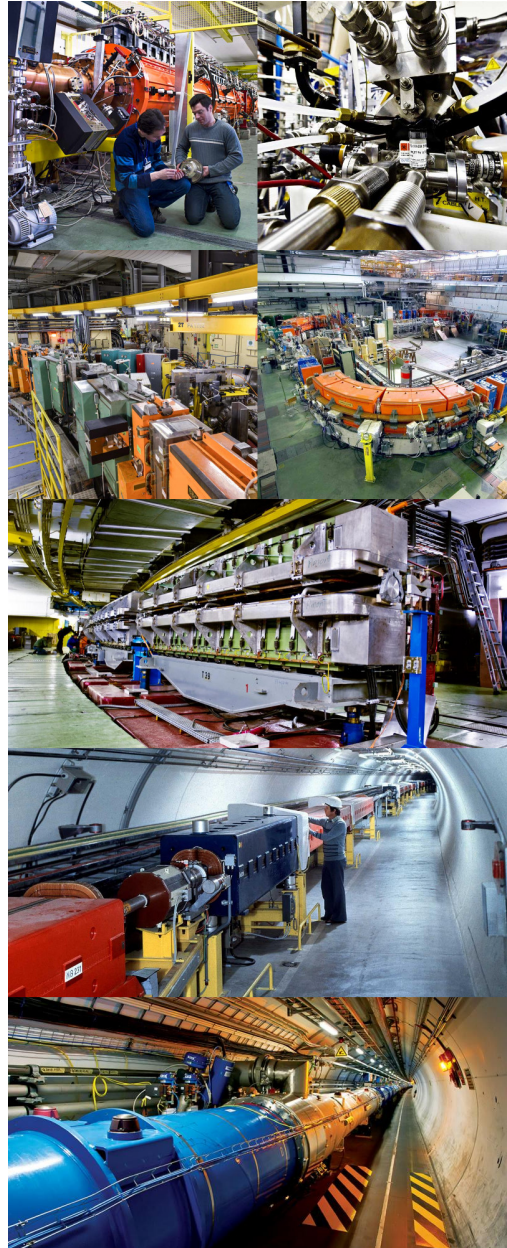


Figure 2.16: Pictures of the different accelerators. From top to bottom: first the LINAC 2 and the Pb source of LINAC 3. Then the Booster and the LEIR. Finally, the PS, the SPS and the LHC.

these acceleration stages are visible on Figure 2.15 and pictures of the accelerators are shown in Figure 2.16.

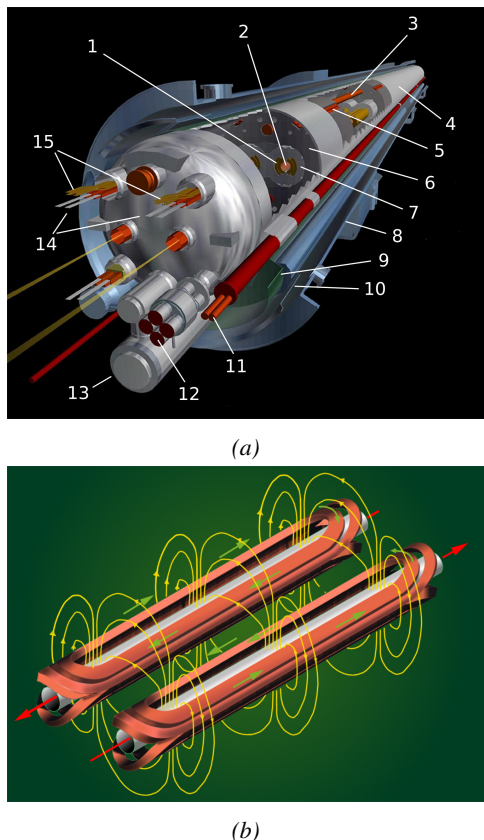


Figure 2.17: Figure 2.17a: schematics of the LHC cryodipoles. 1: Superconducting Coils, 2: Beam pipe, 3: Heat exchanger Pipe, 4: Helium-II Vessel, 5: Superconducting Bus-bar, 6: Iron Yoke, 7: Non-Magnetic Collars, 8: Vacuum Vessel, 9: Radiation Screen, 10: Thermal Shield, 11: Auxiliary Bus-bar Tube, 12: Instrumentation Feed Throughs, 13: Protection Diode, 14: Quadrupole Bus-bars, 15: Spool Piece Bus-bars. Figure 2.17b: magnetic field and resulting motion force applied on the beam particles.

The story of accelerated protons at CERN starts with a bottle of hydrogen gas injected into the source chamber of the linear particle accelerator *LINAC 2* in which a strong electric field strips the electron off the hydrogen molecules only to keep their nuclei, the protons. The cylindrical conductors then accelerate the protons to an energy of 50 MeV. When exiting the *LINAC 2*, the protons are divided into four bunches and injected into the four superimposed synchrotron rings of the *Booster* where they are then accelerated to reach an energy of 1.4 GeV before being injected into the *PS*. The four proton bunches are hence sent as one to the *PS* where their energy eventually reaches 26 GeV. The *PS* not only accelerates protons. It also accelerates heavy ions from the *Low Energy Ion Ring (LEIR)*. Lead is first injected into the dedicated linear collider *LINAC 3*, that accelerates the ions. Electrons are stripped off the lead ions all along the acceleration process and eventually, only bare nuclei are injected in the *LEIR* whose goal is to transform the long ion pulses received into short dense bunches for *LHC*. Ions injected and stored in the *PS* were accelerated by the *LEIR* from 4.2 MeV to 72 MeV. Directly following the *PS*, is finally the last acceleration stage before the *LHC*, the 7 km long *SPS*. The *SPS* accelerates the protons to 450 GeV and inject them in both *LHC* accelerator rings that will increase their energy up to 7 TeV. When the *LHC* runs with heavy lead ions for *ALICE* and *LHCb*, ions are injected and accelerated to reach the energy of 2.8 TeV/A.

The *LHC* beams are not continuous but are rather organised in bunches of particles. When in *pp*-collision mode, the 592 *Pb* bunches are on the contrary composed of 2.2×10^8 ions separated by 100 ns. The two parallel proton beams of the *LHC* are contained in a single twin-bore magnet due to the space restriction in the *LEP* tunnel. Indeed, building two completely separate accelerator rings next to each other was impossible. The dipoles of the 1232 twin-bore magnets are shown in Figure 2.17 alongside the magnetic field generated along the dipole section to accelerate the particles. The dipoles generate a nominal field of 8.33 T, needed to give protons and lead nucleons their nominal energy. Some 392 quadrupoles, presented in Figure 2.18, are also used to focus to the beams, as well as other multipoles to correct smaller imperfections.

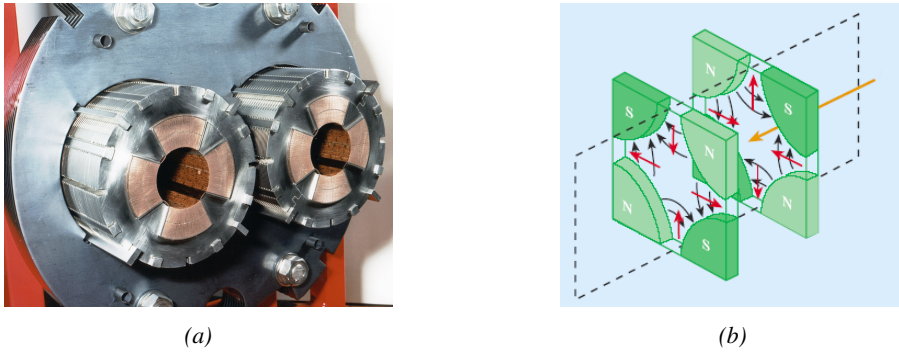


Figure 2.18: The LHC quadrupoles (Figure 2.18a) showed together with the magnetic fields and resulting focussing force applied on the beam by two consecutive quadrupoles (Figure 2.18b).

2.2.2 Timeline of operation

LHC accelerated its first proton in September 2008 but the first collisions only started one year later in November 2009. At this moment the LHC machine officially became the world's most powerful particle accelerator and entered its Physics Run 1 that lasted until February 2013. During Run 1 of the LHC program, the center-of-mass energy was only half of the nominal LHC energy. Nevertheless, the energy and luminosity displayed during Run 1 were enough for both CMS and ATLAS to discover the Higgs boson [112, 113] as showed in Figure 2.19 and for LHCb to discover pentaquarks [170] and confirm the existence of tetraquarks [171]. During this period, ALICE also reported a successful observation of the quark-gluon plasma aimed at studying the early universe [172], ATLAS reported the observation of a new particle before the discovery of the Higgs [173] and a first test of super-symmetric models was performed [174].

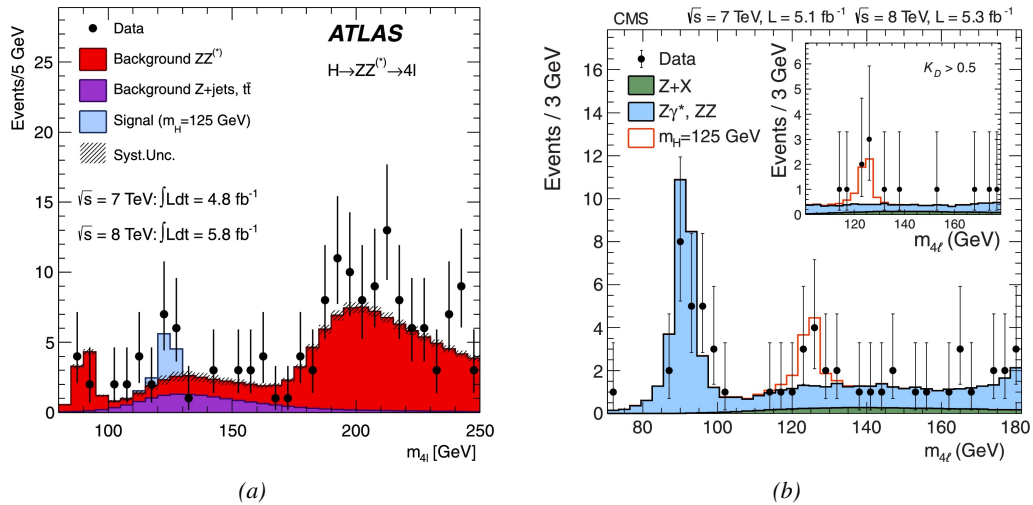


Figure 2.19: Distribution of the four-lepton invariant mass for the $ZZ \rightarrow 4l$ analysis as presented by both ATLAS [112] and CMS [113] in 2012.

Run 1 was brought to an end with the start of the First Long Shutdown, an almost two years technical stop aimed at increasing the energy of the center-of-mass collisions to $\sqrt{s} = 13$ TeV

as well as the instantaneous luminosity. This maintenance stop was also effectively used by the experiments which upgraded part of their detection systems. Run 2 then started in 2015 and lasted until end of 2018 where the activities ended with a last heavy ion run. During the operation, the instantaneous was successfully brought to a value of $1.7 \times 10^{34} \text{ cm}^{-2} \text{ s}^{-1}$ exceeding the design value. Run 2 has been the occasion to acquire more data to study the properties of the Higgs boson with more precision. The boson discovered in the first physics run seems to be consistent with the SM Higgs boson [114].

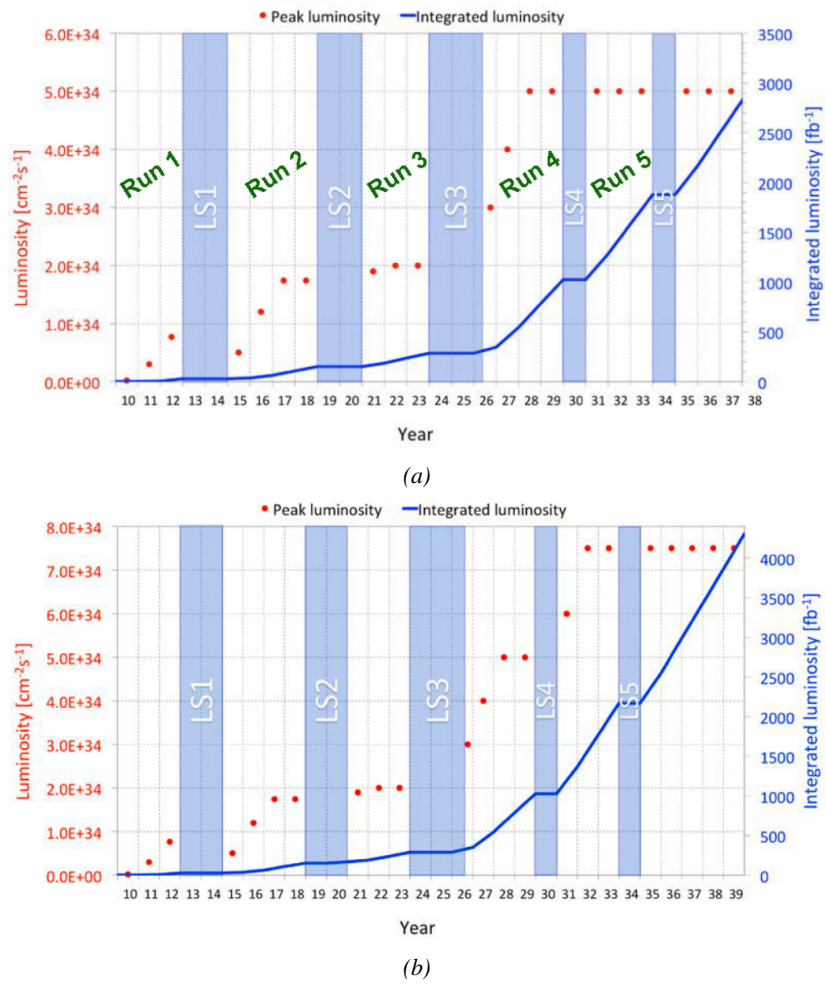


Figure 2.20: Detailed timeline projection of LHC and HL-LHC operation until 2039 showing the evolution of the instantaneous and integrated luminosity as designed (Figure 2.20a) and in the ultimate case where the instantaneous luminosity is increased to $7.5 \times 10^{34} \text{ cm}^{-2} \text{ s}^{-1}$ thanks to a new increase of instantaneous luminosity during Run 5 (Figure 2.20b) [175–177].

From the end of 2018 to early 2021 the Second Long Shutdown will take place. This second maintenance stop will be the occasion to boost once again the beam energy to finally reach the design energy of LHC, 14 TeV. On the side of the maintenance work, preliminary work for the High Luminosity LHC will be performed. The preparations will consist of detector, on the side of the

1637 experiments, and beam machine upgrades, on the side of LHC. In 2021, the physics program will
 1638 be resumed with an instantaneous luminosity fixed at $2 \times 10^{34} \text{ cm}^{-2} \text{ s}^{-1}$. During these 3 years of
 1639 run, the LHC will deliver as much integrated luminosity as what was brought during the almost 7
 1640 years of both Run 1 and 2 of data taking. Phase-1 will end with an overall 300 fb^{-1} delivered. The
 1641 timeline so far described is summarized through the evolution of the instantaneous luminosity and
 1642 of the corresponding integrated luminosity provided in Figure 2.20.

1643 After the Third Long Shutdown (2024-2026) that will close the activities of Run 3, the accel-
 1644 erator will enter the HL-LHC configuration [175], increasing the instantaneous luminosity to an
 1645 unprecedented level of $5 \times 10^{34} \text{ cm}^{-2} \text{ s}^{-1}$ for pp -collisions ($4.5 \times 10^{27} \text{ cm}^{-2} \text{ s}^{-1}$ for Pb -collisions),
 1646 boosting the discovery potential of the LHC. The HL-LHC phase should last at least another 10 years
 1647 depending on the breakthrough this machine would lead to. Already a new accelerating device, the
 1648 FCC, as been proposed and is being investigated to prepare the future of high-energy physics after
 1649 the LHC.

1650 2.2.3 High Luminosity LHC

1651 After approximately fifteen years of operation, the LHC will undergo a new series of upgrades during
 1652 the LS3 in order to boost its discovery potential as previously discussed. The period after LS3 is
 1653 what is referred to HL-LHC or Phase-2. The goal is to aim for a luminosity 5 to 7 times stronger
 1654 than the nominal one trying to reach even 10 times this value if possible [175, 176]. Increasing
 1655 the luminosity means that the beam size at the collision points needs to be reduced to boost the
 1656 number of collisions per bunch crossing. For this purpose, new focusing and bending magnets and
 1657 collimators will be installed at the collision points as well as newly developed "crab cavities" that
 1658 will tilt the particle bunches just prior to the collisions by giving them transverse momentum and
 1659 thus increasing their meeting area. In addition, the full proton injection line will be upgraded.

1660 On the experiments side, the pile-up (PU) will be increased up to 150 to 200 interactions per
 1661 bunch crossing in ATLAS and CMS, making necessary a strong upgrade of the trigger system and
 1662 of the inner trackers and of the calorimeters. Both ATLAS and CMS will also need to upgrade the
 1663 muon trigger at the level of their endcaps mainly focusing on the coverage near the beam line in
 1664 order to increase the detection acceptance and event selection. Moreover, the increased luminosity
 1665 will also lead to an increased background rate and a faster ageing of the detectors.

1666 The end of 2018 marked the beginning of LS2 and the start of Phase-2 upgrade activities. From
 1667 the HL-LHC period onwards, i.e. past LS3, the performance degradation due to integrated radiation
 1668 as well as the average number of inelastic collisions per bunch crossing will rise substantially. This
 1669 has become a major challenge for all of the LHC experiments, like CMS, that were forced to address
 1670 an upgrade program for Phase-2 [177]. Dealing with the data from the muon detectors will force to
 1671 upgrade the detectors and electronics towards the most recent technologies.

1672 2.2.4 The Compact Muon Solenoid experiment

1673 Among the four main LHC experiments is the Compact Muon Solenoid used as a multipurpose
 1674 tool to investigate the SM and the physics beyond its scope. The CMS apparatus in itself is the
 1675 heaviest detector ever built starring a 15 m diameter and a 29 m length for a total weight of 14 kT.
 1676 A thick 4 T solenoid magnet located at the beam interaction point hosts trackers and calorimeters.
 1677 Extending in all directions around the magnet, heavy iron return yokes are installed to extend the
 1678 magnetic field and support a muon system. The apparatus consists of a barrel, referring to the magnet

and the detectors contained in it and the part of the muon system built directly in the cylinder around the magnet, and of two endcaps in the forward and backward region of the detector that closes the apparatus and complete the detection coverage along the beam line. A front view on the barrel is provided in Figure 2.21 while a detailed view of the apparatus is given in Figure 2.22.

In order to efficiently detect all long living particles and measure their properties with good precision, the CMS detector uses an onion like layout around of the interaction point in order to maximize the covered solid angle. As detailed in Figure 2.23, in the innermost region of the detector, closest to the interaction point, the silicon tracker records the trajectory of charged particles. Around it, the electromagnetic calorimeter (ECAL) stops and measures the energy deposition of electrons and photons. In the next layer, the hadron calorimeter (HCAL), hadrons are stopped and their energy measured. These layers are contained inside of the magnet of CMS, the superconducting solenoid. Outside of the magnet are the muon chambers embedded into iron return yokes used to control the magnetic field and gives muons, the only particles traveling completely through the whole detector, a double bending helping in reconstructing their energy and trajectory. Note that photons and neutral hadrons are differentiated from electrons and charged hadrons in the calorimeters by the fact that they don't interact with the silicon tracker and are not influenced by the magnetic field, as can be seen in Figure 2.23.

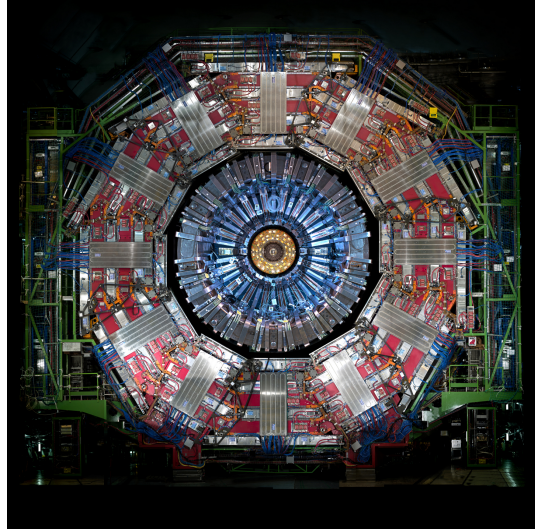


Figure 2.21: Picture of the CMS barrel. The red outer layer is the muon system hosted into the red iron return yokes. The calorimeters are the blue cylinder inside in magnet solenoid and the tracker is the inner yellow cylinder built around the beam pipe.

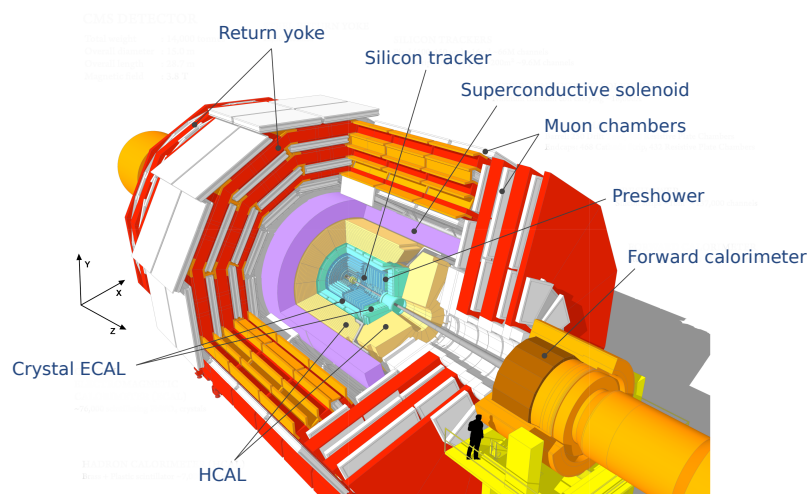


Figure 2.22: View of the CMS apparatus and of its different components.

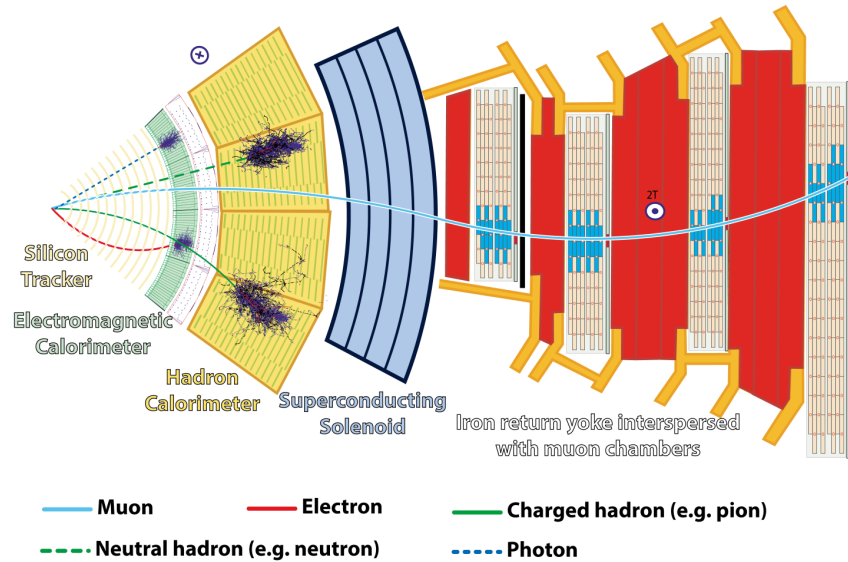


Figure 2.23: Slice showing CMS sub-detectors and how particles interact with them.

1708 2.2.4.1 The silicon tracker

1709 The silicon tracker visible in
 1710 Figure 2.24 is divided into two
 1711 different sub-systems: the *pixel*
 1712 *detector* at the very core and
 1713 the *microstrip detector* around
 1714 it. This system is composed
 1715 of 75 million individual read-
 1716 out channels with up to 6000
 1717 channels per squared centime-
 1718 ter for the pixels making it the
 1719 world's biggest silicon detec-
 1720 tor. This density allows for
 1721 measurements of the particle
 1722 tracks with a precision of the
 1723 order of $10\ \mu\text{m}$. This is neces-
 1724 sary to reconstruct all the dif-
 1725 ferent interaction vertices with precision and have a precise measure of the curvature of the charged
 1726 particles traveling through the magnetic field to estimate their charge and momentum.

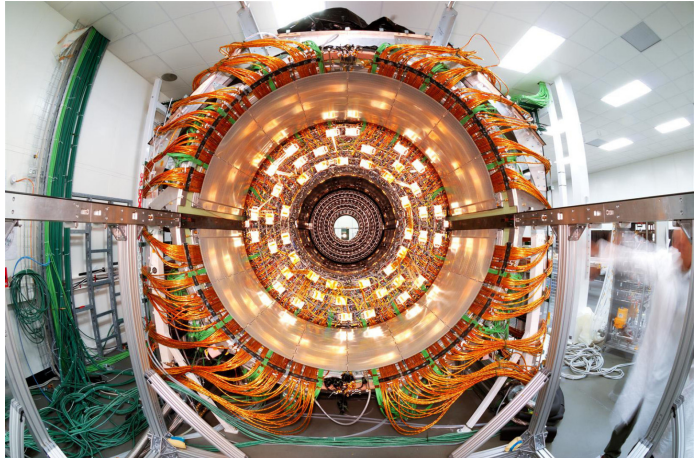


Figure 2.24: The CMS tracker.

1727 2.2.4.2 The calorimeters

1728 The ECAL directly surrounding the tracker is composed of crystals of lead tungstate, PbWO_4 , a
 1729 very dense but optically transparent material used to stop high-energy electrons and photons. These
 1730 crystal blocks basically are extremely dense scintillators which scintillate in fast, short light bursts
 1731 proportionally to the energy deposition. The light is contained at 80% in the corresponding 25 ns

1732 lasting bunch crossing. Each crystal is isolated from the other by the carbon fiber matrix they are
 1733 embedded in.

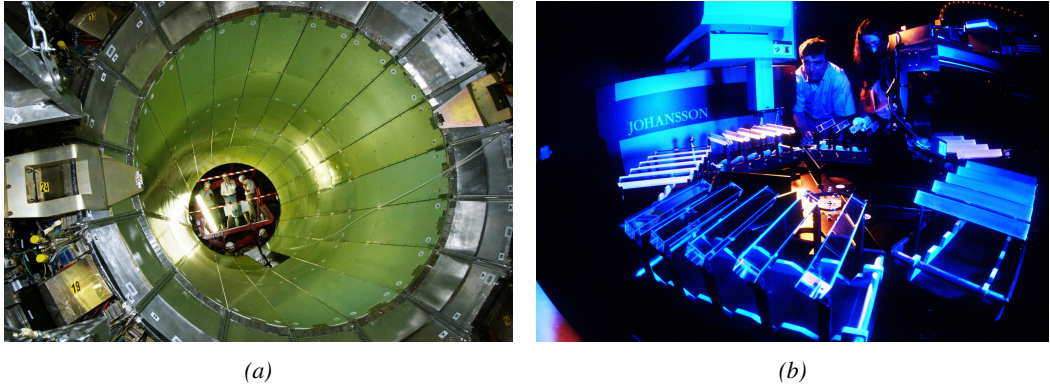


Figure 2.25: Figure 2.25a: The electromagnetic calorimeter. Figure 2.25b: The lead tungstate crystals composing the ECAL.

1734 The ECAL is composed of a barrel containing
 1735 more than 60,000 crystals and of closing
 1736 endcaps containing another 15,000 crys-
 1737 tals. In front of the ECAL endcap is installed
 1738 a preshower detector made out of two layers
 1739 of lead and silicon strip detectors to increase
 1740 the spatial resolution close to the beam line
 1741 for pion-photon and single-double photon dis-
 1742 crimination purposes. Figure 2.25 shows the
 1743 calorimeter inside of the magnet and the crys-
 1744 tals.

1745 The next layer is the HCAL. The role of
 1746 these forward calorimeters, made using steel
 1747 and quartz fibers, is to precisely measure the momentum very energetic hadrons. Several layers
 1748 of brass or steel are interleaved with plastic scintillators readout by photodiodes using wavelength-
 1749 shifting fibers. The HCAL is also composed of a barrel, shown in Figure 2.26 and of endcaps. It
 1750 also features forward calorimeters on both sides of CMS in the region very close to the beam line at
 1751 high pseudorapidity ($3.0 < |\eta| < 5.0$).



Figure 2.26: The CMS hadron calorimeter barrel.

1752 **2.2.4.3 The muon system**

1753 Finally, in the outer region of the apparatus, a muon system is used to trigger on potentially interest-
 1754 ing event by identifying muons. Three different subsystems compose the muon system as shown in
 1755 Figure 2.27 in which a quadrant of the CMS detector focuses on muon system. Drift Tubes (DTs)
 1756 are found in the barrel region covering the low pseudorapidity region where particles transverse
 1757 momentum is lower and Cathode Strip Chambers (CSCs) are found in the endcap region covering
 1758 higher pseudorapidity region closer to beam line where particles have a stronger momentum. The
 1759 redundancy of the system is insured by Resistive Plate Chambers (RPCs) in both the barrel and end-
 1760 cap. Nevertheless, the region closest to the beam line ($|\eta| > 1.8$) was not equipped with RPCs. This

lack of redundancy in the high pseudo rapidity region will be solved during LS2, the following Year End Technical Stop (YETS) in 2021 and 2022, and LS3 where the necessary services, detectors and Link System, that collects the data and synchronizes them, will be installed.

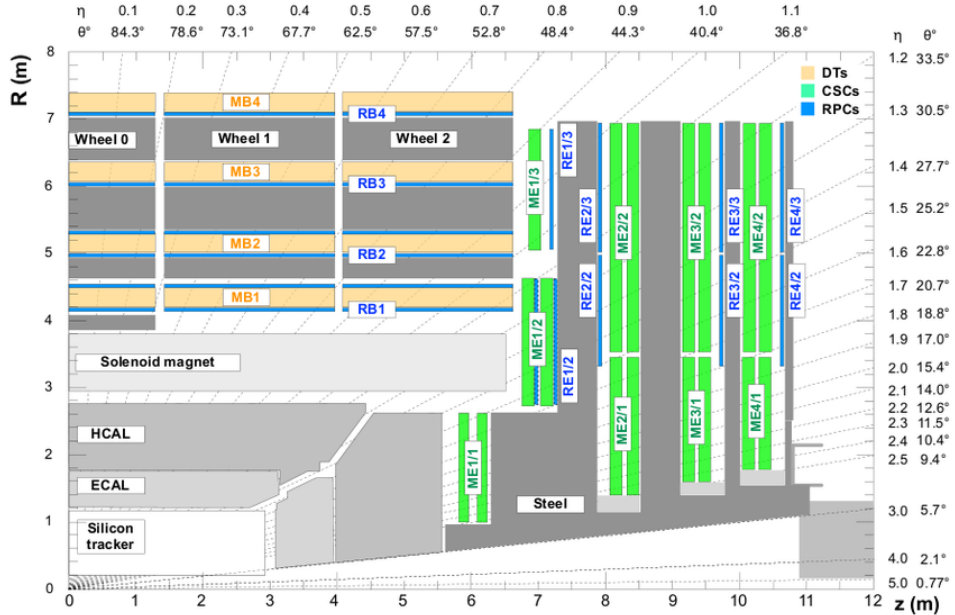


Figure 2.27: A quadrant of the muon system, showing DTs (yellow), RPCs (blue), and CSCs (green).

3

1764

1765

Muon Phase-2 Upgrade

1766 In the previous chapter, the timeline of the LHC has been described and the upcoming High Lumi-
1767 nosity LHC was introduced. LS3 has now started and the first HL-LHC related upgrade of CMS will
1768 take place. In order to understand the context in which the work of this thesis was performed as well
1769 as its motivations, it is necessary to give more insight into the reasons behind the increased instantan-
1770 eous luminosity of LHC. In a first section of the chapter, these motivations will be discussed.

1771 The muon system of CMS will then be presented in greater details than what was done in the
1772 previous chapter in order to have a better understanding of the need for upgrades of its different
1773 sub-systems in the perspective of HL-LHC. Most of the detectors will require new electronics to
1774 adapt to the new data flow and be integrated into a more robust trigger. Moreover, the redundancy
1775 of the muon system in the endcaps will need to be improved. This will be achieved by the addition
1776 of new detectors.

1777 Finally some insight will be given on ecofriendly gas studies for the specific case of Resistive
1778 Plate Chambers. This studies don't fall into the scope of the HL-LHC upgrades but the necessity of
1779 operating the detectors with gas mixtures that are more respectful of the environment is real. The
1780 European union is starting to press the scientific community for solutions and the research institutes
1781 are investing time into finding replacements to the gases used while maintaining similar working
1782 performances.

1783 3.1 Motivations for HL-LHC and the upgrade of CMS

1784 As detailed in Section 2.2.2, the first data taking period, during which the LHC was only operated
1785 at a center-of-mass energy of 7 TeV, took place until the start of LS1. It has been sufficient to
1786 claim the discovery of a new $125 \text{ GeV}/c^2$ particle compatible with the Higgs boson by both CMS
1787 and ATLAS in July 2012 and hence achieve a major milestone in the history of science towards the
1788 understanding of the fundamental nature of the universe. Nevertheless, the LHC machine holds the
1789 potential to go further and help unravel the remaining mysteries the High-Energy Physics (HEP)
1790 community is facing.

Over its full lifetime, the HL-LHC is expected to deliver an outstanding integrated luminosity of 3000 fb^{-1} , nearly an order of magnitude higher than what will be delivered by LHC until LS3 start, as shown in Figure 2.20. In the case of Higgs studies, this will lead to measuring the couplings of the boson to a precision of 2 to 5%. Thanks to the estimated 15 millions of Higgs bosons created every year, a more precise measurement of potential deviations from the theoretical predictions is expected. The properties of the boson will hence be tested and compared to the SM Higgs neutral boson. SUSY and heavy gauge boson studies would also see their mass range limits pushed away by at least 1 TeV and could lead to a new breakthrough. Many of the Standard Model extensions discussed in Section 2.1.3 yield Heavy Stable Charged Particles (HSCPs), i.e. heavy long-lived particles. These particles would be produced at the LHC with a high momentum but a velocity significantly lower than the speed of light ($\beta < 0.9$) [178–182] and/or a charge that differs from the elementary charge ($|Q| = e$, $|Q| < e$ or $|Q| > e$) [181–186]. Depending on the model considered, HSCPs could be lepton-like heavy particles or on the contrary R-hadron, i.e. particles composed of a supersymmetric particle and at least one quark [181].

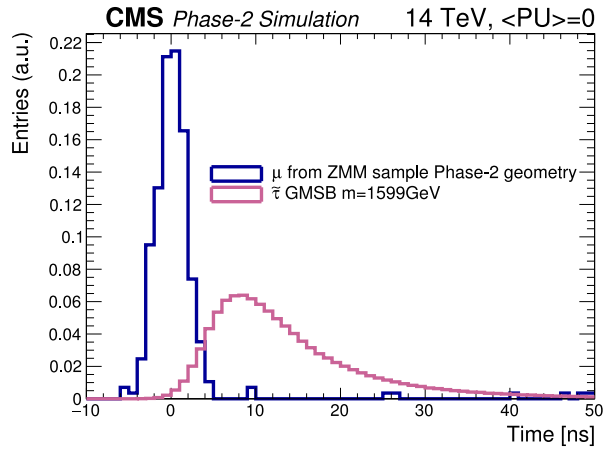


Figure 3.1: The measured transit time of a HSCP in CMS is compared to the transit time of a particle traveling at near the speed of light [177].

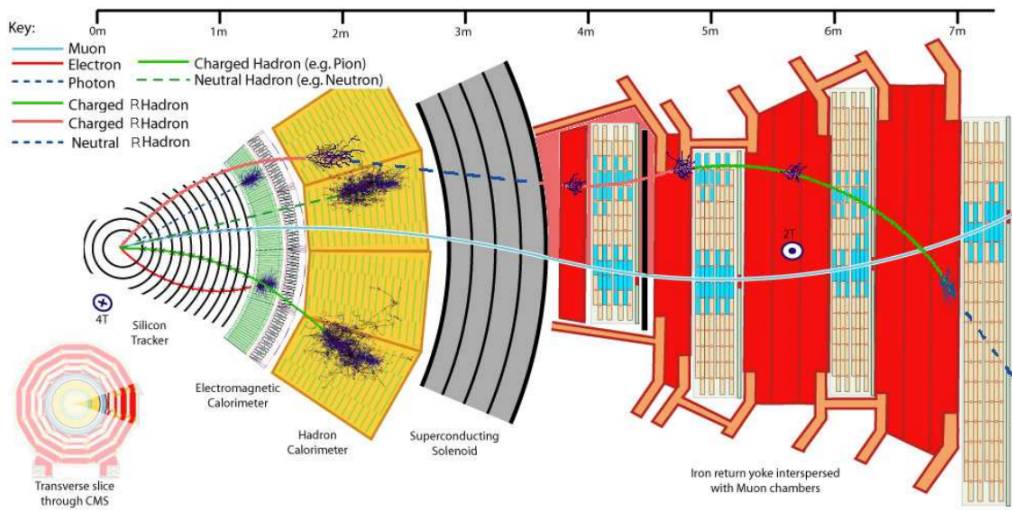


Figure 3.2: Slice of the CMS detector showing example of passage of SM particles and R-hadrons. On the one hand, lepton-like HSCPs will appear to behave like slow and heavy muons. On the other hand, R-hadrons are likely to convert into other kind of charged or neutral R-hadrons due to interactions inside the detector volume.

1817 Due to lifetimes of the order of a few ns,
 1818 HSCPs would travel for long enough distances
 1819 to cross through entire typical collider detec-
 1820 tors while appearing almost stable. Because
 1821 of their low velocity, they can be reconstructed
 1822 and assigned to bunch crossings different to
 1823 the ones they effectively have been produced,
 1824 as shown in Figure 3.1, if reconstructed at
 1825 all. Indeed, the trigger algorithms in use at
 1826 CMS were not designed for such slow parti-
 1827 cles and they assume most particles of inter-
 1828 est will have a velocity close to the speed of
 1829 light [182, 187].

1830 As HSCPs are long-lived particles, their
 1831 identification would be possible thanks to the
 1832 muon system. The main background will con-
 1833 sist of wrongly measured muons which should
 1834 have a lower transverse momentum, a near to
 1835 speed-of-light velocity and a low ionisation
 1836 energy loss. An example of passage of HSCPs
 1837 through a slice of the CMS detector is showed
 1838 in Figure 3.2. The tracks associated to the
 1839 HSCPs would then have to be reconstructed in
 1840 both the silicon detectors, for precise dE/dx
 1841 measurement, and the muon system detectors. In this case, the muon system will be used to perform
 1842 Time-of-flight (ToF) measurements to discriminate between near speed-of-light particles and slower
 1843 ones. The full reconstruction will then look for useful signatures such as the large transverse mo-
 1844 mentum of the candidates or their large ionisation energy loss alongside the low velocity accurately
 1845 measured thanks to the muon system as depicted in Figure 3.3. The ToF measurement to identify
 1846 beyond the Standard Model particles will mostly rely on the time information provided by the Drift
 1847 Tubes, in the barrel region of the detector, and Cathode Strip Chambers, in the endcaps. From CMS
 1848 point of view it will then become necessary to increase the acceptance and redundancy of the end-
 1849 caps toward higher pseudo-rapidity as the pseudo-rapidity region $1.6 < |\eta| < 2.5$ is only covered
 1850 by CSCs.

1851
 1852 A natural consequence of the higher instantaneous luminosity will be the increase of collisions
 1853 per bunch crossing. It is estimated that the pile-up will rise from the approximate average of 40
 1854 collisions per bunch crossing in 2017 and 2018, presented in Figure 3.4, to 140 to 200 depending on
 1855 the scenario considered [188]. The trigger rate will then be affected in the same way putting a lot
 1856 of stress on the trigger algorithms. Upgrading the electronics of some of the detectors and working
 1857 on the data flow within the experiment would help going through HL-LHC with keeping similar
 1858 performance than during Phase-1. On the other hand, the impact of the increased background will
 1859 become problematic in many ways and will force for upgrades or many sub-systems of CMS. The
 1860 main effects will be a large increase of the irradiation of the detectors, mainly close to the beam
 1861 line. The detectors already installed will need to be certified for the irradiation levels they will be

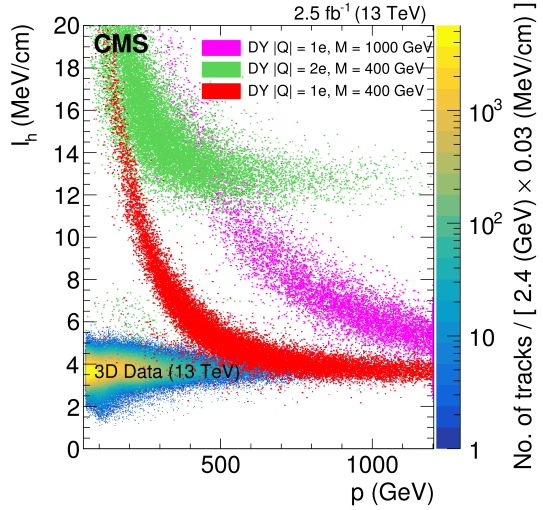


Figure 3.3: Distribution of the energy-loss dE/dx as described by Bethe-Bloch formula through the estimator I_h with increasing particle momentum for tracks in the 13 TeV data. The estimator depends on the charge deposition of the particles per unit length in the silicon detectors of CMS which is related to their energy loss as explained in a publication by the CMS Collaboration [181]. The simulated HSCPs are singly or multiply charged particles with masses of 400 and 1000 GeV.

subjected to until the end of HL-LHC while the new detectors that will extend the coverage of the muon system toward higher pseudo-rapidity will need to take the strong radiations they will suffer close to the beam line into account. Simulations of the expected distribution of absorbed dose in the CMS detector under HL-LHC conditions show, in Figure 3.5, that detectors placed close to the beam line will have to withstand high irradiation, the radiation dose being of the order of a few tens of Gy.

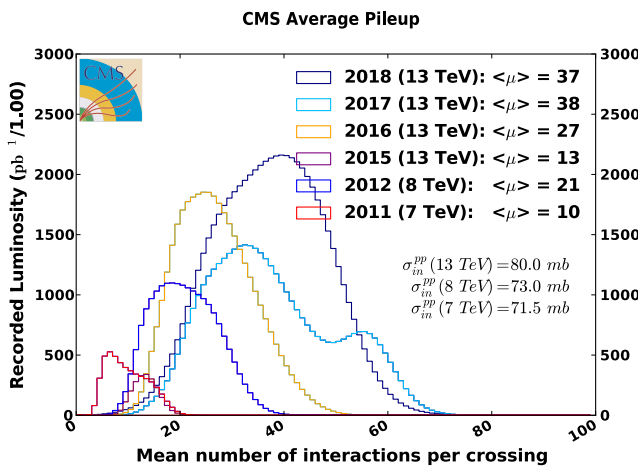


Figure 3.4: Distribution of the average number of interactions per crossing (pileup) for pp collisions in 2011 (red), 2012 (blue), 2015 (purple), 2016 (orange), 2017 (light blue), and 2018 (navy blue). The overall mean values and the minimum bias cross sections are also shown [189].

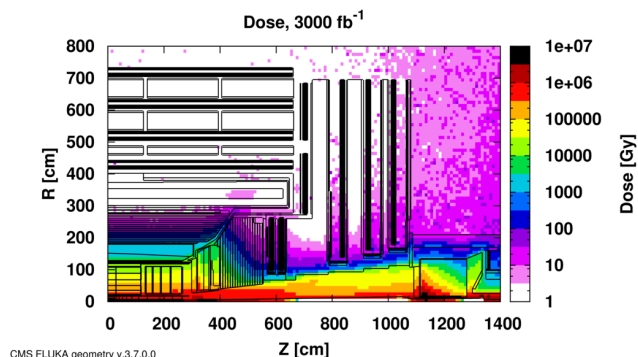


Figure 3.5: Absorbed dose in the CMS cavern after an integrated luminosity of 3000 fb^{-1} . Using the interaction point as reference, R is the transverse distance from the beamline and Z is the distance along the beamline [177].

measurement of their energy with reasonable precision only using the tracker is nearly impossible. Thus, this increased tracker coverage range needs to be put in parallel with a matching muon detector and will open doors to multi-lepton final states in which leptons are likely to have a low transverse momentum and to be found near the beam line.

Finally, as the muon system is composed only of gaseous detectors, strong environmental concerns have risen over the last years as the European directives will restrict the use of fluorine based

Improving this situation will come with the increase of hit numbers recorded along the particle track to reduce the ambiguity on muon versus background detection. Moreover, the measurement of small production cross-section and/or decay branching ratio processes, such as the Higgs boson coupling to charge leptons, and in particular to muons, or the $B_s \rightarrow \mu^+ \mu^-$ decay, is of major interest. Such considerations give more weight to the upgrade of the forward regions to maximize the physics acceptance to the largest possible solid angle.

To ensure proper trigger performance within the present coverage, the muon system will be completed with new chambers and the electronics of the present system will need to be upgraded. A first step into this direction will be taken by installing new gaseous detectors in each endcap layers and extend the coverage up to $|\eta| = 2.8$. Nevertheless, the region beyond $|\eta| > 2.8$ and extending to $|\eta| = 5.0$ only is covered by the forward HCAL detectors and lack redundant muon detector coverage. Extensions of the tracker in the context of HL-LHC will increase its coverage up to $|\eta| = 4.0$ but the identification of muons and

¹⁹⁰⁸ gas mixtures. Both the CSC and RPC subsystems, using CF_4 , $C_2H_2F_4$, or SF_6 , will need to adapt
¹⁹⁰⁹ their working gas in order to strongly reduce the greenhouse potential of the mixtures released into
¹⁹¹⁰ the atmosphere due to gas leaks.

¹⁹¹¹ 3.2 Description of the muon system

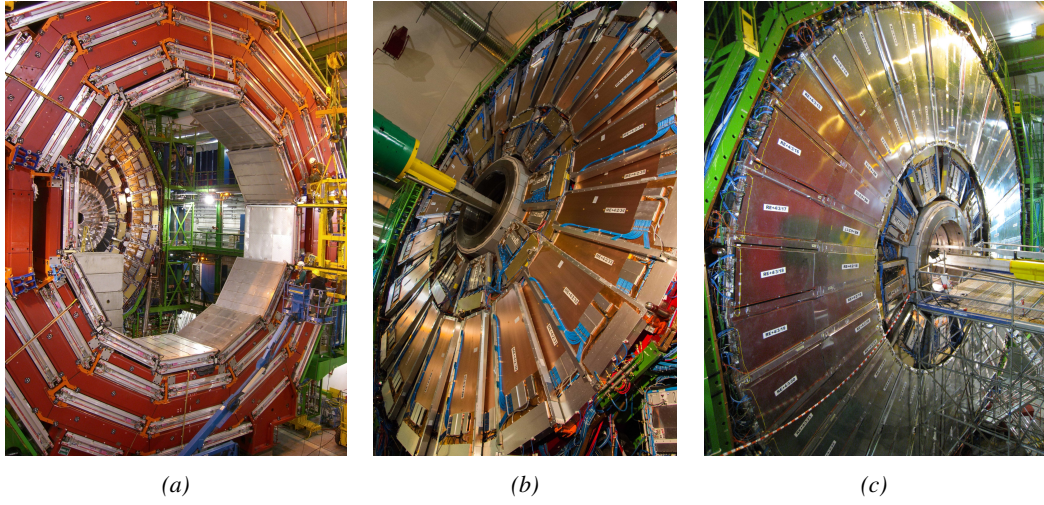


Figure 3.6: Figure 3.6a: Barrel wheel with its detector rings and return yokes. Figure 3.6b: CSC endcap disk with the 2 CSC stations. The outer station is made of 10 deg detectors while the inner station is made of 20 deg detectors. Figure 3.6c: RPC endcap disk. The inner station is not equipped and the inner CSC station can be seen.

¹⁹¹² The barrel region is divided into 5 *wheels* made out of 4 *rings* of detectors with iron return yokes in
¹⁹¹³ between them whereas the endcaps are made out of 4 disks, each divided into pseudorapidity stations,
¹⁹¹⁴ 2 for CSCs (except for the first disk where 3 stations are equipped) and 3 for RPCs, although only 2
¹⁹¹⁵ RPCs stations are equipped at present. The wheels and disks are shown in Figure 3.6. So far, each
¹⁹¹⁶ subsystem was dedicated to a particular task. DTs, in the barrel, and CSCs, in the endcaps, are used
¹⁹¹⁷ mainly for their spatial resolution. Indeed, DTs' resolution is of the order of 100 μm along both
¹⁹¹⁸ the $(r - \phi)$ and $(r - z)$ components while the resolution of CSCs is similar but varies in a range
¹⁹¹⁹ from 50 μm to 140 μm depending on the distance to the beamline. On the other hand, RPCs are used
¹⁹²⁰ as redundant detection system in the whole muon system. They display a very good intrinsic time
¹⁹²¹ resolution of 1.5 ns although the electronics only provide bunch crossing information with a time
¹⁹²² resolution of 25 ns.

¹⁹²³ 3.2.1 The Drift Tubes

¹⁹²⁴ The 250 CMS DTs, found in the barrel covering the pseudorapidity region $0 < |\eta| < 1.2$ and whose
¹⁹²⁵ structure is shown in Figure 3.7, are composed of 3 *superlayers* of DT cells. Two of these superlayers
¹⁹²⁶ are dedicated to measuring the ϕ coordinate of the muons and while the last one measures the η (or z)
¹⁹²⁷ coordinate. Each superlayer consists on 4 layers of 60 to 70 DT cells arranged in quincunx to allow
¹⁹²⁸ for a precise reconstruction of the muon path through the DT layers. Each DT cell is a rectangular

1929 aluminium gas volume with a central anode wire. Cathode strips are placed on the narrow surface
 1930 of the cells and electrode strips are placed on the wide surface to help shaping the electric field to
 1931 ensure a consistent drift velocity of electrons in the drift volume. These detectors are operated using
 1932 a 85/15 mixture of Ar and CO_2 . Outside the gas volume of each DT chamber is attached a Minicrate
 1933 electronics (MiC) that hosts both read-out and trigger electronics.

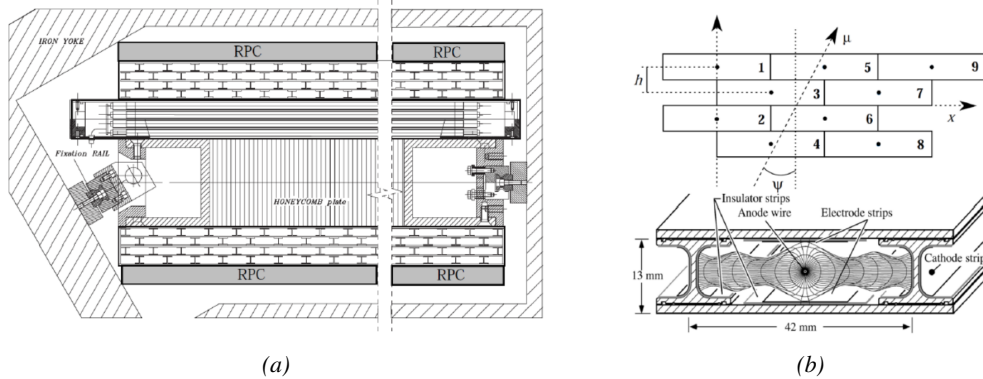


Figure 3.7: Figure 3.7a: Cross section of a DT module showing the two superlayers measuring the ϕ coordinate, perpendicular to the cross section plane, and the superlayer measuring the η coordinate, placed in between the two others with honeycomb and parallel to the cross section plane. The DT detector is sandwiched in between 2 RPCs whose readout strips are perpendicular to the cross section plane, measuring the ϕ coordinate. Figure 3.7b: A DT cell is shown together with its electric field. The path of a muon through a superlayer is shown.

3.2.2 The Cathode Strip Chambers

1934 The 540 CMS CSCs, found in the endcaps covering the pseudorapidity region $0.9 < |\eta| < 2.5$
 1935 and described through Figures 3.8 and 3.9, are composed of 6 panels of CSC, each panel consisting
 1936 in a wide gas volume of 9.5 mm (7 mm in the case of ME1/1 station) containing anode wires and
 1937 whose surfaces are cathodes. The top cathode is a wide copper plane of the size of the gas volume.
 1938 The bottom cathode is divided into thin trapezoidal copper strips radially arranged to measure the
 1939 azimuthal coordinate ϕ with a pitch ranging from 8 to 16 mm. The $0.50\text{ }\mu\text{m}$ anode wires are placed
 1940 perpendicularly to the strips to measure radial coordinate r and are grouped by 10 to 15 with a wire
 1941 to wire space of 3.2 mm. In the specific case of ME1/1 placed against the HCAL endcap, the $0.30\text{ }\mu\text{m}$
 1942 anode wires have a wire to wire distance of 2.5 mm and are not disposed perpendicularly to the strips
 1943 but slightly tilted by an angle of 29 deg to compensate for the lorentz force due to the very strong
 1944 local magnetic field of 4 T. These detectors are operated with a 40/50/10 mixture of Ar , CO_2 and
 1945 CF_4 . Combining the information of the multiple CSC panels, the detectors achieve a very precise
 1946 measurement of the muon track. The read-out of the cathode strip signals is performed by cathode
 1947 front-end boards (CFEBs) mounted on the detectors. The boards are used to collect and digitize
 1948 the charge of the singals and transfer it to off-chamber electronics called Data acquisition mother
 1949 boards (DMBs). In parallel, the data from the CFEBs together with the data from the anode wires,
 1950 after treatment by on-chamber electronics called Anode local charged track boards (ALCTs), is used
 1951 to build a fast trigger information which is sent other off-chamber electronics called Trigger mother
 1952 boards (TMBs).

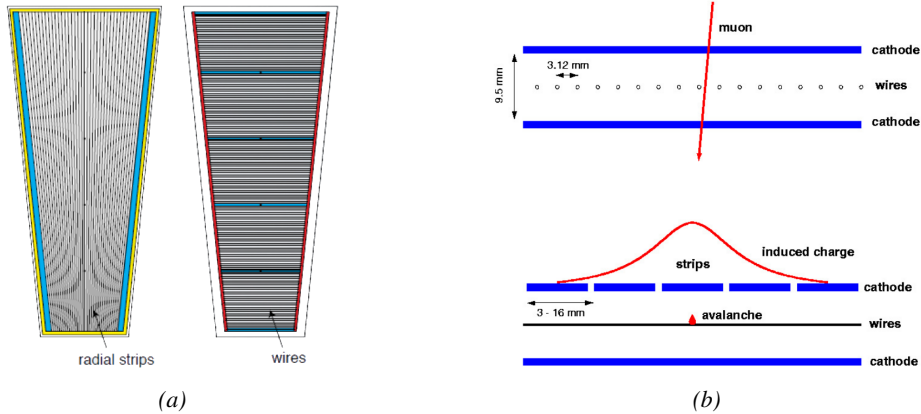


Figure 3.8: Figure 3.8a: Cathode strips and anode wire layout of a CSC panel. Figure 3.8b: Avalanche development and charge collection by anode wires and induction on cathode strips inside of a CSC panel.

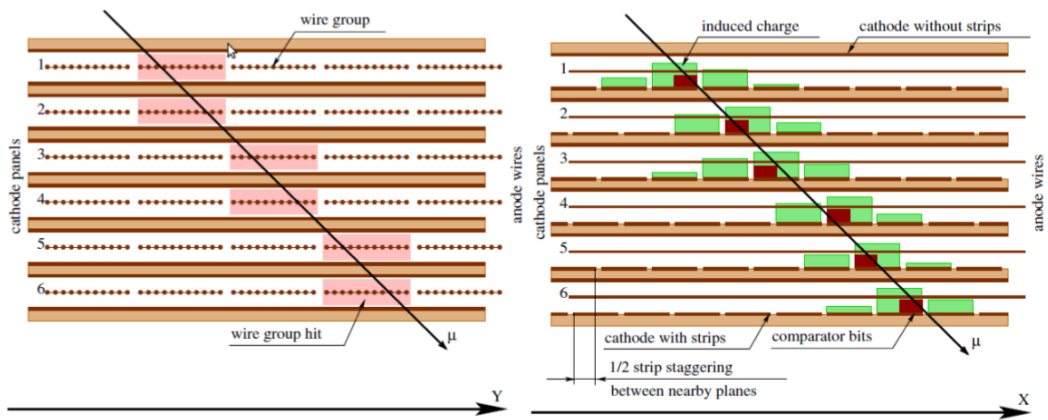


Figure 3.9: Muon track reconstruction through the 6 panels of a CMS CSC using the information of anode wire groups and cathode strip charge distribution combined with comparator bits to decide on which half strip the muon is more likely to have passed.

1954 3.2.3 The Resistive Plate Chambers

1955 Despite their excellent spatial resolution, the wire chambers (DTs and CSCs) are limited in terms
 1956 of time resolution by the fact that the charge needs to drift towards the anode wire and be collected
 1957 before having the confirmation that a particle was detected as the drift volume is not used to develop
 1958 avalanches. Indeed, the stronger electric field close to the anode wire triggers the avalanche and the
 1959 gain of the detector. Due to the drift, the time resolution is thus limited at best to approximately 2 to
 1960 3 ns. In addition, even though the intrinsic time resolution of the tracking chambers is rather good
 1961 compared to the 25 ns in between successive collisions, the processing time of the trigger system
 1962 doesn't allow for very fast triggering as it provides a time precision of only 12.5 ns. Thus, detectors
 1963 fully dedicated to timing measurement have been installed as a redundant system. These detectors
 1964 are RPCs, also gaseous detectors but that use current induction instead of charge collection allowing
 1965 for a time resolution of the order of 1 ns only. Theoretically, depending on the design used, RPCs

1966 could reach a time resolution of the order of 10 ps but in the context of LHC where bunch crossing
 1967 happen every 25 ns, a time resolution of 1 ns is sufficient to accurately assign the right bunch crossing
 1968 to each detected muon.

1969 The 1056 RPCs equip the
 1970 CMS muon system both in
 1971 the barrel and endcap regions
 1972 and cover the pseudorapidity
 1973 region $0 < |\eta| < 1.6$.
 1974 They are composed of two
 1975 layers of RPC *gaps* as de-
 1976 scribed in Figure 3.10. Each
 1977 gap consists in two resis-
 1978 tive electrodes made out of
 1979 2 mm thick Bakelite enclos-
 1980 ing a 2 mm thick gas volume con-
 1981 taining a 95.2/4.5/0.3 mixture
 1982 of $C_2H_2F_4$, $i - C_4H_{10}$ and SF_6 . Due to this geometry, the electric field inside of a gap is ho-
 1983 mogeneous and linear at every point in the gas translating into a uniform development of avalanches
 1984 in the gas volume as soon as a passing muon ionises the gas. The two gaps sandwich a readout
 1985 copper strip plane. A negative voltage is applied on the outer electrodes, used as cathodes, and the
 1986 inner electrodes, the anodes, are simply connected to the ground as well as the readout panel that
 1987 picks up the current induced by the accumulated charge of the growing avalanches in one or both
 1988 of the gas gaps. This OR system allows for a lower gain (i.e. a lower electric field) on both gaps to
 1989 reach the maximal efficiency of such a detector.

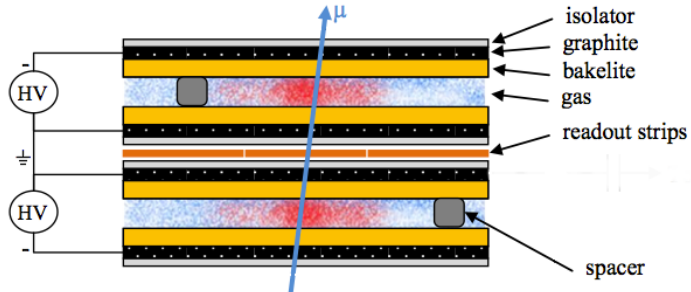


Figure 3.10: Double gap layout of CMS RPCs. Muons passing through the gas volumes will create electron-ion pairs by ionising the gas. this ionisation will immediately translate into a developing avalanche.

1990 3.3 Necessity for improved electronics

1991 Drift Tubes and Cathode Strip
 1992 Chambers are important compo-
 1993 nents used to identify and measure
 1994 muons, especially thanks to their
 1995 spatial resolution of the order of
 1996 $100 \mu\text{m}$. Nevertheless, the lumi-
 1997 nosity and irradiation during HL-
 1998 LHC will cause serious event loss
 1999 and ageing on the electronics of
 2000 these subsystems that will comprise
 2001 the triggering and data transfering
 2002 needs of CMS. Thus, electronics up-
 2003 grade are foreseen to address these
 2004 expected problems. While only
 2005 the RPCs' electronic system is able
 2006 to operate under Phase-2 require-
 2007 ments [190], DTs and CSCs will
 2008 need to improve their trigger acceptance rate and latency to ensure that the Level-1 trigger thresh-

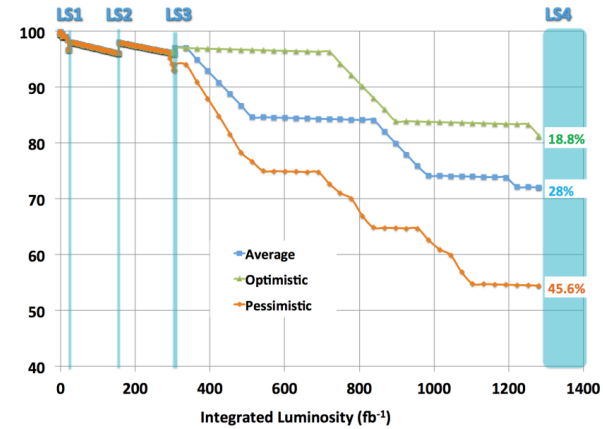


Figure 3.11: Extrapolated fraction of failing channels of the present DT MiC1 electronics as a function of the integrated luminosity for different scenari until LS4 [177].

old can stay at the same level [191]. The Level-1 trigger consists of custom hardware processors receiving data from the calorimeters and the muon system. In return, they generate a trigger signal within $3\ \mu\text{s}$, with a maximum rate of 100 kHz. In the perspective of HL-LHC, each subsystem needs to achieve a minimum rate of 500 kHz with a latency not greater than $12.5\ \mu\text{s}$. DTs and CSCs will also need to improve their Data Acquisition (DAQ) transfer rate to reach a minimum near 1 Tbit/s. The foreseen upgrades are expected to exceed the requirements.

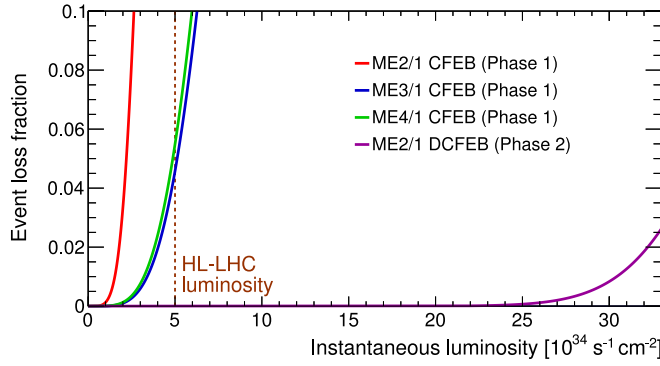


Figure 3.12: The event loss fractions as a function of the instantaneous luminosity is compared for CFEBs (Phase-1) and DCFEBs (Phase-2) at different CSC locations. HL-LHC luminosity is marked with the dashed line [177].

and High Voltage (HV) modules will not need any replacement. On the other hand, CSCs showed that their electronics would be able to live through the 10 years of Phase-2 but the limited buffer depth might cause memory overflows and read-out inefficiencies with a fraction of event loss ranging from 5 to more than 10% at an instantaneous luminosity similar to which of HL-LHC depending on the expected background. The replacement of CSCs' CFEBs by digital ones, DCFEBs, with deeper buffer would permit to make event loss negligible and satisfy HL-LHC requirements as can be seen in Figure 3.12. All these new DT and CSC electronics will be connected to the trigger electronics via optical links to ensure a faster communication [177].

The upgrade on the side of Resistive Plate Chambers will not be done at the level of the electronics but rather that of the Link System located in the service cavern of CMS. RPC Link System connects the front-end electronics data of RPCs into CMS trigger processors. The main motivation for such an upgrade is that the electronic board composing the link system are built using ob-

The first version of Mini-crake electronics (MiC1) used by DTs don't allow for high enough trigger rate. In addition to this problem, it was shown that these electronics contain components that are not radiation hard enough to sustain HL-LHC conditions and hence, a too large number of channels may fail due to radiations as showed in Figure 3.11. The MiC1 will be replaced on each detector by an improved version referred to as MiC2 while Front-End Electronics (FEE)

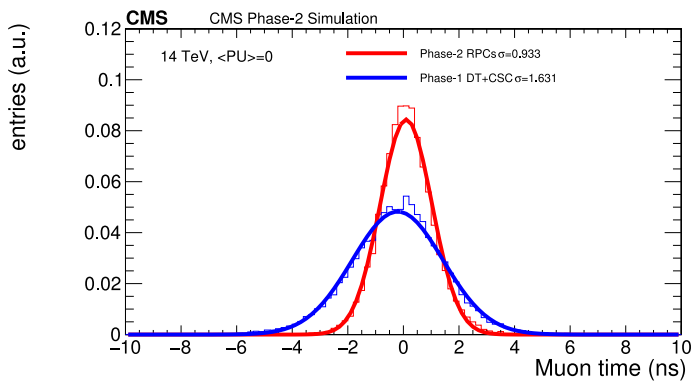


Figure 3.13: Comparison of the simulated time residuals in between reconstructed and true muon times without (blue) and with (red) the upgraded RPC link system [177].

solete and/or weak components that can easily suffer from the electromagnetic noise. These components may become the source of failing channels throughout Phase-2. Moreover, these link boards were originally designed only to match RPC digitized signals with the corresponding bunch crossing. Due to this feature, the time resolution of the full RPC chain is hence limited to 25 ns and does not exploit the full time resolution of the detectors. The time resolution foreseen after the upgrade can be seen through Figure 3.13 and is of the order of 1 ns. The exploitation of the full time resolution would make the synchronization of the RPC system easier and allow to have a finer offline out-of-time background removal within the 25 ns between consecutive bunch crossings. Moreover, this would greatly improve the trigger and reconstruction on HSCPs. Using the TOF information in between consecutive RPC stations, the minimal particle velocity than could be probed will drop from approximately 0.6 to 0.25 times the speed of light as showed in Figure 3.14.

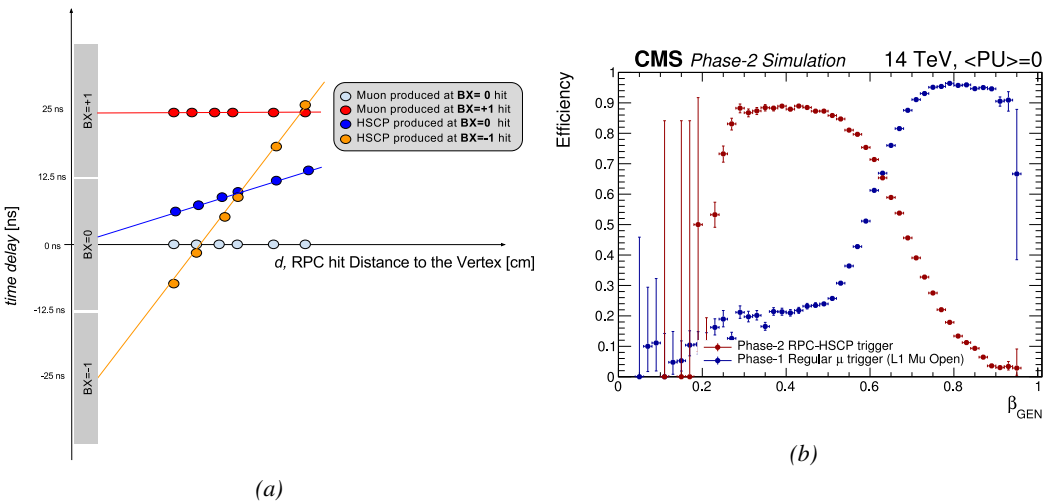


Figure 3.14: Figure 3.14a: Time delay with respect to a particle traveling at the speed of light measured at consecutive RPC stations for particles originating at different bunch crossings and traveling at different velocities [177]. Figure 3.14b: In blue is showed the standard level-1 muon trigger efficiency as a function of β and in blue is showed the RPC-HSCP trigger efficiency after upgrade of the RPC Link System [177].

Upgrading RPC link system will require the installation of 1376 new link boards and 216 control boards. The new boards will make use of the recent progress made with fast FPGAs and will be a great improvement to the ASICs formerly used as they will be able to process signals from several detectors in parallel.

3.4 New detectors and increased acceptance

In the present muon system, the redundancy is assured by RPCs used for their robust bunch crossing assignments. The extension of the muon system towards higher pseudo-rapidity in an effort to complete the redundancy and to contribute to the precision of muon momentum measurements will require muon chambers with a spatial resolution less or comparable to the multiple scattering muons are subjected to while traveling through the detector volume [192].

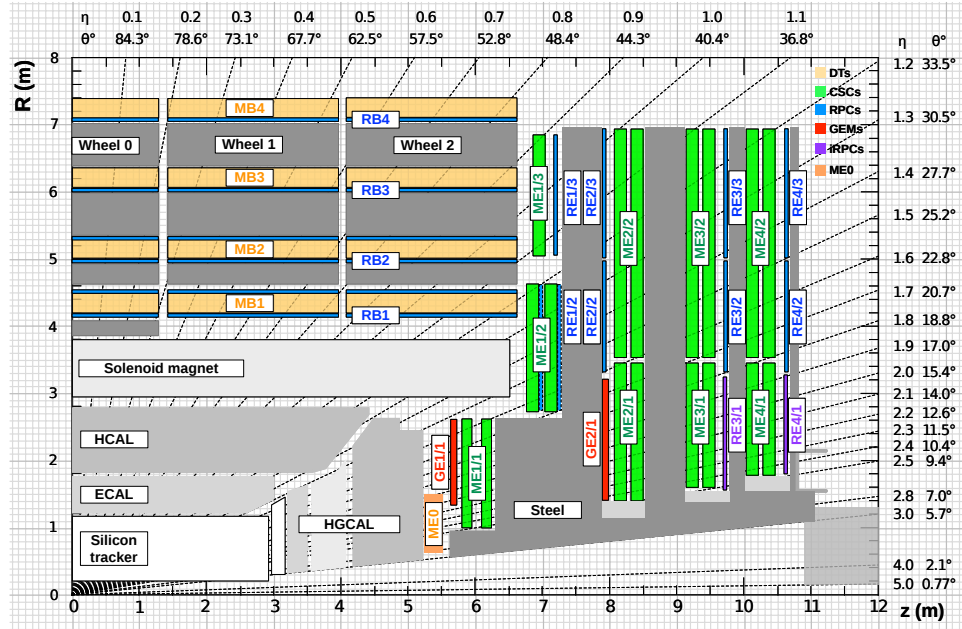


Figure 3.15: A quadrant of the muon system, showing DTs (yellow), RPCs (blue), and CSCs (green). The locations of new forward muon detectors for Phase-2 are contained within the dashed box and indicated in red for GEM stations (ME0, GE1/1, and GE2/1) and dark blue for improved RPC (iRPC) stations (RE3/1 and RE4/1).

Figure 3.15 shows a similar quadrant of CMS than the one presented in Figure 2.27 with the addition of Gas Electron Multiplier (GEM) (ME0, GE1/1 and GE2/1) and improved RPC (iRPC) (RE3/1 and RE4/1) in the pseudo-rapidity region $1.6 < |\eta| < 2.4$. The completion of the redundancy was already scheduled in the original CMS Technical Proposal [193] but never addressed. The coming Phase-2I is then the occasion to equip the region with the newest GEM and RPC technology. In order to match CMS requirements, a spatial resolution of $\mathcal{O}(\text{few mm})$ will be necessary for the proposed new RPC stations while the GEMs will need a resolution better than 1 mm, as showed by the simulation in Figure 3.16. Indeed, most of the plausible physics will be covered only considering muons with $p_T < 100 \text{ GeV}$.

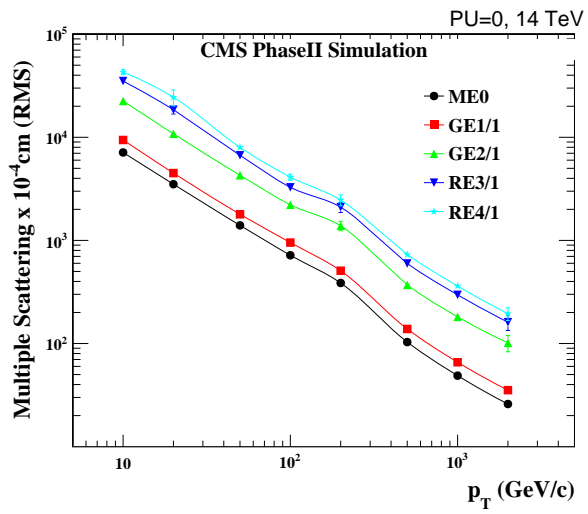


Figure 3.16: RMS of the multiple scattering displacement as a function of muon p_T for the proposed forward muon stations. All of the electromagnetic processes such as bremsstrahlung and magnetic field effect are included in the simulation.

2098 3.4.1 Gas electron multipliers

2100 In the region closer to the interaction point
 2101 where the spatial resolution is requested for
 2102 the new detectors to be better than 1 mm (at
 2103 least for ME0 and GE1/1 according to Figure
 2104 3.16) and where the background rate will
 2105 be the highest for muon detectors, the choice
 2106 has been made to use triple GEMs, micro pat-
 2107 tern gaseous detectors, instead of the origi-
 2108 nally planned RPCs. The GE1/1 project has
 2109 been the first to be approved and demonstra-
 2110 tors have been installed in CMS already during
 2111 LS1. The rest of the detectors will be installed
 2112 during LS2 while the GE2/1 and ME0 projects
 2113 are still under development. ME0, GE1/1 and
 2114 GE2/1 will be installed respectively close to
 2115 the HCAL endcap, on the first and on the sec-
 2116 ond muon endcap disks as can be seen from
 2117 Figure 3.15.

2118 Gas Electron Multipliers are gaseous de-
 2119 tectors [194] whose gas volume is confined be-
 2120 tween two planar electrodes, the anode serv-
 2121 ing as read-out panel. The gas volume is di-
 2122 vided in two or more regions by a single or
 2123 multiple *GEM foils* as showed in Figure 3.17.
 2124 These foils are very thin, of the order of a few
 2125 tens of μm , and are pierced with holes as can
 2126 be seen in Figure 3.18. Both surfaces of the
 2127 GEM foils are clad with copper in order to ap-
 2128 plly a strong electric field in between each side
 2129 that will generate very strong potentials in the
 2130 holes. The gas region contained in between
 2131 the cathode and the GEM foil is called the drift
 2132 region as the electric field is not strong enough
 2133 to cause avalanches and thus start an amplifi-
 2134 cation. The primary electrons drift toward the
 2135 foil and are accelerated and amplified by the
 2136 very high potential within the holes, as showed
 2137 in Figure 3.18. Then the electrons reach the
 2138 second drift region in which they will induce
 2139 signal on the read-out located on the anode.
 2140 By restraining the amplification process at the
 2141 level of the holes, the electrons can stay in a
 2142 very confined space and thus induce a very
 2143 localized current, providing the GEMs with a

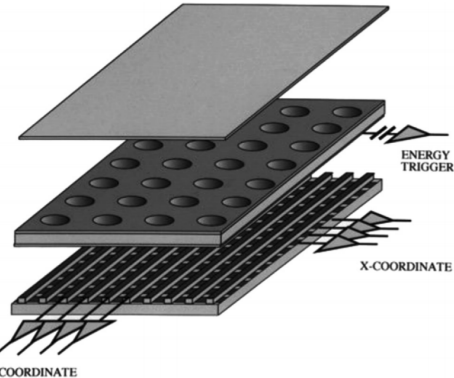


Figure 3.17: Schematics of a GEM showing the cathode on top, the GEM foil separating the gas volume into the drift region, in between the cathode and foil, and the induction region, in between the GEM foil and the anode, and finally the anode on which a 2D read-out is installed. A negative voltage is applied on the cathode. The anode is connected to the ground.

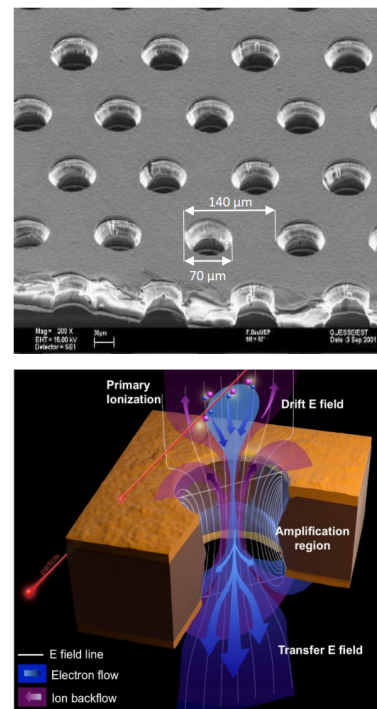


Figure 3.18: Top: Picture of a CMS GEM foil provided by a scanning electron microscope. Bottom: Representation of the electric field in a GEM hole and of the amplification electrons and ions undergo due to the very intense electric field.

2143 very good spatial resolution.

2144 The process can be re-
 2145 peated several times in a row,
 2146 in order to achieve a stronger
 2147 amplification. The GEMs that
 2148 will be used in CMS are triple-
 2149 GEM detectors operated with a
 2150 70/30 gas mixture of Ar/CO_2 .
 2151 They contain three GEM foils
 2152 and hence three electron am-
 2153 plifications, as can be seen
 2154 in Figure 3.19. The GEM
 2155 foils used in CMS are 50 μm
 2156 foils clad with 5 μm of copper
 2157 on each side. The foils are
 2158 pierced with double-canonical
 2159 holes which inner and outer
 2160 diameters are respectively 50
 2161 and 70 μm which are placed
 2162 140 μm from each other in an
 2163 hexagonal pattern, as showed in Figure 3.18. These detectors have a time resolution better than
 2164 10 ns and reach very good spatial resolutions of less than 200 μrad as indeed the position of the
 2165 hits is not measured along the strips but following the azimuthal angle granularity of the radially
 2166 organized trapezoidal strips.

2167 The GEM Upgrade project started with GE1/1 [195]. GE1/1 detectors will already be installed
 2168 during LS2. GE2/1 and ME0, on the other hand, will profit of the R&D knowledge and skills
 2169 developed for GE1/1 while the requirements for each subsystem are different as they are not placed
 2170 at the same distance from the interaction point. In this very forward region, a different position with
 2171 respect to the center of the detector can change dramatically the conditions in which the detectors
 2172 will have to be operated. In terms of rate capability, GE2/1, which is the furthest, is required to
 2173 withstand 2.1 kHz/cm² while GE1/1 needs to be better than 10 kHz/cm² and ME0, better than
 2174 150 kHz/cm². In terms of ageing with respect to charge deposition, ME0 needs to be certified to
 2175 840 mC/cm², GE1/1 to 200 mC/cm² and GE2/1 only to 9 mC/cm². All 3 detectors need to have a
 2176 time resolution better than 10 ns and an angular resolution better than 500 μrad .

2177 On each GE1/1 ring, 36 super chambers, consisting of two single GEM layers and spanning 10°,
 2178 will be installed covering the pseudo-rapidity region $1.6 < |\eta| < 2.2$ together with ME1/1 CSCs.
 2179 The reach of the muon system will be improved thanks to the GE2/1 that will overlap with the GE1/1
 2180 and cover a region from $|\eta| > 1.6$ to $|\eta| < 2.4$ and complete the redundancy of ME2/1. The super
 2181 chambers, built with two triple-GEM layers each consisting of four single GEM modules due to
 2182 the rather large surface of the GE2/1 chambers, that will be installed on the first ring of the second
 2183 endcap will span 20° each. Hence, a total of 72 chambers will be assembled to equip the muon
 2184 system. Finally, the ME0 installed near the HCAL endcap will cover the region $2.0 < |\eta| < 2.8$.
 2185 This subsystem will consist in super modules of six layers of triple-GEM detectors covering an
 2186 azimuthal angle of 20° leading to the construction of 216 single detectors.

2187 Adding the GEMs into the forward region of the muon system will allow to strongly enhance
 2188 the Level-1 Trigger performance as shown in Figure 3.20. In the region $1.6 < |\eta| < 2.4$, the trigger

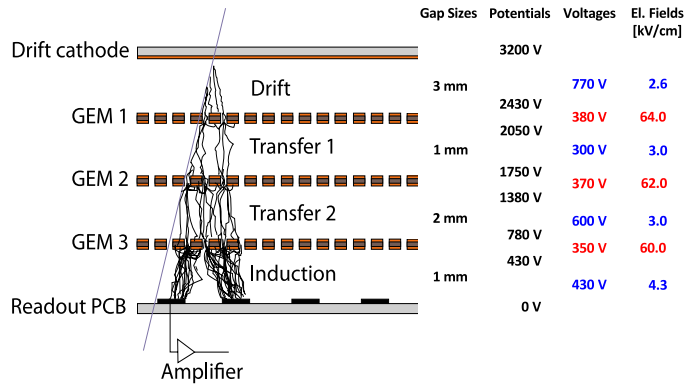


Figure 3.19: Schematic representation of CMS triple GEMs. The gas volume is divided into four areas. The drift area is the region where the primary electrons are created before being amplified a first time while passing through the first GEM foil. Then the process of drift and amplification is repeated twice in following two transfer areas and GEM foils. Finally, the charges have been amplified enough to induce current in the read-out strips while in the last drift area. The typical dimensions, potentials and electric fields are provided.

efficiency of the current system would lie between 80 and 90% under HL-LHC conditions. The installation of GEMs would bring the efficiency to a consistent 92 to 94% on the entire region. At the same time, the trigger rate is expected to fluctuate from 3 to 10 kHz with the current system alone. The addition of detectors to complete the redundancy would allow to keep the rate mostly under 2 kHz. Moreover, benefiting from the good spatial and angular resolution of the GEMs, the precision into the muon measurement will also be improved by an order of magnitude thanks to the addition of GEMs as can be seen from the simulation presented in Figure 3.21.

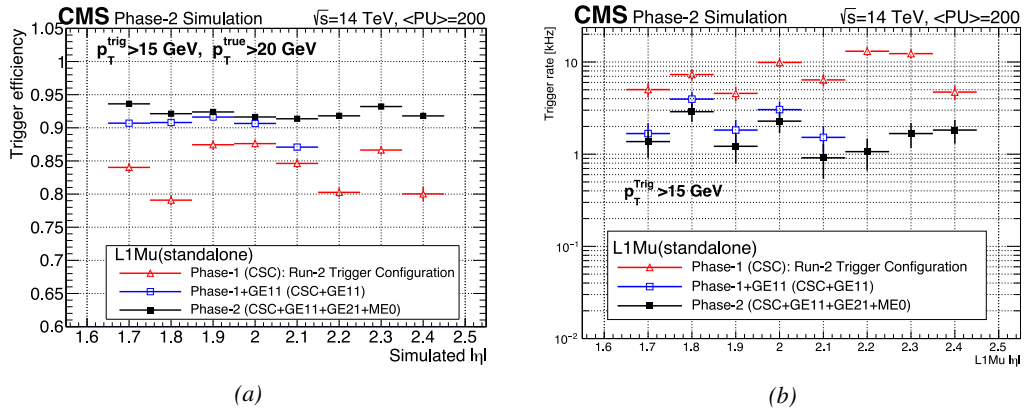


Figure 3.20: Simulated efficiency and rate of the standalone Level-1 muon trigger using tracks reconstructed in CSCs and all GEM stations compared with Phase-1 values in the case where only CSCs are used or CSCs+GE11. The zones of inefficiency of the CSC subsystem are compensated by the addition of GEMs during Phase-2 and the trigger rates is kept from increasing due to the high luminosity [177].

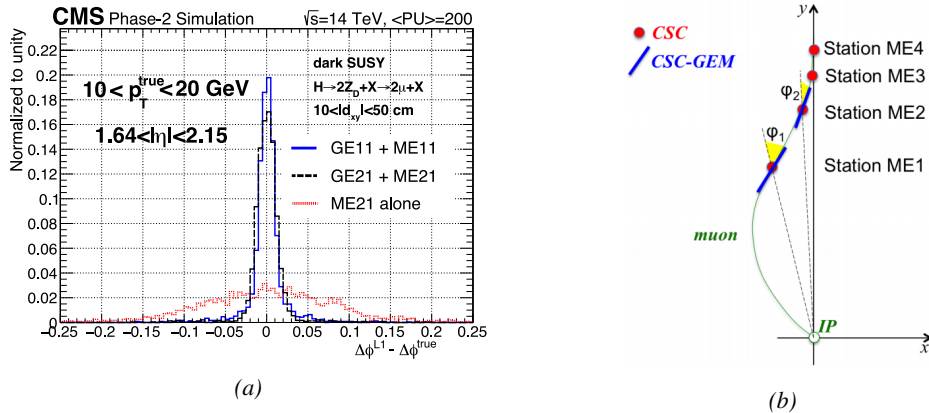


Figure 3.21: Figure 3.21a: Simulated resolution of the muon direction measurement $\Delta\phi$ with Phase-2 conditions. In the second endcap station, the resolution is compared in the case of CSCs (ME2/1) alone and CSCs+GEMs (GE2/1+ME2/1) while a similar resolution measurement is given in the case of the first station (GE1/1+ME1/1) [177]. Figure 3.21b: The addition of GEM detectors on stations 1 and 2 (ME0 is considered to contribute to station station 1) as redundant system to CSCs allows to improve the muon momentum improvement through a more accurate measurement of the local bending angles ϕ_1 and ϕ_2 [177].

3.4.2 Improved forward resistive plate chambers

Figure 3.15 shows that the iRPCs that will equip the third and fourth endcap disks in position RE3/1 and RE4/1 will finally be the partners of the CSCs in position ME3/1 and ME4/1. They will complete Phase-1 plans by bringing the needed upgrades in the perspective of Phase-2 as the older chambers are not suitable to equip the forward region of CMS due to HL-LHC rates and charge deposition. By completing the redundancy, more hits along the muon track will be available and the lever arm will be improved. The benefits from extending the redundancy of the muon system with iRPCs to the forward most region is shown in Figure 3.22 in which the trigger efficiency is presented with and without RPCs. It is possible to see that the efficiency of the CMS muon trigger with the complete redundancy is consistently improved to a level above 95% in the region $|\eta| > 1.8$ as the iRPCs help filling the holes in the CSC system.

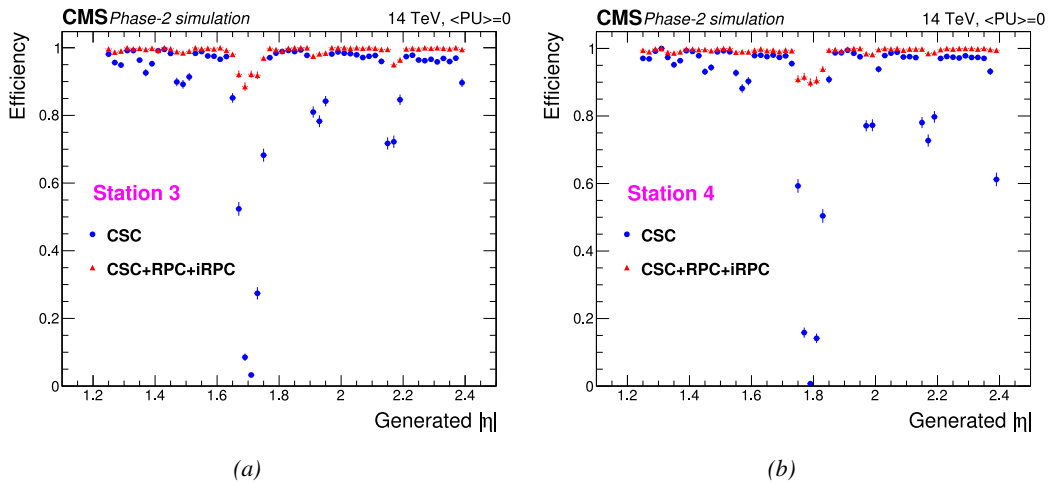


Figure 3.22: Simulation of the impact of RPC hit inclusion onto the local trigger primitive efficiency in station 3 (Figure 3.22a) and station 4 (Figure 3.22b) [177]. The contribution of iRPC starts above $|\eta| = 1.8$.

The detectors that will be installed in the coming years will have similarities with the already existing RPC system. 18 of the new chambers, each spanning 20° in φ around the beam axis with 96 radially oriented trapezoidal read-out strips, will cover each muon endcap disk leading to the production of 72 iRPCs. The main difference with the old RPC detectors will be found at the level of the read-out panels. Indeed, the new chambers will not feature read-out strips segmented in η but rather will favor a read-out on both strip ends to determine the position of the hits along the chamber. By using fast front-end electronics a radial spatial resolution of the order of 2 cm could be achieved to contribute to the better reconstruction of muons in the forward region where the bending due to the magnetic field is low. This technical choice is motivated by the fact that, in the case a η segmentation were to be used, at least five pseudo-rapidity partitions would have been necessary to reach the minimal radial spatial resolution (≈ 20 cm). Having only one strip along the chamber read-out from both ends reduces by 60% the total number of channels and the necessary cabling, and allows for a better spatial resolution. The strip pitch will range from 6.0 mm (5.9 mm) on the high pseudo-rapidity end to 12.3 mm (10.9 mm) on the low one on position RE3/1 (RE4/1). The spatial resolution in the direction perpendicular to the strips should reach approximately 3 mm, better than the minimal needed resolution (Figure 3.16). Finally, the overall time resolution of the

new installation will be equally 1 ns, as for the present due to the same link system being used even though the detector itself can achieve a time resolution of less than 100 ps, necessary for a spatial reconstruction of the hits with a resolution of 2 cm or less along the strip length.

Having only a single strip instead of pseudo-rapidity segmentation will increase the probability of double hits in the same channel. The probability was estimated to be low enough as it shouldn't exceed 0.7%. This estimation was made assuming an average hit rate per unit area of 600 Hz/cm^2 in the iRPCs (see Figure 3.23), a cluster size (average number of strips fired per muon) of 2, a strip active area of $158.4 \times 0.87 \text{ cm}^2$ and a safety factor 3. The corresponding rate per strip is estimated to be 380 kHz leading to an average time interval in between two consecutive hits of 2600 ns. This is compared to the minimal time interval of 16 ns necessary to avoid ambiguities. Indeed, a maximum of 10 ns is spent by the signal traveling through the strip to reach the electronics to which can be added 1 ns of dead time and 2 Time-to-Digital Converter (TDC) clock cycles of 2.5 ns to convert the signal arrival time into a digital value in the FEEs. The probability of having ambiguous double hits in a strip is then the ratio between the minimal time interval in between two consecutive hits and the average time interval estimated from the rate the detectors would be subjected to.

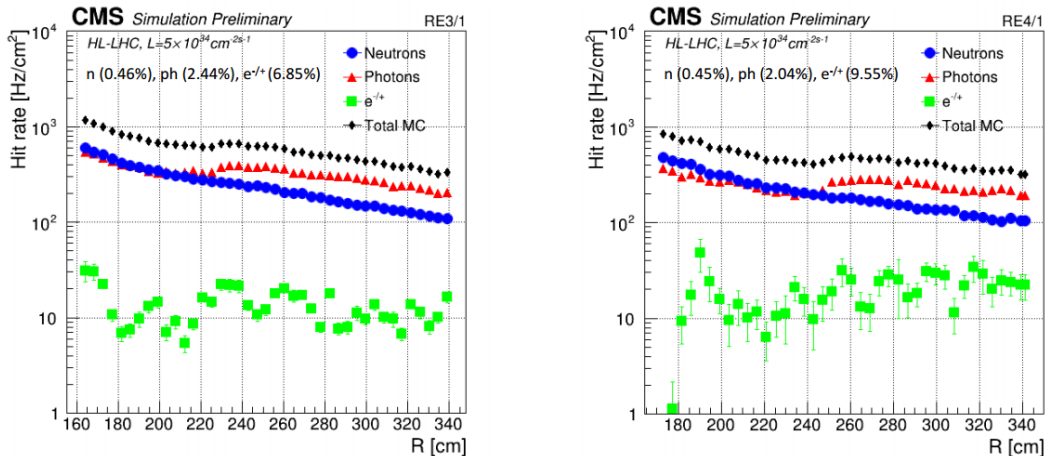


Figure 3.23: Expected hit rate due to neutrons, photons, electrons and positrons at HL-LHC instantaneous luminosity of $5 \times 10^{34} \text{ cm}^{-2}\text{s}^{-1}$ in RE3/1 and RE4/1 chambers [196, 197]. The sensitivities of iRPCs used in the simulation for each particle are reported and differ from one endcap disk to another as the energies of the considered particles varies with the increasing distance from the interaction point.

The instantaneous luminosity at HL-LHC being very high, the rates at the position of the new chambers needed to be simulated in order to understand the necessary requirements for these detectors. The simulated results for different background components (neutrons, photons, electrons and positrons) are shown in Figure 3.23 assuming known sensitivities to these particles. It is shown that on average over the iRPC areas the rates would be of the order of 600 Hz/cm^2 (600 Hz/cm^2 seen in RE3/1 and 480 Hz/cm^2 in RE4/1) [196, 197]. Thus, taking into account a safety factor of about 3, it was decided that improved RPCs should at least be certified for rates reaching 2 Hz/cm^2 which will be achieved thanks to several improvements on the design and on the electronics. The detectors design will be based on the existing RPCs as they will also feature double RPC gaps. Similarly to the existing RPC system, the electrode material will be HPL although the thickness of the electrodes and of the gas gap will be reduced to 1.4 mm as a thinner gas gap leads to a decrease

of deposited charge per avalanche as showed in Figure 3.24. The charge deposition in the case of 1.4 mm thick electrodes is reduced by a factor greater than 5 when compared to 2 mm electrodes at similar electric field. The smaller the gas gap, the more the detector becomes sensitive to gap non-uniformities across the electrode planes, making a gap of 1.4 mm a good compromise in between these two competing factors.

A lower charge deposition inside of the detector volume means a slower ageing and a longer lifetime for detectors subjected to high irradiation. But, in order to take advantage of the lower detector gain, more sensitive electronics are required such that part of the gain that was formerly achieved in the gas volume can be moved to the electronics. Achieving this with the technology developed more than ten years ago for the present system is not possible as the signal over noise ratio of such electronics doesn't allow to detect charges as low as 10 fC. Moreover, the new front-end electronics will need to be radiation hard to survive more than ten years of HL-LHC conditions. The new technology that has been chosen is based on the PETIROC ASIC manufactured by OMEGA and is a 64-channel ASIC called CMS RPCROC[177, 198, 199]. The properties of these electronics will be discussed in Chapter 6.

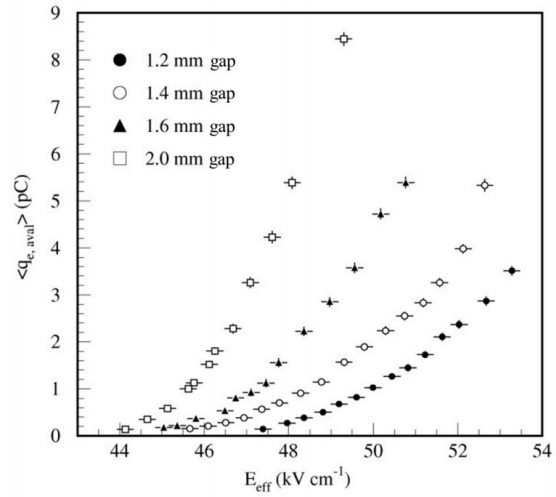


Figure 3.24: Measured average charge per avalanche as a function of the effective electric field for different gas gap thickness in double-gap RPCs using HPL electrodes [177].

The properties of these electronics will be discussed in Chapter 6.

3.5 Impact on Level-1 Trigger and physics performance

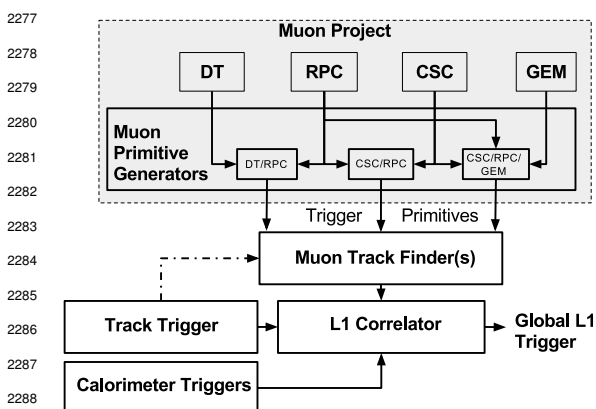


Figure 3.25: Level-1 Trigger data flow during Phase-2 operations [177].

The upgrades of the different subsystems will have a subsequent impact on the Level-1 Trigger. Indeed, although its main scheme will not be affected, the efficiency of the trigger in identifying muons and provide the DAQ with good and fast trigger that can cope with HL-LHC instantaneous luminosity is a major improvement. In addition to the upgrade of the muon system in terms of trigger accept rate and latency, the Level-1 Trigger will get extra information by including the Tracker Trigger into its Muon Track Finder logic and combine the L1 Muon Trigger with Tracker and Calorimeter Triggers to generate a Global L1 Trigger, as shown in Figure 3.25. Using the

track candidates of both the muon system and the tracker in spatial coincidence will allow for a much better momentum resolution thanks to better identified muons and, hence, better measured transverse impulsion as described in reference [177].

In terms of muon trigger, three regions are considered due to their different track finding logic: the Barrel Muon Track Finder (BMTF), the Endcap Muon Track Finder (EMTF) for both the barrel and endcap regions, and finally the Overlap Muon Track Finder (OMTF) which concerns the pseudo-rapidity region in which there is a common coverage by both the barrel and endcap muon systems. This region can be seen in Figure 3.15 for $0.9 < |\eta| < 1.2$ and requires a specific more complex logic to provide an efficient reconstruction of muons due to the different orientation of the detectors and of the more complex magnetic field of this region. The development of a track finder specific to the overlap region was achieved during the Phase-1 upgrade of the L1-Trigger [200].

The upgraded RPC link system, allowing to take profit of the full 1 ns resolution of the detectors, will help reducing the neutron induced background, slightly improve the bunch crossing assignment, and help increasing the trigger efficiency in every sector. The upgrade of DT electronics is also to take into account as the trigger primitive generator will be renewed through the use of TDCs that will send the digitized signals directly to common DT/RPC back-end electronics instead of having an on-detector trigger logic as it will be the case until the end of Phase-1. The combination of RPC hits together with DT primitives will bring extra improvement in the bunch crossing assignment in the barrel and overlap regions and improve the efficiency of the trigger between the wheels were the quality of DT primitives is the poorest.

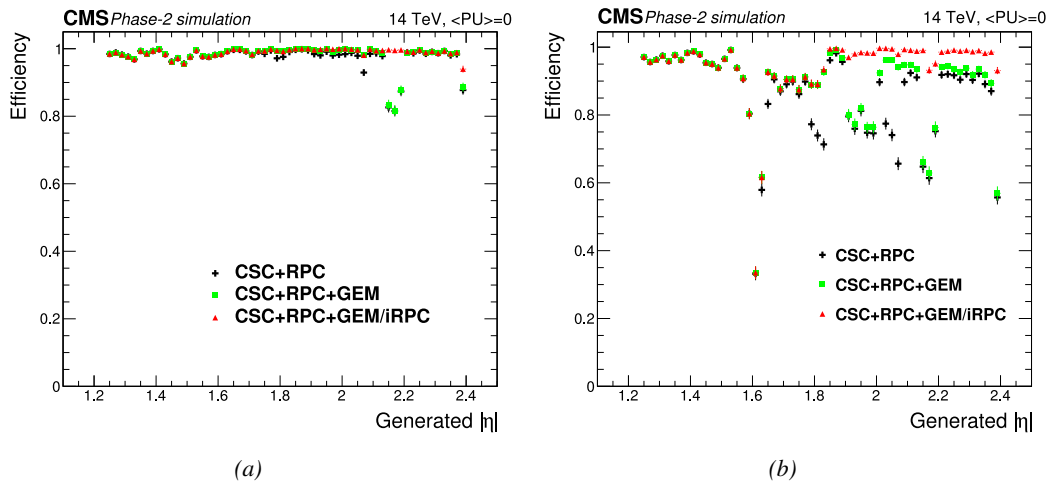


Figure 3.26: Efficiency of the L1 trigger in the endcap region after Phase-2 upgrade in the case CSC/GEM/RPC hits are requested in at least 2 stations out of four (3.26a) and in all four stations (3.26b) [177].

The current EMTF already uses more sophisticated algorithms by combining together RPC hits and CSC primitives. The GEMs, in stations 1 and 2, and the iRPCs, in stations 3 and 4, will be added into the EMTF algorithm. Both these contributions will help increasing the efficiency of the L1 trigger in the endcap region in one hand, as showed by Figure 3.26, and help lowering the L1 trigger rate in the other hand, especially in the most forward region. Similarly to the RPC/CSC algorithms, data from both CSCs and GEMs are combined into the Optical TMBs (OTMBs) to build on each station, GEM/CSC primitives matching space and time information from both subsystems. The

efficiency improvement and rate reduction close to the beam line will be naturally enhanced by the addition of more hits along the muon tracks, as can be seen from Figure 3.27 that focuses especially in the most challenging pseudo-rapidity region. Indeed, the contribution from the GEMs to the lever arm of each track thanks to their high angular resolution will be a great asset in achieving such results, as can be seen in Figure 3.28. The rate will be partly reduced in the forward region thanks to the better spatial resolution of iRPCs, with respect to the current RPC system. The ambiguity brought by multiple local charged tracks in CSCs will be reduced, as explained through Figure 3.29. Indeed, as the rates will increase, the probability to record more than a single local charged track will greatly increase. This is due to the fact that the trigger algorithm uses information from three consecutive bunch crossings to find muon tracks. It is estimated that with iRPCs operated at 95% efficiency the resolution of ambiguous events would be of the order of 99.7%.

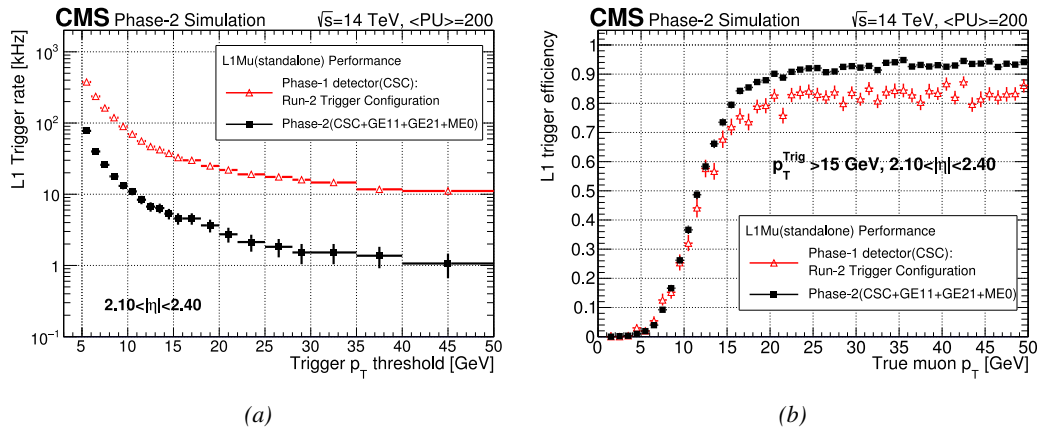


Figure 3.27: Comparison of L1 trigger performances for prompt muons with and without the addition of GEMs in the region $2.1 < |\eta| < 2.4$ at Phase-2 conditions [177]. GEMs would allow a reduction of the trigger accept rate by an order of magnitude (Figure 3.27a) while increasing the trigger efficiency (Figure 3.27b).

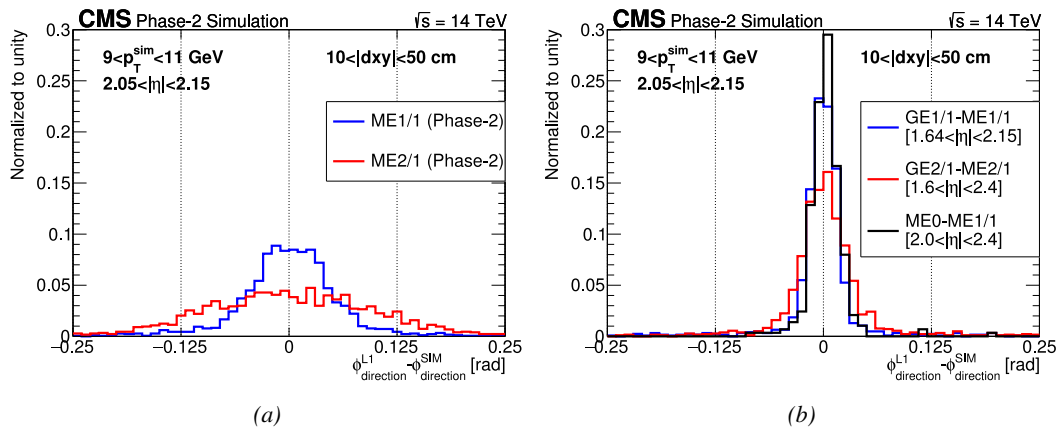


Figure 3.28: The angular resolution on reconstructed muon tracks in the GEM overlap region $2.0 < |\eta| < 2.15$ is compared for Phase-2 conditions in the case CSC are alone (Figure 3.28a) and in the case the GEMs' data, including ME0, is combined to which of CSCs (Figure 3.28b) [177].

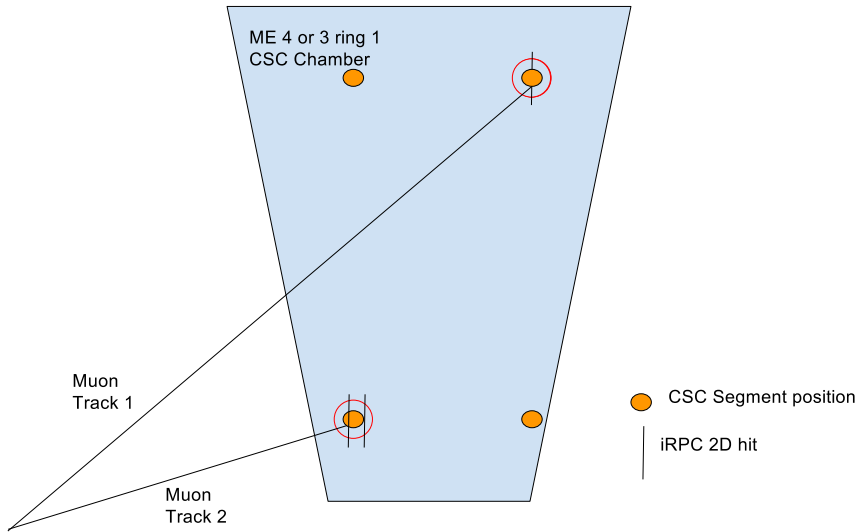


Figure 3.29: Resolution of the LCT ambiguous events thanks to the combination of CSC and iRPC readout data. Using CSCs only, 2 pairs of hits are possible [177].

3.6 Ecofriendly gas studies

The European Commission adopted a new "F-gas regulation" in 2014 [201] with the goal to strongly control and reduce the use of fluorinated gases with high Global Warming Potential (GWP). Using CF_4 , $C_2H_2F_4$ and SF_6 , both CSC and RPC subsystems will need to address this problem by finding new gas mixture for the operation of their detectors. Finding a replacement for these gas component that were used for very specific reasons is a great challenge. Indeed, CSCs use CF_4 in order to enhance the longevity of the detectors, increase the drift velocity of electrons and quench photons with a non-flammable gas mixture. RPCs use a mixture mainly composed of $C_2H_2F_4$, or $R134a$, that features a high effective Townsend coefficient and the great average fast charge allowing for operations with a high threshold. The mixture also contains a small fraction of SF_6 that is used for its electronegative properties that prevents the development of delta-rays in the gas volume that might trigger multiple ionization and avalanches.

	CSC	RPC
Greenhouse gases used	CF_4	$C_2H_2F_4$ and SF_6
Greenhouse gases fraction in the gas mixture	10%	95.2% and 0.3%
Global Warming Potential (relative to CO_2)	6500	1300 and 23900
Gas mixture re-circulation	Yes, 90%	Yes, 85%
Gas mixture replenishing rate (l/hr)	700	1100
F-gas recuperation	Yes, $\approx 40\%$	No
F-gas venting rate (l/hr)	42	1047 and 3.3
CO_2 -equivalent rate (m^3/h)	273	1440
Relative impact (entire muon system = 100%)	16%	84%

Table 3.1: Details of the greenhouse fluorinated gases used in CMS and of their GWP [177].

Nevertheless, all these gases have a very high GWP, as reported in Table 3.1, and only few

options are left. The subsystems need to work on strongly decreasing the loss of these gases due to leaks in the gas system or need to completely change their gas mixture for more ecofriendly ones. Reducing the amount of F-gas released in the atmosphere due to leaks on the current gas system will require installation of a F-gas recuperation system on RPCs side and an upgrade of CSCs existing one in addition to the repair of existing leaks. With such measures, it is expected that the total rate of greenhouses gas vented in the atmosphere would represent only 1.6% of the current levels [177]. In the most critical case the F-gas were to be banned, it would be necessary to have replacement mixtures to operate CMS. CSC is presently investigating replacement for CF_4 such as CF_3I , C_4F_6 , IC_3F_6 , C_3F_8 or CHF_3 . RPCs, in collaboration with the ATLAS RPC group which uses the same gas mixture, have identified CF_3I ($GWP \leq 1$) and $C_3H_2F_4$ ($GWP \sim 6$), referred to as *HFO-1234ze*, as potential candidates with mixtures containing CO_2 . CO_2 is already widely used by various RPC experiments in mixtures with argon. More R&D needs to be conducted for both subsystems before concluding on the best alternative. Finding no good alternative to the present mixtures will require very efficient abatement system in CMS to burn and convert the greenhouse gases into less harmful ones. This way, the air pollution would be strongly reduced.

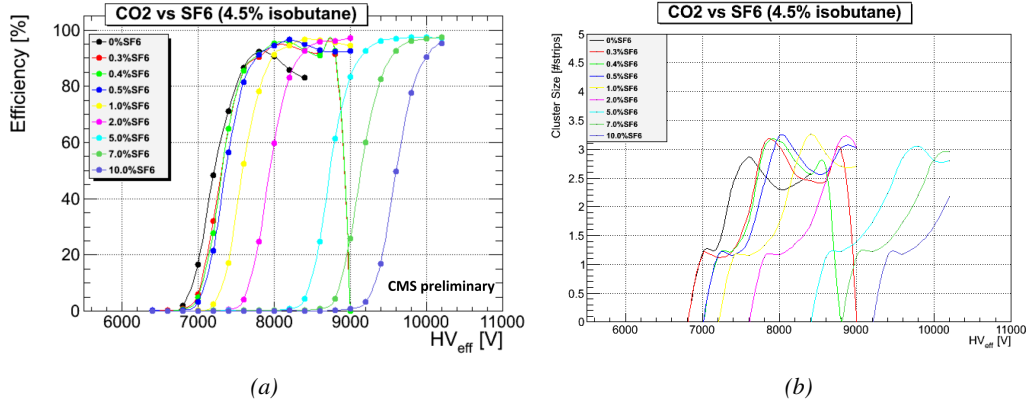


Figure 3.30: Efficiency (Figure 3.30a) and cluster size (Figure 3.30b) of a standard double-gap RPC operated with CO_2 mixtures for different ratios of SF_6 .

Preliminary studies conducted in Ghent confirmed that CO_2 alone would require more than 1% of SF_6 to reach full efficiency, as presented in Figure 3.30. Even though the results obtained in Ghent don't show the streamer probability (probability to have very large avalanches whose induced charge is greater than 20 pC), the variation of the cluster size indicates that the streamers become predominant before the efficiency plateau is reached. Then, a very first test with an *HFO/CO₂* was performed. Only one ratio was tested as can be seen from Figure 3.31 that displays a good efficiency with a plateau located at a similar high voltage than with *R134a* based mixtures

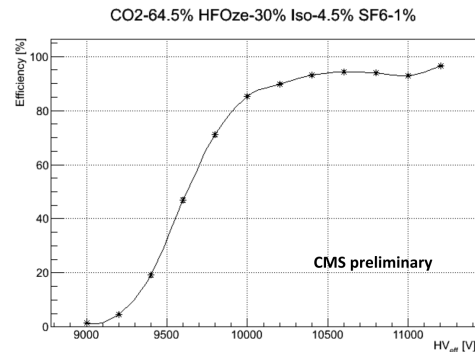


Figure 3.31: Efficiency of a CMS double-gap RPC operated with 30% of *HFO*, 4.5% of iC_4H_{10} , 1% of SF_6 and 64.5% of CO_2 .

(Figure 3.32). The status of RPC studies is presented in Figure 3.32 in which the performance (efficiency and streamer probability) of a CMS double-gap RPC operated with alternative gas mixtures is compared to the present CMS RPC mixture. Although the efficiency of detectors operated with mixtures containing CO_2/CF_3I or CO_2/HFO as a replacement for $C_2H_2F_4$ seems to reach similar levels than which of the detectors operated with the present mixture, the new gas mixtures feature a streamer probability that far exceeds which of the present fluorinated mixture. The SF_6 doesn't seem to prevent the formation of streamers as efficiently even when used at levels more than three times higher than with the standard CMS RPC mixture. Nevertheless, it is important to note that these results were obtained with a single gap RPC while the use of a double gap RPC reduces the operation voltage by 200 to 300 V, lowering the induced charge. A compromise in between good efficiency and acceptable level of streamer probability, and the fine tuned composition of potential replacement gas mixtures will be kept on being studied using a standard double-gap CMS RPC.

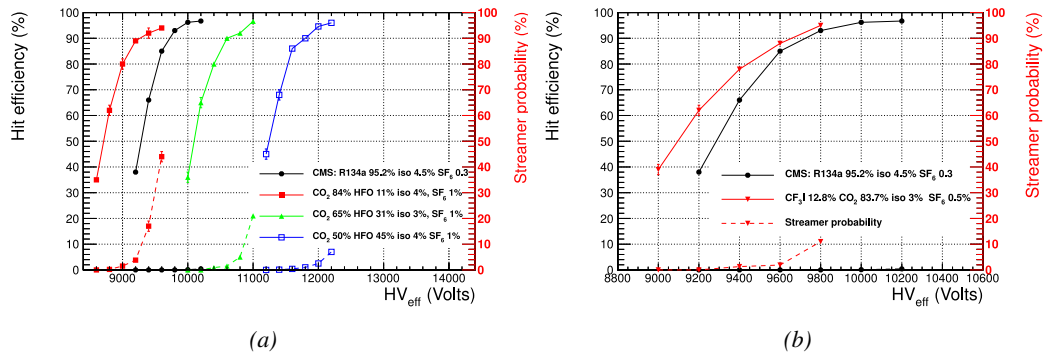


Figure 3.32: The efficiency (solid lines) and streamer probability (dashed lines) of HFO/CO_2 (Figure 3.32a) and CF_3I/CO_2 (Figure 3.32b) based gas mixtures as a function of the effective high-voltage are compared with the present CMS RPC gas mixture represented in black [177]. The detector used for the study is a single gap RPC with similar properties than CMS RPCs. The streamer probability is defined as the proportion of events with a deposited charge greater than 20 pC.

Although the technology certification was conducted with the standard CMS gas mixture which is a known reference, the iRPCs will need to be operated with new environmental-friendly gas mixtures. Studies have then been conducted with iRPCs, assuming that the HFO/CO_2 mixture containing an almost equal level of both components was the most likely candidate to replace the standard mixture. In this purpose, an iRPC prototype has been built to be tested with an HFO/CO_2 gas mixture. The mixture, referred to as "eco-gas" in Figure 3.33, contained 50% of HFO , 4.5% of iC_4H_{10} , 0.3% of SF_6 and 45.2% of CO_2 . In Figure 3.33 is presented a result consistent with the blue curve obtained with 45% of HFO , 4% of iC_4H_{10} , 1% of SF_6 and 50%

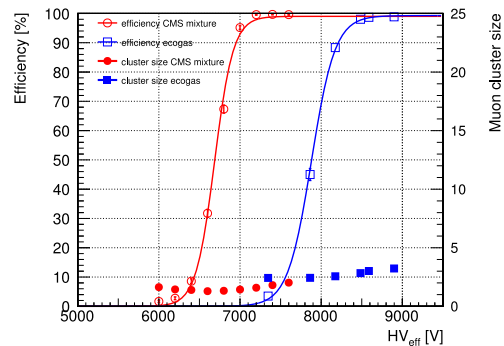


Figure 3.33: Efficiency (open symbols) and cluster size (full symbols) of an iRPC as a function of the effective voltage for the standard CMS gas mixture and an environmental-friendly gas mixture. [177].

²⁴⁰² of CO_2 flushed into a standard double-gap RPC. Instead of the streamer probability, the cluster size
²⁴⁰³ is shown. The average number of hits generated by a muon passing through the chamber seem to
²⁴⁰⁴ have increased by 1 at the level of the knee of the sigmoid plateau using the ecogas.

4

2405

2406

Physics of Resistive plate chambers

2407 A Resistive Plate Chamber (RPC) is a gaseous detector used in high-energy physics experiments
2408 as described in Chapter 3. It has been developed in 1981 by Santonico and Cardarelli [202], under
2409 the name of *Resistive Plate Counter*, as an alternative to the local-discharge spark counters pro-
2410 posed in 1978 by Pestov and Fedotovich [203, 204]. Working with spark chambers implied using
2411 high-pressure gas and high mechanical precision which the RPC simplified by formerly using a gas
2412 mixture of argon and butane flowed at atmospheric pressure and a constant and uniform electric
2413 field propagated in between two parallel electrode plates. Moreover, a significant increase in rate
2414 capability was introduced by the use of electrode plate material with high bulk resistivity, preventing
2415 the discharge from growing throughout the whole gas gap. Indeed, the effect of using resistive elec-
2416 trodes is that the constant electric field is locally canceled out by the development of the discharge,
2417 limiting its growth.

2418 Through its development history, different operating modes [205–207], gas mixtures [202, 207–
2419 212] and new detector designs [213–215] have been discovered, leading to further improvement of
2420 the rate capability of such a detector. The low developing costs and easily achievable large detection
2421 areas offered by RPCs, as well as the wide range of possible designs, made them a natural choice
2422 to as muon chambers and/or trigger detectors in multipurpose experiments such as CMS [192] or
2423 ATLAS [216], time-of-flight detectors in ALICE [217], calorimeter with CALICE [218] or even
2424 detectors for volcanic muography with ToMuVol [219].

2425 4.1 Principle

2426 RPCs are ionisation detectors composed of two parallel resistive plate electrodes in between which
2427 a constant electric field is set. The space in between the electrodes, referred to as *gap*, is filled with
2428 a dense gas that is used to generate primary ionization into the gas volume. The free charge carriers
2429 (electrons and cations) created by the ionization of the gas molecules are then accelerated towards the
2430 electrodes by the electric field, as shown in Figure 4.1 [220]. RPCs being passive detectors, a current
2431 on pick-up copper read-out placed outside of the gas volume is induced by the charge accumulation

2432 during the growth of the avalanche resulting from the acceleration of the charge carriers. As a
 2433 consequence, the time resolution of the detector is substantially increased as the output signal is
 2434 generated while the electrons are still in movement. The advantage of a constant electric field, over
 2435 multi-wire proportional chambers, is that the electrons are being fully accelerated from the moment
 2436 charge carriers are freed and feel the full strength of the electric field that doesn't depend on the
 2437 distance to the readout and that the output signal doesn't need for the electrons to be physically
 2438 collected.

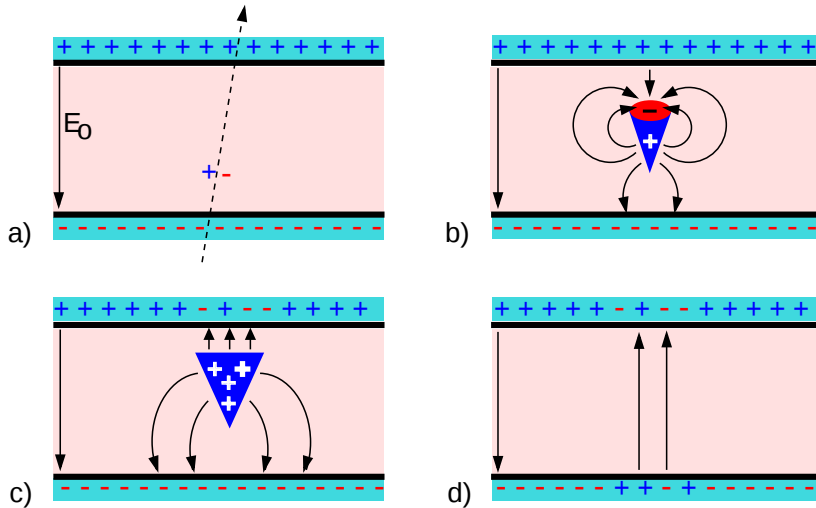


Figure 4.1: Different phases of the avalanche development in the RPC gas volume subjected to a constant electric field E_0 . a) An avalanche is initiated by the primary ionisation caused by the passage of a charged particle through the gas volume. b) Due to its growing size, the avalanche starts to locally influence the electric field. c) The electrons, lighter than the cations reach the anode first. d) The ions reach the cathode. While the charges have not recombined, the electric field in the small region around the avalanche stays affected and locally blinds the detector.

2439 After an avalanche developed in the gas, a time long compared to the development of a discharge
 2440 is needed to recombine the charge carriers in the electrode material due to their resistivity. This
 2441 property has the advantage of affecting the local electric field and avoiding sparks in the detector
 2442 but, on the other hand, the rate capability is intrinsically limited by the time constant τ_{RPC} of the
 2443 detector. Using a quasi-static approximation of Maxwell's equations for weakly conducting media,
 2444 it can be shown that the time constant τ_{RPC} necessary to the charge recombination at the interface
 2445 in between the electrode and the gas volume is given by the Formula 4.1 [221].

$$(4.1) \quad \tau_{RPC} = \frac{\epsilon_{electrode} + \epsilon_{gas}}{\sigma_{electrode} + \sigma_{gas}}$$

2446 A gas can be assimilated to vacuum, leading to $\epsilon_{gas} = \epsilon_0$ and $\sigma_{gas} = 0$, and the electrodes
 2447 permittivity and conductivity can be written as $\epsilon_{electrode} = \epsilon_r \epsilon_0$ and $\sigma_{electrode} = 1/\rho_{electrode}$,
 2448 showing the strong dependence of the time constant to the electrodes resistivity in Formula 4.2.

$$(4.2) \quad \tau_{RPC} = (\epsilon_r + 1)\epsilon_0 \times \rho_{electrode}$$

Very few materials with a low enough resistivity exist in nature. The resistivity targeted to build RPCs ranges from 10^9 to $10^{12} \Omega \cdot \text{cm}$. The most common RPC electrode materials are displayed in Table 4.1. When the doped glass and ceramics can offer short time constants of the order of 1 ms, the developing cost of such materials is quite high due to the very low demand. Thus, High-pressure laminate (HPL) is often the choice for high rate experiments using very large RPC detection areas. Other experiments working at cosmic muon fluxes can safely operate with ordinary float glass.

Material	$\rho_{\text{electrode}} (\Omega \cdot \text{cm})$	ϵ_r	$\tau_{\text{RPC}} (\text{ms})$
Float glass	10^{12}	~ 7	~ 700
High-pressure laminate	10^{10} to 10^{12}	~ 6	~ 6 to 600
Doped glass (LR S)	10^9 to 10^{11}	~ 10	~ 1 to 100
Doped ceramics (SiN/SiC)	10^9	~ 8.5	~ 1
Doped ceramics (Ferrite)	10^8 to 10^{12}	~ 20	~ 0.2 to 2000

Table 4.1: Properties of the most used electrode materials for RPCs.

4.2 Rate capability and time resolution of Resistive Plate Chambers

The electrode material plays a key role in the maximum intrinsic rate capability of RPCs. R&D is continuously being done to develop at always cheaper costs material with lower resistivity. Nevertheless, the amount of charge released, i.e. the size of the discharge, if reduced leads to a smaller blind area in the detector, increasing the rate capability of the detector. On the other hand, the drift velocity of electrons in the gas volume being quite stable with the applied electric field, the design of a detector and the associated read-out and pulse-processing electronics will be a major component of the time resolution of RPCs. Moreover, the sensitivity of the electronics will also help increasing the rate capability by lowering the gain the gas volume needs to be operated at, increasingly lowering the gas volume in which the signals will develop.

4.2.1 Operation modes

Being a gaseous detector using an accelerating electric field to amplify the signal of primary charge carriers, the RPC can be operated into different modes as the electric field intensity varies. Each mode offers different performances for such a detector, and it will be showed that the operating mode corresponding to the lowest electric field possible is best suited for high rate detectors working in collider experiments.

RPCs where developed early 1980s. At that time it was using an operating mode now referred to as *streamer mode*. Streamers are large discharges that develop in between the 2 electrodes enough to locally discharge the electrodes. If the electric field inside of the gas volume is strong enough, with electrons being fast compared to ions, a large and dense cloud of positive ions will develop nearby the anode and extend toward the cathode while the electrons are being collected, eventually leading to a streamer discharge due to the increase of field seen at the cathode. The field is then strong enough so that electrons are pulled out of the cathode. Electrodes, though they are a unique volume of resistive material, can be assimilated to capacitors. At the moment an electric field is applied in between their outer surfaces, the charge carriers inside of the volume will start moving leading to a situation where there is no voltage across the electrodes and a higher density of negative charges,

i.e. electrons, on the inner surface of the cathode. Finally, when a streamer discharge occurs, these electrons are partially released in the gas volume contributing to increase the discharge strength until the formation of a conductive plasma, the streamer. This can be understood through Figure 4.2 [205]. Streamer signals are very convenient in terms of read-out as no further amplification is required with output pulses amplitudes of the order of a few tens to few hundreds of mV as can be seen on Figure 4.3.

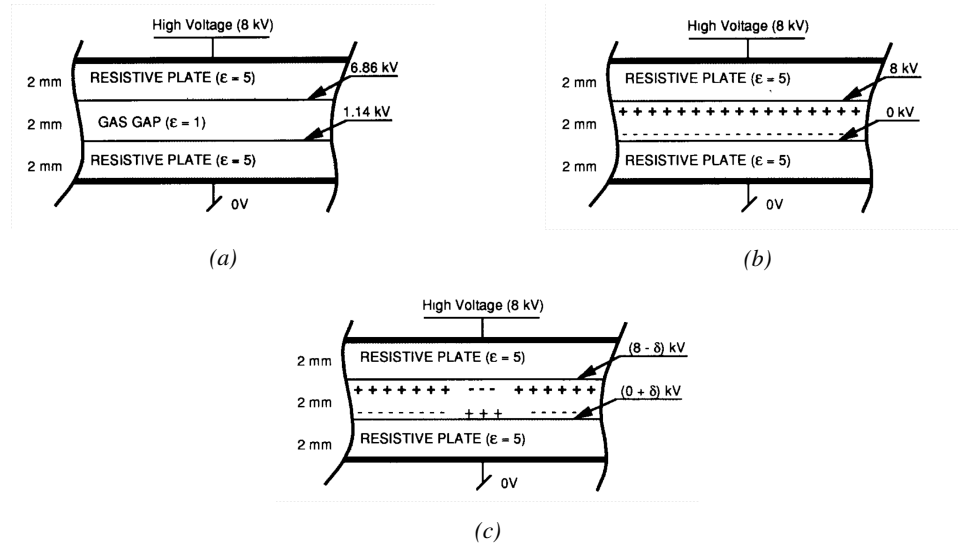


Figure 4.2: Movement of the charge carriers in an RPC. Figure 4.2a: Voltage across an RPC whose electrode have a relative permittivity of 5 at the moment the tension is applied. Figure 4.2b: After the charge carriers moved, the electrodes are charged and there is no voltage drop over the electrodes anymore. The full potential is applied on the gas gap only. Figure 4.2c: The streamer discharge initiated by a charged particle transports electrons and cations towards the anode and cathode respectively.

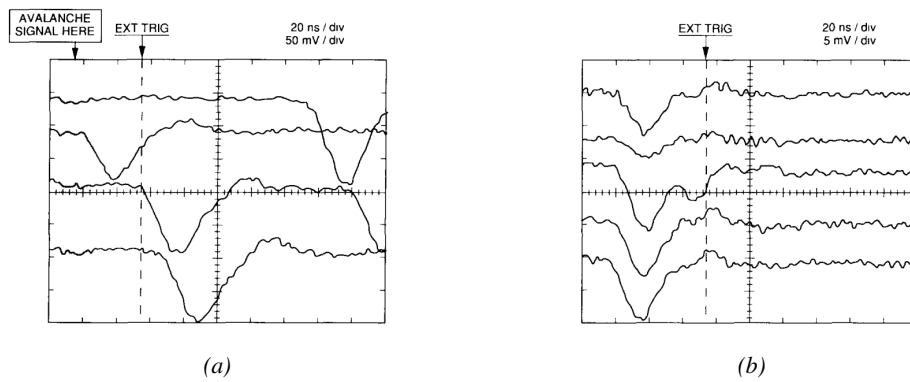


Figure 4.3: Typical oscilloscope pulses in streamer mode (Figure 4.3a) and avalanche mode (Figure 4.3b). In the case of streamer mode, the very small avalanche signal is visible.

When the electric field is reduced though, the electronic gain is small until the electrons get close enough to the anode and the positive ion cloud is much smaller. The electric field cannot rise to the

point a field emission of electrons on the cathode is possible. The resulting signal is weak, of the order of a few mv as shown on Figure 4.3, and requires amplification. This is the *avalanche mode* of RPC operation. This mode offers a higher rate capability by providing smaller discharges that don't affect the electrodes charge and are more locally contained in the gas volume as was demonstrated by Crotty with Figure 4.4 [205]. The detector only stays locally blind the time the charge carriers are recombined and there is no need for electrode recharge which is a long process affecting a large portion of the detector. Another advantage of avalanche signals over streamer is the great time consistency. Figure 4.3 shows very clearly that avalanche signals have a very small time jitter. Thus, using such a mode is a natural choice for experiments in which the detectors are required to have a high detection rate.

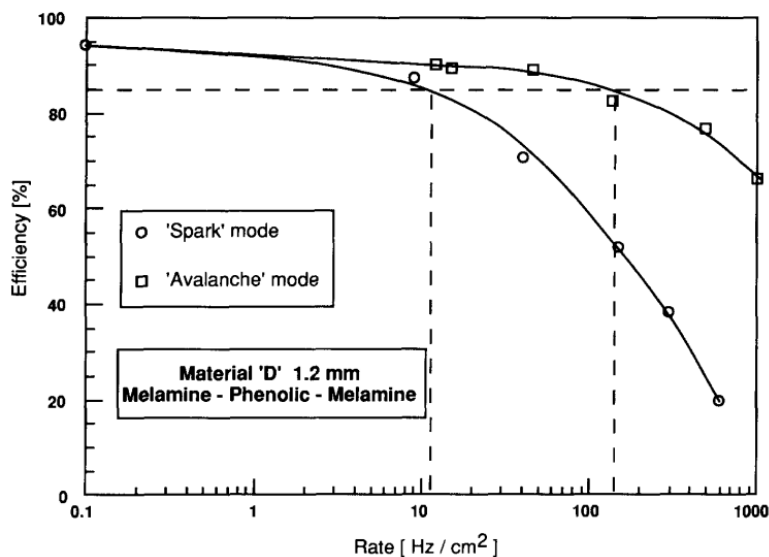


Figure 4.4: Rate capability comparison for the streamer and avalanche mode of operation. An order of magnitude in rate capability for a maximal efficiency drop of 10% is gained by using the avalanche mode over the streamer mode.

4.2.2 Standard gas mixture for RPCs operated in collider experiments

The first RPC working in streamer mode was operated with a 50/50 mixture of argon and butane [202], a standard mixture used at that time in multi-wire proportional chambers, taking profit of the good effective Townsend coefficient of argon to maximize the number of primary charge carriers freed in the gas by ionizing particles and of the quenching properties of butane. Before the discovery of the avalanche mode of RPC operation and concerned about the rate capability of RPCs operated in streamer mode, the performance improvement of the detectors through the increase of fast charge ratio in the signal development ,decreasing the charge induced per avalanche as can be seen through Figure 4.5, was studied by adding Freon based gases, such as CF_3Br , into the typical Ar/C_4H_{10} gas mixture was studied and showed that a lower induced charge could lead to an improvement the rate capability [208]. This consideration lead to the discovery of the avalanche mode which confirmed that the smaller the induced charge, the better the rate capability of the RPCs [205]. This discovery could happen thanks to the increased number of lower induced charge events allowed by adding a

2513 fraction of strong quencher in the gas mixture.

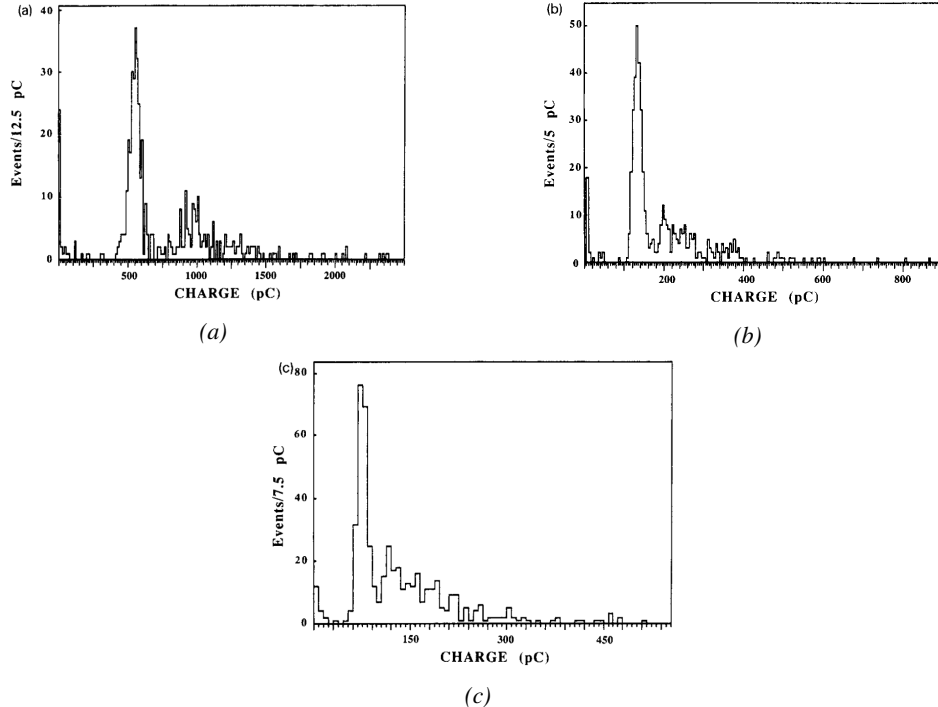


Figure 4.5: Comparison of the charge distribution of signals induced by cosmic muons in an RPC operated with a gas mixture of argon, butane and bromotrifluoromethane (CF₃Br). The Ar/C₄H₁₀ is kept constant at 60/40 in volume while the total amount of CF₃Br in the mixture is varied: 0% (Figure 4.5a), 4% (Figure 4.5b) and 8% (Figure 4.5c) [208].

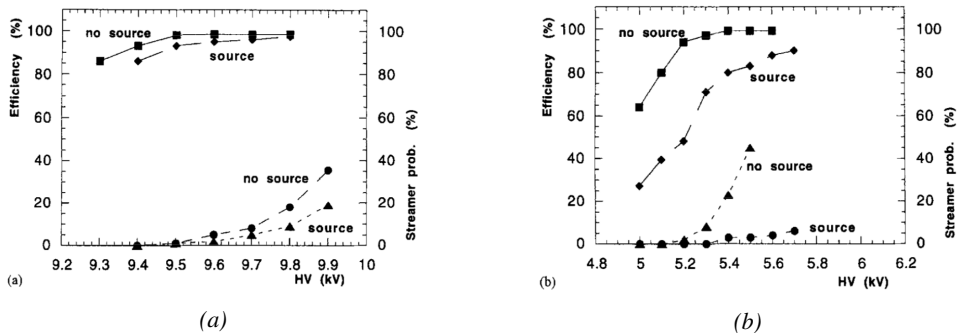


Figure 4.6: Comparison of the efficiency and streamer probability, defined as the fraction of events with an induced charge 10 times larger than that of the average avalanche, with and without irradiation by a 24 GBq ¹³⁷Cs source of an RPC successively operated with a 90/10 mixture C₂H₂F₄/i-C₄H₁₀ (Figure 4.6a) and a 70/5/10/15 mixture of Ar/i-C₄H₁₀/CO₂/C₂H₂F₄ (Figure 4.6b) [209].

2514 From this moment onward, more and more studies were conducted in order to find a gas mixture
2515 that would allow for the best suppression of streamers for the benefit of low charge avalanches. Most

R&D groups working with narrow gaps started using freon-based gas mixtures while users of wide gap RPCs kept using Ar/CO_2 based mixtures. The differences in between narrow and wide gaps will be later discussed in Section 4.2.3. The CF_3Br having a high GWP, tetrafluoroethane ($C_2H_2F_4$) was preferred to it as more suitable ecofriendly gas in the middle of the 90s. An advantage of this new freon component is that it featured a high primary ionization and a low operating voltage, as reported by Cardarelli [207]. Thus, the new gas mixtures used were mainly composed of tetrafluoroethane alone with lower content of isobutane in order to reduce the flammability of the mixtures in the case it were to be used in accelerator experiments for safety reasons. Performance and models about such mixtures were discussed in papers of Abbrescia [209, 210] and showed a better suitability of such a gas mixture, with respect to argon based ones, for operations with high radiation backgrounds leading to a need for high rate capability of the detectors, as can be seen from Figures 4.6 and 4.7. Indeed, although the operating voltage of a tetrafluoroethane based mixture is higher than which of an argon based mixture but the efficiency under irradiation is more stable, the voltage range with negligible streamer probability is much wider, and the fast charge ratio available is much greater, providing with more stable operation of the detector.

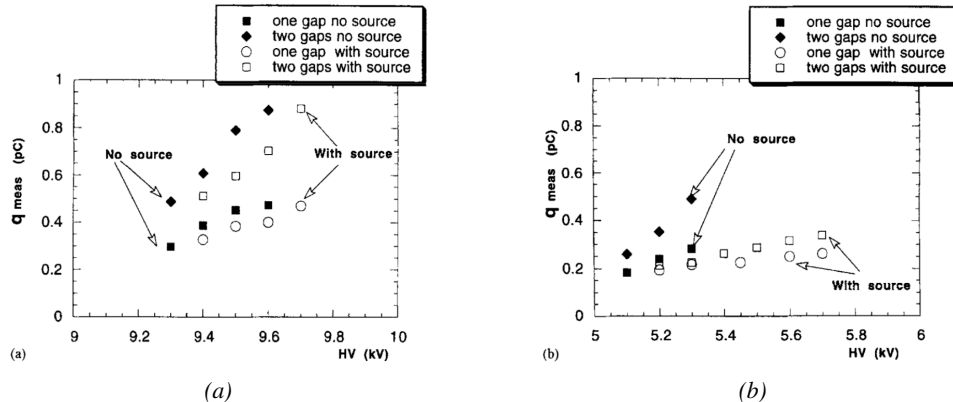


Figure 4.7: Comparison of the fast charge ratio with and without irradiation by a 24 GBq ^{137}Cs source of an RPC successively operated with a 90/10 mixture $C_2H_2F_4/i-C_4H_{10}$ (Figure 4.7a) and a 70/5/10/15 mixture of $Ar/i-C_4H_{10}/CO_2/C_2H_2F_4$ (Figure 4.7b). The results are provided for both single gap and double gap operation [209].

Aside of the improvement of the rate capability through linseed oil surface treatment of HPL electrodes, which allowed for a lower intrinsic noise rate and dark current of the detectors by improving the smoothness of the electrodes surface [222], it was later found that the streamers could be further suppressed by adding an electronegative compound into the gas mixture. The benefits of adding SF_6 in order to push the transitions from avalanche to streamers towards high voltages has been discussed in 1998 [211, 212] and eventually the high rate RPC destined to be used in accelerator physics would unanimously start using this compound into RPC gas mixtures. Being able to control the creation of streamers allows for slower ageing of the detector and lower power consumption as the currents driven by the electrodes consecutively to the induced charges would be smaller. In summary, the typical gas mixture RPCs are operated with is generally composed of the following 3 gas compounds, although, as mentioned in Chapter 3.6, research is being conducted into new more ecofriendly gas mixture using gases with a much lower Global Warming Potential:

- Tetrafluoroethane ($C_2F_4H_2$), also referred to as *Freon* or *R134a*, is the principal compound

of the RPC gas mixtures, with a typical fraction above 90%. It is used for its high effective Townsend coefficient and the great average fast charge that allows to operate the detector with a high threshold with respect to argon, for example, that has similar effective Townsend coefficient but suffers from a lower fast charge. To operate with similar conditions, argon would require a higher electric field leading to a higher fraction of streamers, thus limiting the rate capability of the detector [209, 210].

- Isobutane ($i\text{-C}_4\text{H}_{10}$), only present in a few percent in the gas mixtures, is used for its UV quenching properties [223] helping to prevent streamers due to UV photon emission during the avalanche growth.
- Sulfur hexafluoride, (SF_6), simply referred to as SF_6 , is used in very little quantities for its high electronegativity. Excess of electrons are being absorbed by the compound and streamers are suppressed [211, 212]. Nevertheless, a fraction of SF_6 higher than 1% will not bring any extra benefice in terms of streamer cancelation power but will lead to higher operating voltage [211], as can be understood through Figure 4.8.

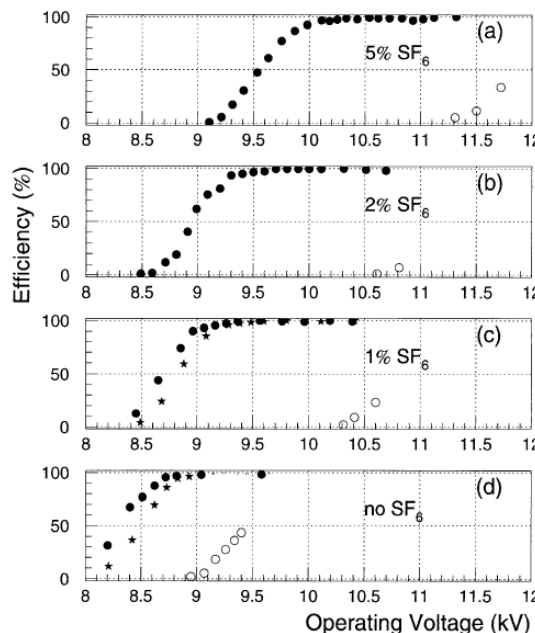


Figure 4.8: Efficiency (circles and stars with 30 mV and 100 mV thresholds respectively) and streamer probability (open circles) as function of the operating voltage of a 2 mm single gap HPL RPC flushed with a gas mixture containing (a) 5%, (b) 2%, (c) 1% and (d) no SF_6 [211].

In the last steps of R&D, the gas mixture of CMS RPCs was foreseen to be a 96.2/3.5/0.3 composition of $C_2H_2F_4/i\text{-C}_4\text{H}_{10}/SF_6$ [224] but finally it was slightly changed into a 95.2/4.5/0.3 mixture of the same gases [225]. A summary of the operation performance of the RPCs since the start of LHC and of CMS data taking is given in Figure 4.9 [226]. The performance of the detectors is regularly monitored and the operating voltages updated in order to obtain a very stable performance through time. Nevertheless, the detectors will face new challenges during Phase-II during which they

will exposed to more extreme radiation conditions. Description of the longevity tests with extreme irradiation and the conclusions regarding the operation of the present RPC system will be given in Chapter 5.

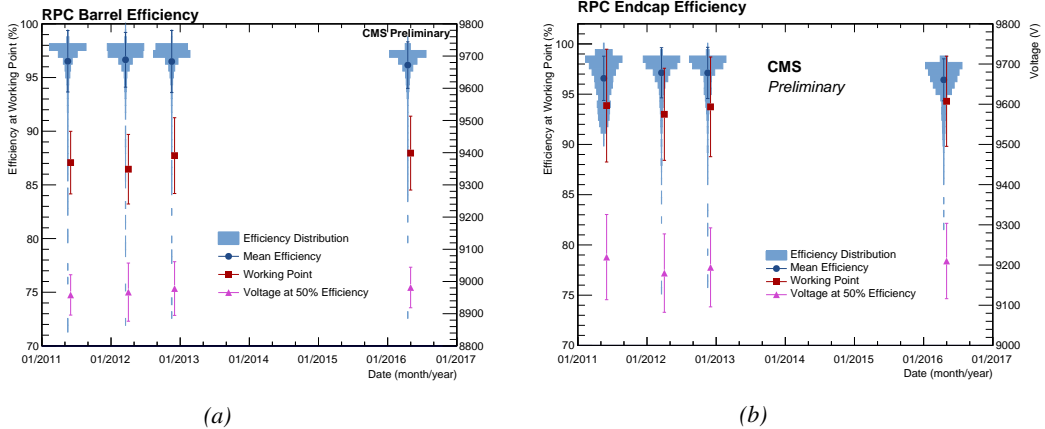


Figure 4.9: Evolution of the efficiency, working voltage, and voltage at 50% of maximum efficiency for CMS Barrel (Figure 4.9a) and Endcap (Figure 4.9b) RPCs obtained through yearly voltage scans since 2011. The working voltage of each RPC is updated after each voltage scan to ensure optimal operation [226].

It was already discussed that in the future, it is likely that the use of freon gases could be banned. As potential replacement for tetrafluoroethane was proposed the trifluoriodomethane (CF_3I), a molecule with similar properties than CF_3Br which was replaced by the tetrafluoroethane, and the 1,3,3,3-tetrafluoropropene ($C_3H_2F_4$ or HFO-1234re), a molecule with similar properties than the actual tetrafluoroethane and proposed as a replacement in refrigerating and air conditioning systems [227]. These 2 gases have stronger quenching properties than $C_2H_2F_4$ which means a much stronger electric field needs to be applied on the parallel electrodes of the RPCs in order to reach full efficiency. But the power supply system of CMS RPC is limited to 15 kV and so is ATLAS power supply system which is participating in a joined R&D. As can be seen from Figure 3.32, reducing the working voltage was achieved by mixing the potential replacements together with CO_2 . Introducing carbon dioxide into the mixture while keeping similar levels of isobutane and SF_6 increases the streamer probability and the best candidate identified for a compromise in between low enough working voltage and acceptable levels of streamers corresponds to a mixture containing 50% of CO_2 , 45% of HFO, 4% of isobutane and 1% of SF_6 but is not yet considered satisfactory. On the other hand, no good replacement for SF_6 has yet been identified. With its very high Global Warming Potential (23900), even small fraction of this gas in the mixture (it only represents 0.3% of CMS standard mixture but more than 5% of its overall GWP) substantially increase the danger for the environment. Although finding a replacement for this gas is less critical than for the tetrafluoroethane composing more than 90% of usual RPC standard mixtures, the problem will need to be addressed.

4.2.3 Detector designs and performance

Different RPC design have been used and each of them present its own advantages. Historically, the first type of RPC to have been developed is what is now referred to as *narrow gap* RPC [202, 228].

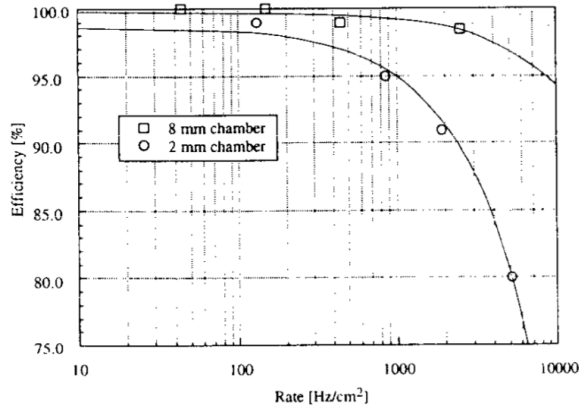


Figure 4.10: Comparison of the rate capability of 8 mm and 2 mm wide RPCs. The lines are linear fits on the data [228].

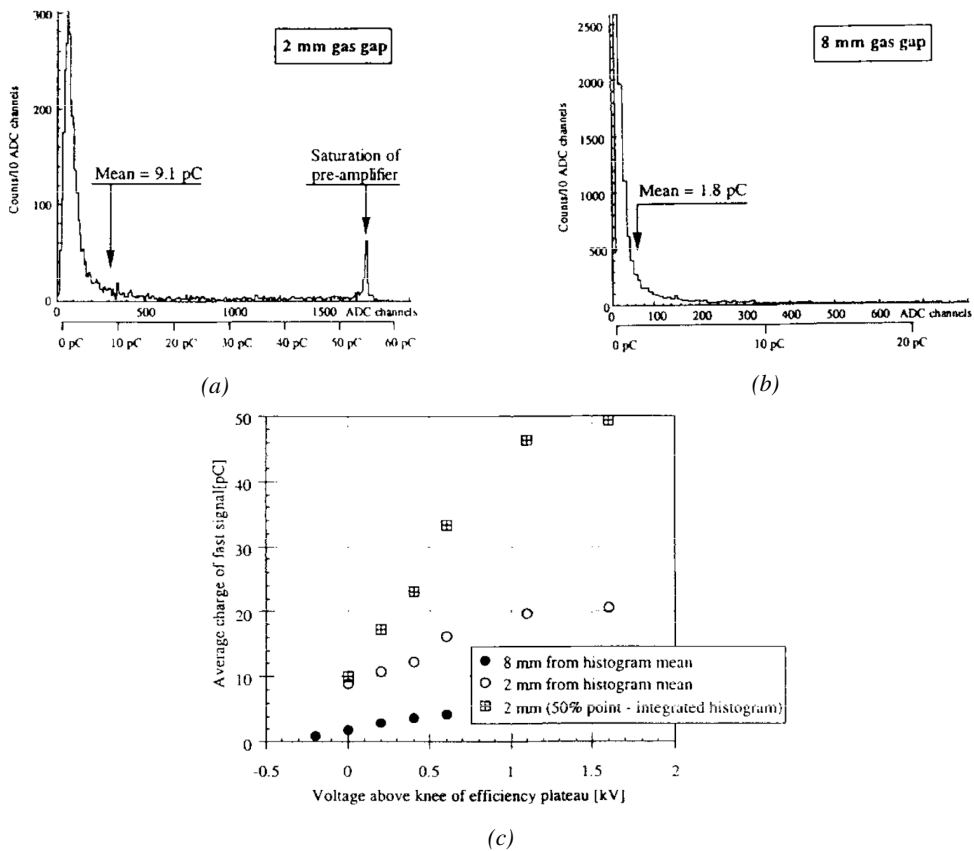


Figure 4.11: Distributions of the induced charge of fast signals on 2 mm (Figure 4.11a) and 8 mm (Figure 4.11b) RPCs exposed to a radiation rate of 100 Hz/cm^2 . Average induced charge of fast signals as a function of the high voltage applied on 2 mm and 8 mm RPCs (Figure 4.11c). In the case of the 2 mm RPC, a saturation of the pre-amplifier was observed. The average of the distribution is underestimated and the median is showed together with the average to account for this bias [228].

After the avalanche mode has been discovered [205], it has been showed that increasing the width of the gas gap lead to higher rate capability, due to lower charge deposition per avalanche, and lower power dissipation [228], as is showed in Figures 4.10 and 4.11. The distance in between the electrode being greater, a weaker electric field can be applied and a lower gain used as a longer gas volume will contribute to the signal induction on the read-out circuit. Nevertheless, by increasing the gas gap width, the time resolution of the detector decreases. This is a natural result if the increase of active gas volume in the detector is taken into account. Indeed, for a given detection threshold on the induced charge per signal, only the small fraction of gas closest to the cathode will provide enough gain to have a detectable signal. In the case of a wider gas volume, the active region is then larger and a larger time jitter is introduced with the variation of starting position of the avalanche, as discussed in [213] and showed in Figure 4.12.

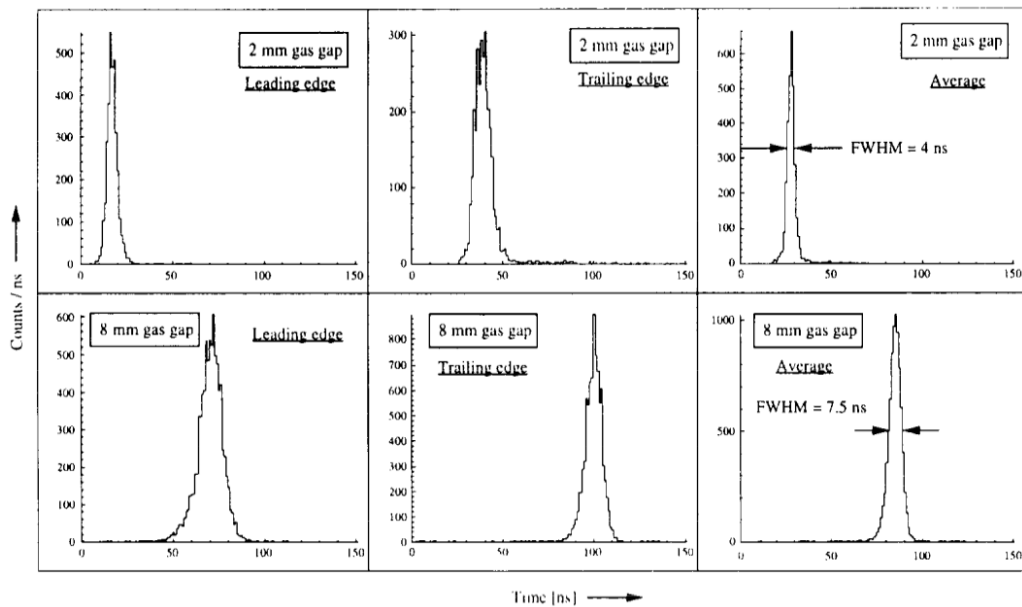


Figure 4.12: Time distributions of the leading, trailing, and average of both leading and trailing edges for 2 mm (top row) and 8 mm (bottom row) RPCs exposed to a 100 Hz/cm² radiation rate. The data was collected with RPCs operated at the voltage corresponding to the knee of the efficiency distribution, defined as the point where 95% of the maximum efficiency is obtained [228].

To improve both the time resolution and the rate capability, different methods were used trying to take advantage of both narrow and wide gap RPCs into a single design. Thus, double gap RPCs, combining two narrow gaps into a single detector to increase the effective sensitive volume, and multigap RPCs, which divided the large volume of a wide gap RPC into thinner sub-gaps by adding intermediate electrodes in between the cathode and anode to improve the time resolution by mimicking narrow gap RPCs, were developed starting from the middle of the 90s.

4.2.3.1 Double gap RPC

Made out of 2 narrow RPC detectors stacked on top of each other as shown in Figure 4.13, this detector layout, popularized by the two multipurpose experiments CMS [192] and ATLAS [216] at LHC, can be used as an OR system in which each individual chamber participates in the output signal

and increases the overall sensitive volume of the detector apparatus. Keeping the copper strip read-out system at the ground, CMS and ATLAS, due to different goals, have chosen different designs as CMS RPCs possess a 1D read-out while ATLAS RPCs offer a 2D read-out. The difference comes from placing the read-out in between the gaps, the anodes facing each other, or to have both RPC gaps in between 2 layers of read-out panels, one along the X-axis and one along the Y-axis, the cathodes facing each other.

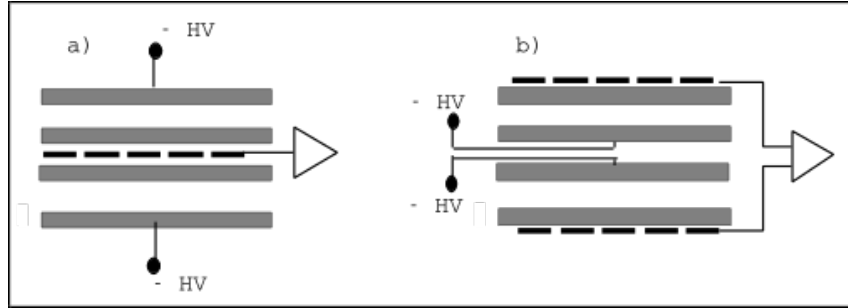


Figure 4.13: Possible double-gap RPC layouts: a) "standard" 1D double-gap RPC, as used in CMS experiment, where the anodes are facing each other and a 1D read-out plane is sandwiched in between them, b) double read-out double-gap RPC as used in ATLAS experiment, where the cathodes are facing each other and 2 read-out planes are used on the outer surfaces. This last layout can offer the possibility to use a 2D reconstruction by using orthogonal read-out planes.

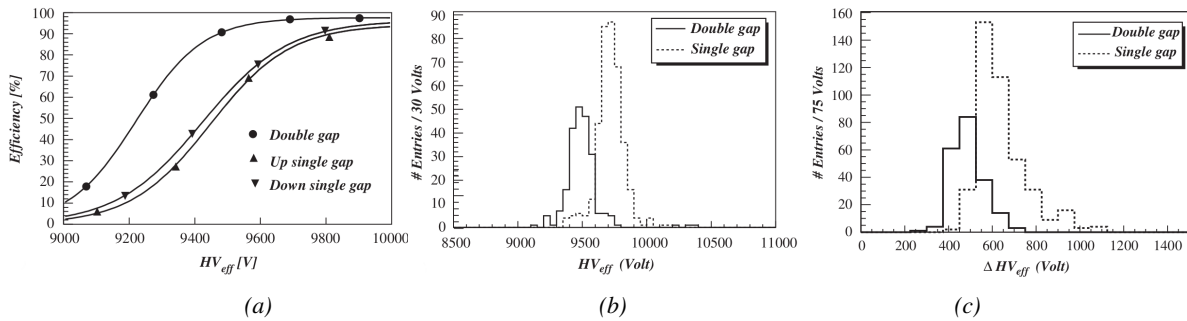


Figure 4.14: Comparison of performance of CMS double and single gap RPCs using cosmic muons [224]. Figure 4.14a: Comparison of efficiency sigmoids. Figure 4.14b: Voltage distribution at 95% of maximum efficiency. Figure 4.14c: $\Delta_{10\%}$ distribution.

The gain of such a detector is reduced by a factor 2 with respect to single-gap RPCs with an efficiency plateau reached at lower voltage, as visible on Figure 4.14, due to the two gas gaps contributing to the signal formation and offering a dynamic range closer to that of a wide gap RPC. A double gap is then fully efficient while the individual RPC gaps composing it are only 70 to 80% efficient. Naturally, by operating the double gap at a lower voltage, the rate capability is found to be increased as the induced charge per gap is then lower than in the case of a single gap detector also leading to a reduction of the streamer probability and a better extraction of the fast charge of the total signal as could be seen through previously presented Figure 4.7.

2625 **4.2.3.2 Multigap RPC (MRPC)**

2626 MRPCs are layouts in which floating sub electrode plates are placed into a wide gap RPC to divide
 2627 the gas volume and create a sum of narrow gaps [213, 214]. Similarly to the double gap RPC for
 2628 which the gain could be reduced by increasing the dynamic range, the multigap reduces the gain
 2629 while keeping a total dynamic range similar to which of a wide gap RPC by reducing the size of
 2630 each individual sub-gap composing the detector. The dynamic range, associated to the sensitive
 2631 volume, and the comparison of each detector layout to the wide gap RPC is showed in Figure 4.15.

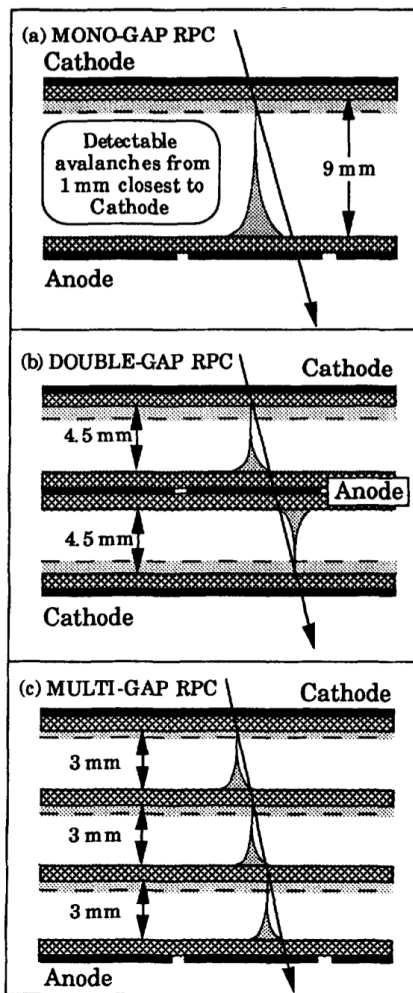


Figure 4.15: Representation of different RPC layouts (wide gap on Figure (a), double gap on Figure (b) and multigap on Figure (c)), of the corresponding sensitive volume in gray, and of the associated avalanche size [214].

2632 By operating the detector with thinner gaps, the time resolution is improved. Comparatively to
 2633 the time resolution presented in Figure 4.12 for the wide gap RPC of 8 mm, a complementary study
 2634 was conducted on multigaps using two 4 mm and four 2 mm subgaps and showed, via Figure 4.16,
 2635 an improvement of the time resolution with the reduction of the gap width and of the number of gaps

while the same sensitive volume was kept [214].

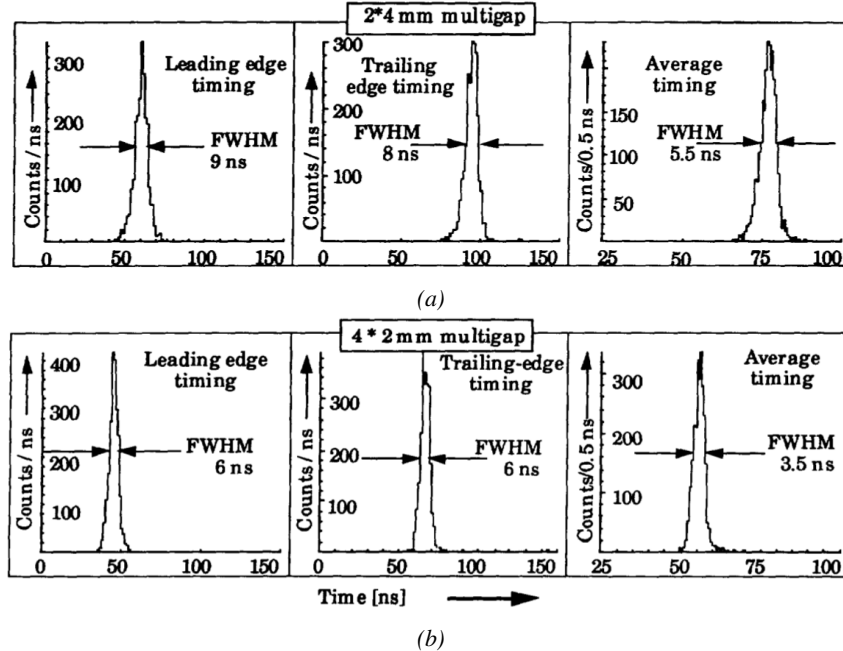


Figure 4.16: Time distributions of the leading, trailing, and average of both leading and trailing edges for multigap RPCs consisting in two 4 mm (Figure 4.16a) and four 2 mm (Figure 4.16b) exposed to a 100 Hz/cm^2 radiation rate. The data was collected with RPCs operated at the voltage corresponding to the knee of the efficiency distribution, defined as the point where 95% of the maximum efficiency is obtained [214].

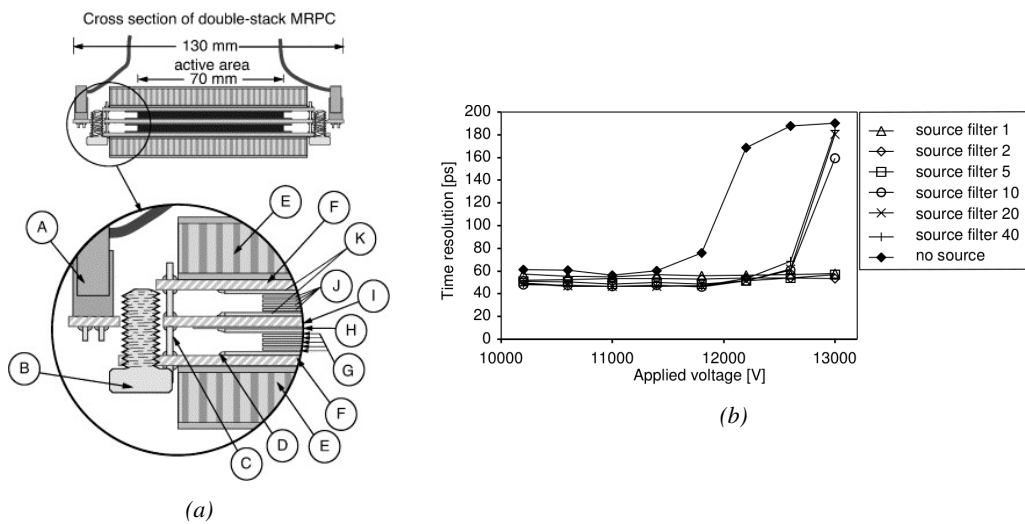


Figure 4.17: Presentation of a study of a possible ALICE MRPC cell using $250 \mu\text{m}$ gas gaps, $620 \mu\text{m}$ outer glass electrodes, and $550 \mu\text{m}$ inner floating electrodes (Figure 4.17a), and of its time resolution performance as a function of the applied high voltage for different radiation levels referred through different filter settings of the $740 \text{ GBq } ^{137}\text{Cs}$ source the former CERN GIF facility [229].

After the problem of streamers was solved by adding SF_6 into the gas mixture, the size of the MRPCs decreased as the research groups started applying the concept of dividing the gas volume into subvolumes to the narrow gap RPCs leading to the now widely used micro gap MRPCs. The time resolution of such a detector can reach of few tens of ps, with gas gaps of the order of a few hundred μm as showed in Figure 4.17 representing a single cell of ALICE Time-of-flight (ToF) system consisting of double MRPCs, as it was studied in the early 2000s [229].

Sometimes used as a double multigap RPC, taking advantage of the OR of double gap RPCs to both be able to operate a higher number of gaps while keeping a reasonable high voltage applied in between the cathode and anode and to further reduce the gain, the MRPC is mainly used as ToF detector [229–233] due to its excellent timing properties that allow to perform particle identification as explained by Williams in [234]. The principle of particle identification using ToF is simply the measurement of the velocity of a particle. Indeed, particles are defined by their mass (for the parameter of interest here, their electric charge being measured using the bending angle of the particles traveling through a magnetic field) and this mass can be calculated by measuring the velocity β and momentum of the particle:

$$(4.3) \quad \beta = \frac{p}{\sqrt{p^2 + m^2}}$$

Intuitively, it is trivial to understand that 2 different particles having the same momentum will have a different velocity due to the mass difference and thus a different flight time T_1 and T_2 through the detector and this is used to separate and identify particles. The better the time resolution of the ToF system used, the stronger will the separation be:

$$(4.4) \quad T = \frac{L}{v} = \frac{L}{c \cdot \beta}, \quad \Delta T = T_1 - T_2 = \frac{L}{c} \left(\sqrt{1 + m_1^2/p^2} - \sqrt{1 + m_2^2/p^2} \right) \cong (m_1^2 - m_2^2) \frac{L}{2cp^2}$$

An example of particle identification is given for the case of STAR experiment in Figure 4.18.

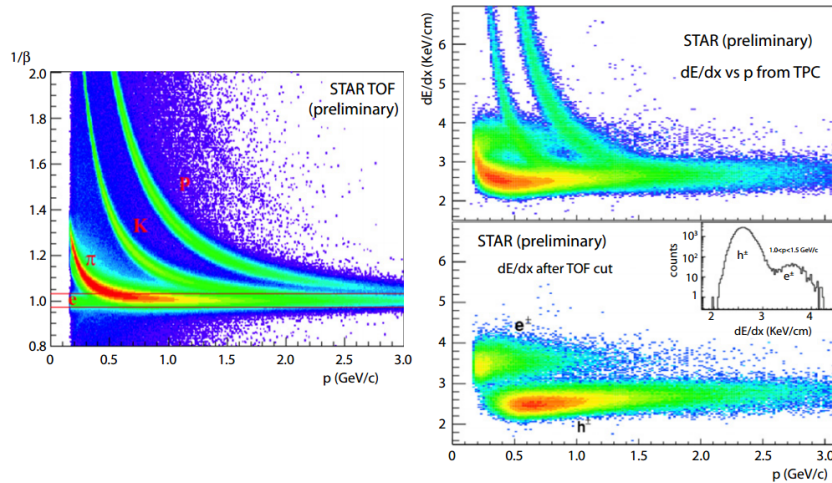


Figure 4.18: Particle identification applied to electrons in the STAR experiment. The identification is performed combining ToF and dE/dx measurements [234].

2657 Taking into account the distortion effect on the electric field inside of a MRPC built using micro
 2658 gaps due to the exposition to irradiation, distortion that can be understood by monitoring the current
 2659 drawn by the detector which should stay constant at constant electric field, another benefice of using
 2660 such small gas gaps is the strong reduction of the average avalanche volume and thus of the blind
 2661 spot on MRPCs leading to an improved rate capability. Multigaps can sustain backgrounds of several
 2662 kHz/cm² as demonstrated in Figure 4.19.

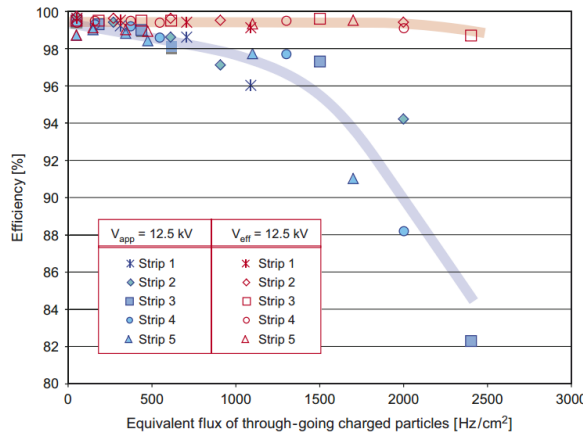


Figure 4.19: Comparison of the detector performance of ALICE ToF MRPC [235] at fixed applied voltage (in blue) and at fixed effective voltage (in red). The effective voltage is kept fixed by increasing the applied voltage accordingly to the current drawn by the detector.

2663 4.2.3.3 Charge distribution and performance limitations

2664 [This part could be moved in the next section of the chapter and deepened using the perspective
 2665 of the avalanche physics.]

2666 The direct consequence of the different RPC layouts is a variation of intrinsic time resolution of
 2667 the RPC as the gap size decreases and of the rate capability when the deposited charge per event is
 2668 spread over a larger number of amplification volumes, allowing for a reduction of the overall gain of
 2669 the detectors which is replaced by an on-electronics pre-amplification of the signals. in this sense,
 2670 an advantage is given to multigaps whose design use sub-millimeter gas volumes providing very
 2671 consistent signals.

2672 From the charge spectrum point of view, each layout has its own advantages. When the double-
 2673 gap has the highest induced over drifting charge ratio, as seen in Figure 4.20, the multigap has a
 2674 charge spectrum strongly detached from the origin, as visible in Figure 4.21. A high induced over
 2675 drifting charge ratio means that the double gap can be safely operated at high threshold or that at
 2676 similar threshold it can be operated with a twice smaller drifting charge, meaning a higher rate
 2677 capability if operated with sensitive enough electronics. On the other hand, the strong detachment
 2678 of the charge spectrum from the origin in the MRPC case allows to reach a higher efficiency with
 2679 increasing threshold as most of the induced charge is not low due to the convolution of several
 2680 single gap spectra. The range of stable efficiency increases with the number of gap, as presented in
 2681 Figure 4.22.

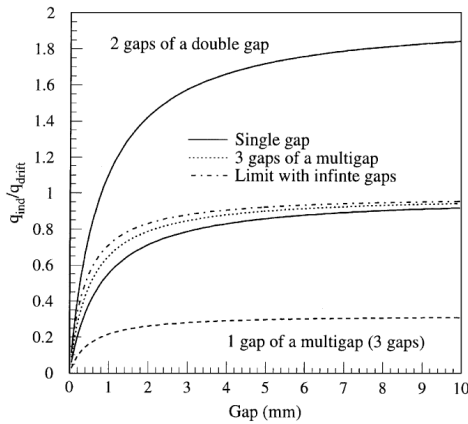


Figure 4.20: Ratio between total induced and drifting charge have been simulated for single gap, double-gap and multigap layouts [236]. The total induced charge for a double-gap RPC is a factor 2 higher than for a multigap.

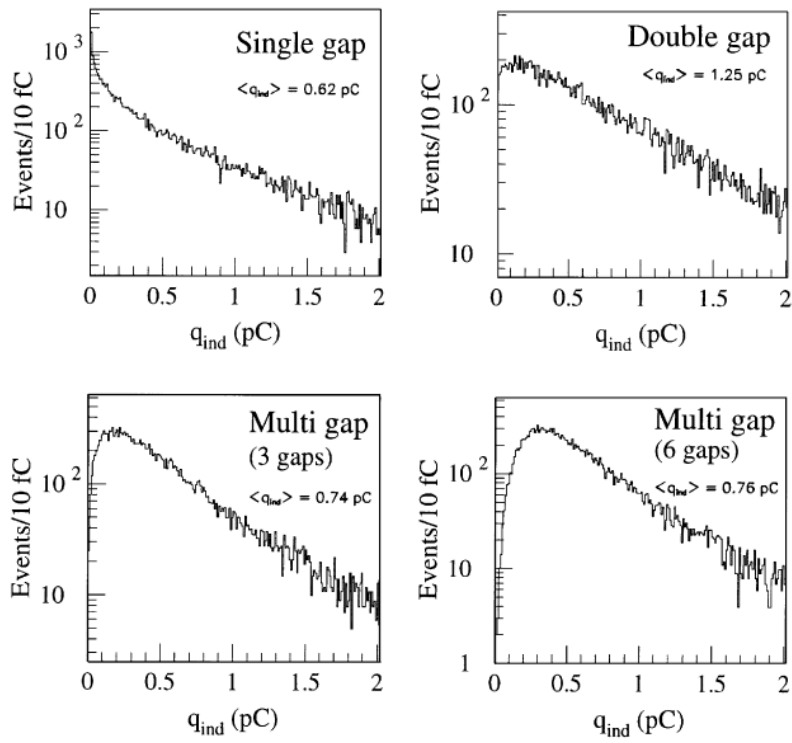


Figure 4.21: Charge spectra have been simulated for single gap, double-gap and multigap layouts [236]. It appears that when single gap shows a decreasing spectrum, double and multigap layouts exhibit a spectrum whose peak is detached from the origin. The detachment gets stronger as the number of gaps increases.

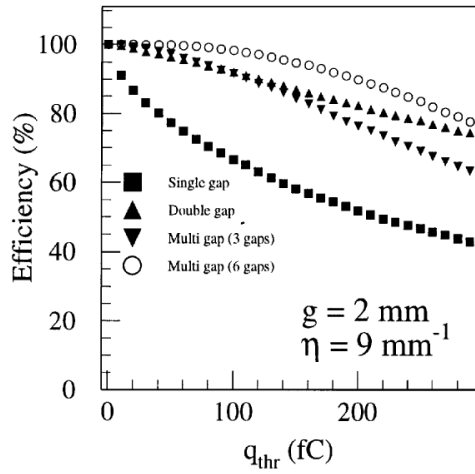


Figure 4.22: The maximal theoretical efficiency is simulated for single gap, double-gap and multigap layouts [236] at a constant gap thickness of 2 mm and using an effective Townsend coefficient of 9 mm^{-1} .

4.3 Signal formation

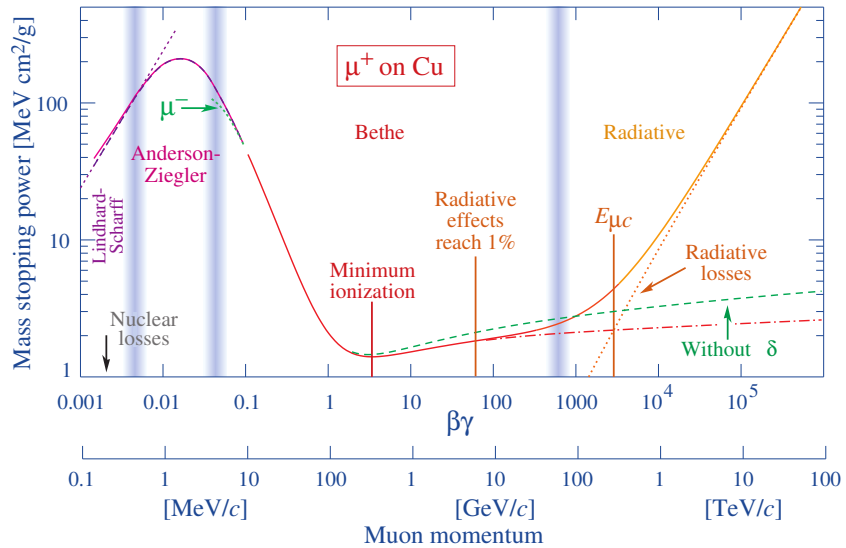


Figure 4.23: Mass stopping power as a function of $\beta\gamma = p/Mc$ for positive muons in copper [115]. The total stopping power is indicated with solid line and local components with dashed lines. The vertical bands are used to indicate boundaries between different approximations used at different energy range.

The physics of Resistive Plate Chambers still is far from being fully understood and work is regularly being accomplished in trying to model these detectors the best way possible by phenomenological models using well-defined physics [220, 237, 238]. These theoretical works have nevertheless lead to a better understanding of the key principles that account for RPCs signal formation. As previously

discussed, the typical mixture of such a detector is in great majority composed by a ionizing gas with some quenching properties and a low ionization potential to easily produce electrons, with the addition of UV quencher and electronegative compounds. The electronic avalanche formation will be triggered by a charged particle passing through the gas, typically a muon in the case of most uses of RPCs. The production of electrons in the gas of a detector is related to the energy lost by the incoming particle traveling through a material medium. The example of the mass stopping power of copper on muons is given in Figure 4.23 on which the different energy loss mechanisms at different energy ranges are visible. Once primary electrons have been freed in the gas volume, the electric field applied in between the electrodes of the RPC will make the charges move and there will be a competition in the gas in between the Townsend and attachment coefficient which describe the evolution of the number of electrons in an avalanche. While drifting through the gas, the electrons are also subjected to diffusion that will affect the evolution of the avalanches. Finally, when the avalanche is big enough, the accumulation of negative (electrons) and positive (ions) charges in the gas volume will start affecting the local electric field. This effect is known as space charge effect.

4.3.1 Energy loss at intermediate energies

Intuitively, a particle traveling through a medium will interact with its components, losing energy. When a muon travels through the gas of a gaseous detector, at the energy range usually observed, it interacts with the molecules of the gas leading to dissipation of the transferred energy in the form of inelastic diffusion or ionization. The photons and electron-ion pairs resulting from these interaction can trigger avalanches in the gas which will contribute to feed the avalanche growth thanks to the strong electric field applied in between the 2 electrodes of a RPC.

The mass stopping power of moderately relativistic ($0.1 \lesssim \beta\gamma \lesssim 1000$) heavy particles ($M \gg m_e$) traveling through a medium via excitation and ionization processes was studied by Bethe in 1930 [239] and is well described by the so called the Bethe Formula given in Equation 4.5.

$$(4.5) \quad \left\langle -\frac{dE}{dx} \right\rangle = K z^2 \frac{Z}{A} \frac{1}{\beta^2} \left(\frac{1}{2} \ln \frac{2m_e c^2 \beta^2 \gamma^2 W_{max}}{I^2} - \beta^2 - \delta(\beta\gamma) \right)$$

The different parameters used in this equation are

E	- incident particle energy γMc^2	MeV
x	- mass per unit area	g cm^{-2}
N_A	- Avogadro's number	$6.022\ 140\ 857(74) \times 10^{23} \text{ mol}^{-1}$
c	- speed of light in vacuum	$299\ 792\ 458 \text{ m s}^{-1}$
μ_0	- permeability of free space	$4\pi \times 10^{-7} \text{ N A}^{-2}$
ϵ_0	- permittivity of free space $\epsilon_0 = 1/\mu_0 c^2$	$8.854\ 187\ 817\dots \times 10^{-12} \text{ F m}^{-1}$
α	- fine structure constant $\alpha = e^2/4\pi\epsilon_0\hbar c$	$1/137.035\ 999\ 139(31)$
r_e	- classical electron radius $r_e = e^2/4\pi\epsilon_0 m_e c^2$	$2.817\ 940\ 3227(19) \text{ fm}$
e	- elementary charge of the electron	$-1.6021766208(98) \times 10^{-19} \text{ C}$
$m_e c^2$	- electron mass $\times c^2$	$0.510\ 998\ 9461(31) \text{ MeV}$
K	- constant defined as $K = 4\pi N_A r_e^2 m_e c^2$	$0.307\ 075 \text{ MeV mol}^{-1} \text{ cm}^2$
z	- charge number of incident particle	
Z	- atomic number of absorbing medium	
A	- atomic mass of absorbing medium	g mol^{-1}
β	- velocity of particle $\beta = v/c$	
γ	- Lorentz factor $\gamma = (1 - \beta^2)^{-1/2}$	

W_{max}	- maximum energy transfer through a single collision	MeV
I	- mean excitation energy of absorbing medium	eV
$\delta(\beta\gamma)$	- density effect correction to ionization energy loss	

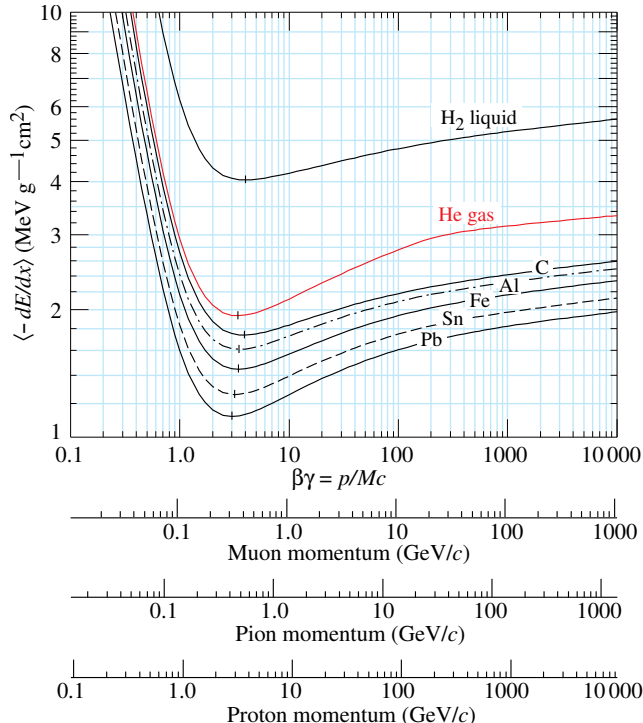


Figure 4.24: Mean mass stopping power for liquid hydrogen, as used in bubble chambers, gaseous helium, carbon, aluminum, iron, tin, and lead without the inclusion of radiative effect at higher $\beta\gamma$ necessary for pions and muons in denser materials [115].

In this equation, the maximum energy transfer W_{max} is defined as function of the incident particle mass M , expressed in MeV/c^2

$$(4.6) \quad W_{max} = \frac{2m_e c^2 \beta^2 \gamma^2}{1 + 2\gamma m_e / M + (m_e / M)^2}$$

and the mean excitation energy I depends on the absorber and its determination is non-trivial but recommendation are given by the International Commission on Radiation Units & Measurements (ICRU) based on experimental measurements and interpolations as showed in Figure 4.25.

For the case of copper, the mean stopping power is visible in Figure 4.23. The mean stopping power corresponding only to the Bethe range for other materials is given in Figure 4.24 and shows that $\langle -dE/dx \rangle$ is similar for each material with a slow decrease with Z . The factor affecting the equation the most is β as the dependence on M is introduced at higher energies in the logarithm via the max transfer energy per single collision but in most practice cases, only the dependence on β is considered as most of the relativistic particles are closed to the lowest mean energy loss rate and are

2723 referred to as minimum ionizing particles (mip's). The almost logarithmic relation in between the
 2724 mean energy loss rate for minimum ionizing particles and Z is showed in Figure 4.26.

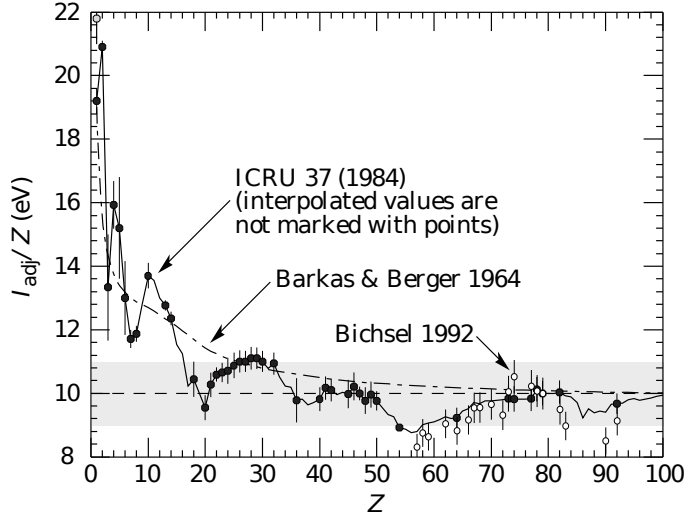


Figure 4.25: Mean excitation energies normalized to the atomic number as adopted by the ICRU [115, 240, 241].

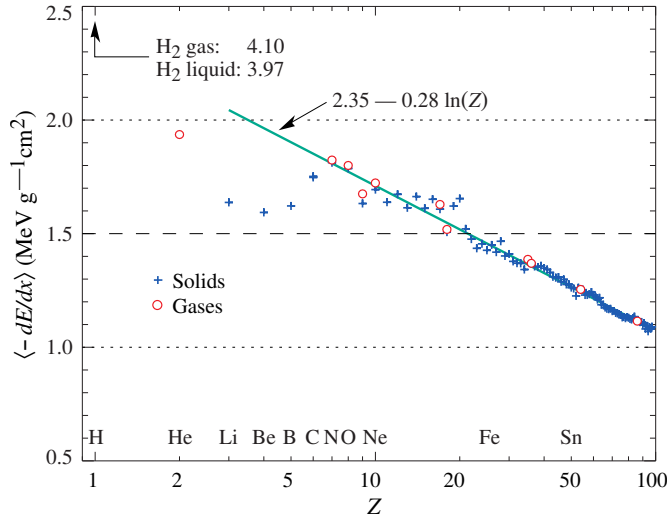


Figure 4.26: Mean mass stopping power at minimum ionization as a function of the atomic number [115].

2725 Finally, the term $\delta(\beta\gamma)/2$ corresponds to the density effect correction introduced to account for
 2726 the polarization of a real media that limits the spatial extension of the electric field of relativistic
 2727 particles. Indeed, as the energy of a particle increases, the associated electric field will flatten and
 2728 extend. Due to this effect, the distant collision contribution to Equation 4.5 will increase as $\ln(\beta\gamma)$
 2729 but the polarization of the media trunc this rise. At high energies, the correction is given by Equa-

2730 tition 4.7

$$(4.7) \quad \delta/2 \longrightarrow \ln(\hbar\omega_p/I) + \ln(\beta\gamma) - 1/2$$

2731 where $\hbar\omega_p$ represents the plasma energy that depends on the electron density of the media and
 2732 the electron mass and can be calculated as $\sqrt{\rho\langle Z/A\rangle} \times 28.816$ eV. The introduction of this cor-
 2733 rection term reduces the increase of the mean stopping power at higher energies as can be seen in
 2734 Figure 4.23. Moreover, due to poorer electron density, the effect is less visible on gases than on
 2735 liquids and solids has van be seen from Figure 4.24.

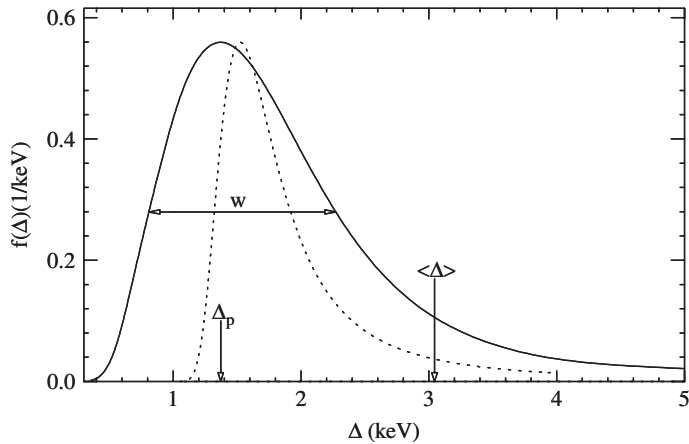


Figure 4.27: Example of straggling function $f(\Delta)$ of particles passing through 1.2 cm of Argon gas with a $\beta\gamma$ of 3.6 and represented with a solid line. The original Landau distribution is showed with a dashed line [242].

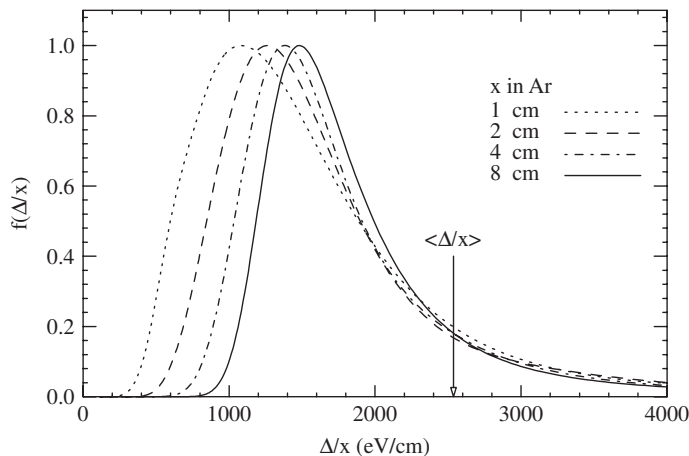


Figure 4.28: Evolution of straggling functions $f(\Delta)$ of particles passing through a volume of Argon gas with a $\beta\gamma$ of 3.6 with increasing thickness x [242].

2736 The mean energy loss per collision can be difficult to measure for low data samples and is not
 2737 always representative of the energy loss distribution for a given incident particle energy. Hence, it is

2738 easier to access the most probable energy loss which is a lower value than than the average loss due
 2739 to the distribution of the energy transfer. This value is well described by a highly skewed Landau
 2740 distribution for detectors with "moderate" thickness x , expressed in g mol⁻¹. But for gas volumes,
 2741 a Landau distribution greatly underestimates the width w of the distribution and only succeeds to
 2742 provide with a correct value for the most probable energy loss, as showed in Figure 4.27. Thus,
 2743 the energy loss distribution is better represented by its most probable energy loss Δ_p and its full-
 2744 width-at-half-maximum (FWHM) w . As showed by Figure 4.28, the distribution is affected by
 2745 the thickness of the gas volume and the most probable energy loss normalized to the thickness is
 2746 increased and the width decreased, converging towards the Landau distribution, whereas the mean
 2747 energy loss is unchanged. Correction are brought to the original Landau equation in order to account
 2748 better for the number of collisions leading to an increased width of the energy loss distribution [242].

2749 In the case of gas mixtures, composed of several elements, using Bragg additivity it can be
 2750 understood that the mean energy loss of the mixture is the sum of the mean energy losses in each
 2751 individual element j layer of weight w_j .

$$(4.8) \quad \left\langle \frac{dE}{dx} \right\rangle = \sum w_j \left\langle \frac{dE}{dx} \right\rangle_j$$

2752 4.3.2 Primary ionization

2753 Using Bethe formula to understand the mean energy transfer of charged particle when traveling
 2754 through a gas volume give an intuition of the physics that affect the particle but doesn't provide a
 2755 detailed enough information about the individual ionizations along its tracks at a microscopic level.
 2756 In order to simulate efficiently an RPC and hence understand the processes governing avalanches
 2757 creation and growth, knowledge on the ionization process is necessary.

2758 To convert the energy loss rate into a number of primary ionizations was developed in 1980 the
 2759 Photo-Absorption Ionisation (PAI) model [243] based on the cross section of ionization of gas atoms
 2760 to real photons and the dielectric constant of the medium through which the charged particles are
 2761 going. Indeed, the interaction of charged particles with the gas molecules being of electromagnetic
 2762 nature, it is mediated by quasi-real photons and, hence, the cross section to photon ionization is
 2763 important to understand. This approach is nevertheless semi-classical as it relies on classical elec-
 2764 trodynamics and it only gives access to the energy transfer to the gas atoms and no information on
 2765 the energy dissipation and secondary emissions is available on the output of the model. The energy
 2766 transferred to the medium is not all used for ionization. For an energy deposition Δ , the number of
 2767 electron-ion pairs produced is:

$$(4.9) \quad \Delta = n_i W$$

2768 W corresponds to the mean work per pair production that depends on the medium and is greater
 2769 than the ionization potential leading to the conclusion that part of the transferred energy is dissipated
 2770 through other processes [238, 244]. In order to understand the energy dissipation and the secondary
 2771 emissions, the fine structure of each atom is taken into account. Through the PAI model, the incident
 2772 charged particle interacts is assumed to interact with the full atom rather than with a single electron.

2773 Although, considering that the particle interacts with a single electron, leads to the possibility
 2774 to study the excited state of the atom once the photo-electron has been emitted with an energy

corresponding to the transferred energy minus the binding energy of the electronic shell. The resulting vacancies in the electronic shell will be filled through emission of photons or Auger electrons and can contribute to further ionization or excitation in the gas volume. Fluorescence photons are usually not considered as they only constitute a very small fraction of secondary emissions [245]. Assuming that the transferred energy is absorbed in its totality by a single electronic shell, the PAI model was modified to include relaxations and constitute the new Photo-Absorption Ionisation with Relaxation (PAIR) model [245]. In this model, the cross section corresponding to the whole atom is re-expressed using a sum of partial cross sections corresponding to the different electronic shells. When one or more electrons are knocked out of the atom, the vacancies are filled by electrons of the shell above with relaxation by Auger electron emission. These processes happen in cascade from the inner shell to the outer one until all the vacancies are filled and the energy has been released.

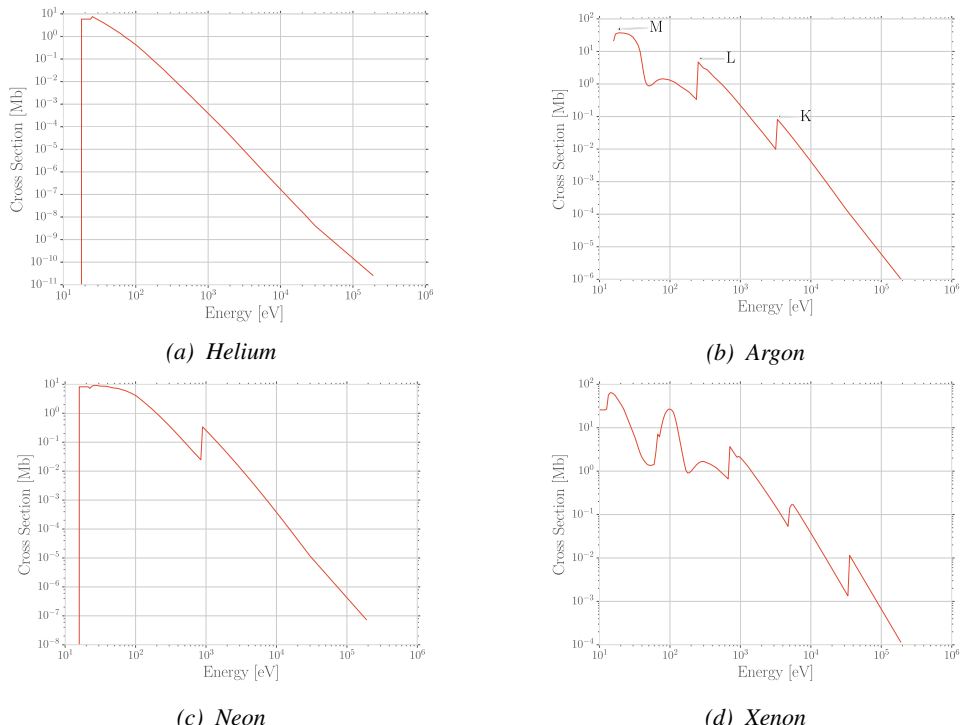


Figure 4.29: Photo-absorption cross section as computed by HEED for nobles gases with different electric shell numbers [238].

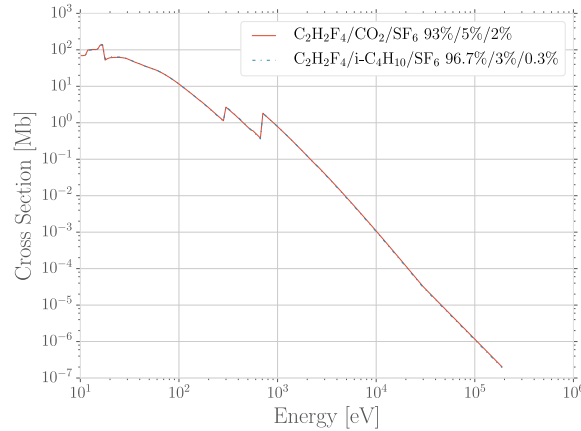


Figure 4.30: Photo-absorption cross section as computed by HEED for typical RPC gas mixtures [238]. The RPC mixture with CO₂ corresponds to the mixture used by CALICE SDHCAL [246] while the other one was foreseen for the experiment ATLAS [247] but has been changed since then.

This model is included in the program HEED developed at CERN [248] and called by Garfield, a program developed for the simulation of gaseous detectors. The results for the cross section for a few noble gases are given in Figure 4.29. It can be seen that for each shell, the cross section is increased. More complex patterns are seen with bigger atoms such as Xenon on Figure 4.29d. For gas mixtures, like the typical RPC mixtures, the cross section is showed in Figure 4.30. Both mixtures being mainly composed of C₂H₂F₄, the variations in between the 2 cross section profiles are very subtle and depends on the concentration of the other compounds.

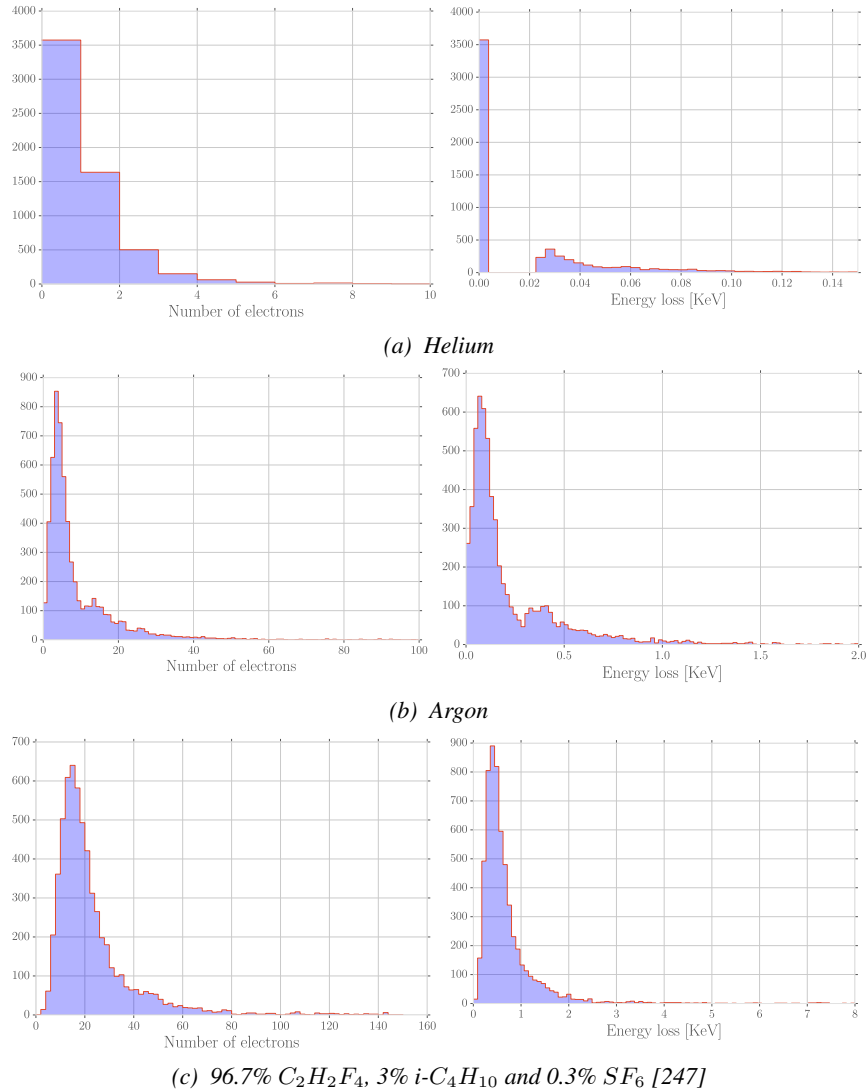


Figure 4.31: Distributions of number of electrons (left) and energy loss (right) for a 5 GeV/c muon passing through 1.2 mm of Helium (Figure 4.31a), Argon (Figure 4.31b) or a typical RPC gas mixture (Figure 4.31c) [238].

Once the cross section of interaction is known, it is possible to extract the distribution of energy loss and of the number of electron produced, as showed in Figure 4.31 for Helium, Argon, which is used in gaseous detectors, and for a typical RPC mixture [238]. The distributions are computed using HEED and show typical straggling function profiles with some complex structures that can be related to interaction of the incoming particle with the different electronic shells. Helium does not have a great photo-absorption cross-section according to Figure 4.29a and a muon will not be likely to lose a lot of energy and to create a lot of electrons whereas in a more complex atom like Argon, the cross-section is greater and will lead to a greater energy loss of muons and more electron produced. Finally, a complex gas mixture used in RPCs will offer an even greater cross-section, a wider energy loss distribution and will be able to produce more electrons. The same information is seen by looking

at the evolution of the mean number of cluster as a function of the lorentz factor associated to muons showed in Figure 4.32a. Indeed, the greater photo-absorption cross-section of RPC mixtures allow for a much greater amount of clusters to be created by charged particles. The size of these clusters is studied through Figure 4.32b which shows that, in most of the cases ($\approx 80\%$), the clusters only are composed of a single electron which is consistent with minimum ionizing particles.

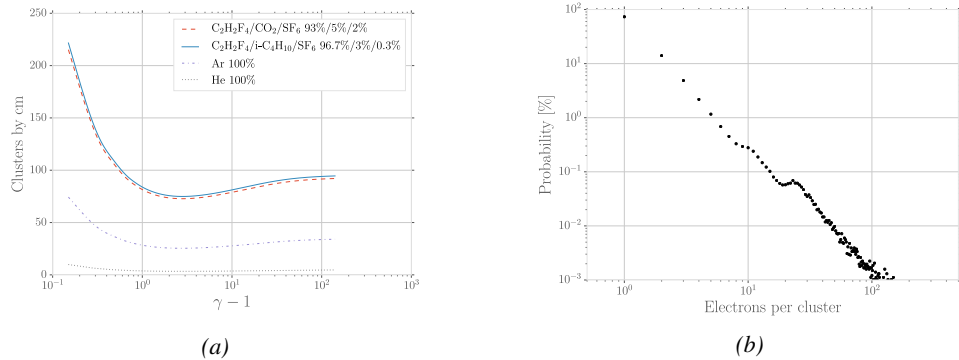


Figure 4.32: Figure 4.32a: Mean cluster density for muons through different gas volumes [238]. Figure 4.32b: Distribution of the number of electrons per cluster for a 5 GeV/c muon traveling through a mixture of 96.7% $C_2H_2F_4$, 3% $i-C_4H_{10}$ and 0.3% SF_6 [238, 247].

4.3.3 Development and propagation of avalanches

From the clusters released in the gas volume by the charged particles, free electrons will start drifting due to the electric applied in between the electrodes of the RPC. Gaining velocity and energy, these electrons in their turn will be able to ionize the gas. This process being repeated by all the produced electrons will trigger an avalanche to develop.

The growth of the avalanche can be intuitively understood as a competition between 2 effects. Due to their increasing energy, electrons have a probability to trigger new ionizations by interacting with gas molecules. On the other hand, before the minimal amount of energy is reached, the electrons can get attached to a gas molecule instead. These two effects can be described using a simple model in which the multiplication and attachment processes are given by the Townsend coefficient α and the attachment coefficient η , assuming that the history of previous interactions in the gas does not influence new interactions. This model simply takes into account probabilities to have at the gas depth z for a given number n of free electrons in the gas $n+1$ or $n-1$ electrons at the depth $z+dz$ (respectively $n\alpha dz$ and $n\eta dz$). Then, the mean number of electrons \bar{n} and cations \bar{p} can be written for single compound gases as

$$(4.10) \quad \frac{d\bar{n}}{dz} = (\alpha - \eta)\bar{n}, \quad \frac{d\bar{p}}{dz} = \alpha\bar{n}$$

which, assuming the initial conditions $\bar{n}(0) = 1$ and $\bar{p}(0) = 0$, lead to the mean number of electrons and cations at a depth z

$$(4.11) \quad \bar{n}(z) = e^{(\alpha-\eta)z}, \quad \bar{p}(z) = \frac{\alpha}{\alpha-\eta} \left(e^{(\alpha-\eta)z} - 1 \right)$$

2825 The Townsend and attachment coefficient as a function of the applied electric field are given in
 2826 Figure 4.33 for a standard RPC gas mixture using Magboltz [249].

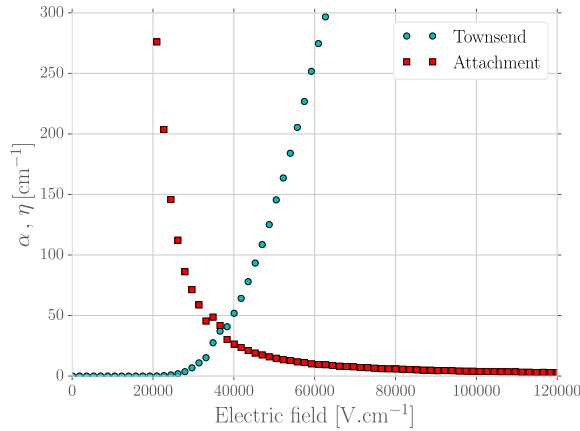


Figure 4.33: Townsend and attachment coefficient for a typical 96.7/3/0.3 mixture of $C_2H_2F_4/i-C_4H_{10}/SF_6$, at a temperature $T = 296.15\text{ K}$ and a pressure $P = 1013\text{ hPa}$ [238, 247].

2827 Nevertheless, there are more to the avalanche growth than simply these two factors. Throughout
 2828 the 20th century, models have been developed to better understand the physics of discharges in gas.
 2829 In 1937, Furry developed a model to describe electromagnetic cascades [250] that would be used for
 2830 electron avalanches in gas during the 1950s. Furry realized that the use of a Poisson law to describe
 2831 the distribution of shower sizes could not be accurate as he understood that the events occurring in
 2832 the development of a cascade are not independent from each other, as a Poisson law would suggest.
 2833 Indeed, part of the particles produce others and this process depends on both their original energy
 2834 and energy lost. Experimental results showed excess of small showers and an under estimate of very
 2835 large ones. To solve this problem, Furry proposed a distribution of sizes of following the likelihood
 2836 described in Equation 4.12, in which $\bar{n} = e^{\alpha z}$, compared with a Poisson law in Figure 4.34.

$$(4.12) \quad P(n, \bar{n}) = \bar{n}^{-1}(1 - \bar{n}^{-1})^{n-1}$$

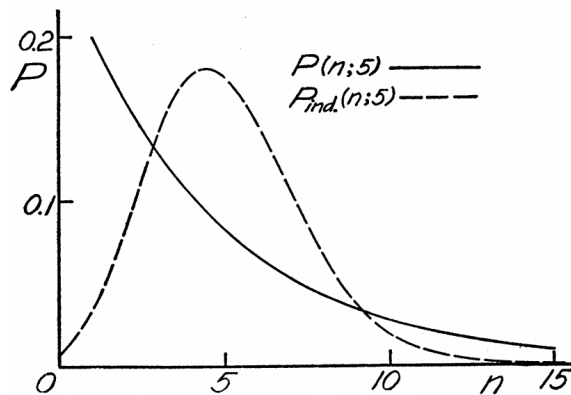


Figure 4.34: Comparison of the distribution law of Furry and the Poisson law for $\bar{n} = 5$ [250].

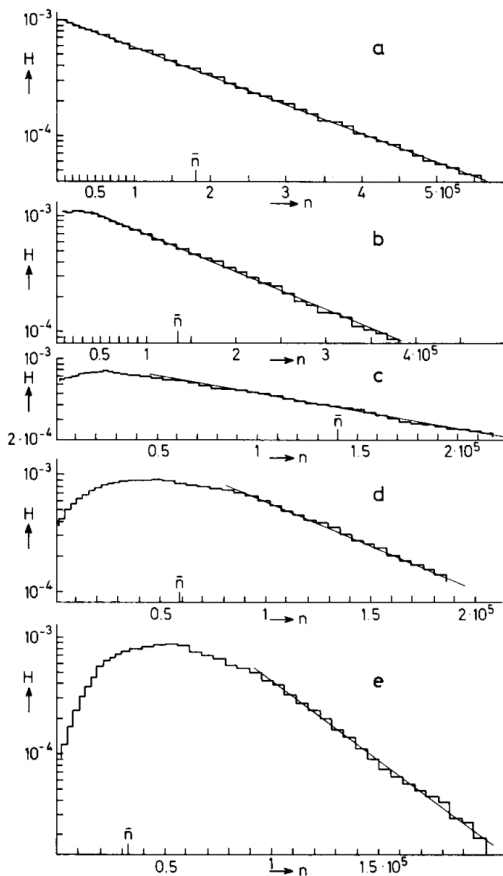


Figure 4.35: Single-electron avalanche size distribution in a proportionnal counter filled with methylal at different E/p values. (a) 70, (b) 76.5, (c) 105, (d) 186.5, (e) 426V/cm torr [251].

In this model, no extra energy is brought to the electrons in the showers, contrary to the case of a gaseous detector such as a RPC where an electric field accelerates them. Using the Furry model, Genz studied the fluctuations in electron avalanches in gaseous detectors [251]. Collisions leading to ionizations leave electrons with an energy much smaller than the ionization energy eU_i , where U_i is the ionization potential of a gas molecule. Hence, the electrons need to travel a distance $s = U_i/E$ along the electric field E to acquire a high enough energy to trigger a new ionization. For the probability of a new ionization to be independent from the path followed by the electrons since the previous ionization, the mean free path $1/\alpha$ of electrons in the gas has to be large compared to s and thus $E/\alpha \gg U_i$. The Townsend coefficient is related to the gas pressure leading to conditions on the value of E/p . Avalanches in gas are large compared to the showers Furry has studied in his original paper. For very large avalanche sizes, Equation 4.12 can be written as an exponential, as showed in Equation 4.13.

$$(4.13) \quad P(n, \bar{n}) = \bar{n}^{-1} e^{-n/\bar{n}}$$

This exponential behaviour is showed through Figure 4.35. In practice, to fully understand the avalanche growth, taking into account the path followed by electrons from one ionization to another

will become necessary. In the same paper, Genz then discusses models using Polya distributions to estimate the multiplication by looking at the size of the avalanche it self. Indeed, the number of charge carriers in the avalanche might become important enough to have an effect on the multiplication process. To account for this, it was proposed to use a varying Townsend coefficient such as described by Equation 4.14 depending on the position x in which θ is an empirical parameter leading to the probability distribution of Equation 4.15. In the limit case where θ goes to 0, the formula describes again the Furry model. But the data deviates from this model as well at large n values. Moreover, the introduction of an empirical parameters makes the model hard to interpret physically.

$$(4.14) \quad \alpha(n, x) = \alpha(x) \left(1 + \frac{\theta}{n}\right), \quad n > 0$$

$$(4.15) \quad P(n, x) = \frac{1 + \theta}{\bar{n}} \frac{1}{\theta!} \left(\frac{n(1 + \theta)}{\bar{n}}\right)^{\theta} e^{-\frac{n(1 + \theta)}{\bar{n}}}$$

In order to have a model that describes reality better, the introduction of the attachment into the model is an important step. Despite its limitations, the Furry model had the advantage to describe well avalanches occurring when the attachment could be ignored. This is only natural that this model was then extended to included attachment. This was done by Riegler, Lippmann and Veenhof [247] which showed that what was important was to consider both the Townsend coefficient describing the multiplication *and* the attachment coefficient, not only the effective multiplication coefficient $\bar{\alpha} = \alpha - \eta$. The probability to see an avalanche started by a single electron grow to a size n after having traveled a distance z through the gas is given by Equation 4.16.

$$(4.16) \quad \begin{aligned} P(n, z) = & P(n-1, z) (n-1)\alpha dz (1 - (n-1)\eta dz) \\ & + P(n, z) (1 - n\alpha dz) (1 - n\eta dz) \\ & + P(n, z) n\alpha dz n\eta dz \\ & + P(n+1, z) (1 - (n+1)\alpha dz) (n+1)\eta dz \end{aligned}$$

The first term of this probability that from a state with $n-1$ electrons, only 1 multiplies while the others don't get attached. Both the second and third terms describes the probability that from a state with already n electrons the total number of electrons stay the same. On the second term, no electron gets attached nor multiplies while on the third term, 1 electron gets multiplied and 1 gets attached to compensate. Finally, the fourth term describes the probability to fall from a state with $n+1$ to a state with n electrons due to the attachment of a single electron. At the first order, the evaluation of the previous expression leads to Equation 4.17 which general solution is given in Equation 4.18 in which are introduced the variables $\bar{n}(z)$, defined as in Equation 4.11, and $k = \eta/\alpha$ making explicit the fact that the distribution not only depends on the effective Townsend coefficient.

$$(4.17) \quad \frac{dP(n, z)}{dz} = -P(n, z)n(\alpha + \eta) + P(n-1, z)(n-1)\alpha + P(n+1, z)(n+1)\eta$$

$$(4.18) \quad P(n, z) = \begin{cases} k^{\frac{\bar{n}(z)-1}{\bar{n}(z)-k}}, & n = 0 \\ \bar{n}(z) \left(\frac{1-k}{\bar{n}(z)-k}\right)^2 \left(\frac{\bar{n}(z)-1}{\bar{n}(z)-k}\right)^{n-1}, & n > 0 \end{cases}$$

The example given through Figure 4.36 shows the importance of each individual process in the growth of avalanches and the fluctuation of their size. The values of α and η will influence the probability distribution, as can be seen from Figure 4.36a. Then, Figure 4.36b shows that the fluctuation really takes place within the very first interactions. Indeed, when the avalanche contains a large enough amount of charge carriers (a few hundreds), its size then increases like $e^{z(\alpha-\eta)}$.

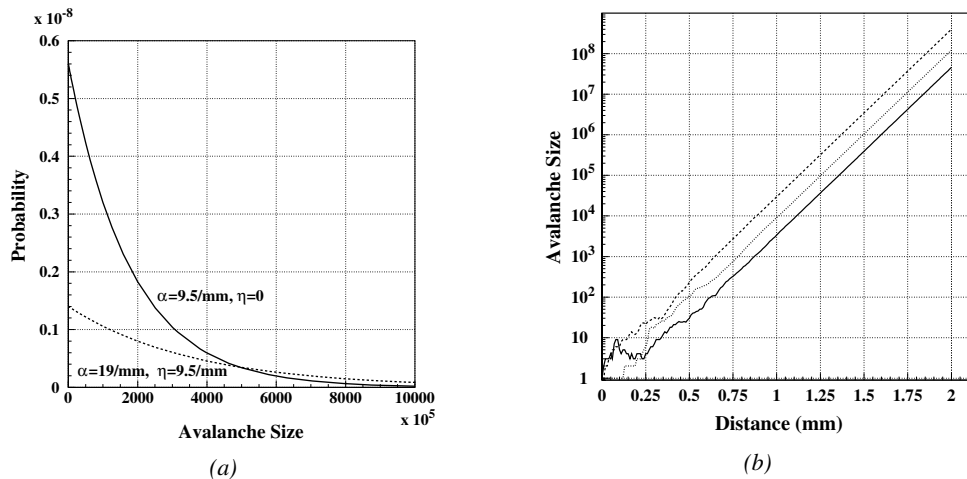


Figure 4.36: Figure 4.36a: Comparison of avalanche size distributions for different values of Townsend and attachment coefficients. The effective Townsend coefficient is the same for both distributions. Figure 4.36b: Fluctuation in avalanche size for avalanche started by a single electron with $\alpha = 13 \text{ mm}^{-1}$ and $\eta = 3.5 \text{ mm}^{-1}$ [247].

4.3.4 Drift and diffusion of the electron cloud

During the growth of avalanches, an electron cloud drifting along the electric field through the gas will undergo thermal diffusion due to random collisions with the gas molecules. This phenomenon can be studied using Maxwell-Boltzmann distribution whose mean is defined by the thermal energy of the cloud $\langle E \rangle = 3/2kT$ with an extra component coming from the constant drift motion. The drift of electrons along the field lines is usually observed on a macroscopic scale through which the speed can be assimilated to a constant v_D which corresponds to the mean drift speed over a large number of collisions in the gas.

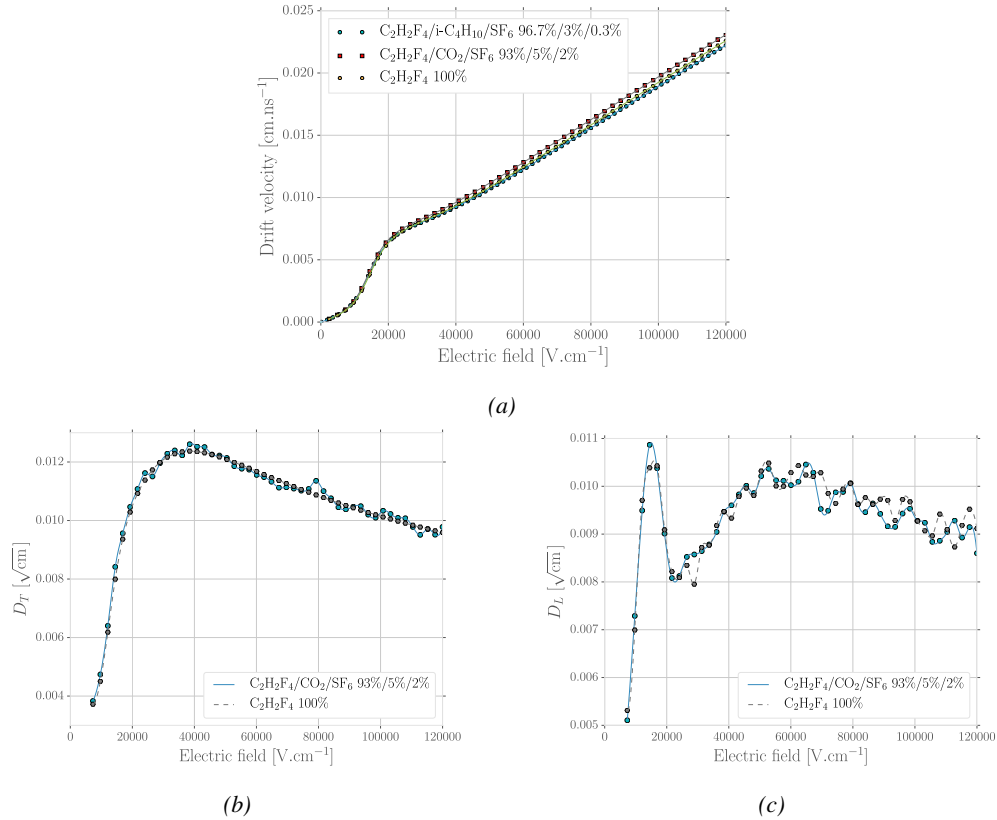


Figure 4.37: Figure 4.37a: Electron mean drift velocity v_D in pure C₂H₂F₄ and typical RPC gas mixtures. Figure 4.37b: Transverse diffusion coefficient in pure C₂H₂F₄ and a typical RPC gas mixture. Figure 4.37c: Longitudinal diffusion coefficient in pure C₂H₂F₄ and a typical RPC gas mixture. All results are given with a pressure $P = 760$ Torr and a temperature $T = 296.15$ K [238].

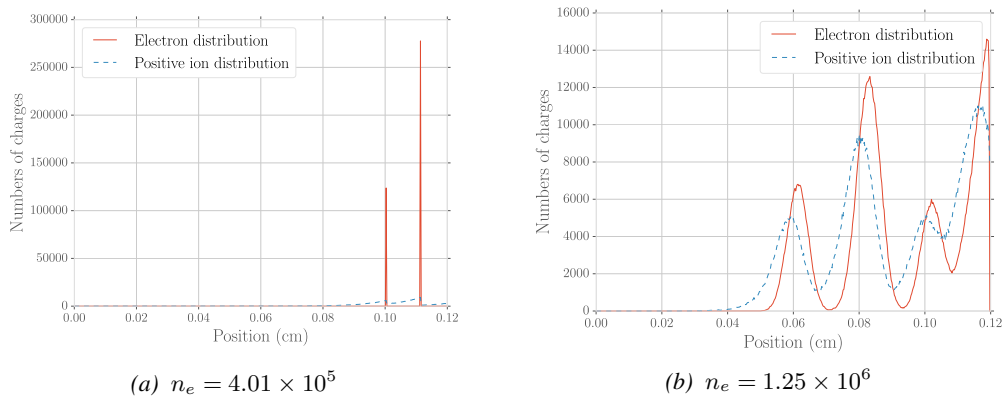


Figure 4.38: Comparison of the free charge carriers in the gas after a time $t = 7.90$ ns in the case where no diffusion is taken into account to simulate the avalanche (Figure 4.38a) and in the case where the diffusion is implemented (Figure 4.38b) [238].

Indeed, at the microscopic scale, the electrons are drifting over a distance δz while acquiring the corresponding kinetic energy $T = e_0 |\vec{E}| \delta z$ until they are slowed down by a collision in which they lose part of their energy. This process is repeated as long as electrons are free carriers. Starting from a point-like electron cloud, the Gaussian density distribution at \vec{r}_0 will be described by Formula 4.19 in which the width of the isotropic distribution is $\sigma = 2\bar{D}t$, with \bar{D} being a diffusion coefficient expressed in m^2/s [220].

$$(4.19) \quad \varphi(\vec{r}, t) = \frac{1}{(\sqrt{2\pi}\sigma(t))^3} \exp\left(-\frac{(\vec{r} - \vec{r}_0)^2}{2\sigma^2(t)}\right)$$

Now, if the constant drifting motion is added, the distribution is anisotropic and can be divided onto transversal (Formula 4.20) and longitudinal (Formula 4.21) terms, $\varphi(r, z, t) = \varphi_T(r, t)\varphi_L(z, t)$, with a cylindrical symmetry around the field axis [220]. The variables t and $\sigma_{T,L}(t)$ can be hidden to the profit of the diffusion coefficients by using the relations $v_D = l/t$ and $\sigma_{T,L}^2(t) = 2\bar{D}_{T,L}l/v_D$ and introducing new diffusion coefficients $D_{T,L} = \sqrt{2\bar{D}_{T,L}/v_D}$ in order to explicitly show the dependence of the Gaussian width in drifted distance l .

$$(4.20) \quad \varphi_T(r, t) = \frac{1}{D_T^2 l} \exp\left(-\frac{(r - r_0)^2}{2D_T^2 l}\right)$$

$$(4.21) \quad \varphi_L(z, t) = \frac{1}{\sqrt{2\pi l} D_L} \exp\left(-\frac{(z - z_0)^2}{2D_L^2 l}\right)$$

These coefficients, as well as the drift velocity of the electrons, can be calculated thanks to Magboltz as showed in Figure 4.37. The influence of the diffusion on the distribution of charge carriers throughout the gas volume is depicted in Figure 4.38. From very localised electron clusters in the gas in Figure 4.38a, a Gaussian diffusion is then visible in Figure 4.38b. Due to the interactions with gas molecules during the drift, diffusions can occur in the forward and backward direction. Electrons diffused backward will effectively drift over a longer distance and multiply more than electrons diffused forward that will see a shorter drift length. As an effect, the avalanche develops over a longer time and extends over a greater gas volume than in the case the electron cloud is considered as point like and without diffusion. Moreover, as a side effect to the longer growth of the avalanche due to backward longitudinal diffusion, the total production of electrons is increased.

4.3.5 Space charge effect & streamers

Now that have been considered the basic processes that influence the development of avalanches in a gaseous detector in the previous sections, it is now important to consider the influence of the charge carriers present in the avalanche on the electric field seen by the avalanche. Indeed, each charged particle induces an electric field and it is only natural that the increasing density of electrons and ions in the detector volume will affect the electric field. Thus, parameters such as the Townsend and attachment coefficients, drift velocity or diffusion coefficients will find themselves to be modified along the gas gap length due to this effect referred to as *space charge effect*. Figure 4.39 is a more detailed version of Figure 4.1 (b) in which three electric regions are distinguished [220]. When compared to the linear electric field of strength E_0 that is developed in between the detector's electrodes, the

accumulation of negative charges (electrons) on the front of the avalanche will reinforce the effective electric field in between the anode of the avalanche front. Deeper in the gas volume, the positive charges (cations) slowly drift towards the cathode and can induce together with the avalanche front opposite electric field loops. Finally, due to the density of positive charges, the electric field seen in between the ions tails and the cathode charged with negative charges is on average stronger than E_0 and compensate for the locally reversed field E_2 . Lippmann roughly estimated by considering that 10^6 charges were contained in a sphere of radius $r_d = 0.1$ mm that the space charge effect could change the electric field by 3% and the Townsend and attachment coefficient up to 14% [220, 238].

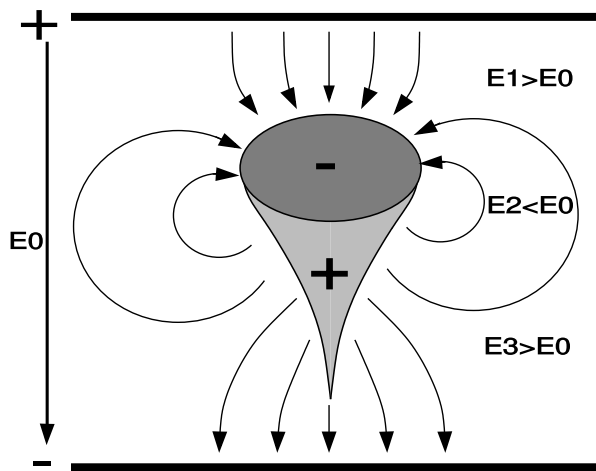


Figure 4.39: Schematic representation of an avalanche and of the electric field deformation it causes due to the local concentration of charge carriers [220].

To account for the space charge effect, the electric potential and field of free charges are solved and applied to each charges in the avalanche [220, 238]. As discussed by Français who has been working on simulating RPCs similar to that used by the SDHCAL project of ILC, the computation of these equations for each individual charge carrier to dynamically know the space charge field at every stage of an avalanche development is a difficult task and would require far too much computation time and a solution is to pre-compute an interpolation table keeping an adequately large number of values of the space charge field for each positions in space thanks to which the values stored in the interpolation table become very close to the analytic solution and allow for a much faster simulation.

The study of space charge effect through simulation shows that it can lead to a saturation of the avalanche growth due to the deformation of the electric field, as showed through Figure 4.40. Additionnally, a more precise understanding of the space charge effect is given through Figure 4.41 which looks at the distribution of charges and the distortion of the electric field at different steps of the evolution of an avalanche in a RPC. At the moment a 5 GeV muon ionizes the gas, electron-ion pairs are created in the gas in different clusters (Figure 4.41a). Later, the first clusters have reached the anode while the clusters that where created the closest to the cathode are now big enough to start influencing the electric field in the gap (Figure 4.41b). When a cluster is big enough, the electric field in front of it locally increases a lot and contributes to a stronger but very localised multiplication. At the same moment, the positive ions right behind the cluster avalanche front decrease the electric field, saturating the electron multiplication on the tail of the electron cloud (Figure 4.41c). Finally, when

2949 all the electrons have reached the anode and are relaxing, the electric field still is very deformed
 2950 by the distribution of both positive and negative ions in the the gas volume closest to the anode
 2951 (Figure 4.41d).

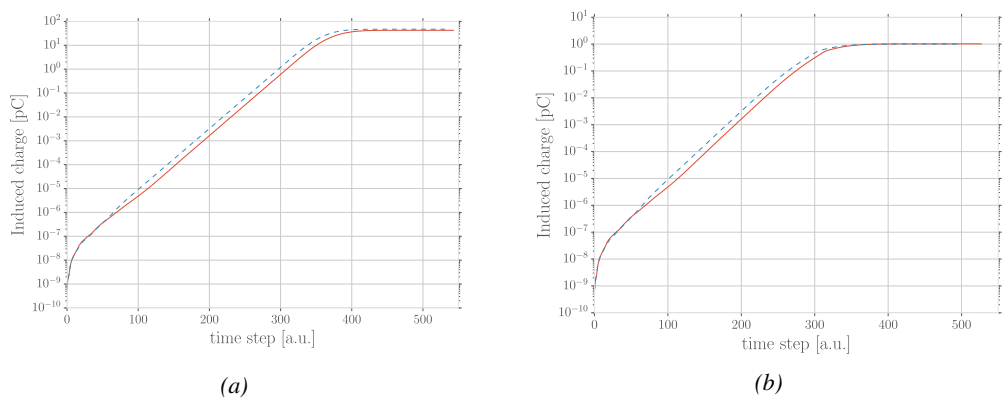


Figure 4.40: Evolution of the charge induced by an avalanche started by a single electron in a 1.2 mm thick RPC with an applied electric field of 54 kV/cm in the case space charge is not taken into account (Figure 4.40a) and in the case it is implemented into the simulation (Figure 4.40b). The total induced charge is correlated to the size of the avalanche [238].

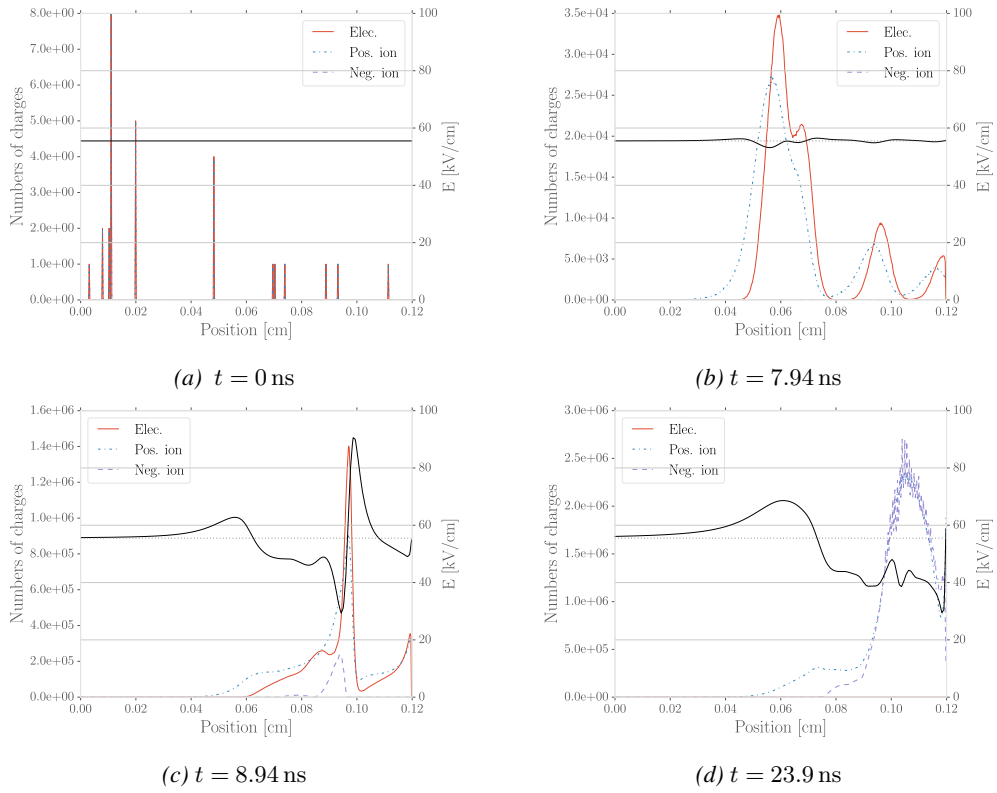


Figure 4.41: Distributions of charge carriers within the gas volume of a 1.2 mm thick RPC and the corresponding deformation of the electric field at different time steps with an applied electric field of 55.5 kV/cm [238].

2952 The electric field following the development of an avalanche can stay perturbed for a long time
 2953 with respect to the avalanche development due to the slow drift of the much heavier ions. This can
 2954 result in powerful secondary avalanches triggered by the fluctuation of the electric field together with
 2955 the emission of UV-photons leading to emission of electrons at the surface of the electrode. This is
 2956 a slow phenomenon compared to the development of avalanches. Experimentally, it is observed that
 2957 the stronger the electric field applied over the gap, the sooner after the avalanche, referred to as *pre-*
 2958 *cursor signal* in this context, and the stronger will the secondary avalanche be, possibly reaching the
 2959 streamer regime. This could be due to the amount of UV-photons emitted by the growing precursor.
 2960 These photons will be able to trigger new avalanches in a radius of a few mm around the precursor
 2961 by knocking electrons from the cathode by photoelectric effect. The strong distortions of the electric
 2962 field due to a large avalanche will be more likely to emit UV-photons as the electric field at the front
 2963 of the precursor avalanche will be large, providing the electrons with a larger energy. Eventually, the
 2964 new avalanches can grow to form streamers.

4.4 Effect of atmospherical conditions on the detector's performance

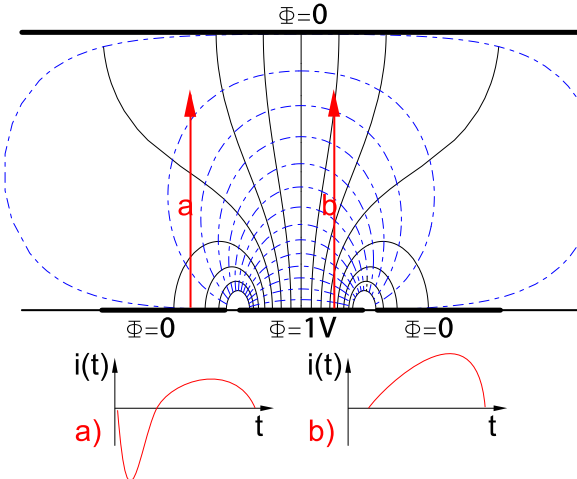


Figure 4.42: Representation of the weighting field in the volume of a RPC and the resulting induced current in the strip placed at 1 V and its neighbour connected to the ground. The induced current corresponds, as can be understood from Formula 4.22 [220].

Accordingly to Ramo's theorem, the movement of charge carriers, and in particular, the movement of a dense electron cloud toward the anode induces a current signal on one or more of the readout electrodes (strips or pads). The ions on the other hand induce only a very small current as their movement is much slower than which of the electrons. The current induced by n_{Cl} clusters of $N_j(t)$ charge carriers drifting at velocities $\vec{v}_{Dj}(t) = \vec{x}_j(t)$ at a time t is given by Formula 4.22 in which e_0 is the unit charge and \vec{E}_w is the weighting field.

$$(4.22) \quad i(t) = \sum_{j=1}^{n_{Cl}} \vec{E}_{wj}(\vec{x}_j(t)) \cdot \vec{v}_{Dj}(t) e_0 N_j(t)$$

The weighting field, that has been schematised in Figure 4.42, corresponds to the electric field that would be observed in the gas gap if a readout electrode is placed at a potential of 1 V while keeping all the other electrodes grounded. Then the induced charge in the readout can be simply obtained by integrating Formula 4.22 over the duration T of the signal, as given by Formula 4.23.

$$(4.23) \quad Q(t) = \int_0^T \sum_{j=1}^{n_{Cl}} \vec{E}_{wj}(\vec{x}_j(t)) \cdot \vec{v}_{Dj}(t) e_0 N_j(t)$$

The signal induced in the readout of RPCs operated in avalanche mode is then sent into Front-End Electronics in which they will be pre-amplified and discriminated. The discrimination and digitization of signals in CMS FEE is described through Figure 4.43. On a first stage, analogic signals are amplified, following the curve given on Figure 4.44, and then sent to the Constant Fraction

Discriminator (CFD) described in Figure 4.45. At the end of the chain, 100 ns long pulses are sent in the LVDS output. The digital signals are both used as trigger for CMS and to evaluate the performance of the detectors. The performance will depend on the applied HV, i.e. on the electric field inside of the gas volume, but also on the threshold applied on the CFDs. Indeed, in order to reduce the probability to measure noise, the threshold is set to a level where the noise is strongly suppressed while the signals are not too affected. Typically, CMS FEEs are set to a threshold of 215 mV after pre-amplification, corresponding to an input charge of about 140 fC.

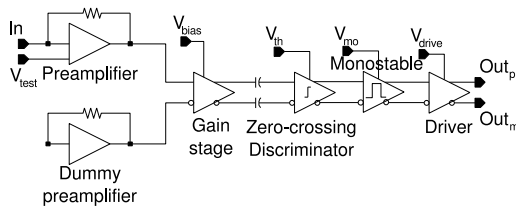


Figure 4.43: Schematics of CMS RPC FEE logic.

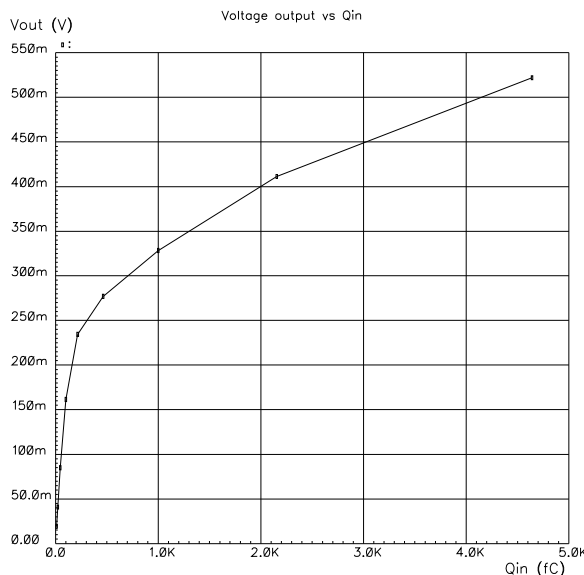


Figure 4.44: Equivalence in between the charge of the induced signal in input of the CMS FEE and the signal strength on the output of the pre-amplifier.

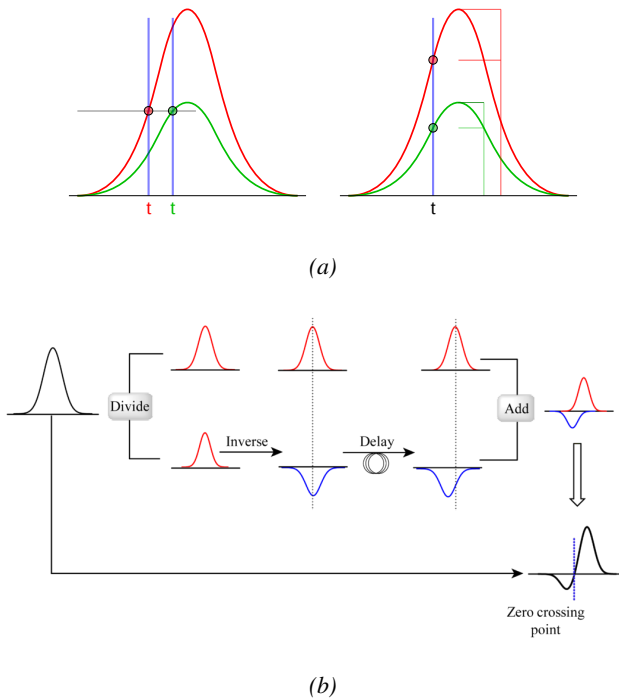


Figure 4.45: Description of the principle of a CFD. A comparison of threshold triggering (left) and constant fraction triggering (right) is shown in Figure 4.45a. Constant fraction triggering is obtained thanks to zero-crossing technique as explained in Figure 4.45b. The signal arriving at the input of the CFD is split into three components. A first one is delayed and connected to the inverting input of a first comparator. A second component is connected to the noninverting input of this first comparator. A third component is connected to the noninverting input of another comparator along with a threshold value connected to the inverting input. Finally, the output of both comparators is fed through an AND gate.

The performance of a detector is then simply measured relatively to which of a reference detector used as trigger as the ratio in between the number of events recorded in coincidence in the detector and the reference and the total amount of trigger events, $\epsilon = n_{events}/n_{triggers}$. An example of efficiency measured as a function of the effective voltage HV_{eff} is given in Figure 4.46 and can be fitted thanks to a sigmoidal function described as in Formula 4.24 and where ϵ_{max} is the maximal efficiency of the detector, λ is proportional to the slope at half maximum and HV_{50} is the value of the voltage when the efficiency reaches half of the maximum.

$$(4.24) \quad \epsilon(HV_{eff}) = \frac{\epsilon_{max}}{1 + e^{-\lambda(HV_{eff} - HV_{50})}}$$

CMS RPC also define two points on this sigmoid that called *knee* and *working point*. The corresponding voltages HV_{knee} is defined as the voltage at 95% of the maximum efficiency, and HV_{WP} is defined as in Formula 4.25.

$$(4.25) \quad HV_{WP} = HV_{knee} + \begin{cases} 100V & (\text{barrel}) \\ 150V & (\text{endcap}) \end{cases}$$

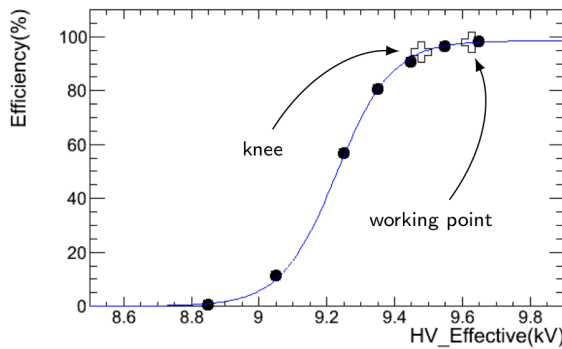


Figure 4.46: Typical efficiency sigmoid of a CMS RPC detector. The black dots correspond to the data, the blue line to the sigmoid fit and the opened cross to the knee and working extracted from the fit line.

Nevertheless, the voltage applied on a detector may vary due to a change in environmental conditions. Indeed, the variation of temperature and/or pressure will have effects on the gas density and the electrodes' resistivity which can be overcome by changing the electric field accordingly. The variation in temperature and pressure are depicted respectively in Figure 4.47 and Figure 4.48. A standard procedure to correct for temperature and pressure variations is to keep the factor $HV \cdot T/P$ constant using Formula 4.26 [252, 253] with reference values for T_0 and P_0 . For example, CMS uses $T_0 = 293.15$ K and $P_0 = 965$ hPa.

$$(4.26) \quad HV_{app} = HV_{eff} \frac{P_0}{P} \frac{T}{T_0}$$

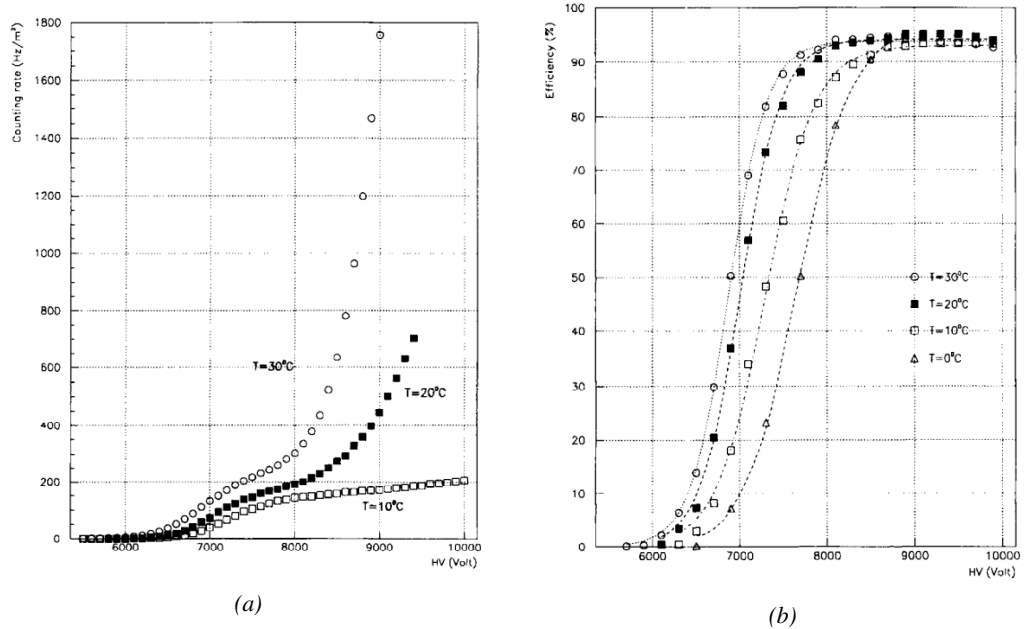


Figure 4.47: Effect of the temperature variation on the rate (Figure 4.47a) and the efficiency (Figure 4.47b) of a RPC [252].

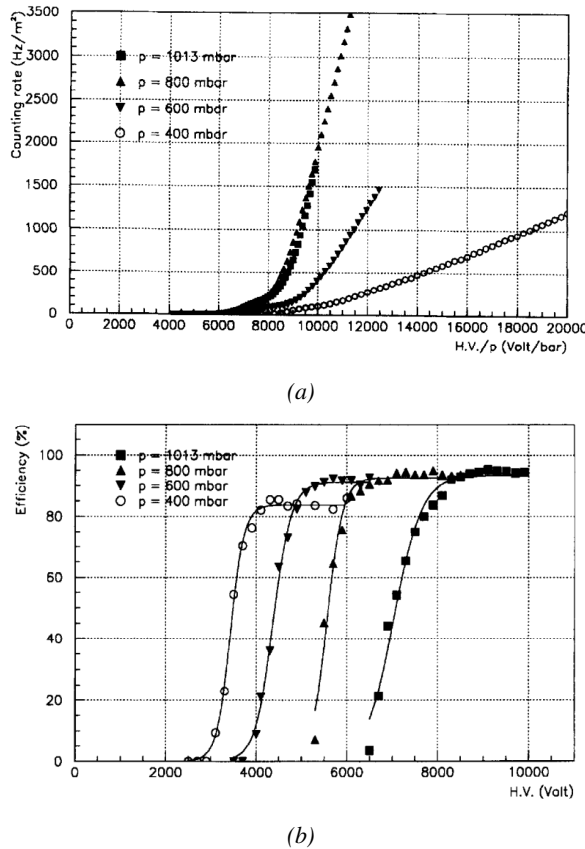


Figure 4.48: Effect of the pressure variation on the rate (Figure 4.48a) and the efficiency (Figure 4.48b) of a RPC [253].

It was actually found that such a simple procedure would overcorrect the applied voltage in the case the variations of temperature or pressure were too important [254–257]. CMS, considering that the temperature variations in the detector cavern were very small, decided only to improve the pressure correction, giving rise to Formula 4.27 [254] while on the other hand, ATLAS decided to have a more robust correction for both parameters and uses Formula 4.28 instead [257]. The coefficients α , in the case of CMS, and α, β , in the case of ATLAS, are extracted from fit on available dataset obtained during the operation of the detectors.

$$(4.27) \quad HV_{app} = HV_{eff} \left(1 - \alpha + \alpha \frac{P_0}{P} \right) \frac{T}{T_0}, \quad \alpha = 0.8$$

$$(4.28) \quad HV_{eff} = HV_{app} \left(1 + \alpha \frac{\Delta T}{T_0} \right) \left(1 - \beta \frac{\Delta P}{P_0} \right), \quad \alpha = 0.5, \beta = 0.71$$

5

3012

3013

3014

Longevity studies and Consolidation of the present CMS RPC subsystem

3015 The RPC system, located in both barrel and endcap regions, provides a fast, independent muon trigger
3016 with a looser p_T threshold over a large portion of the pseudo-rapidity range ($|\eta| < 1.6$). During
3017 HL-LHC operations the expected conditions in terms of background and pile-up will make the iden-
3018 tification and correct p_T assignment a challenge for the muon system. The goal of RPC upgrade is to
3019 provide additional hits to the Muon System with more precise timing. All this information will be
3020 elaborated by the Trigger System in a global way enhancing the performance of the trigger in terms
3021 of efficiency and rate control. The RPC Upgrade is based on two projects: an improved Link Board
3022 System and the extension of the RPC coverage up to $|\eta| = 2.4$.

3023 The Link Board System is responsible for the processing, the synchronization and the zero-
3024 suppression the signals coming from the RPC FEBs. The Link Board components have been pro-
3025 duced between 2006 and 2007 and will be subjected to ageing and failure on a long term scale. An
3026 upgraded Link Board System will overcome the ageing problems and will allow for a more precise
3027 timing information to the RPC hits from 25 to 1.5 ns.

3028 In order to develop an improved RPC that fulfills CMS requirements, an extensive R&D program is
3029 being conducted. The benefits of adding two new RPC layers in the innermost ring of stations 3 and
3030 4 will be mainly observed in the neutron-induced background reduction and efficiency improvement
3031 for both trigger and offline reconstruction.

3032 The coverage of the RPC System up to higher pseudo-rapidity $|\eta| = 2.1$ was part of the original
3033 CMS TDR. Nevertheless, the expected background rates being higher than the certified rate capabili-
3034 ty of the present CMS RPCs in that region and the budget being limited, RPCs were restricted to a
3035 shorter range. Even though the iRPC technology that will equip the extension of the Muon System
3036 will be different than the current CMS RPC technology, it is necessary to certify the rate capability
3037 and longevity of the existing detectors as the radiation level will increase together with the increase
3038 of instantaneous luminosity of the LHC. For this purpose, spare RPC detectors built but not installed
3039 in CMS have been installed in different irradiation facilities, first of all, to certify the detectors to the

3040 new levels of irradiation they will be subjected to and, finally, to study their ageing and certify their
 3041 good operation throughout the HL-LHC program.

3042 5.1 Testing detectors under extreme conditions

3043 The upgrade from LHC to HL-LHC will increase the peak luminosity from $10^{34} \text{ cm}^{-2} \text{ s}^{-1}$ to reach
 3044 $5 \times 10^{34} \text{ cm}^{-2} \text{ s}^{-1}$, increasing in the same way the total expected background to which the RPC
 3045 System will be subjected to. Mainly composed of low energy gammas, neutrons, and electrons and
 3046 positrons from $p\text{-}p$ collisions, but also of low momentum primary and secondary muons, punch-
 3047 through hadrons from calorimeters, and particles produced in the interaction of the beams with
 3048 collimators, the background will mostly affect the regions of CMS that are the closest to the beam
 3049 line, i.e. the RPC detectors located in the endcaps.

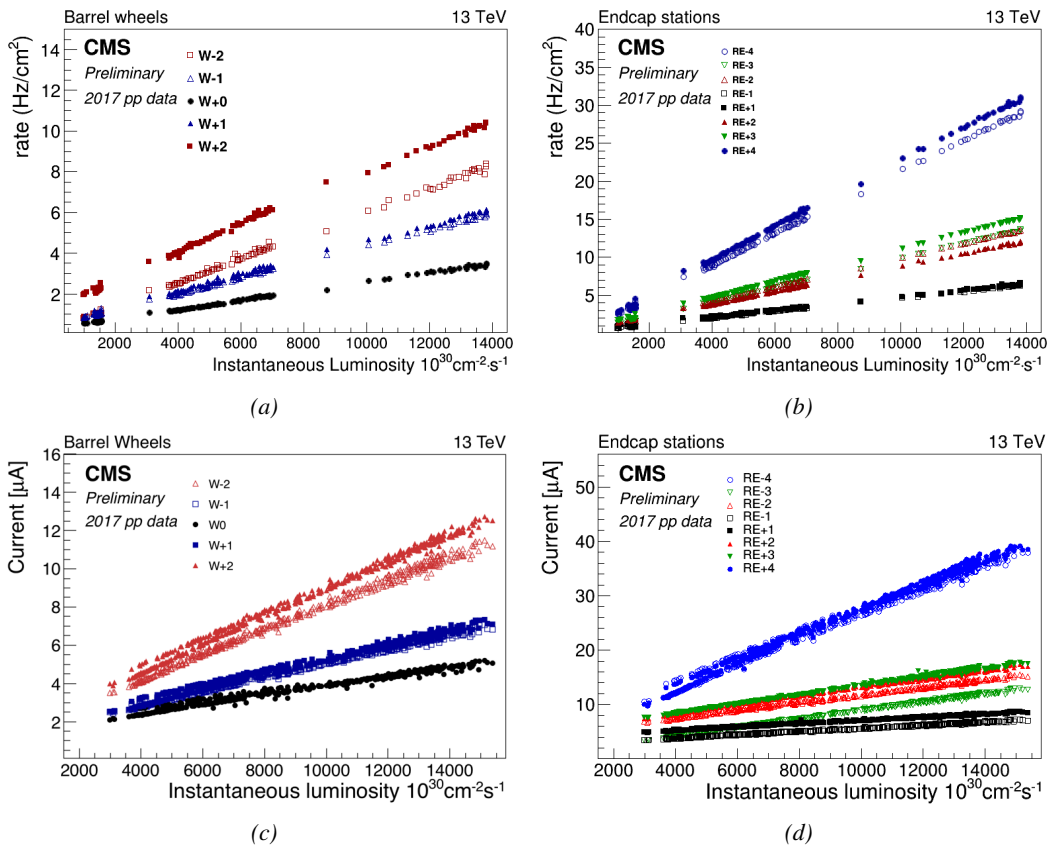


Figure 5.1: Mean RPC Barrel (left column) and Endcap (right column) rate (top row) and current (bottom row) as a function of the instantaneous luminosity as measured in 2017 $p\text{-}p$ collision data.

3050 Data collected over 2017, presented through Figure 5.1, allows to study the values of the back-
 3051 ground rate in all the RPC System. This was achieved thanks to a monitoring of the rates in each
 3052 RPC rolls, where rolls correspond to the pseudo-rapidity partitioning of the readout electronics, and
 3053 of the current in each HV channel. A linear dependence in between the mean rate or current with

instantaneous luminosity is showed in selected runs with identical LHC running parameters. In Figure 5.2, a linear extrapolation of the distribution of the background hit rate per unit area as well as the integrated charge is showed at a HL-LHC condition. The maximum rate per unit area in the endcap detectors at HL-LHC conditions is expected to be of the order of 600 Hz/cm^2 while the charge deposition should exceed 800 mC/cm^2 . The detectors will then be certified up to an irradiation of 840 mC/cm^2 . These extrapolations are provided with a required safety factor 3 for the certification study.

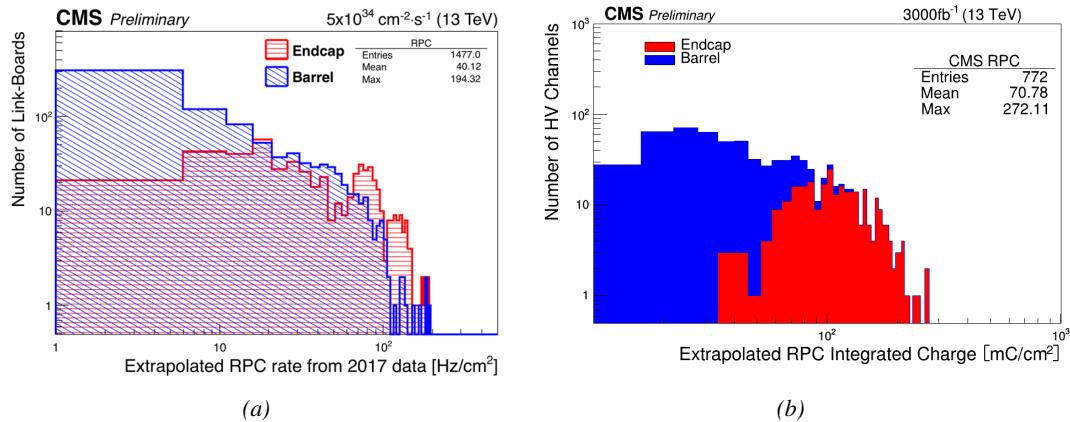


Figure 5.2: Figure 5.2a: The hit rate per region (Barrel, Endcap) is linearly extrapolated to HL-LHC highest instantaneous luminosity ($5 \times 10^{34} \text{ cm}^{-2} \text{ s}^{-1}$) using the rate as a function of instantaneous luminosity recorded by RPCs in 2017 showing a linear dependence. Figure 5.2b: The integrated charge per region (Barrel, Endcap) is extrapolated to HL-LHC integrated luminosity (3000 fb^{-1}) using the data accumulated in 2016 in every HV channels.

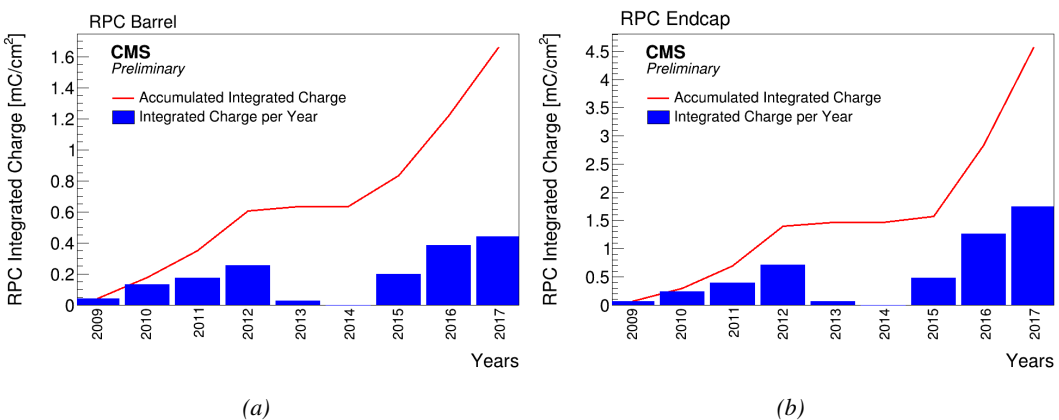


Figure 5.3: CMS RPC mean integrated charge in the Barrel region (Figure 5.3a) and the Endcap region (Figure 5.3b). The integrated charge per year is shown in blue. The red curve shows the evolution of the accumulated integrated charge through time. The blank period in 2013 and 2014 corresponds to LS1. The total integrated charge for the entire operation period (Oct. 2009 - Dec. 2017) is estimated to be about $1.66 \text{ mC}/\text{cm}^2$ in the Barrel and $4.58 \text{ mC}/\text{cm}^2$ in the Endcap.

In the past, extensive long-term tests were carried out at several gamma and neutron facilities

certifying the detector performance. Both full size and small prototype RPCs have been irradiated with photons up to an integrated charge of $\sim 0.05 \text{ C/cm}^2$ and $\sim 0.4 \text{ C/cm}^2$ respectively and were certified for rates reaching 200 Hz/cm^2 [258, 259]. Since the beginning of Run-I until December 2017, the RPC system provided stable operation and excellent performance and did not show any ageing effects for a maximum integrated charge in a detector of the order of 0.01 C/cm^2 - the average being of the order of 2 mC/cm^2 in the Barrel and 5 mC/cm^2 in the Endcap, closer to the beam line, as can be seen from Figure 5.3 - and a peak luminosity reaching $1.4 \times 10^{34} \text{ cm}^{-2} \text{ s}^{-1}$ during 2017 data taking period.

To perform the necessary studies on the present CMS RPC detectors, facilities offering the possibility to irradiate the chambers are necessary in order to recreate HL-LHC conditions or stronger and study their performance through time. Such facilities exist at CERN and were exploited to conduct this study. A first series of preliminary studies were conducted in the former gamma facility of CERN (GIF) before its dismantlement. This preliminary study was used as a stepping stone towards the building of a more powerful irradiation fully dedicated to longevity studies of CMS and ATLAS subsystems in the perspective of HL-LHC. The period of preliminary work has also been a key moment in the elaboration and improvement of data acquisition, offline analysis and online monitoring tools that are extensively used in the new gamma irradiation facility.

5.1.1 GIF

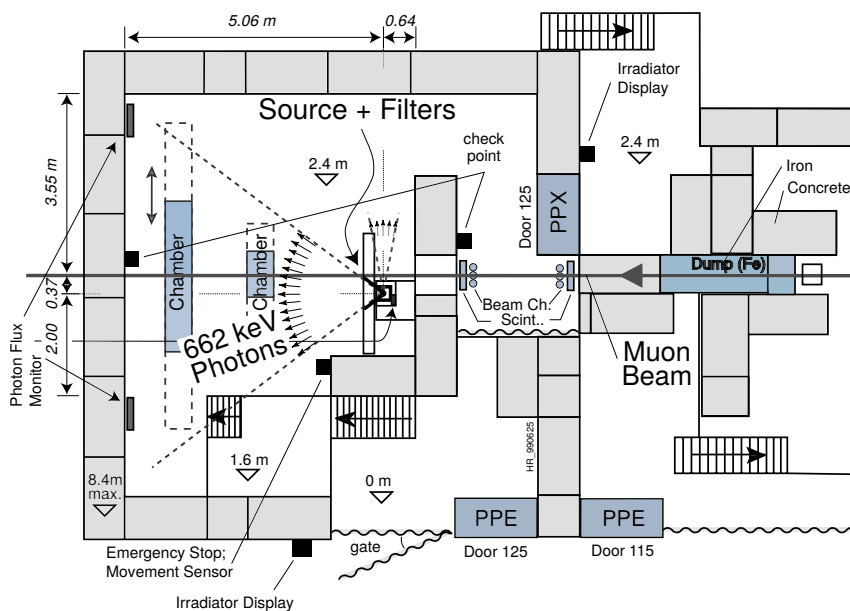


Figure 5.4: Layout of the test beam zone called X5c GIF at CERN. Photons from the radioactive source produce a sustained high rate of random hits over the whole area. The zone is surrounded by 8 m high and 80 cm thick concrete walls. Access is possible through three entry points. Two access doors for personnel and one large gate for material. A crane allows installation of heavy equipment in the area.

Located in the SPS West Area at the downstream end of the X5 test beam, the Gamma Irradiation Facility (GIF) was a test area in which particle detectors were exposed to a particle beam in presence of an adjustable gamma background [260]. Its goal was to reproduce background conditions these

detectors would suffer in their operating environment at LHC. GIF layout is showed in Figure 5.4. Gamma photons are produced by a strong ^{137}Cs source installed in the upstream part of the zone inside a lead container. The source container includes a collimator, designed to irradiate a $6 \times 6 \text{ m}^2$ area at 5 m maximum to the source. A thin lens-shaped lead filter helps providing with a uniform out-coming flux in a vertical plane, orthogonal to the beam direction. The photon rate is controlled by further lead filters allowing the maximum rate to be limited and to vary within a range of four orders of magnitude. Particle detectors under test are then placed within the pyramidal volume in front of the source, perpendicularly to the beam line in order to profit from the homogeneous photon flux. Adjusting the background flux of photons can then be done by using the filters and choosing the position of the detectors with respect to the source.

As described on Figure 5.5, the ^{137}Cs source emits a 662 keV photon in 85% of the decays. An activity of 740 GBq was measured on the 5th of March 1997. To estimate the strength of the flux in 2014, was considered the nuclear decay through time associated to the Cesium source whose half-life is well known ($t_{1/2} = (30.05 \pm 0.08) \text{ y}$). The GIF tests were done in between the 20th and the 31st of August 2014, i.e. at a time $t = (17.47 \pm 0.02) \text{ y}$ resulting in an attenuation of the activity from 740 GBq in 1997 to 494 GBq in 2014.

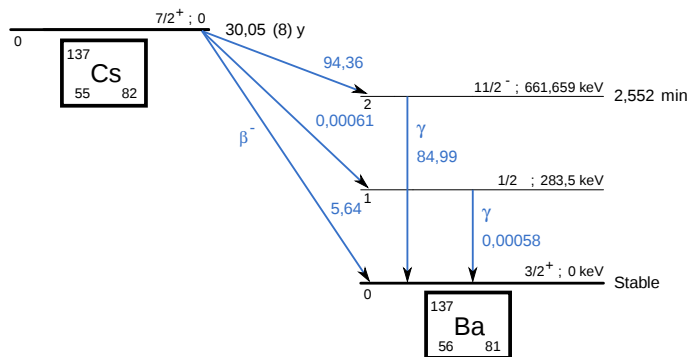


Figure 5.5: ^{137}Cs decays by β^- emission to the ground state of ^{137}Ba (BR = 5.64%) and via the 662 keV isomeric level of ^{137}Ba (BR = 94.36%) whose half-life is 2.55 min.

5.1.2 GIF++

The new Gamma Irradiation Facility (GIF++), located in the SPS North Area at the downstream end of the H4 test beam, has replaced its predecessor during LS1 and has been operational since spring 2015 [261]. Like GIF, GIF++ features a ^{137}Cs source of 662 keV gamma photons, their fluence being controlled with a set of filters of various attenuation factors. The source provides two separated large irradiation areas for testing several full-size muon detectors with homogeneous irradiation, as presented in Figure 5.6.

The source activity was measured to be about 13.5 TBq in March 2016. The photon flux being far greater than HL-LHC expectations, GIF++ provides an excellent facility for accelerated ageing tests of muon detectors. The source is situated in a bunker designed to perform irradiation test along a muon beam line, the muon beam being available during selected periods throughout the year. The H4 beam, providing the area with muons with a maximum momentum of about 150 GeV/c, passes through the GIF++ zone and is used to periodically study the performance of the detectors placed under long term irradiation. Its flux is of $104 \text{ particles/s/cm}^2$ focused in an area similar to

3113 $10 \times 10 \text{ cm}^2$. Therefore, with properly adjusted filters, one can simulate the background expected at
 3114 HL-LHC and study the performance and ageing of muon detectors in HL-LHC environment.

3115

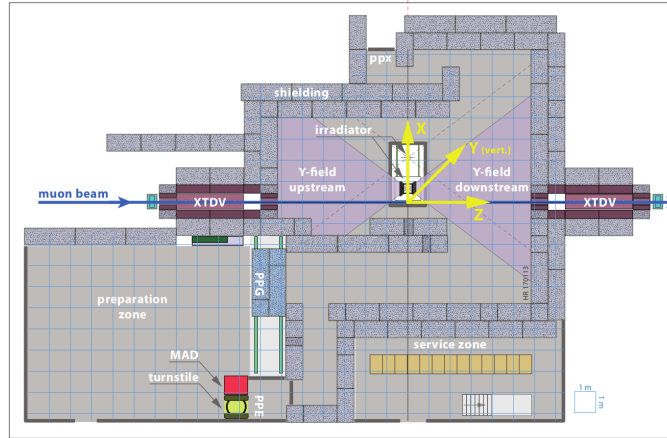


Figure 5.6: Floor plan of the *GIF++* facility. When the facility downstream of the *GIF++* takes electron beam, a beam pipe is installed along the beam line (z -axis). The irradiator can be displaced laterally (its center moves from $x = 0.65 \text{ m}$ to 2.15 m), to increase the distance to the beam pipe.

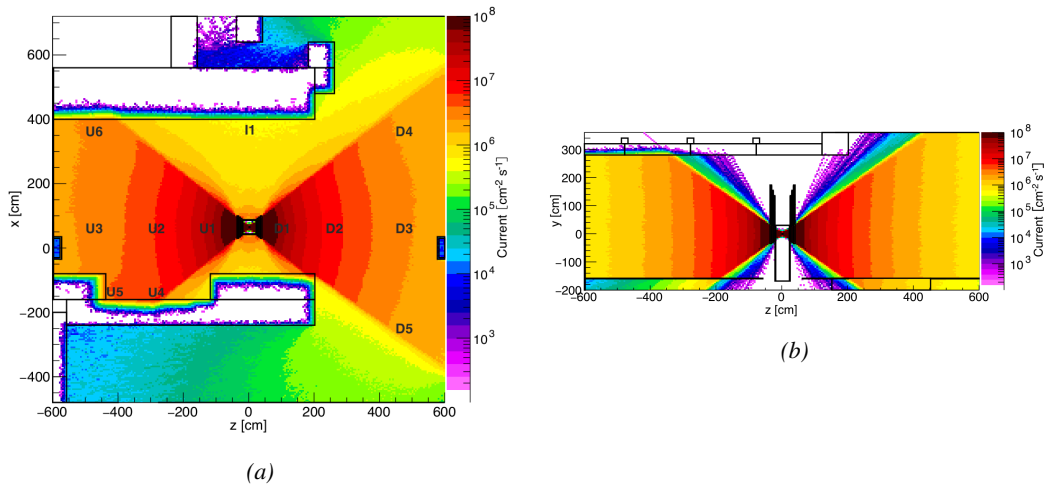


Figure 5.7: Simulated unattenuated current of photons in the xz plane (Figure 5.7a) and yz plane (Figure 5.7b) through the source at $x = 0.65 \text{ m}$ and $y = 0 \text{ m}$ [262]. With angular correction filters, the current of 662 keV photons is made uniform in xy planes.

3116 The gamma current as simulated with GEANT4 is presented in Figure 5.7 in which the labels
 3117 UN, DN, with $N \in [1 : 5]$ and I1 correspond to the position of different Radiation Monitoring
 3118 (RADMON) sensors dedicated to measuring the irradiation in the bunker area [262]. According to
 3119 the simulation results, that agree within 12% to the doses measured with the RADMONs, the RPCs
 3120 that will be tested in *GIF++* can expect a maximal gamma current of the order of 2 to 5×10^6

3121 $\text{cm}^{-2} \text{s}^{-1}$ assuming they will always stay in a region in between sensor U5 and the back wall of the
 3122 upstream area.

3123 5.2 Preliminary studies at GIF

3124 5.2.1 RPC test setup

3125 During summer 2014, preliminary tests have been conducted in the GIF area on an endcap chamber
 3126 of type RE4/2 and labeled RE-4-2-BARC-161 produced for the extension of the endcap with a
 3127 fourth disk in 2013. This chamber has been placed into a trolley covered with a tent. The position
 3128 of the RPC inside the tent and of the tent with respect to the source in the bunker are described in
 3129 Figure 5.8. The goal of the study were to have a preliminary understanding of the rate capability
 3130 of the present technology used in CMS. It was decided to measure the efficiency of the RPC under
 3131 irradiation at detecting cosmic muons as, at the time of the tests, the beam not operational anymore.
 3132 Three different absorber settings were used and compared to the case where the detector was not ir-
 3133 radated in order to study the evolution of the performance of the detector with increasing exposition
 3134 to gamma radiation. First of all, measurements were done with fully opened source. To complete
 3135 this preliminary study, the gamma flux has been attenuated by a factor 2, a factor 5 and finally the
 3136 source was shut down. Was measured the efficiency of the RPC at detecting the cosmic muons in
 3137 coincidence with a cosmic trigger as well as the background rate as seen by the detectors.

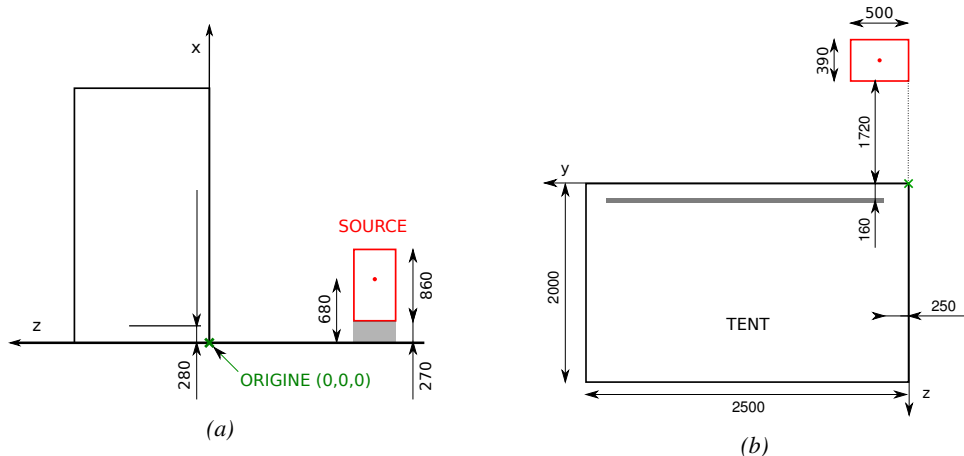


Figure 5.8: Description of the RPC setup. Dimensions are given in mm. A tent containing RPCs is placed at 1720 mm from the source container. The source is situated in the center of the container. RE-4-2-BARC-161 chamber is 160 mm inside the tent. This way, the distance between the source and the chambers plan is 2060 mm. Figure 5.8a provides a side view of the setup in the xz plane while Figure 5.8b shows a top view in the yz plane.

3138 The trigger system was composed of 2 plastic scintillators and was placed in front of the setup
 3139 with an inclination of 10° with respect to the detector plane in order to look at cosmic muons. Using
 3140 this particular trigger layout, showed in Figure 5.9, leads to a cosmic muon hit distribution into the
 3141 chamber similar to the one of Figure 5.10. Measured without gamma irradiation, two peaks can
 3142 be seen on the profile of readout partition B, centered on strips 52 and 59. Section 5.2.2 will help
 3143 us understand that these two peaks are due respectively to forward and backward coming cosmic

³¹⁴⁴ particles where forward coming particles are first detected by the scintillators and then the RPC
³¹⁴⁵ while the backward coming muons are first detected in the RPC.



Figure 5.9: RE-4-2-BARC-161 chamber is inside the tent as described in Figure 5.8. In the top right, the two scintillators used as trigger can be seen. This trigger system has an inclination of 10° relative to horizontal and is placed above half-partition B2 of the RPCs. PMT electronics are shielded thanks to lead blocks placed in order to protect them without stopping photons from going through the scintillators and the chamber.

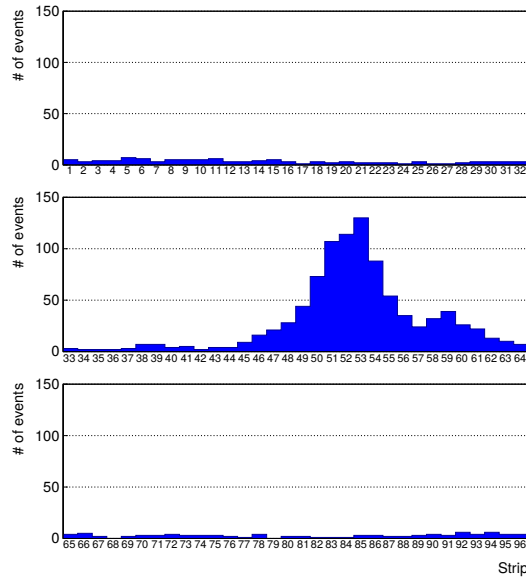


Figure 5.10: Hit distributions over all 3 partitions of RE-4-2-BARC-161 chamber is showed. Top, middle and bottom figures respectively correspond to partitions A, B, and C. The profiles show that some events still occur in other half-partitions than B2, which corresponds to strips 49 to 64, in front of which the trigger is placed, contributing to the inefficiency of detection of cosmic muons. In the case of partitions A and C, the very low amount of data can be interpreted as noise. On the other hand, it is clear that a little portion of muons reach the half-partition B1, corresponding to strips 33 to 48.

3146 The data taking is then performed thanks to a CEAN TDC module of type V1190A [263] to
 3147 which is connected the digitized output of the RPC Front-End Board, as described in Figure 5.11a
 3148 and the trigger signal from the telescope. The communication with the computer is performed thanks
 3149 to a CAEN communication module of type V1718 [264]. In order to control the rates recorded by
 3150 the detector, the digitized RPC signals are also sent to scalers as described in Figure 5.11b. The
 3151 C++ DAQ software used in GIF was developed as an early attempt towards the understanding of
 3152 the CAEN libraries and the data collected by the TDCs was saved into .dat files is analysed with
 3153 an algorithm computing parameters such as efficiency, hit profile, cluster size, or gamma and noise
 3154 rates which was developed with C++ as well. Finally, histograms and curves are produced using
 3155 ROOT.

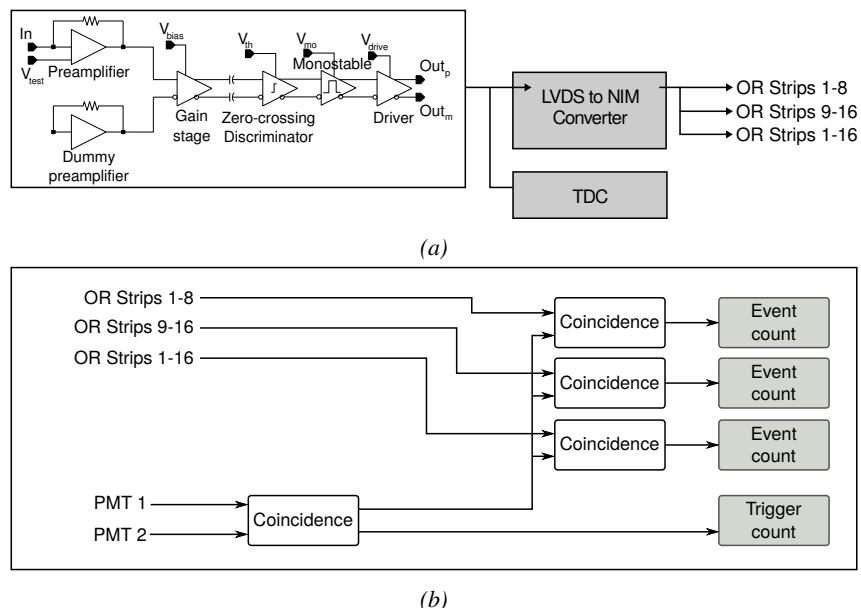


Figure 5.11: Signals from the RPC strips are shaped by the FEE described on Figure 5.11a. Output LVDS signals are then read-out by a TDC module connected to a computer or converted into NIM and sent to scalers. Figure 5.11b describes how these converted signals are put in coincidence with the trigger.

3156 5.2.2 Geometrical acceptance of the setup layout to cosmic muons

3157 In order to profit from a constant gamma irradiation, the detectors inside of the GIF bunker need
 3158 to be placed in a plane orthogonal to the beam line. The muon beam that used to be available was
 3159 meant to test the performance of detectors under test. This beam not being active anymore, an other
 3160 solution to test detector performance had to be used. Thus, it has been decided to use cosmic muons
 3161 detected through a telescope composed of two scintillators. Lead blocks were used as shielding to
 3162 protect the photomultipliers from gammas as can be seen from Figure 5.9.

3163 An inclination of $\sim 10^\circ$ has been given to the cosmic telescope to maximize the muon flux. A
 3164 good compromise had to be found between good enough muon flux and narrow enough hit distribution
 3165 to be sure to contain all the events into only one half partitions as required from the limited
 3166 available readout hardware. It was then foreseen to detect muons and read them out only from
 3167 half-partition B2, the last 16 channels of readout partition B (i.e. strips 49 to 64). Nevertheless,

3168 a consequence of the misplaced trigger, that can be seen as a loss of events in half-partition B1
 3169 (strips 33 to 48) in Figure 5.10, is an inefficiency. The observed inefficiency of approximately 20%
 3170 highlighted in Figure 5.12 by comparing the performance of chamber RE-4-2-BARC-161 as mea-
 3171 sured prior to the study at GIF and at GIF without irradiation seems too important, compared to the
 3172 12.7% of data contained into the first 16 strips observed on Figure 5.10, to only be explained by the
 3173 geometrical acceptance of the setup itself. Simulations have been conducted to show how the setup
 3174 brings inefficiency.

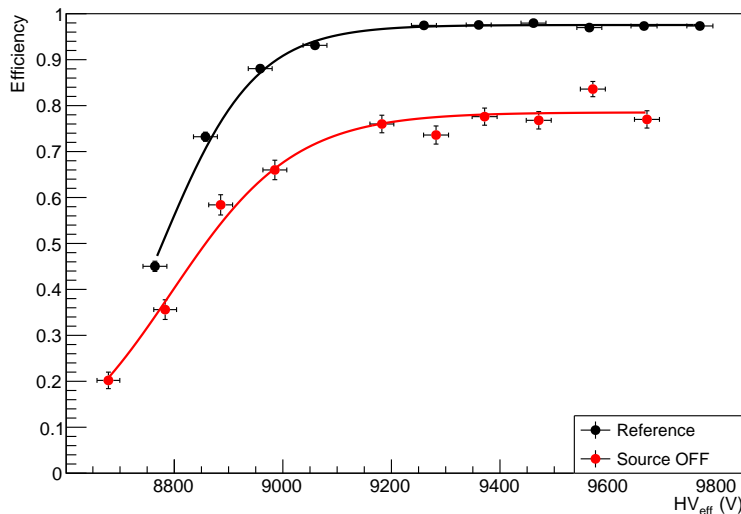


Figure 5.12: Results are derived from data taken on half-partition B2 only. On the 18th of June 2014, data has been taken on chamber RE-4-2-BARC-161 at CERN building 904 (Prevessin Site) with cosmic muons providing us a reference efficiency plateau of $(97.54 \pm 0.15)\%$ represented by a black curve. A similar measurement has been done at GIF on the 21st of July with the same chamber giving a plateau of $(78.52 \pm 0.94)\%$ represented by a red curve.

3175 5.2.2.1 Description of the simulation layout

3176 The layout of GIF setup has been reproduced, only roughly using Figure 5.9 due to the lack of
 3177 measures, and incorporated into a C++ Monte Carlo (MC) simulation to study the geometrical ac-
 3178 ceptance of the telescope projected onto the readout strips [265]. A 3D view of the simulated layout
 3179 is given into Figure 5.13. Muons are generated randomly in a horizontal plane located at a height
 3180 corresponding to the lowest point of the PMTs. This way, the needed size of the plane in order to
 3181 simulate events happening at very large azimuthal angles (i.e. $\theta \approx \pi$) can be kept relatively small
 3182 while the total number of muon tracks to propagate is kept relatively small. The muon flux is de-
 3183 signed to follow the usual $\cos^2\theta$ distribution for cosmic particles. The goal of the simulation is to
 3184 look at muons that pass through the telescope composed of the two scintillators and define their dis-
 3185 tribution onto the RPC read-out plane. During the reconstruction, the read-out plane is then divided
 3186 into read-out strips and each muon track is assigned to a strip.

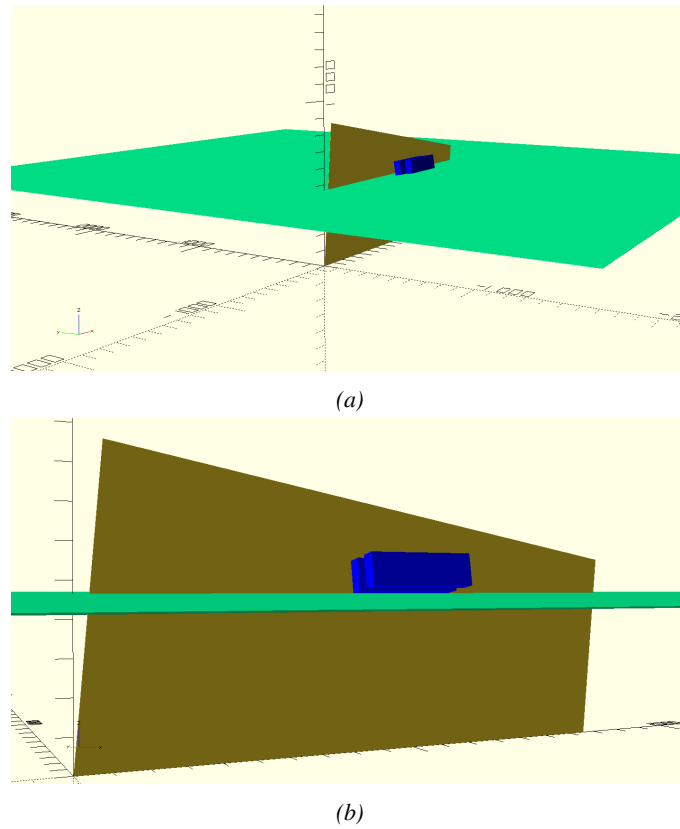


Figure 5.13: Representation of the layout used for the simulations of the test setup. The RPC read-out plane is represented as a yellow trapezoid while the two scintillators as blue cuboids looking at the sky. The green plane corresponds to the muon generation plane within the simulation. Figure 5.8a shows a global view of the simulated setup. Figure 5.8b shows a zoomed view that allows to see the 2 scintillators as well as the full RPC plane.

5.2.2.2 Simulation procedure

3187 $N_\mu = 10^8$ muons are randomly generated inside the muon plane with an azimuthal angle θ chosen
 3188 to follow a $\cos^2\theta$ distribution. Infinite planes are associated to each surface of the scintillators.
 3189 Knowing the muon position into the muon generation plane and its direction allows, by assuming
 3190 that muons travel in a straight line, to compute the intersection of the muon track with these planes.
 3191 Applying conditions to the limits on the contours of the scintillators' faces then gives an answer to
 3192 whether or not the muon passed through the scintillators. In the case the muon was not *detected* into
 3193 both scintillators, the simulation discards the muon and generates a new one.
 3194

3195 On the contrary, if the muon is labeled as good, its position within the RPC read-out plane
 3196 is computed and the corresponding strip, determined through geometrical tests, gets a *hit*. Muon
 3197 hits fill different histograms whether they are associated to forward or backward coming muons.
 3198 A discrimination is performed according to their direction components. An (x, y, z) position into
 3199 the generation plane as well as a $(\theta; \phi)$ pair are associated to each generated muon providing with
 3200 information on the direction the track follows. This way, muons satisfying the condition $0 \leq \phi < \pi$
 3201 are labeled as *backward* coming muons while muons satisfying $\pi \leq \phi < 2\pi$ as *forward* coming

3202 muons.

3203 **5.2.2.3 Results and limitations**

3204 The output from the simulation is given in Figure 5.14 in which the distribution is showed for all
 3205 muons but also for the separate contributions of forward and backward coming muons. The strip
 3206 number is here given in a range of 1 to 32 corresponding to the 32 strips contained in each RPC
 3207 read-out partition, without taking into account the fact that partition B of an RPC correponds, by
 3208 convention, to strips 33 to 64. Comparing the number of muons recorded respectively in the first 16
 3209 strips and the in all of the 32 strips of the RPC read-out panel, it can be established than, out of the
 3210 total amount of muons that have passed through the telescope and reached the RPC, 16.8% where to
 3211 be detected in the 16 first strip of the read-out plane corresponding to half partition B1. This brings
 3212 a geometrical inefficiency of the same amount that can then be used to correct the data by scaling up
 3213 by a factor $c_{geo} = 1/(1 - 0.168)$ the maximum efficiency measured during data taking.

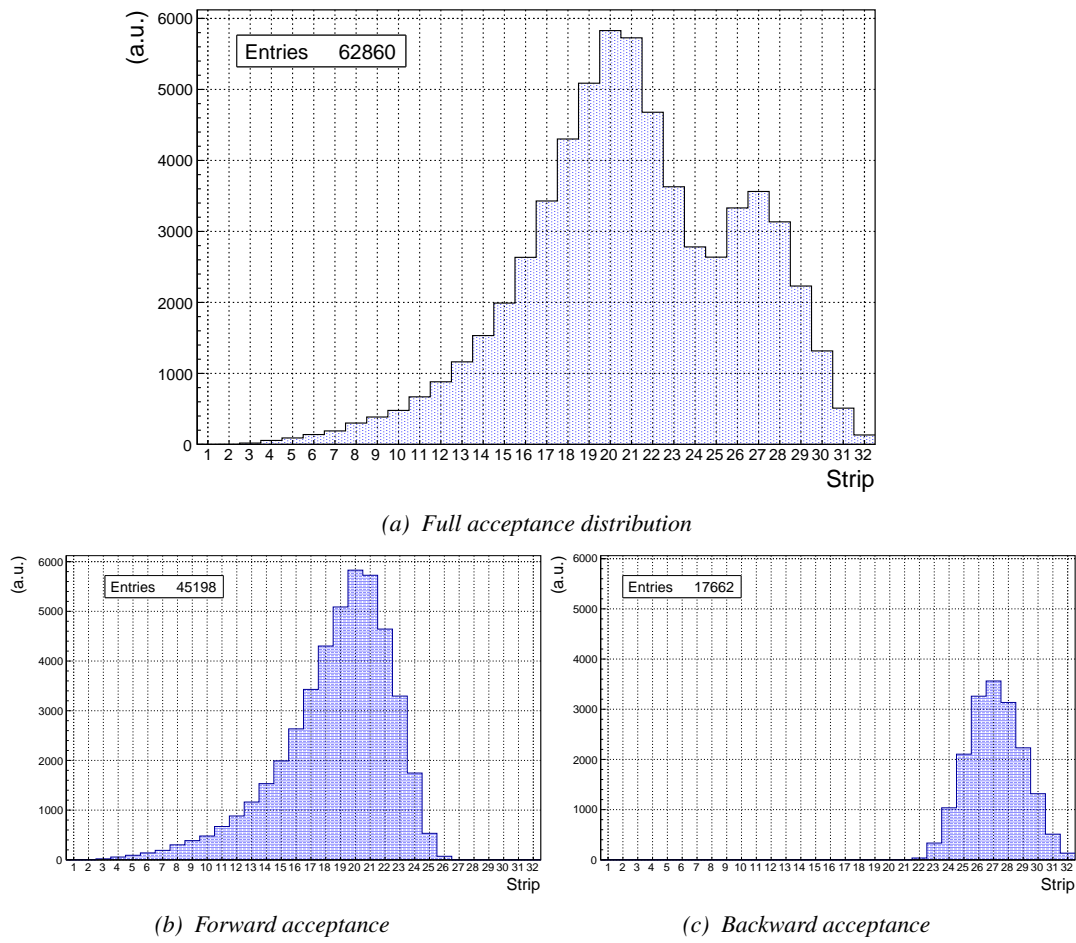


Figure 5.14: Geometrical acceptance distribution as provided by the Monte Carlo simulation.

3214 Nevertheless, it is difficult to evaluate a systematical uncertainty on this geometrical correction

for different reasons. First of all, even though the dimensions of the scintillators and of the RPC are well known, the position of each element of the setup with respect to one another was not measured. It was then necessary, using known dimensions, to extract the positions of each element from Figure 5.9 with unknown uncertainty. The inclination is also roughly measured to be 10° and even if the position of each peak, distant in the simulation of 7 strips, tends to confirm this assumption, the geometrical inefficiency would be affected by a variation of the inclination angle. Introducing in the simulation an error of $\pm 2^\circ$ would lead to a correction factor $c_{geo} = 1.20^{+0.04}_{-0.03}$ that allows for a good improvement of the efficiency measured in GIF, as can be seen from Figure 5.15. GIF measurement is in agreement with the reference curve within statistical errors.

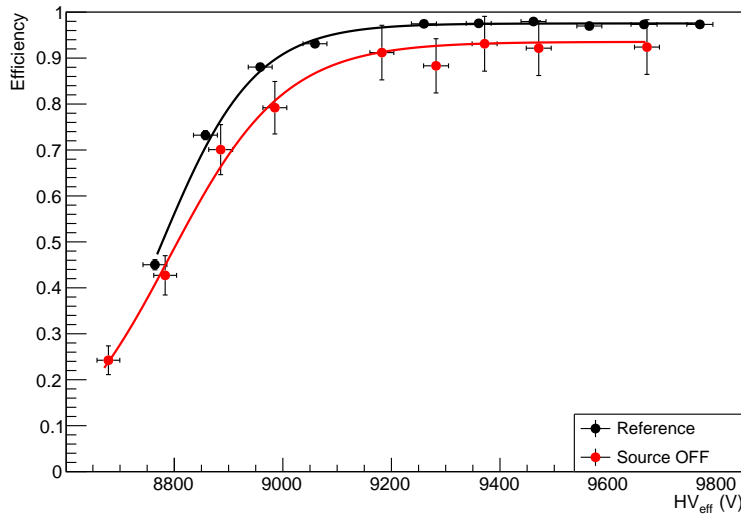


Figure 5.15: Correction of the efficiency without source. The efficiency after correction gets much closer to the Reference measurement performed before the study in GIF by reaching a plateau of $(93.52 \pm 2.64)\%$.

Further corrections could be also be brought as it can easily be understood that the distribution showed through Figure 5.14a differs from the measured hit profile showed in Figure 5.10. The contributions of forward and backward muon indicate that 28.1% of the total geometrical acceptance should contribute to detecting backward muons whereas it is measured that the hit profile contains 22.0% of backward data only. This estimation of the backward versus forward content in the data was done through a fit using a sum of two skew distribution, one acting on the forward muon peak while the other acts on the backward muon fit, as showed in Figure 5.16. Although a skew distribution lacks physical interpretation, it allows to easily fit such kind of data. A description of a skew distribution, as the product of a gaussian and a sigmoid (Formula 5.1), is given through Formula 5.2.

$$(5.1) \quad g(x) = A_g e^{\frac{-(x-\bar{x})^2}{2\sigma^2}}, \quad s(x) = \frac{A_s}{1 + e^{-\lambda(x-x_i)}}$$

$$(5.2) \quad sk(x) = g(x) \times s(x) = A_{sk} \frac{e^{\frac{-(x-\bar{x})^2}{2\sigma^2}}}{1 + e^{-\lambda(x-x_i)}}$$

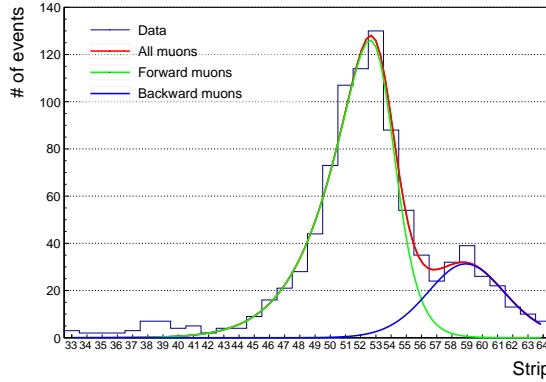


Figure 5.16: Hit distributions over read-out partition B of RE-4-2-BARC-161 chamber together with skew distribution fits corresponding to forward and backward coming muons.

From the obvious difference in between geometrical simulation and data, it is necessary to realize that the geometrical acceptance and the hit profile are two distinct information. When the geometrical acceptance only provides with the information about what the detector can expect to see in a perfect world where all muons are detected in the exact same way independently from their energy, angle of incidence, fluctuation of the detector gain due to complexe avalanche development, thresholds applied on the scintillators and on the RPC FEEs to reduce the noise, the cross-talk and corresponding spread of the induced charge observed on the read-out strips, the hit profile provides the final product of all the previously mentioned contributions and can greatly differ from purely geometrical considerations. A full physics analysis involving softwares such as GEANT would be required to further refine the correction on the measured efficiency at GIF.

5.2.3 Photon flux at GIF

In order to understand and evaluate the γ flux in the GIF area, simulations had been conducted at the time GIF was opened for research purposes [260]. Table 5.1 presented in this article gives the γ flux for different distances D to the source. The simulation was done using GEANT and a Monte Carlo N-Particle (MCNP) transport code, and the flux F is given with the estimated error from these packages expressed in %.

Nominal ABS	Photon flux F [$\text{cm}^{-2} \text{s}^{-1}$]			
	at $D = 50 \text{ cm}$	at $D = 155 \text{ cm}$	at $D = 300 \text{ cm}$	at $D = 400 \text{ cm}$
1	$0.12 \times 10^8 \pm 0.2\%$	$0.14 \times 10^7 \pm 0.5\%$	$0.45 \times 10^6 \pm 0.5\%$	$0.28 \times 10^6 \pm 0.5\%$
2	$0.68 \times 10^7 \pm 0.3\%$	$0.80 \times 10^6 \pm 0.8\%$	$0.25 \times 10^6 \pm 0.8\%$	$0.16 \times 10^6 \pm 0.6\%$
5	$0.31 \times 10^7 \pm 0.4\%$	$0.36 \times 10^6 \pm 1.2\%$	$0.11 \times 10^6 \pm 1.2\%$	$0.70 \times 10^5 \pm 0.9\%$

Table 5.1: Total photon flux ($E\gamma \leq 662 \text{ keV}$) with statistical error predicted considering a ^{137}Cs activity of 740 GBq at different values of the distance D to the source along the x-axis of irradiation field [260].

The simulation does not provide with an estimated flux at the level of the RPC under test. First of all, it is necessary to extract the value of the flux from the available data contained in the original paper and then to estimate the flux in 2014 at the time the experimentation took place. In the case of a pointlike source emitting isotropic and homogeneous gamma radiations, the gamma flux F at a

3253 distance D from the source with respect to a reference point situated at D_0 where a known flux F_0
 3254 is measured will be expressed like in Formula 5.3, assuming that the flux decreases as $1/D^2$, where
 3255 c is a fitting factor that can be written from Formula 5.3 as Formula 5.4. Finally, using Equation 5.4
 3256 and the data of Table 5.1, with $D_0 = 50$ cm as reference point, Table 5.2 can be built. It is interesting
 3257 to note that c for each value of D doesn't depend on the absorption factor.

$$(5.3) \quad F^{ABS} = F_0^{ABS} \times \left(\frac{cD_0}{D} \right)^2$$

$$(5.4) \quad c = \frac{D}{D_0} \sqrt{\frac{F^{ABS}}{F_0^{ABS}}} , \quad \Delta c = \frac{c}{2} \left(\frac{\Delta F^{ABS}}{F^{ABS}} + \frac{\Delta F_0^{ABS}}{F_0^{ABS}} \right)$$

Nominal ABS	Correction factor c		
	at $D = 155$ cm	at $D = 300$ cm	at $D = 400$ cm
1	$1.059 \pm 0.70\%$	$1.162 \pm 0.70\%$	$1.222 \pm 0.70\%$
2	$1.063 \pm 1.10\%$	$1.150 \pm 1.10\%$	$1.227 \pm 0.90\%$
5	$1.056 \pm 1.60\%$	$1.130 \pm 1.60\%$	$1.202 \pm 1.30\%$

Table 5.2: Correction factor c is computed thanks to Formula 5.4 taking as reference $D_0 = 50$ cm and the associated flux F_0^{ABS} for each absorption factor available in table 5.1.

3258 For the range of D/D_0 values available, it is possible to use a simple linear fit to get the evolution
 3259 of c that can be expressed as $c(D/D_0) = aD/D_0 + b$. Using Formula 5.5, but neglecting the
 3260 uncertainty on D that will only be used when extrapolating the values for the position of the RPC
 3261 under test whose position is not perfectly known, the results showed in Figure 5.17 is obtained.
 3262 Figure 5.17b confirms that using only a linear fit to extract c is enough as the evolution of the rate
 3263 that can be obtained superimposes well on the simulation points.

$$(5.5) \quad F^{ABS} = F_0^{ABS} \left(a + \frac{bD_0}{D} \right)^2 , \quad \Delta F^{ABS} = F^{ABS} \left[\frac{\Delta F_0^{ABS}}{F_0^{ABS}} + 2 \frac{\Delta a + \Delta b \frac{D_0}{D} + \Delta D \frac{bD_0}{D^2}}{a + \frac{bD_0}{D}} \right]$$

3264 In the context of the 2014 GIF tests, the RPC read-out plane is located at a distance $D = 206$ cm
 3265 from the source. Moreover, to estimate the strength of the flux in 2014 it is necessary to consider the
 3266 nuclear decay through time assiciated to the Cesium source whose half-life is well known ($t_{1/2} =$
 3267 (30.05 ± 0.08) y). The very first source activity measurement has been done on the 5th of March
 3268 1997 while the GIF tests where done in between the 20th and the 31th of August 2014, i.e. at a time
 3269 $t = (17.47 \pm 0.02)$ y resulting in an attenuation of the activity from 740 GBq in 1997 to 494 GBq in
 3270 2014. All the needed information to extrapolate the expected flux through the detector at the moment
 3271 of GIF preliminary tests has now been assembled, leading to Table 5.3. By assuming a sensitivity of
 3272 the RPC to γ of 2×10^{-3} , the order of magnitude of the expected hit rate per unit area would be of
 3273 the order of the kHz for the fully opened source, as reported in the last column of the table.

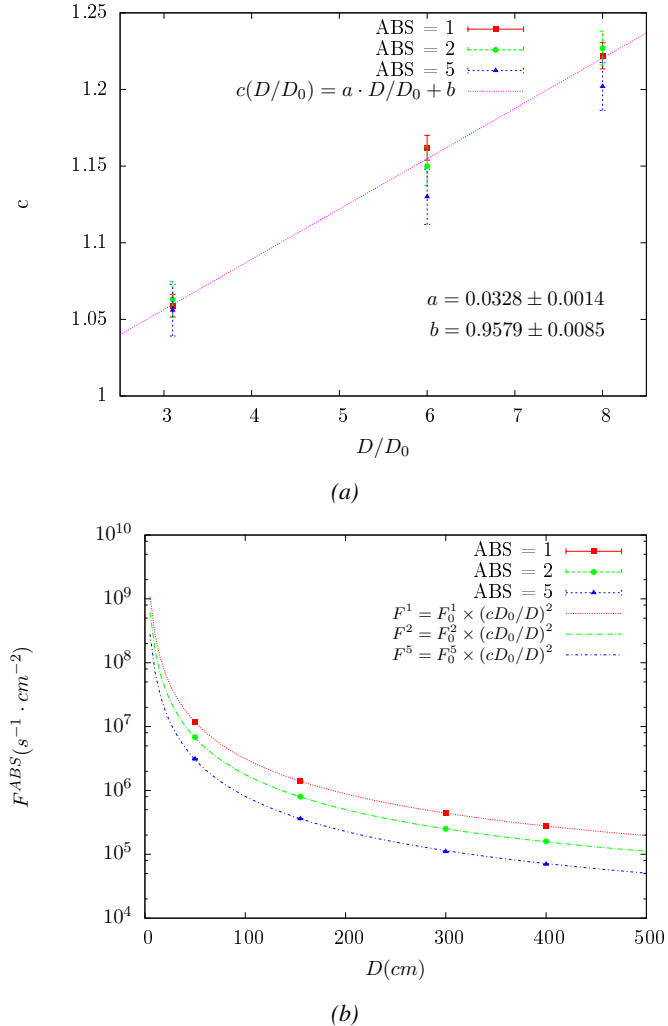


Figure 5.17: Figure 5.17a shows the linear approximation fit performed on data extracted from table 5.2. Figure 5.17b shows a comparison of Formula 5.5 with the simulated flux using a and b given in figure 5.17a in formulae 5.3 and the reference value $D_0 = 50\text{ cm}$ and the associated flux for each absorption factor F_0^{ABS} from table 5.1

Nominal ABS	Photon flux F [$\text{cm}^{-2} \text{s}^{-1}$]			Rate [Hz/cm^2] at $D^{2014} = 206\text{ cm}$
	at $D_0^{97} = 50\text{ cm}$	at $D^{97} = 206\text{ cm}$	at $D^{2014} = 206\text{ cm}$	
1	$0.12 \times 10^8 \pm 0.2\%$	$0.84 \times 10^6 \pm 1.2\%$	$0.56 \times 10^6 \pm 1.2\%$	1129 ± 14
2	$0.68 \times 10^7 \pm 0.3\%$	$0.48 \times 10^6 \pm 1.2\%$	$0.32 \times 10^6 \pm 1.2\%$	640 ± 8
5	$0.31 \times 10^7 \pm 0.4\%$	$0.22 \times 10^6 \pm 1.2\%$	$0.15 \times 10^6 \pm 1.2\%$	292 ± 4

Table 5.3: The data at D_0 in 1997 is taken from [260]. Using Formula 5.5, the flux at D , including an error of 1 cm, can be estimated in 1997. Then, taking into account the attenuation of the source activity, the flux at D can be estimated at the time of the tests in GIF in 2014. Assuming a sensitivity of the RPC to γ s = 2×10^{-3} , an estimation of the hit rate per unit area is obtained.

3274 The goal of the study will be to have a good measurement of the intrinsic performance without
 3275 source irradiation. Then, taking profit of the two working absorbers, at absorbtion factors 5 (300 Hz)
 3276 and 2 (~ 600 Hz) the goal will be to show that the detectors fulfill the performance certification of
 3277 CMS RPCs. Finally, a first idea of the performance of the detectors at higher background will be
 3278 provided with absorbtion factor 1 (no absorbtion and >1 kHz)).

3279 5.2.4 Results and discussions

3280 The data taking at GIF has been conducted in between the 21st and the 31st of August, 2014. Data
 3281 has been collected with both source OFF and ON using three different absorber settings (ABS 5, 2
 3282 and 1) in order to vary the irradiation on the RPC. For each source setting, two HV scans have been
 3283 performed with two different trigger settings. During a first scan the trigger sent to the TDC module
 3284 was the coincidence of the two scintillators composing the telescope while during a second scan the
 3285 trigger was a pulse coming from a pulse generator in order to measure the noise or gamma rate seen
 3286 by the chamber. Indeed, using a pulse allows to trigger at moments not linked to any physical event
 3287 and, hence, to obtain a *RANDOM* trigger on noise and gamma events to measure the associated rates,
 3288 the probability to have a pulse in coincidence with a cosmic muon being negligible.

3289 From the cosmic trigger scans, a summary of the efficiencies and corresponding cluster sizes is
 3290 showed in Figure 5.18. The efficiency curves with Source ON show a shift with respect to the case
 3291 without irradiation. With ABS 5, the general shape of the efficiency curve stays unchanged whereas
 3292 a clear alteration of the performance is observed at ABS 2 and ABS 1. From the cluster size results,
 3293 a reduction of the cluster size under irradiation can be oberved at equivalent efficiency. This effect
 3294 can be due to the perturbation of the electric field by the strong rate of gamma particles starting
 3295 avalanches in the gas volume of the detector.

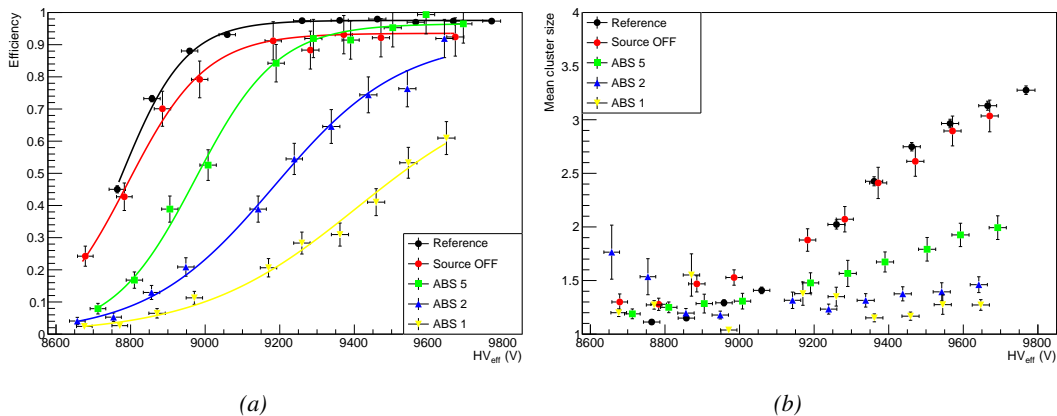


Figure 5.18: Efficiency (Figure 5.18a) and cluster size (Figure 5.18b) of chamber RE-4-2-BARC-161 measured at GIF with Source OFF (red) and Source ON using different absorber settings: ABS 5 (green), ABS 2 (blue) and ABS 1 (yellow). The results are compared to the Reference values obtained with cosmics.

3296 It is necessary to study the evolution of the performance of the chamber with the increasing rate.
 3297 In Figure 5.19a, the noise rate when the source is OFF stays low but increases at voltages above
 3298 9500 V. The rise of the noise rate in the detector can be related to the increased streamer probability
 3299 observed with such a large electric field. The rates with source ON measured at GIF all show a

similar behaviour until a high voltage of approximately 9400 V at which the rate of ABS 5 saturates, corresponding to the chamber reaching full efficiency. It is important to note that, even though the rates look similar independently from the gamma flux, relatively to the efficiency of the chamber, the rate actually increases with increasing flux at equivalent efficiency. A rough way to measure the rate effectively observed by the detector for each source setting would be to normalize the measured rates to the efficiency of the detector. This exercise was done with Figure 5.19b from which constant fits were done on Source ON data in order to extract the rate the chamber was subjected to.

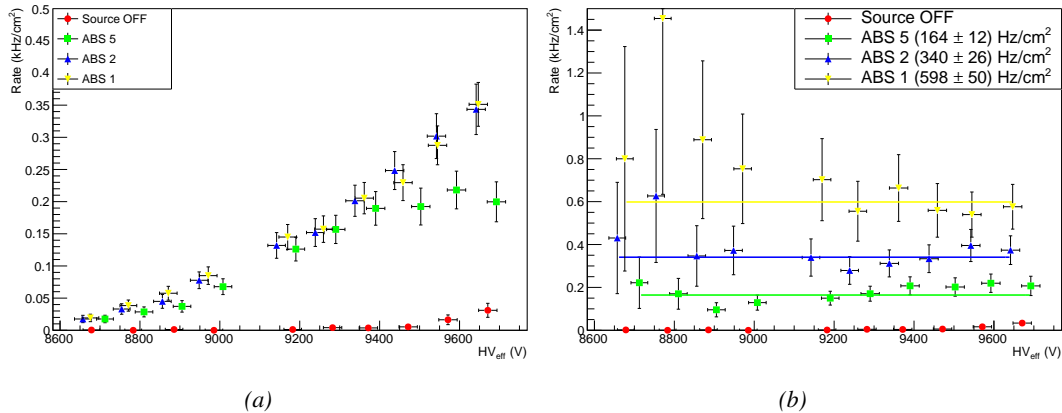


Figure 5.19: Rates in chamber RE-4-2-BARC-161 measured at GIF with Source OFF (red) and Source ON using different absorber settings: ABS 5 (green), ABS 2 (blue) and ABS 1 (yellow). On Figure 5.19b, the rates of Figure 5.19a were normalized to the measured efficiency and constant fits are performed on Source ON data showing the gamma rate in the chamber.

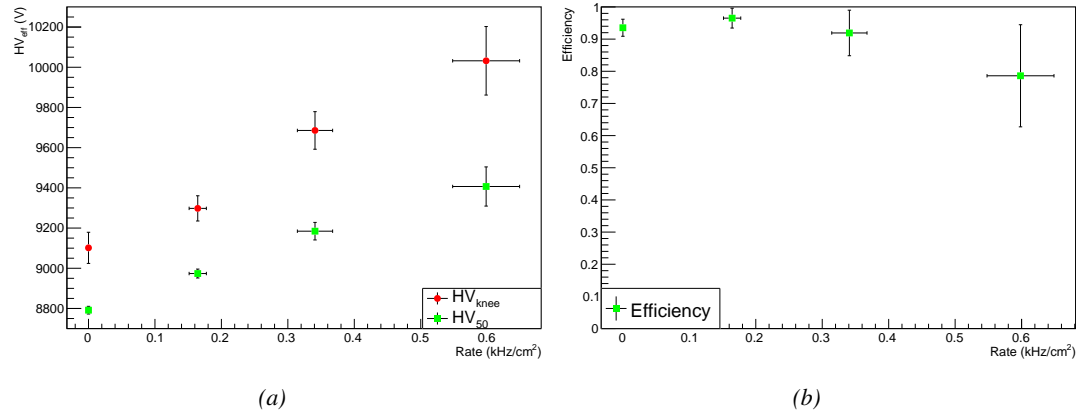


Figure 5.20: Evolution of the voltages at half maximum and at 95% of the maximum efficiency (Figure 5.20a), and of the maximum efficiency (Figure 5.20b) as a function of the rate in chamber RE-4-2-BARC-161. The data is extracted from the fits in Figures 5.18a and 5.19b.

The results need to be taken with care as a better estimation of the rate would have been to push the detector towards higher voltages to reach the efficiency plateau for each absorber configuration

and only then extract the measured rate at working voltage, defined as in Formula 4.25. Nevertheless, using this method to estimate the rate the chamber is subjected to, it is possible to look at the evolution of the HV_{50} and HV_{knee} (the working voltage being defined to be 150 V above the knee in the endcap) as a function of the increasing rate as showed in Figure 5.20. The results from GIF suggest that at a rate of 600 Hz/cm^2 the working voltage of the chamber is increased by a thousand V while the efficiency is reduced to approximately 80%, although the result still is consistent with an efficiency better than 90% due to the large error on the measurement. Moreover, it is likely that the rates obtained through fitting on normalized values is underestimated. Indeed, monitoring the current in the 3 gaps composing a CMS endcap RPC (Figure 5.21) while knowing the rate, the charge deposition per avalanche q_γ can be computed.

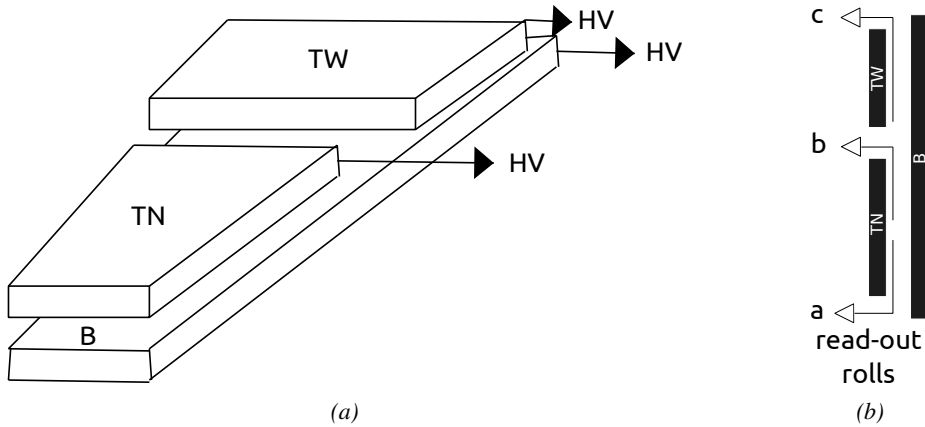


Figure 5.21: Presentation of a double-gap endcap RPC with its 3 RPC gaps. Due to the partitioning of the read-out strips into 3 rolls, the TOP layer of gap is divided into 2 gaps: TOP NARROW (TN) and TOP WIDE (TW). The BOTTOM (B) only consists in 1 gap.

A charge is expressed in C which is consistent with a current density, expressed in A/cm^2 , divided by a rate per unit area, expressed in Hz/cm^2 . The current driven by the RPC is assumed to be due to the irradiation, hence, to the avalanches developing in the gas volume due to the photons of the Cesium source. On the other hand, the rate is supposed to be a measure of the number of photons interacting with the detector. This way, it comes that the charge deposition per avalanche is expressed like $q_\gamma = J_{mon}/R_\gamma$, J_{mon} being the monitored current density and R_γ the measured γ rate. The current density is computed as the sum of the current density measured on the top gap layer and of which measured in the bottom gap layer, $J_{mon} = (I_{mon}^{TW} + I_{mon}^{TN})/(A_{TW} + A_{TN}) + I_{mon}^B/A_B$, $A_{B,TN,TW}$ being the active area and $I_{mon}^{B,TN,TW}$ the monitored currents of the gaps. According to Figure 5.22, the charge deposition per avalanche consistently converges to a value of the order of 50 pC for each absorber setting which corresponds to a value more than twice greater than what reported in literature for CMS detectors [266, 267] indicating that the rates could have been wrongly evaluated during the short study performed at GIF. An increase of the γ rate by a factor 2 would be consistent with the expected rates calculated in Table 5.3, assuming the sensitivity to γ to be of the order of 2×10^{-3} .

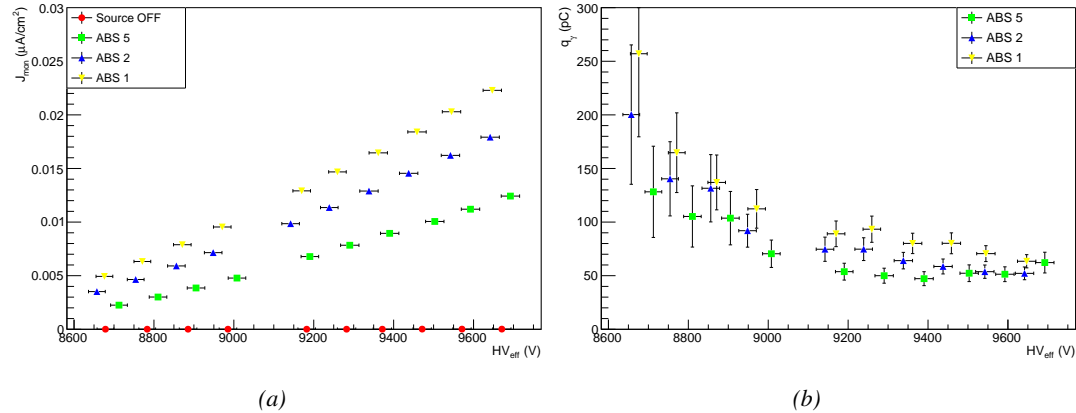


Figure 5.22: Current density and charge deposition per gamma avalanche, defined as the current density normalized to the measured rate taken from Figure 5.19a as a function of the effective high voltage in chamber RE-4-2-BARC-161 measured at GIF with Source ON using different absorber settings: ABS 5 (green), ABS 2 (blue) and ABS 1 (yellow).

Overall, working at GIF has been a rewarding experience as it offered CMS RPC R&D team the possibility to start developing the necessary skills and tools that would become the core of GIF++ experiment. The quality of the results can be argued both due to the little robustness of the experimental setup and the lack of available statistics to draw conclusions from, bringing large errors on the final result. The confrontation of the data to known results pointed to a failure in correctly measuring the γ rate at working voltage and, hence, to an overestimation of the charge per avalanche and of the drift of working voltage with increasing rate. Nevertheless, the prototypes of DAQ and offline analysis tools proved to be reliable.

5.3 Longevity tests at GIF++

5.3.1 Selection and characterization of CMS RPCs for longevity at GIF++

First proposed in 2009 [268], the new Gamma Irradiation Facility of CERN was thought in the perspective of future upgrades of PHC that would bring detectors to be operated in a high irradiation environment. GIF++ would thus provide all LHC R&D teams working on behalf of the different LHC experiment with a facility to perform longevity studies using a very intense Cesium gamma source.

In the specific case of CMS RPC, the longevity studies imply a constant irradiation of selected detectors in order to accumulate a charge equivalent to what is expected during HL-LHC, i.e. a charge of $0.8 \text{ C}/\text{cm}^2$ according to Figure 5.2 including a safety factor 3, while other detectors are left non irradiated to be used as references. Throughout the irradiation campaign, the performance of the irradiated and reference detectors will be periodically probed using the high intensity H4 muon beam. Dedicated test beam periods will be used to measure the efficiency and γ rate at the level of the detectors with different source absorber settings to have access to the rate capability of CMS RPCs, that needs to be certified above $600 \text{ Hz}/\text{cm}^2$, and to identify signs of ageing in the case the performance of the irradiated detectors diverges from those of the reference detectors with increasing accumulated charge. Other than the performance of the detectors, signs of ageing

3359 could come from increasing dark current that would be related to local ageing of the electrodes
 3360 triggered by the fluoridric acid (*HF*) production in an irradiated environment. *HF* is produced
 3361 by the decomposition of $C_2H_2F_4$ molecules during the charge multiplication process and leads to
 3362 increased dark current and noise in Bakelite RPCs treated with linseed oil. This effect is strongly
 3363 reinforced by the presence of UV photons [269, 270]. A close monitoring of the current driven by
 3364 the detectors will then be necessary as well as dedicated periodical electrode resistivity measurement
 3365 and chromatography measurement on the gas exhaust.

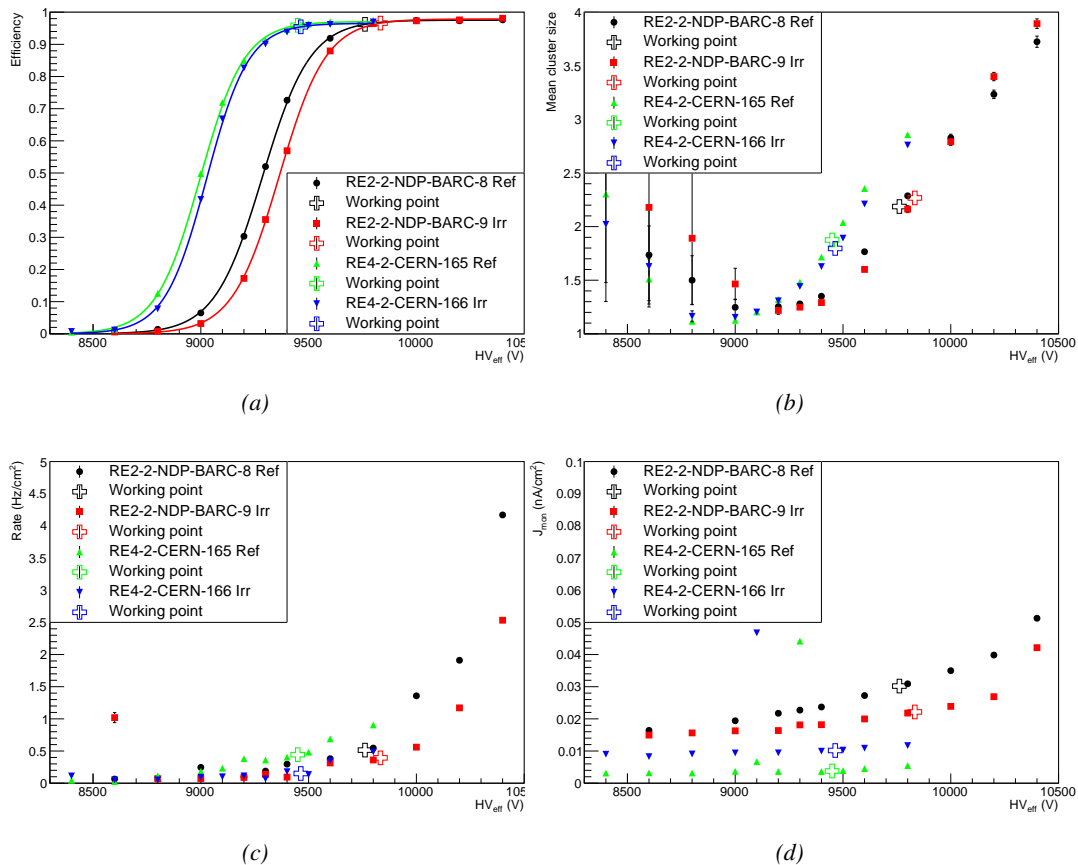


Figure 5.23: Characterization of CMS RPC detectors foreseen to be used at Gif++ for longevity studies of the present system. Using cosmic muons, efficiency (Figure 5.23a) and cluster size (Figure 5.23b) were measured as well as noise rate (Figure 5.23c) and current density (Figure 5.23d). For each detector, the working voltage, defined as in Formula 4.25, was extracted from sigmoid fits performed in Figure 5.23a and the values of efficiency, cluster size, noise rate and current density at this voltage are reported using open crosses.

3366 As the maximum background is found in the endcap, the choice naturally was made to focus
 3367 the Gif++ longevity studies on endcap chambers. Most of the RPC system was installed in 2007.
 3368 Nevertheless, the large chambers in the fourth endcap (RE4/2 and RE4/3) have been installed during
 3369 LS1 in 2014. The Bakelite of these two different productions having different properties, four spare
 3370 chambers of the present system were selected. From the original CMS RPC system, two RE2/2
 3371 spares were selected along two RE4/2 spares from the newest detectors. Having two chambers of

3372 each type allows to always keep one of them non irradiated as reference. Due to the limited gas
 3373 flow in GIF++, the RE4 chamber remained non-irradiated until end of November 2016 where the
 3374 longevity studies could finally be started on those chambers.

3375 The performance of the chambers prior to the start of the longevity campaign has been char-
 3376 acterized in Ghent before being shipped to CERN to be installed in GIF++. The results of the
 3377 characterization are showed in Figure 5.23 and summarized in Table 5.4. A clear difference in per-
 3378 formance for both types of chambers is observed as the working voltages of the newest chambers,
 3379 of type RE4, are 300 to 400 V lower to the older chambers indicating that the gap thickness of RE4
 3380 detectors could be thinner. This conclusion could as well be supported by the lower cluster size at
 3381 working voltages that also are smaller in RE4 chambers. Even though the measured currents are
 3382 low, RE4 detectors draw less current without irradiation than RE2 detectors pointing to a difference
 3383 in electrode resistivity that were produced at different moments. Efficiency and noise rate levels are
 3384 of the same order of magnitude for both type of RPCs.

RPC	RE2-2-NPD-BARC-08	RE2-2-NPD-BARC-09	RE4-2-CERN-165	RE4-2-CERN-166
Used as	Reference	Irradiation	Reference	Irradiation
HV_{WP} [V]	(9762 \pm 6)	(9833 \pm 6)	(9449 \pm 5)	(9464 \pm 5)
Efficiency at WP	(96.2 \pm 0.3)	(96.6 \pm 0.3)	(95.9 \pm 0.3)	(95.5 \pm 0.3)
Cluster size at WP	(2.19 \pm 0.04)	(2.27 \pm 0.05)	(1.88 \pm 0.04)	(1.80 \pm 0.04)
Noise at WP [Hz/cm ²]	(0.51 \pm 0.01)	(0.39 \pm 0.01)	(0.44 \pm 0.00)	(0.15 \pm 0.01)
J^{WP} [pA/cm ²]	(30.1 \pm 0.1)	(22.2 \pm 0.1)	(3.8 \pm 0.0)	(10.2 \pm 0.0)

Table 5.4: Summary of the characterization measurement performed in Ghent on CMS RPC detectors foreseen to be used at GIF++ for longevity studies of the present system. For each detector, the working voltage, defined as in Formula 4.25, was extracted from sigmoid fits performed in Figure 5.23a and the values of efficiency, cluster size, noise rate and current density at this voltage are reported.

5.3.2 RPC test setup

3386 For an easy manipulation of the detectors, a trolley with a structure containing slots in which the
 3387 RPCs can be slid vertically and referred to as T1 was used. In this position, each chamber is in a
 3388 plane perpendicular to the beam line and the source flux as can be seen through Figure 5.24, receiving
 3389 a uniform irradiation. Moreover the trolley allows for easy movement of the system. Indeed, the
 3390 position of trolley varies according to the period of the year.

3391 During the dedicated test beam periods during which GIF++ longevity experiments are in control
 3392 of the muon beam, the trolley is placed in the upstream region of the bunker, in the beam line, as
 3393 described through Figure 5.24a. The CMS RPC detectors are the ones being further away from the
 3394 source on this side of the source as other detectors need to be certified at higher background rates. An
 3395 additional trolley, referred to as T3, containing iRPCs and tracking RPCs is placed in between the
 3396 source and the trolley containing present CMS RPCs. Indeed, iRPCs need to be certified at higher
 3397 rates and thus need to be placed closer to the source to receive a stronger irradiation using the same
 3398 absorber settings. The space on T1 being limited, the tracking RPCs used for extra offline informa-
 3399 tion during the analysis are placed on the same trolley than iRPCs and are kept at full efficiency at
 3400 all time to reconstruct muon tracks in correlate them with hits recorded in T1 chambers. The beam
 3401 trigger system is composed of 2 scintillators placed outside on each side of the bunker and of a third
 3402 scintillator placed in between T1 and the wall of the bunker along the beam line.

3403 However, most of the year, T1 is placed in the so called *ageing position* corresponding to the

furthest position from the source outside of the beam line, which needs to stay clear during periods where GIF++ doesn't have the control of the beam so that a beam tube can be installed through the bunker, as can be seen in Figure 5.24b. The reason for placing the chambers as far as possible from the source comes from the too high irradiation delivered by the source during the irradiation periods where all the other experiment having placed detectors into the bunker requires to integrate as much charge as possible. Hence, the source is operated with any absorbers. On the contrary, during the test beam periods, all the groups working in GIF++ are interested in operating the source using various absorber settings to study the performance of their detectors under different irradiation conditions. The time spent with a source fully opened and during which the RPCs of T1 are kept at a standby voltage of 6500 V much lower than what necessary to grow avalanches in the gas is then small compared to the time spent with other source settings and during which data can be taken.

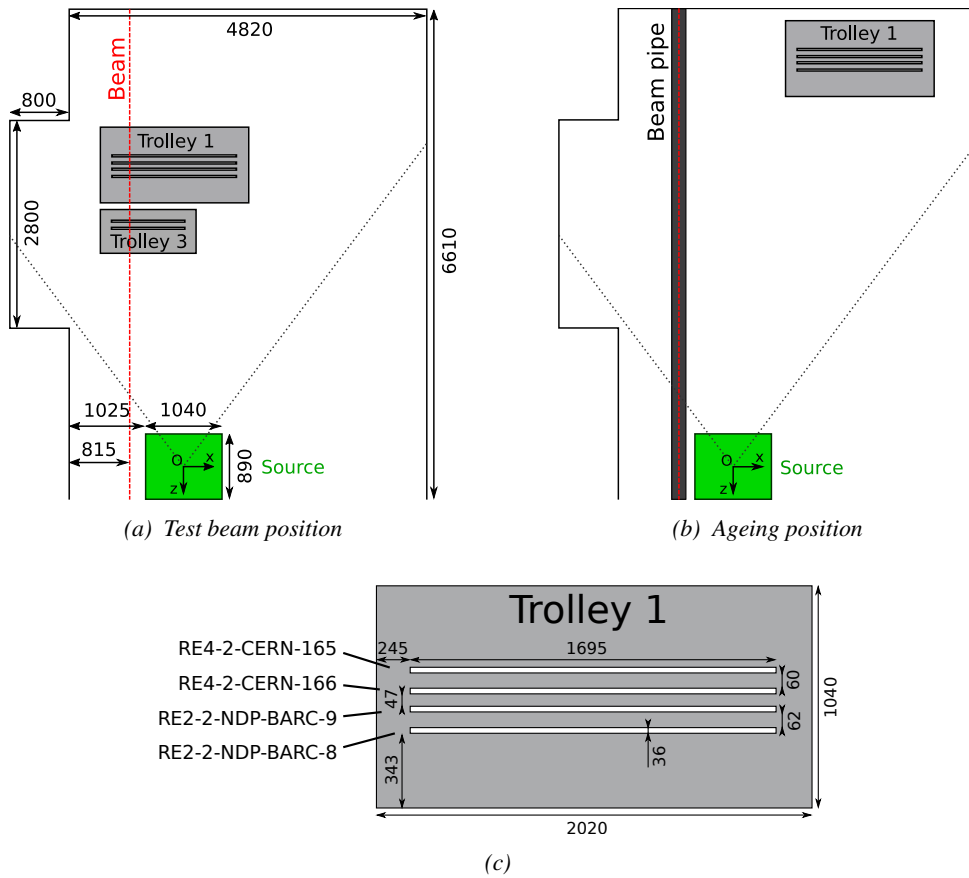


Figure 5.24: CMS RPC setup inside of GIF++ bunker during test beam (Figure 5.24a) and ageing periods (Figure 5.24b). The space in between the RPCs and the source is usually used by other detectors while the space in between T1 and the upstream wall is not filled. Due to the presence of the beam pipe, the trolley is moved away from the beam line during irradiation periods and placed further away from the source for less intense irradiation. The position of the trolley can vary due to the use of the space by other setups and is then not exact. In the contrary, the position of the chambers in the trolley is fixed and given in Figure 5.24c.

From the bunker area, the detectors are connected to the service area, visible in Figure 5.6, through the wooden floor tanks to long cable. The service area hosts all the high and low voltage power

3417 supplies, the TDCs and computers used for data acquisition and preliminary offline analysis used
 3418 to fill the Detector Control Software (DCS) webpage, referred to as WebDCS, with Data Quality
 3419 Monitoring (DQM) histograms useful for the shifters on duty in the control room located further in
 3420 the building, away from the beam lines, as well as the gas system required for the gaseous detectors
 3421 installed in GIF++ [271]. The detectors read-out is, as in the case of GIF, connected to V1190A
 3422 VME TDCs communicating with the DAQ computer thanks to a V1718 VME bridge manufactured
 3423 by CAEN. Moreover, a constant monitoring of all the environmental parameters, in different points
 3424 of the bunker area, gas parameters, to control its composition, temperature and pressure, and of the
 3425 voltages and currents delivered by the power supplies is performed and displayed on the homepage
 3426 of the WebDCS interface.

3427 5.3.3 GIF++ data flow

3428 At GIF++, the CMS RPC R&D experiment collects different types of data coming from the detectors
 3429 monitored parameters, such as voltage and currents, the gas, source, and environmental parameters,
 3430 and, of course, the TDC data in which are collected the actual muon and gamma physics. These
 3431 different data source compose 3 different data flows as presented in Figure 5.25.

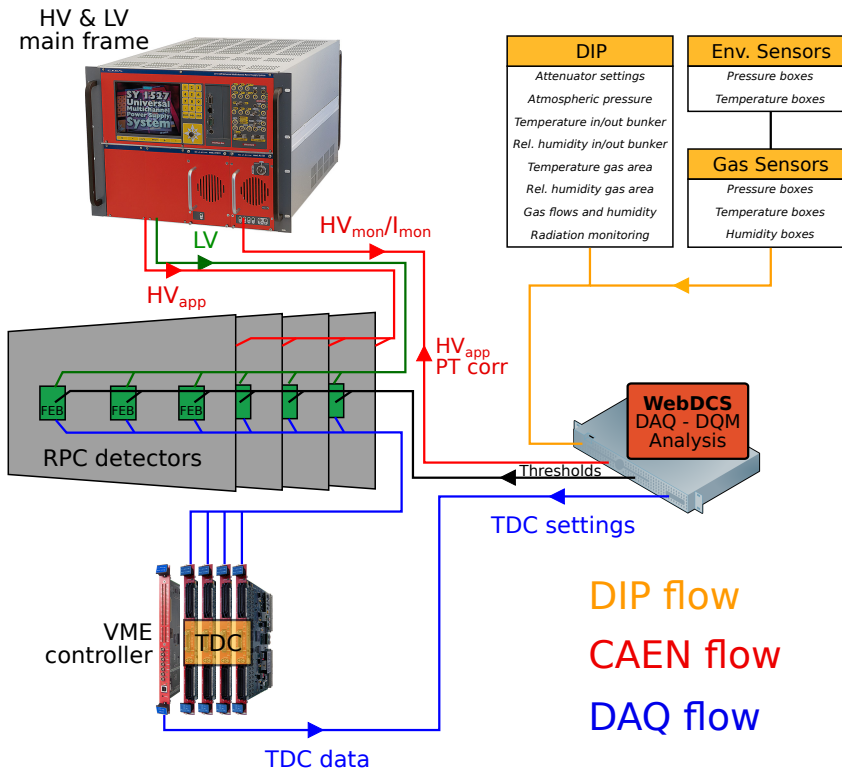


Figure 5.25: Visualtion of the main data flows in GIF++. The yellow flow lines corresponds to the DIP flow used for source, environmental and gas information. The red flow lines are for the CAEN flow through which the WebDCS communicates the voltages to be applied on the detectors using pressure and temperature information and retrieves the monitored voltages and currents. Finally, the blue flow lines corresponds to the DAQ flow through which the RPC data is collected from the TDCs by the computer.

3432 The *DIP flow*, DIP being a communication system allowing for exchange of real-time information
 3433 between systems, concerns all the data coming from the gas composition, temperature and humidity, the environmental temperature and pressure, the source settings and the radiation monitoring sensors. The experimental area is in charge of measuring, storing and distributing the data
 3434 of interest for all of the users of the facility (source settings, radiation monitoring, gas composition
 3435 at the exit of the gas mixer and general environmental information). Retrieving this data is done by
 3436 accessing to the database of the experimental hall in which GIF++ is located through DIP communica-
 3437 tion. More specific data such as gas flow, temperature and humidity at the level of the detectors
 3438 (upstream and downstream of the detectors) as well as environmental parameters are at the charge
 3439 of the users. For this reason, several pressure, temperature and humidity sensors were installed on
 3440 the gas distribution system of the RPC trolleys. The corresponding data flow, although not related
 3441 to DIP itself, is saved together with the DIP data into the local CMS RPC database and displayed
 3442 on the front page of the WebDCS together with alerts in the case the values measured are out of
 3443 optimal working range. The data is particularly important to perform the PT correction described in
 3444 Section 4.4 of Chapter 4 and keep stable the effective voltage of the detectors. Monitoring history
 3445 plots are made using JavaScript are also displayed for an easy access to past information, as
 3446 showed in Figure 5.26.
 3447

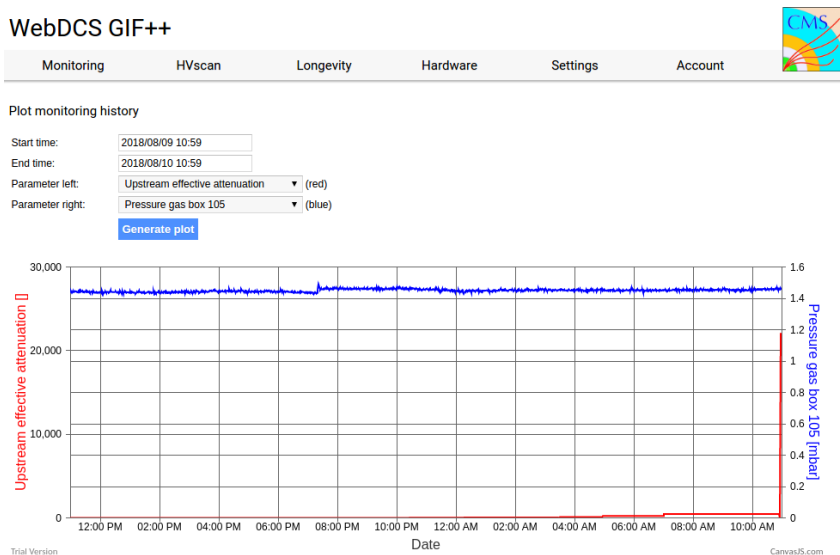


Figure 5.26: *DIP monitoring history accessed through GIF++ WebDCS interface.*

3449 The data flow related to the monitoring of detector high voltages and currents, referred to as
 3450 *CAEN flow* as a reference to the manufacturer of power supplies, is retrieved thanks to computer
 3451 to main frame communications. Indeed, during the operations (irradiation or beam period), these
 3452 values can be accessed directly through the bus of the main frame hosting the high voltage supplies.
 3453 Finally, the DAQ flow concerns all data acquired through the use of the TDCs, i.e. all the muon or
 3454 gamma data recorded by the detectors under test at GIF++.

3455 5.3.4 Measurements performed during beam periods

3456 As previously described, two types of measurement are performed on the chambers during beam
 3457 periods. On one hand, it is interesting to measure the efficiency of the RPCs with increasing voltage
 3458 with different source absorber settings but on the other hand, it is important to correlate the efficiency
 3459 information to the gamma rate seen by the chambers at the voltages that were scanned for efficiency.
 3460 The choice was made to separate efficiency measurements from rate measurements to better manage
 3461 time and data volume. In both cases, TDC data recorded during so called *HV scans* is divided into
 3462 *runs*, one for each high voltage point, whose data is stored into ROOT files. The TDC settings
 3463 used during both these scans as well as the ROOT data structure are detailed in Section A.4.2 of
 3464 Appendix A.

3465 The goal of both efficiency and rate scans is to measure the rate capability of the detectors but
 3466 also to monitor any degradation of the performance due to ageing. This way, during test beam
 3467 periods the efficiency and corresponding gamma background are measured to correlate the evolution
 3468 of rate capability at different stages of irradiation. In the absence of other signs of ageing, a reduction
 3469 of the rate capability could be related to an increase of the electrodes resistivity.

3470 5.3.4.1 Efficiency scans

3471 The HV scans performed to specifically measure the muon detection efficiency under different ir-
 3472 radiation conditions follow a standardized procedure. Data using the DAQ is taken at the same 12
 3473 HV points for all chambers, ranging from 9 kV to 10.1 kV by steps of 100 V. For each HV run, a
 3474 minimum of 5000 muon beam triggers, provided by the coincidence of the 3 scintillators, is required
 3475 in order to accumulate enough statistics for a reliable computation of the efficiency of the detectors.
 3476 In addition to the 4 RPCs held on T1, 2 tracking RPCs installed on T3 are kept at a fixed voltage of
 3477 9.7 kV to provide the analysis software [272] with beam position information to exclude off-track
 3478 signals. The tracking RPCs, whose design is based on which of CMS RPCs, are double gap detectors
 3479 featuring 2 mm HPL electrodes and 2 mm gas gaps. Finally, the monitored currents and voltages are
 3480 recorded in histograms along the TDC data in a different ROOT file for each run.

3481 HV scans are taken for different source settings as the goal is to irradiate all the detectors with a
 3482 minimal rate of 600 Hz/cm². Usually, a full study of the performance of the detectors is performed
 3483 with Source OFF, and then with 9 absorber settings that attenuate the nominal gamma flux by factors
 3484 from more than 200 to only 3, settings with fully opened source being avoided with RPCs in test
 3485 beam position. Adjusting the gamma flux is possible thanks to the 3 layers of absorbers featured on
 3486 the Cesium source [273].

3487 5.3.4.2 Rate scans

3488 These background measurement are performed using a similar HV scan procedure than in the case
 3489 of efficiency measurements. The HV scan in test beam period will be taken fewer HV points than
 3490 for the efficiency scans as the region of interest is located around the knee and efficiency plateau
 3491 of the detectors in order to extract through linear interpolation the value of the rate at the working
 3492 voltage deduced from the efficiency scan. Thus, these scans are performed only on 6 HV points
 3493 ranging from 9.5 kV to 10 kV. Rate scans are substantially heavier than efficiency scans. Indeed, a
 3494 good estimation of the rate requires a long enough integrated time worth of data. The way data is
 3495 collected, detailed in Appendix A, makes the DAQ search for data stored in the TDC buffers prior to
 3496 the trigger signal. The time window from which the data is collected ranges in between only 25 ns

3497 to more than $50\ \mu\text{s}$. The Cesium source delivering a consistent gamma flux, it was decided than a
 3498 total integrated time of $0.2\ \text{s}$ would be enough to have a reliable calculation of the γ rate. This is
 3499 achieved by taking 20,000 random trigger pulses delivered by a pulse generator at a frequency of
 3500 $300\ \text{Hz}$ while extracting $10\ \mu\text{s}$ of data from the buffers for each trigger.

3501 Separating rate measurements from efficiency measurement was motivated by the inconsistency
 3502 of the muon beam provided in GIF++. Using periods without beam to measure rates with a good
 3503 statistics allows for faster study programs. Moreover, depending on the muon strength that can
 3504 strongly vary due to users placed upstream of GIF++ and using magnets, the number of muon de-
 3505 livered per beam spill can make the accumulation of 20,000 events too long for the other users of
 3506 GIF++. Hence, efficiency scans are performed with lower statistics and the time window from which
 3507 the data is extracted is strongly reduced (400ns for efficiency scans versus $10\ \mu\text{s}$ for rate scans) to
 3508 keep the data size to its bare minimum.

3509 5.3.4.3 Offline analysis and Data Quality Monitoring

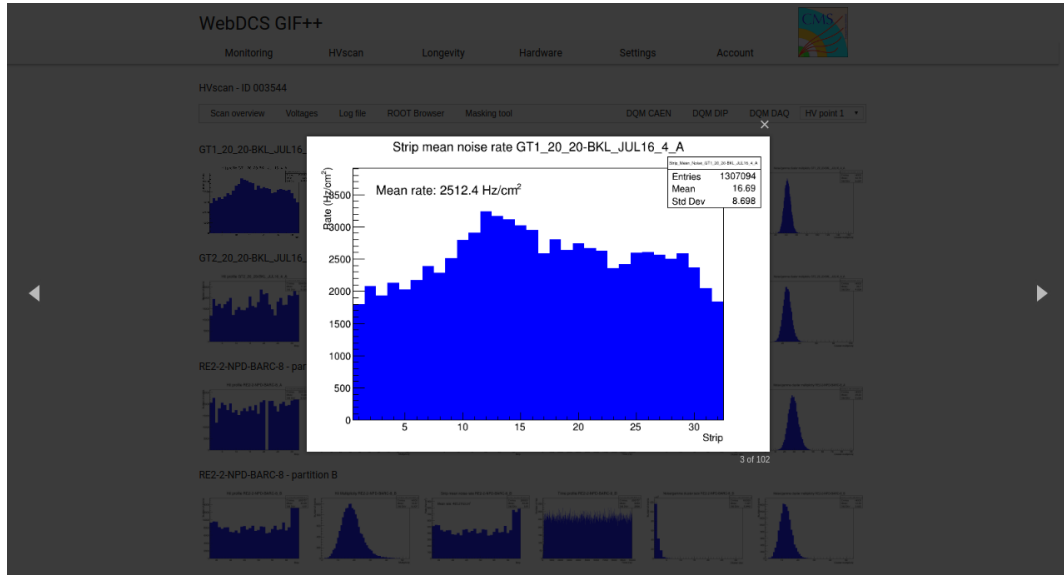


Figure 5.27: Example of DQM page available on CMS WebDCS in GIF++. Here is presented the rate measured in one of the tracking chambers, namely GT1_20_20-BKL_JUL16_4. The DQM page allows to click on each histogram to extend its view and to navigate through the histograms thanks to the left and right arrows.

3510 The data recorded during efficiency and rate scans always consist in two ROOT files per run, a run
 3511 corresponding to a HV point. One of the files corresponds to the TDC data, a collection of hits
 3512 per active channel on the read-out of the RPCs, while the second is the CAEN main frame data,
 3513 offering a monitoring of the currents and high voltages. This data is systematically analysed at the
 3514 end of each scan thanks to the Offline Analysis tool of GIF++, detailed in Appendix B, that produces
 3515 histograms such as hit, rate and time profiles, hit multiplicities, gamma cluster sizes or multiplicities
 3516 for the DQM display of the WebDCS, as showed in Figure 5.27. More histograms can be accessed
 3517 through the ROOT browser included in the WebDCS, as showed in Figure 5.28. Moreover, the
 3518 analysis performed thanks to the Offline tool is definitive in the case of evaluating the rates from rate

3519 scans. On the contrary, the algorithm for efficiency calculation is kept simple and approximative in
3520 the tool as including taking into the analysis requires manual adjustment for each individual scan.

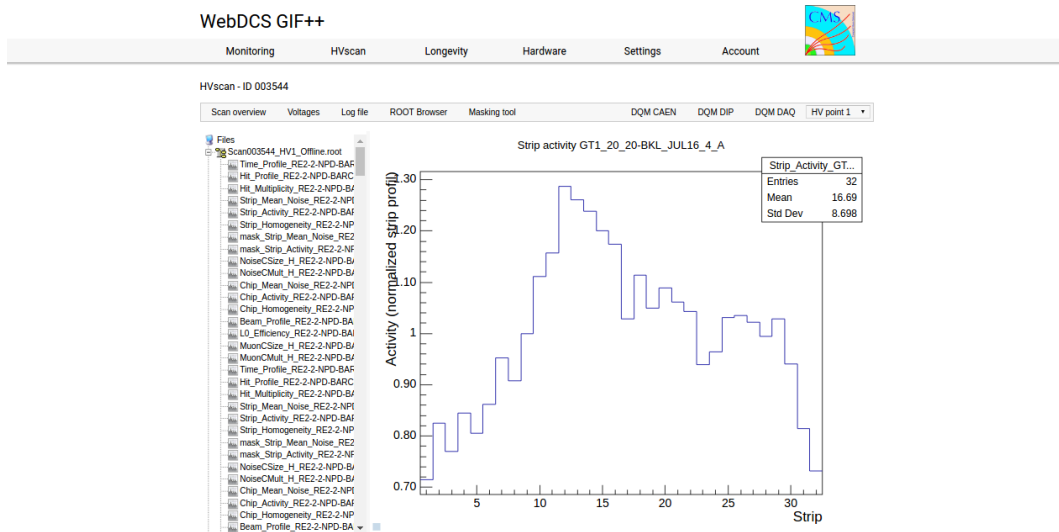


Figure 5.28: Example of DQM ROOT Browser page available on CMS RPC WebDCS in GIF++. Here is presented the strip activity profile, defined as the rate profile normalized to the mean rate, in one of the tracking chambers, namely GT1_20_20-BKL_JUL16_4. Available ROOT files and histograms can be browsed thanks to the left panel showing the directory and files structures.

5.3.5 Measurements performed during irradiation periods

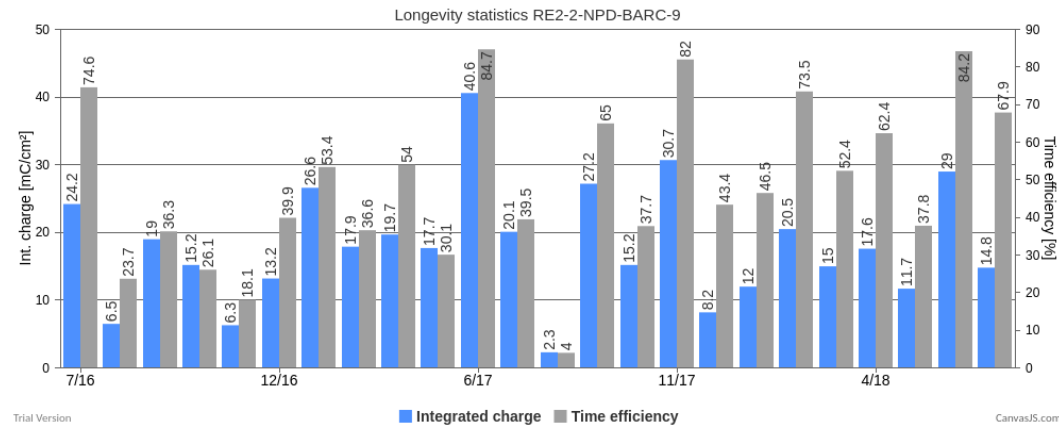


Figure 5.29: Longevity statistics of chamber RE2-2-NPD-BARC-9 in GIF++. For each month since July 2017, the integrated charge (in blue) as well as the time efficiency of irradiation (in gray) is reported.

Even though test beam periods are stressful times has an extensive data taking planing needs to be finalized in a short amount of time, the biggest amount of data comes from irradiation periods.

Indeed, when T1 is moved back to its ageing position in between each test beam periods, data is recorded at any time the source can be switched ON for irradiation. Indeed, other experiments in the area might prevent the source from staying opened continuously. As an example, the time efficiency of irradiation of CMS RPC detectors in Gif++ is presented in Figure 5.29.

Several types of measurement are performed throughout the irradiation period. Indeed, as long as the detectors are being irradiated, a monitoring of the currents is performed to evaluate the corresponding integrated charge considering the irradiation time. Moreover, the corresponding gamma rates need to be measured on a regular basis. Ageing signs can be understood through an increase of the detector noise correlated with an increased dark current. For this purpose, HV scans are performed to measure the noise with increasing voltage and the dark currents. Another way to highlight ageing is through the loss of rate capability of the detectors. During irradiation periods this can be looked through thanks to HV scans performed at various source settings, which are referred to as *source scans*. The loss in rate capability could be understood by a saturation of the measured at higher gamma flux. This effect could be correlated with an increase of the electrodes resistivity. The resistivity is then measure periodically during the year, generally before or after test beam periods by the use of Argon breakdown technic.

5.3.5.1 Longevity scans

The main activity of irradiation periods consist in the *longevity scans* during which the currents of the irradiated chambers is continuously monitored. The two irradiated chambers, RE2-2-NPD-BARC-09 and RE4-2-CERN-166, are both brought to a voltage of 9.8 kV while the source flux can vary depending on the need of experiments using the facility. The currents are recorded on each active gas volume and each gap contribution is then translated into the mean chamber integrated charge as can be seen from Figure 5.30. At the end of each longevity scan the integrated charge accumulated in each chamber is used to update the summary plots providing the collaboration with official results to be spread.

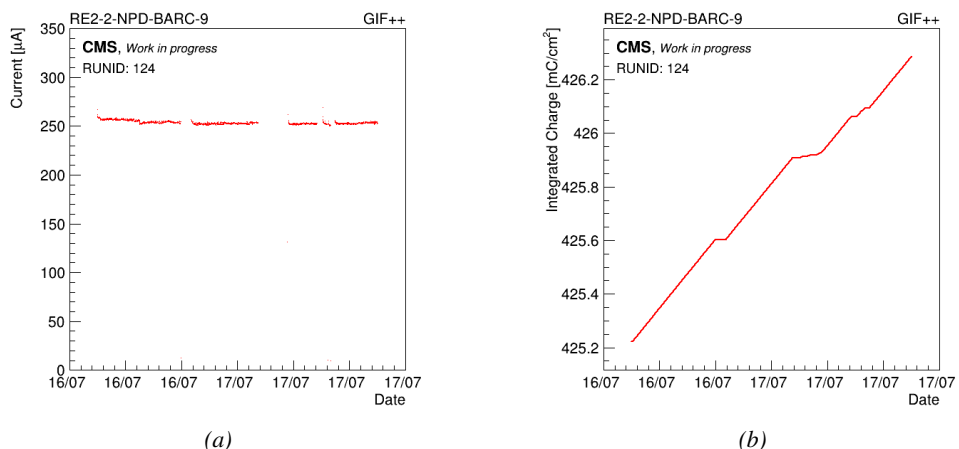


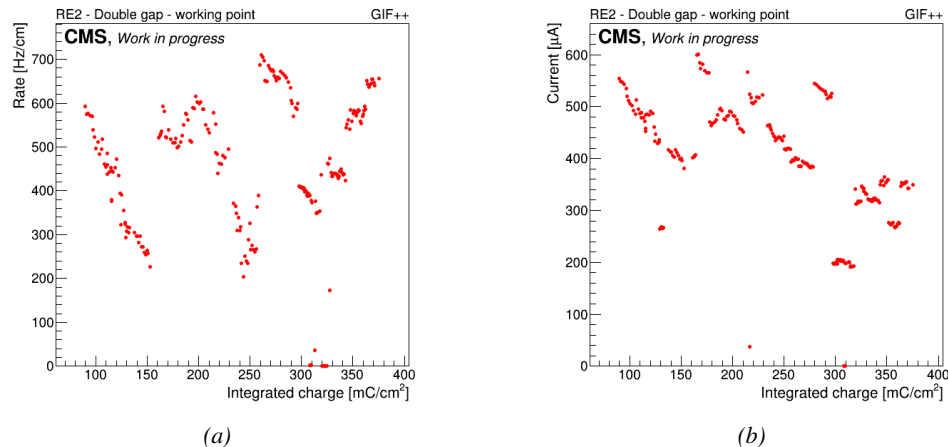
Figure 5.30: Example of current monitoring (Figure 5.30a) and of corresponding integrated charge (Figure 5.30b) of chamber RE2-2-NPD-BARC-09. The decrease of current are related to a decrease of the voltage due to the daily rate scan procedure or to periods during which the source was turned OFF.

3549 **5.3.5.2 Daily rate monitoring scans**

3550 Every night during longevity scans, the DAQ is used to perform *daily rate scans*. These scans aim
 3551 at keeping track of the gamma rate measured in the irradiated RPCs during longevity but is also
 3552 measured the noise rate at standby voltage and this, for each gap individually. The procedure for
 3553 these HV scans consist in 9 runs for which 50,000 random triggers are requested, corresponding to
 3554 0.5 s of total integrated time.

- 3555 1- All gaps are first left at the irradiation voltage of 9.8 kV to measure the γ rate.
 3556 2- Then all gaps are brought to the standby voltage of 6.5 kV to measure the noise rate of the full
 3557 detectors.
 3558 3- Both top gaps (TW and TN) are brought to a voltage equivalent to an OFF status, i.e. 1 kV so
 3559 that the noise contribution of only the bottom gap at standby voltage can be measured.
 3560 4- The bottom gaps are ramped up toward the working voltage of 9.8 kV to measure their contri-
 3561 bution to the gamma rate estimation.
 3562 5-8 The steps 3 and 4 are repeated on TN and then on TW, keeping the bottom and the top gap
 3563 which is not of interest at a voltage of 1 kV. This way, the individual contribution to the noise
 3564 and gamma rates are known.
 3565 9- Finally, both TW and TN are brought to working voltage while the bottom gap is left at 1 kV
 3566 to measure the gamma rate for the full top layer at once.

3567 Finally, the voltages of all gaps are brought back to working voltage for the longevity program
 3568 to continue until the next daily scan.



3569 *Figure 5.31: Example of rate (Figure 5.31a) and current (Figure 5.31b) monitoring of chamber
 3570 RE2-2-NPD-BARC-09 with increasing integrated charge. The variations of rate and current are correlated
 3571 and corresponds to change of source irradiation, gas flow, gas humidity, or environmental conditions.*

3569 Naturally, as this data is taken using Gif++ DAQ, 2 ROOT files containing the DAQ data and
 3570 CAEN data are created for each runs in the exact same way than for efficiency or rate scans taken
 3571 during test beam periods but while the currents are still monitored by the longevity scan and saved

3572 into GIFT++ database for an easy evaluation of the currents to the integrated charge. The Offline
 3573 Analysis tool provides then the DQM page with histograms and daily values can be assembled in
 3574 long term monitoring plots to study the variations of rate and current with increasing integrated
 3575 charge, as presented in Figure 5.31. The rates on every single read-out channel is also tracked to
 3576 control their activity with increasing integrated charge and, this way, understand the appearance of
 3577 hot spots through noisy channels, as showed in Figure 5.32.

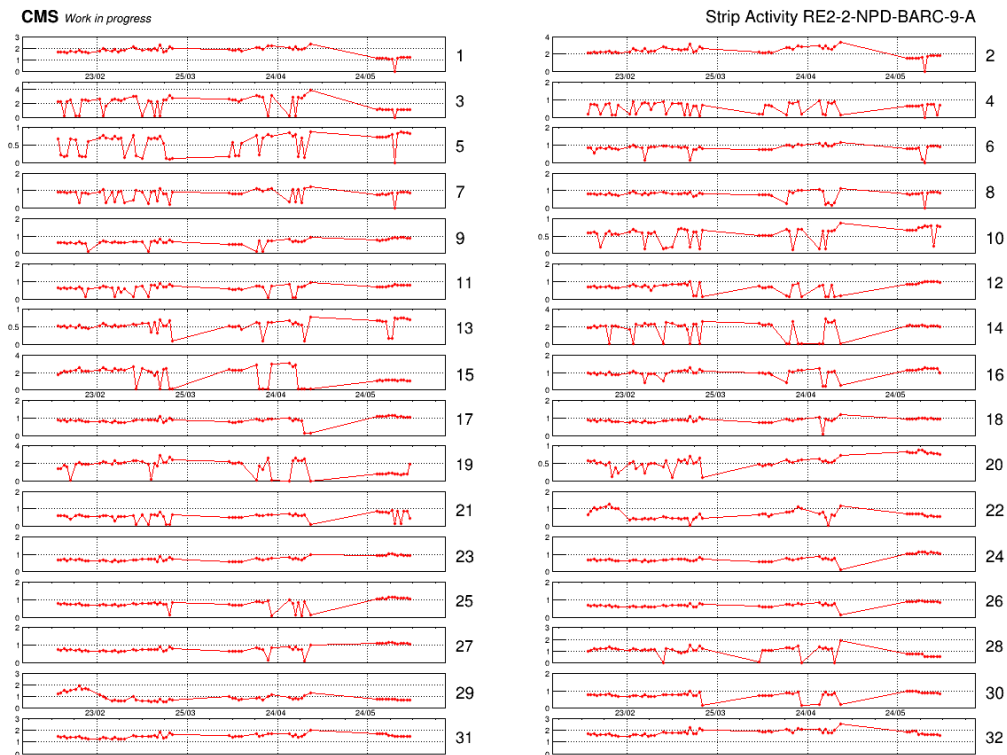


Figure 5.32: Example of strip activity of chamber RE2-2-NPD-BARC-09 monitoring through time. The activity of a strip is defined as the rate of the individual channel normalized to the mean rate measured in the corresponding read-out partition.

3578 5.3.5.3 Weekly noise monitoring scans

3579 Once a week, the source is turned OFF for the CMS RPC to make a noise scan, which consist into
 3580 a HV scan composed of 7 runs and involving both the irradiated but also the reference chambers,
 3581 providing with a weekly monitoring of the evolution of the irradiated chambers noise and dark
 3582 current. The first run is taken at standby voltage for all chambers while the next 6 runs are taken
 3583 with voltages ranging from 9.4 to 9.9 kV in order to have for both type of chambers, RE2 and RE4, a
 3584 coverage of the noise rate in the voltage region in which the efficiency rises and reaches the plateau.

3585 5.3.5.4 Weekly source scans

3586 Directly following the weekly noise scans, HV rate scans are organised at 3 different source settings,
 3587 usually corresponding to ABS 6.8, 4.6 and 3.3. The procedure of these HV scans is strictly similar to

3588 which of weekly noise scans, involving the four RPCs in order to have a weekly comparison of the
 3589 values recorded in every chambers. Measuring with all detectors at the same time allows to get rid
 3590 of potential systematics that might make the rates (noise or gamma) vary from one measurement to
 3591 another. If such systematic effect occurs, it will be observed in all detectors.

3592 **5.3.5.5 Weekly current scans**

3593 The previously detailed daily rate scans, but also the weekly noise and source scans are interesting
 3594 tools to look at an increase of noise rates and dark currents or at a loss of rate capability and point
 3595 to an increase of surface resistivity of the electrodes through the absorption of fluoridric acid. Nev-
 3596 ertheless, periodically measuring the currents on wider high voltage ranges allows to have access
 3597 to the ohmic part of the current driven by the detectors related to the electrodes resistance. This is
 3598 why precise current scans, consisting only in measuring the current driven through the 4 detectors,
 3599 are performed each week. The scan procedure consists in 131 high voltage steps in between 500 V
 3600 and 10 kV by steps of 100 V until the standby voltage of 6.5 kV is reached and then by steps of
 3601 50 V. The current increase in between 500 V and the voltage where charge multiplication starts to
 3602 occur is only driven by the resistance of the detector to current and thus increases linearly. A fit on
 3603 this linear increase of the currents in the range before charge multiplication occurs gives access to
 3604 the resistance of the system electrodes/gas. If any variation of the electrode resistance occurs, the
 3605 global resistance will increase and so will the current. Technically, these scans will record a ROOT
 3606 file per HV step that will have the same format than the CAEN ROOT file saved during other HV
 3607 scans and is also analysed using the Offline Analysis tool to provide with DQM histograms as well
 3608 as standardised I/V tables.

3609 **5.3.5.6 Resistivity measurements**

3610 Aside of the parameters monitored to spot ageing, the resistivity of the HPL planes is measured
 3611 regularly before or after test beam periods through high voltage scans of the detectors operated
 3612 with pure Argon. The electric field strength at which Argon breaks down being well known, the
 3613 breakdown voltage in the detectors is measured and gives an information about the resistance of the
 3614 electrodes, as above the breakdown voltage Argon turns into a conductive plasma and thus does not
 3615 offer electric resistance anymore, which then can be used to calculate the resistivity of the electrode
 3616 material. The Argon line in GIF++ are not kept humid and thus this measurement is not performed
 3617 too often to make sure the electrodes don't dry out, leading to an increase of the electrode resistivity.

3618 **5.3.6 Results and discussions**

3619 Since 2015, CMS RPCs have been irradiated in GIF++ with the goal to reach a total integrated
 3620 charge per irradiated detector of 0.84 C/cm^2 while certifying the detectors to a rate capability of
 3621 600 Hz/cm^2 . As of today, the RE2 and RE4 chambers respectively achieved 51 and 26% of the
 3622 total irradiation program. A few years of irradiation are expected before reaching the end of the
 3623 longevity study and a final answer on whether the detector will be able to live through HL-LHC or
 3624 not. A negative answer to this question would probably lead to solutions to replace the detectors
 3625 before HL-LHC or to improve the shielding of these detectors against background radiation in CMS
 3626 cavern, which could be a more sustainable solution.

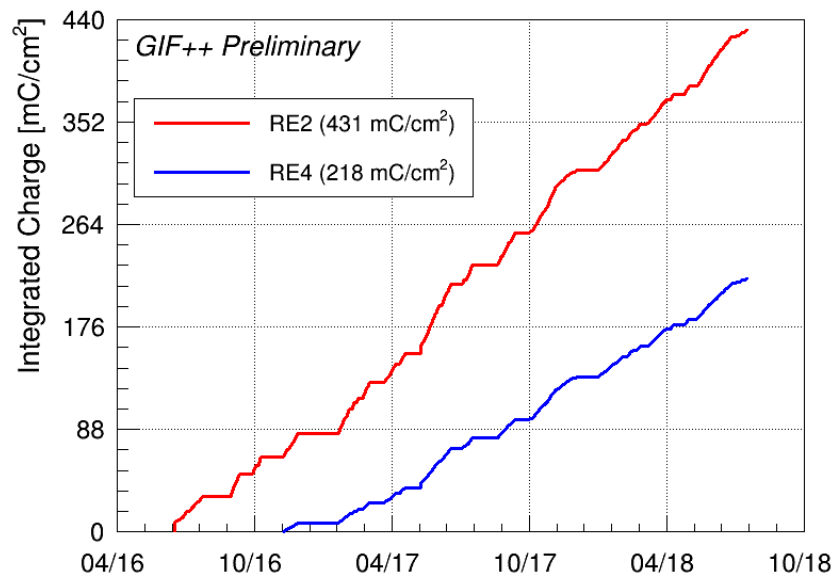


Figure 5.33: Total integrated charge in the irradiated RPCs, RE2–2–NPD–BARC–9 and RE4–2–CERN–165, before starting August 2018 test beam period. The irradiation of the RE2 chamber started in June 2016 while the RE4 chamber couldn't be irradiated before November 2016.

6

3627

3628

3629

Improved RPC investigation and preliminary electronics studies

3630 The extension in the endcap of the RPC sub-system towards higher pseudo-rapidity will bring the
3631 new detectors to be exposed to much more intense background radiations due to the proximity of
3632 the detectors with the beam line. The challenge will be to produce high counting rate detectors
3633 with limited ageing rate to ensure a stable operation of the detector over a period longer than 10
3634 years. In Chapter 4 was discussed the influence of the detector design (number and thickness of
3635 gas volumes, OR system, etc...) on the charge deposition and rate capability. Nevertheless, this
3636 question can also be addressed from the electronics point of view as a better signal to noise ratio
3637 would also mean the possibility to greatly lower the charge threshold on the signals to be detected,
3638 allowing to use the detector at lower gain, hence lowering the charge deposition per avalanche in the
3639 gas volume. Cardarelli showed that the production of low-noise fast FEE could help decreasing the
3640 charge deposition per avalanche at working voltage by an order of magnitude virtually increasing
3641 the life expectancy of such a detector in the same way [274].

3642 **6.1 FEE candidate for the production of iRPCs**

3643 The extension of the third or fourth endcap disks with improved RPCs has been presented in
3644 Chapter 3 together with the expected background levels and the needed requirements from such
3645 detectors to bring out the full potential of the CMS detector by strongly reducing the detection rate
3646 thanks to a more precise reconstruction of the events of interest. An important piece of these iRPCs
3647 will be the Front-End Electronics that will be equipped on the chambers. A fast, low-jitter and low
3648 charge sensitive electronics will help in further reducing the charge deposition in the detector by
3649 making it possible to operate at lower gain.

3650 In the context of the CMS Muon Upgrade, two FEE solutions have been considered to equip the
3651 iRPCs. The baseline for the RPC upgrade is based on the PETIROC ASIC, initially for Time-of-
3652 flight (ToF) applications. A back-up solution is also under study and focusses on a new low-noise

3653 preamplifier designed in INFN laboratories in Rome to replace the preamplification stage of the
 3654 already existing CMS RPC Front-End Board.

3655 The FEEs that are foreseen to equip the new RPCs need to be able to detect charges as small as
 3656 10 fC. Not only the new electronics need to be fast and reliable, they also should be able to sustain
 3657 the high radiation the detectors will be subjected to in the region closest to the beam.

3658 6.1.1 CMS RPCROC: the RPC upgrade baseline

3659 Designed by Weeroc, a spin-off company from the french OMEGA laboratory, the PETIROC 2A
 3660 consists in a fast and low jitter 32-channel ASIC originally developed to read-out Silicon Photomul-
 3661 tiplier (SiPM) in ToF applications and that allows for precise time measurements [198, 199]. The
 3662 ASIC uses an AMS 350 ns SiGe technology. The block diagram of the ASIC is showed on Fig-
 3663 ure 6.1. A 10-bit DAC allows to adjust the trigger level in a dynamical range spanning from 0.5 to
 3664 a few tens of photoelectrons and a 6-bit DAC to adjust the response of each individual channel to
 3665 similar a level.

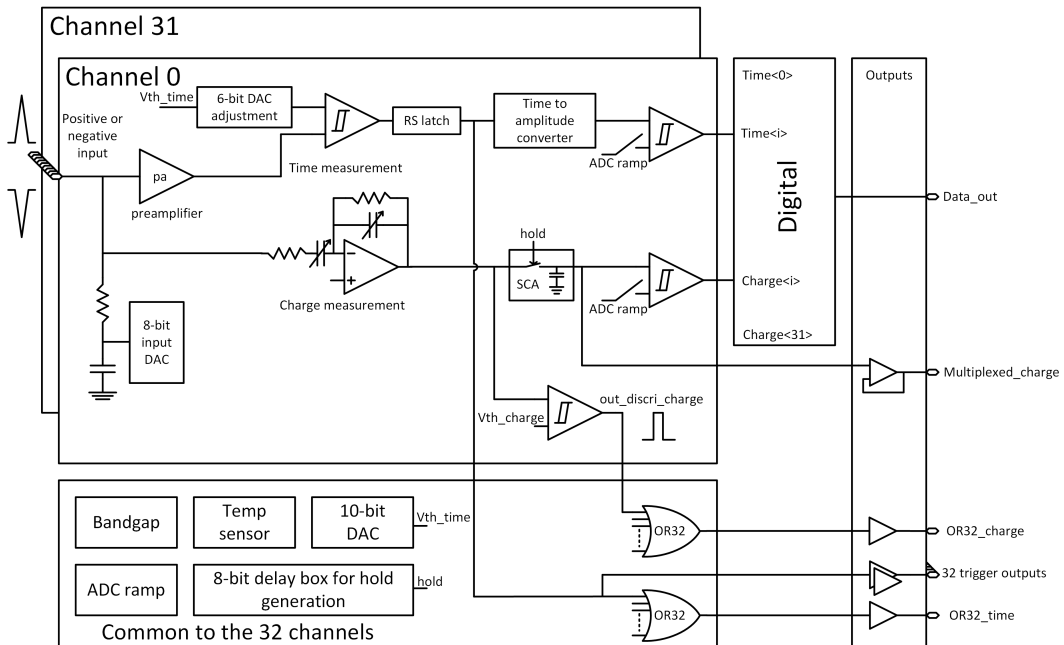


Figure 6.1: PETIROC 2A block diagram.

3666 Nevertheless, in order to adapt this ASIC to CMS, modifications were brought to the PETIROC [177].
 3667 In the new CMS RPCROC, the measurement of the charge will be performed by a TimeOverTech-
 3668 nique, taking profit of the capacity the ASIC has in measuring both the leading and trailing edges of the
 3669 input signals. The dynamic range will be expanded towards lower values to allow for the detection
 3670 of charges as low as 10 fC. Due to the radiation levels that are foreseen at the level of the iRPCs, the
 3671 SiGe technology will be replaced by the Taiwan Semiconductor Manufacturing Company (TSMC)
 3672 130 nm CMOS, to increase its radiation hardness while keeping fast pre-amplification and discrimi-
 3673 nation with a very low jitter that can reach less than 20 ps if no internal clock is used, as can be seen
 3674 from Figure 6.2. The ASIC is associated with an FPGA which purpose is to measure time thanks to

3675 a TDC with a time resolution of 50-100 ps developed by Tsinghua University and that will provide
 3676 a measurement of the signal position along the strip with a precision of a few cm by measuring the
 3677 signal timing on both ends of the strips. In order to read-out all 96 strips, 3 ASICs and 3 TDCs, each
 3678 having an increased number of 64-channels, are hosted on a FEB attached to the chamber.

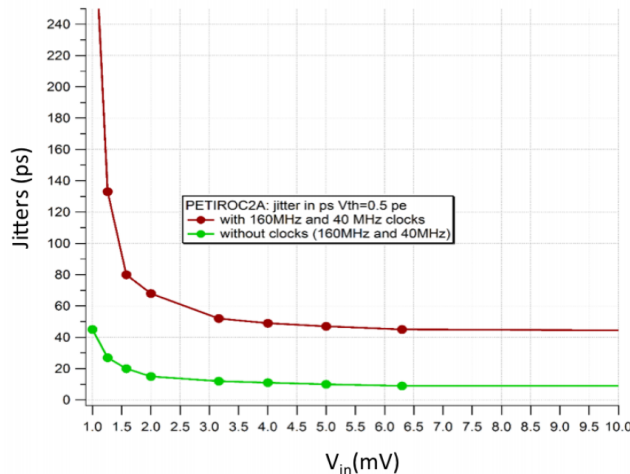


Figure 6.2: The PETIROC time jitter as a function of the input signal amplitude, measured with and without internal clocks.

3679 6.1.2 INFN Front-End Electronics: a robust back-up solution

3680 6.2 Preliminary tests at CERN

7

3681

3682

Conclusions and outlooks

3683 **7.1 Conclusions**

3684 **7.2 Outlooks**

A

3685

3686

A data acquisition software for CAEN VME TDCs

3687

3688 Certifying detectors in the perspective of HL-LHC required to develop tools for the GIF++ experi-
3689 ment. Among them was the C++ Data Acquisition (DAQ) software that allows to make the commu-
3690 nications in between a computer and TDC modules in order to retrieve the RPC data [275]. In this
3691 appendix, details about this software, as of how the software was written, how it functions and how
3692 it can be exported to another similar setup, will be given.

3693 A.1 GIF++ DAQ file tree

3694 GIF++ DAQ source code is fully available on github at [https://github.com/afagot/GIF_](https://github.com/afagot/GIF_DAQ)
3695 DAQ. The software requires 3 non-optional dependencies:

- 3696 • CAEN USB Driver, to mount the VME hardware,
3697 • CAEN VME Library, to communicate with the VME hardware, and
3698 • ROOT, to organize the collected data into a TTree.

3699 The CAEN VME library will not be packaged by distributions and will need to be installed man-
3700 ually. To compile the GIF++ DAQ project via a terminal, from the DAQ folder use the command:

```
3701     mkdir build  
3702     cd build  
3703     cmake ..  
3704     make install
```

3703 The source code tree is provided below along with comments to give an overview of the files' con-
3704 tent. The different objects created for this project (`v1718`, `v1190a`, `IniFile` & `DataReader`) will be

3705 described in details in the following sections.

3706



3707

A.2 Usage of the DAQ

3708 GIF++ DAQ, as used in GIF++, is not a standalone software. Indeed, the system being more com-
 3709 plexe, the DAQ only is a sub-layer of the software architecture developped to control and monitor
 3710 the RPCs that are placed into the bunker for performance study in an irradiated environment. The top
 3711 layer of GIF++ is a Web Detector Control System (webDCS) application. The DAQ is only called
 3712 by the webDCS when data needs to be acquired. The webDCS operates the DAQ through command
 3713 line. To start the DAQ, the webDCS calls:

3714

3715 bin/daq /path/to/the/log/file/in/the/output/data/folder

3716 where /path/to/the/log/file/in/the/output/data/folder is the only argument required. This
 3717 log file is important for the webDCS as this file contains all the content of the communication of the
 3718 webDCS and the different systems monitored by the webDCS. Its content is constantly displayed
 3719 during data taking for the users to be able to follow the operations. The communication messages
 3720 are normally sent to the webDCS log file via the functions declared in file `MsgSvc.h`, typically
 3721 `MSG_INFO(string message)`.

3722

3723 A.3 Description of the readout setup

3724 The CMS RPC setup at GIF++ counts 5 V1190A Time-to-Digital Converter (TDC) manufactured
 3725 by CAEN [263]. V1190A are VME units accepting 128 independent Multi-Hit/Multi-Event TDC
 3726 channels whose signals are treated by 4 100 ps high performance TDC chips developed by CERN
 3727 / ECP-MIC Division. The communication between the computer and the TDCs to transfer data is
 3728 done via a V1718 VME master module also manufactured by CAEN and operated from a USB
 3729 port [264]. These VME modules are all hosted into a 6U VME 6021 powered crate manufactured by
 3730 W-Ie-Ne-R than can accommodate up to 21 VME bus cards [276]. These 3 components of the DAQ
 3731 setup are shown in Figure A.1.

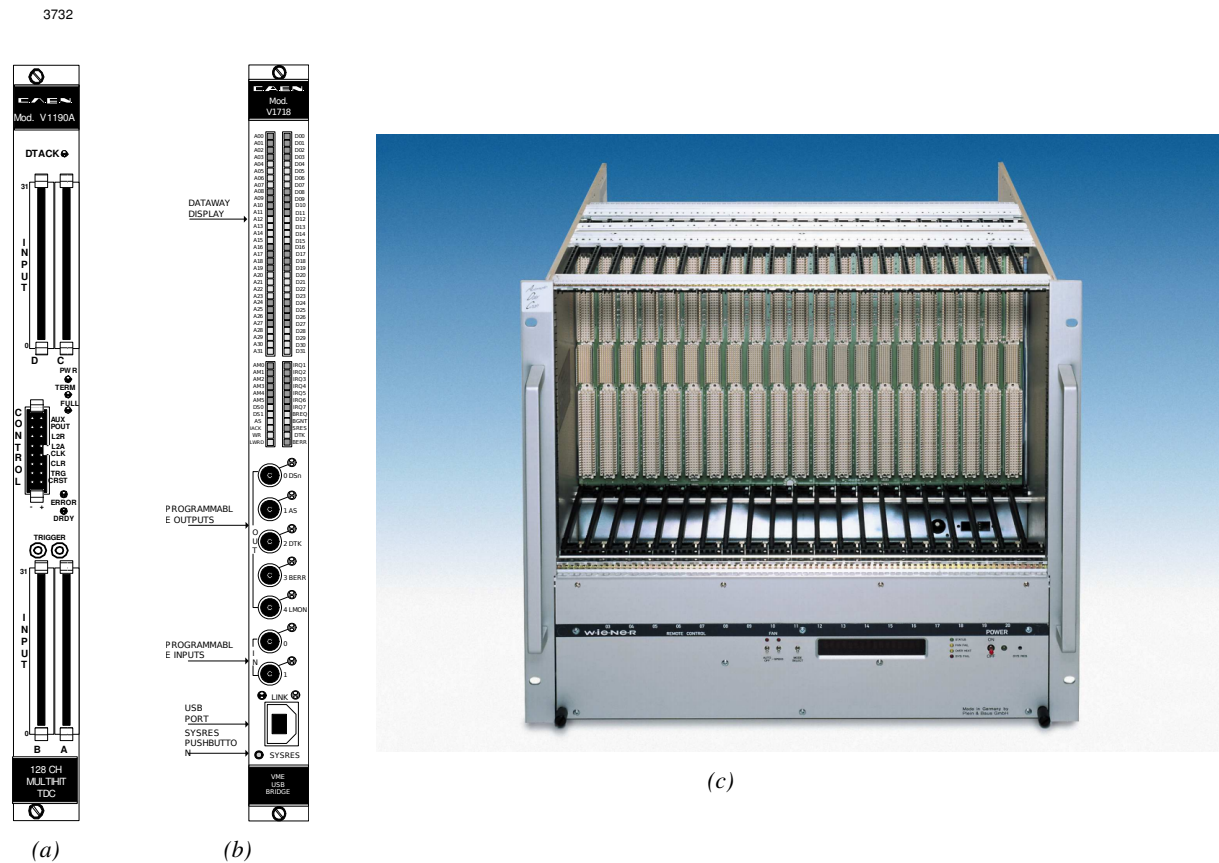


Figure A.1: (A.1a) View of the front panel of a V1190A TDC module [263]. (A.1b) View of the front panel of a V1718 Bridge module [264]. (A.1c) View of the front panel of a 6U 6021 VME crate [276].

3733 A.4 Data read-out

3734 To efficiently perform a data readout algorithm, C++ objects to handle the VME modules (TDCs
 3735 and VME bridge) have been created along with objects to store data and read the configuration file
 3736 that comes as an input of the DAQ software.

A.4.1 V1190A TDCs

The DAQ used at GIF takes profit of the *Trigger Matching Mode* offered by V1190A modules. This setting is enabled through the method `v1190a::SetTrigMatching (int ntdcs)` where `ntdcs` is the total number of TDCs in the setup this setting needs to be enabled for (Source Code A.1). A trigger matching is performed in between a trigger time tag, a trigger signal sent into the TRIGGER input of the TDC visible on Figure A.1a, and the channel time measurements, signals recorded from the detectors under test in our case. Control over this data acquisition mode, explained through Figure A.2, is offered via 4 programmable parameters:

- **match window:** the matching between a trigger and a hit is done within a programmable time window. This is set via the method
`void v1190a::SetTrigWindowWidth(Uint windowHeight, int ntdcs)`
- **window offset:** temporal distance between the trigger tag and the start of the trigger matching window. This is set via the method
`void v1190a::SetTrigWindowWidth(Uint windowHeight, int ntdcs)`
- **extra search margin:** an extended time window is used to ensure that all matching hits are found. This is set via the method
`void v1190a::SetTrigSearchMargin(Uint searchMargin, int ntdcs)`
- **reject margin:** older hits are automatically rejected to prevent buffer overflows and to speed up the search time. This is set via the method
`void v1190a::SetTrigRejectionMargin(Uint rejectMargin, int ntdcs)`

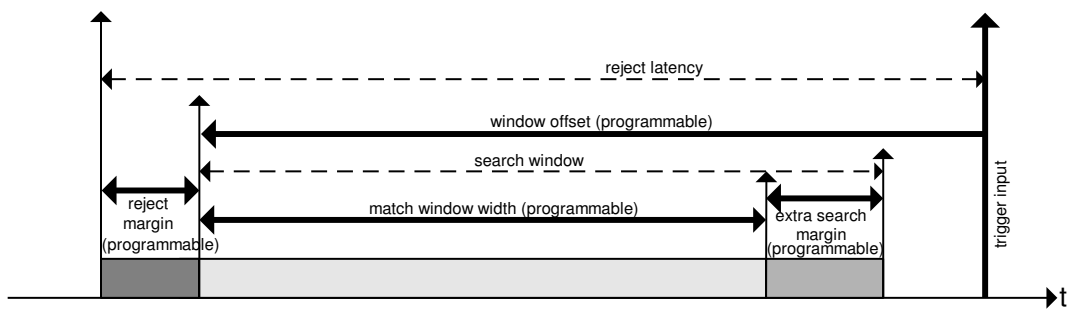


Figure A.2: Module V1190A Trigger Matching Mode timing diagram [263].

Each of these 4 parameters are given in number of clocks, 1 clock being 25 ns long. It is easy to understand at this level that there are 3 possible functioning settings:

- **1:** the match window is entirely contained after the trigger signal,
- **2:** the match window overlaps the trigger signal, or
- **3:** the match window is entirely contained before the trigger signal as displayed on Figure A.2.

In both the first and second cases, the sum of the window width and of the offset can be set to a maximum of 40 clocks, which corresponds to 1 μ s. Evidently, the offset can be negative, allowing

3765 for a longer match window, with the constraint of having the window ending at most 1 μ s after the
3766 trigger signal. In the third case, the maximum negative offset allowed is of 2048 clocks (12 bit) cor-
3767 responding to 51.2 μ s, the match window being strictly smaller than the offset. In the case of GIF++,
3768 the choice has been made to use this last setting by delaying the trigger signal. During the studies
3769 performed in GIF++, both the efficiency of the RPCs, probed using a muon beam, and the noise or
3770 gamma background rate are monitored. The extra search and reject margins are left unused.

3771 To probe the efficiency of RPC detectors, the trigger time tag is provided by the coïncidence of
3772 scintillators when a bunch of muons passes through GIF++ area is used to trigger the data acquisi-
3773 tion. For this measurement, it is useful to reduce the match window width only to contain the muon
3774 information. Indeed, the delay in between a trigger signal and the detection of the corresponding
3775 muon in the RPC being very contant (typically a few tens of ns due to jitter and cable length), the
3776 muon signals are very localised in time. Thus, due to a delay of approximalety 325 ns in between
3777 the muons and the trigger, the settings were chosen to have a window width of 24 clocks (600 ns)
3778 centered on the muon peak thanks to a negative offset of 29 clocks (725 ns).

3779 On the otherhand, monitoring the rates don't require for the DAQ to look at a specific time window.
3780 It is important to integrate enough time to have a robust measurement of the rate as the number of
3781 hits per time unit. The triggering signal is provided by the pulse generator integrated into the com-
3782 munication module V1718 at a frequency of 100 Hz to ensure that the data taking occurs in a random
3783 way, uncorrelated with beam physics, to probe only the irradiation spectrum on the detectors. The
3784 match window is set to 400 clocks (10 μ s) and the negative offset to 401 clocks as it needs to exceed
3785 the value of the match window.

3786

3787 The v1190a object, defined in the DAQ software as in Source Code A.1, offers the possil-
3788 ity to store all TDCs in the readout setup into a single object containing a list of hardware ad-
3789 dresses (addresses to access the TDCs' buffer through the VME crate) and each constructor and
3790 method acts on the list of TDCs to set the different acquisition parameters as describe above.
3791 The type of trigger matching is chosen with `v1190a::SetTrigMatching()` and the time substrac-
3792 tion, used to have a time measurement referring to the beggining of the time window, is set by
3793 `v1190a::SetTrigTimeSubtraction()`. Then, the wiwdow width and offset are respectively set
3794 thanks to `v1190a::SetTrigWindowWidth()` and `v1190a::SetTrigWindowOffset()`. The rejection
3795 and extra search margin, even if left unused and hence set to a default value of 0, can be set through
3796 `v1190a::SetTrigRejectionMargin()` and `v1190a::SetTrigSearchMargin()`. These methods are
3797 then called in `v1190a::SetTrigConfiguration()` that uses the information contained in the config-
3798 uration file `IniFile *iniFile` to set the different TDC parameters. A thorough explaination of the
3799 content of the configuration file is provided in Section A.5.2.

3800

3801 Among the other methods of class `v1190a` can be found a set of the detection mode (`v1190a::SetTDC`
3802 `DetectionMode()`), of the TDC time resolution (`v1190a::SetTDCResolution()`), of the dead time
3803 in between two consecutive signals recorded into a single channel (`v1190a::SetTDCDeadTime()`) or
3804 of the maximal number of signals that can be recorded per event (`v1190a::SetTDCEventSize()`). To
3805 help with setting these parameters, `enum` were used (`EdgeMode`, `Resolution`, `DeadTime` and `HitMax`
3806 are defined in `include/v1190a.h`).

```

3807
class v1190a
{
    private :
        long             Handle;
        vector<Data32>   Address;
        CVDataWidth      DataWidth;
        CVAddressModifier AddressModifier;

    public:

        v1190a(long handle, IniFile *inifile, int ntdcs);
        ~v1190a();
        Data16 write_op_reg(Data32 address, int code, string error);
        Data16 read_op_reg(Data32 address, string error);
        void Reset(int ntdcs);
        void Clear(int ntdcs);
        void TestWR(Data16 value,int ntdcs);
        void CheckTDCStatus(int ntdcs);
        void CheckCommunication(int ntdcs);
        void SetTDCTestMode(Data16 mode,int ntdcs);
        void SetTrigMatching(int ntdcs);
        void SetTrigTimeSubtraction(Data16 mode,int ntdcs);
        void SetTrigWindowWidth(Uint windowHeight,int ntdcs);
        void SetTrigWindowOffset(Uint windowOffset,int ntdcs);
        void SetTrigSearchMargin(Uint searchMargin,int ntdcs);
        void SetTrigRejectionMargin(Uint rejectMargin,int ntdcs);
        void GetTrigConfiguration(int ntdcs);
        void SetTrigConfiguration(IniFile *inifile,int ntdcs);
        void SetTDCDetectionMode(Data16 mode,int ntdcs);
        void SetTDCResolution(Data16 lsb,int ntdcs);
        void SetTDCDeadTime(Data16 time,int ntdcs);
        void SetTDCHeadTrailer(Data16 mode,int ntdcs);
        void SetTDCEventSize(Data16 size,int ntdcs);
        void SwitchChannels(IniFile *inifile,int ntdcs);
        void SetIRQ(Data32 level, Data32 count,int ntdcs);
        void SetBlockTransferMode(Data16 mode,int ntdcs);
        void Set(IniFile *inifile,int ntdcs);
        void CheckStatus(CVErrorCodes status) const;
        int ReadBlockD32(Uint tdc, const Data16 address,
                         Data32 *data, const Uint words, bool ignore_berr);
        Uint Read(RAWData *DataList,int ntdcs);
};

3808

```

3809 *Source Code A.1: Description of C++ object v1190a.*

3810 The detection mode corresponds to the type of edge detection the TDC will be using to
 3811 record the data. The TDCs can record the time stamp of the leading edge alone, of the trailing edge
 3812 alone, of both or they can operate in pair mode, meaning that the leading edge is recorded together
 3813 with the time difference in between leading and trailing edges. This last mode is not very practical
 3814 for the case of GIFT++ measurements as the information is coded into a single words in the TDC's
 3815 buffer, putting strong constraints on the time window and duration of the input signals. Indeed,
 3816 when recording the edges individually (single edge or both edges), a 32-bit word, of which 18 are
 3817 used to provide the time information alone, is stored into memory for each signal edge. With the
 3818 pair mode, instead of having one 32-bit word per edge, only a single 32-bit word is written of which
 3819 12 are used for the leading edge time information and 6 for the width of the pulse, as described on
 3820 p73 of reference [263]. This way, even though the pair mode is convenient to use as it automatically

3821 correlates a leading edge with the corresponding signal width in a single word, it is advised to be
 3822 careful when using it and to be aware of the extra time constraints (for both leading time and signal
 3823 width) that will come for choosing this setting. If it is necessary to work with large input signals,
 3824 the mode recording both edges will be preferred to the pair mode and the association of a leading
 3825 and trailing edges pair will then be performed offline by the user. Then, the time resolution is to be
 3826 chosen in a range from 100 to 800 ps, the dead time in a range from 5 to 100 ns, and the maximal
 3827 number of hits per event in a range from 0 to 128 with the possibility to choose to have no limits.

3828 A.4.2 DataReader

3829 Enabled thanks to `v1190a::SetBlockTransferMode()`, the data transfer is done via Block Transfer
 3830 (BLT). Using BLT allows to transfer a fixed number of events called a *block*. This is used together
 3831 with an Almost Full Level (AFL) of the TDCs' output buffers, defined through `v1190a::SetIRQ()`.
 3832 This AFL gives the maximum amount of 32735 words (16 bits, corresponding to the depth of a TDC
 3833 output buffer) that can be written in a buffer before an Interrupt Request (IRQ) is generated and seen by
 3834 the VME Bridge V1718, which sends a `BUSY` signal intended to stopping the data acquisition during
 3835 the transfer of the content of each TDC buffers before resuming. For each trigger, 6 words or more
 3836 are written into the TDC buffer:

- 3837 • **a global header** providing information of the event number since the beginning of the data
 3838 acquisition,
- 3839 • **a TDC header** which is enabled thanks to `v1190a::SetTDCHeadTrailer()`,
- 3840 • **the TDC data (if any)**, 1 for each hit recorded during the event, providing the channel and the
 3841 time stamp associated to the hit,
- 3842 • **a TDC error** providing error flags,
- 3843 • **a TDC trailer** which is enabled thanks to `v1190a::SetTDCHeadTrailer()`,
- 3844 • **a global trigger time tag** that provides the absolute trigger time relatively to the last reset,
 3845 and
- 3846 • **a global trailer** providing the total word count in the event.

3847 CMS RPC FEEs provide with 100 ns long LVDS output signals that are injected into the TDCs'
 3848 input. Any avalanche signal that gives a signal above the FEEs threshold is thus recorded by the
 3849 TDCs as a hit within the match window. Each hit is assigned to a specific TDC channel with a time
 3850 stamp, with a precision of 100 ps. The reference time, $t_0 = 0$, is provided by the beginning of the
 3851 match window. Thus for each trigger, coming from a scintillator coincidence or the pulse generator,
 3852 a list of hits is stored into the TDCs' buffers and will then be transferred into a ROOT Tree.
 3853 When the BLT is used, it is easy to understand that the maximum number of words that have been set
 3854 as AFL will not be a finite number of events or, at least, the number of events that would be recorded
 3855 into the TDC buffers will not be a multiple of the block size. In the last BLT cycle to transfer data,
 3856 the number of events to transfer will most probably be lower than the block size. In that case, the
 3857 TDC can add fillers at the end of the block but this option requires to send more data to the computer
 3858 and is thus a little slower. Another solution is to finish the transfer after the last event by sending a
 3859 bus error that states that the BLT reached the last event in the pile. This method has been chosen in

3860 GIF++.

3861 Due to irradiation, an event in GIF++ can count up to 300 words per TDC. A limit of 4096 words
 3862 (12 bits) has been set to generate IRQ which represent from 14 to almost 700 events depending on
 3863 the average of hits collected per event. Then the block size has been set to 100 events with enabled
 3864 bus errors. When an AFL is reached for one of the TDCs, the VME bridge stops the acquisition by
 3865 sending a BUSY signal.

3866

3867 The data is then transferred one TDC at a time into a structure called `RAWData` (Source Code A.2).
 3868 Note that the structure as presented here is used when a single edge detection is used as there is only
 3869 one time stamp list associated to the hits. When using detection on both edges, a second time stamp
 3870 list could be added and when using pair detection, a list with the signal width could be added instead.
 3871

```
3872   struct RAWData {
 3873     vector<int>                   *EventList;
 3874     vector<int>                   *NHitsList;
 3875     vector<int>                   *QFlagList;
 3876     vector<vector<int> >   *ChannelList;
 3877     vector<vector<float> > *TimeStampList;
 3878 }
```

3873

Source Code A.2: Description of data holding C++ structure `RAWData`.

```
3874   class DataReader
 3875   {
 3876     private:
 3877       bool              StopFlag;
 3878       IniFile *iniFile;
 3879       Data32          MaxTriggers;
 3880       v1718            *VME;
 3881       int              nTDCs;
 3882       v1190a           *TDCs;
 3883       RAWData          TDCData;

 3884     public:
 3885       DataReader();
 3886       virtual ~DataReader();
 3887       void             SetIniFile(string inifilename);
 3888       void             SetMaxTriggers();
 3889       Data32          GetMaxTriggers();
 3890       void             SetVME();
 3891       void             SetTDC();
 3892       int              GetQFlag(Uint it);
 3893       void             Init(string inifilename);
 3894       void             FlushBuffer();
 3895       void             Update();
 3896       string          GetFileName();
 3897       void             WriteRunRegistry(string filename);
 3898       void             Run();
 3899 }
```

3875

Source Code A.3: Description of C++ object `DataReader`.

3876 In order to organize the data transfer and the data storage, an object called `DataReader` was
 3877 created (Source Code A.3). On one hand, it has `v1718` and `v1190a` objects as private members for
 3878 communication purposes, such as VME modules settings via the configuration file `*iniFile` or data

3879 read-out through `v1190a::Read()` and on the other hand, it contains the structure `RAWData` that allows
 3880 to organise the data in vectors reproducing the tree structure of a ROOT file.
 3881 Each event is transferred from `TDCData` and saved into branches of a ROOT `TTree` as 3 integers
 3882 that represent the event ID (`EventCount`), the number of hits read from the TDCs (`nHits`), and the
 3883 quality flag that provides information for any problem in the data transfer (`qflag`), and 2 lists of
 3884 *nHits* elements containing the fired TDC channels (`TDCCh`) and their respective time stamps (`TDCTS`),
 3885 as presented in Source Code A.4. The ROOT file file is named using information contained into
 3886 the configuration file, presented in section A.5.2. The needed information is extracted using method
 3887 `DataReader::GetFileName()` and allow to build the output filename format `ScanXXXXXX_HVX_DAQ.root`
 3888 where `ScanXXXXXX` is a 6 digit number representing the scan number into GIF++ database and `HVX`
 3889 the HV step within the scan that can be more than a single digit. An example of ROOT data file is
 3890 provided with Figure A.3.

```
3891
  RAWData TDCData;
  TFile *outputFile = new TFile(outputFileName.c_str(), "recreate");
  TTree *RAWDataTree = new TTree("RAWData", "RAWData");

  int EventCount = -9;
  int nHits = -8;
  int qflag = -7;
  vector<int> TDCCh;
  vector<float> TDCTS;

  RAWDataTree->Branch("EventNumber", &EventCount, "EventNumber/I");
  RAWDataTree->Branch("number_of_hits", &nHits, "number_of_hits/I");
  RAWDataTree->Branch("Quality_flag", &qflag, "Quality_flag/I");
  RAWDataTree->Branch("TDC_channel", &TDCCh);
  RAWDataTree->Branch("TDC_TimeStamp", &TDCTS);

  //...
  //Here read the TDC data using v1190a::Read() and place it into
  //TDCData for as long as you didn't collect the requested amount
  //of data.
  //...

  for(Uint i=0; i<TDCData.EventList->size(); i++) {
    EventCount = TDCData.EventList->at(i);
    nHits = TDCData.NHitsList->at(i);
    qflag = TDCData.QFlagList->at(i);
    TDCCh = TDCData.ChannelList->at(i);
    TDCTS = TDCData.TimeStampList->at(i);
    RAWDataTree->Fill();
  }
}
```

3893 *Source Code A.4: Highlight of the data transfer and organisation within `DataReader::Run()` after the data
 has been collected into `TDCData`.*

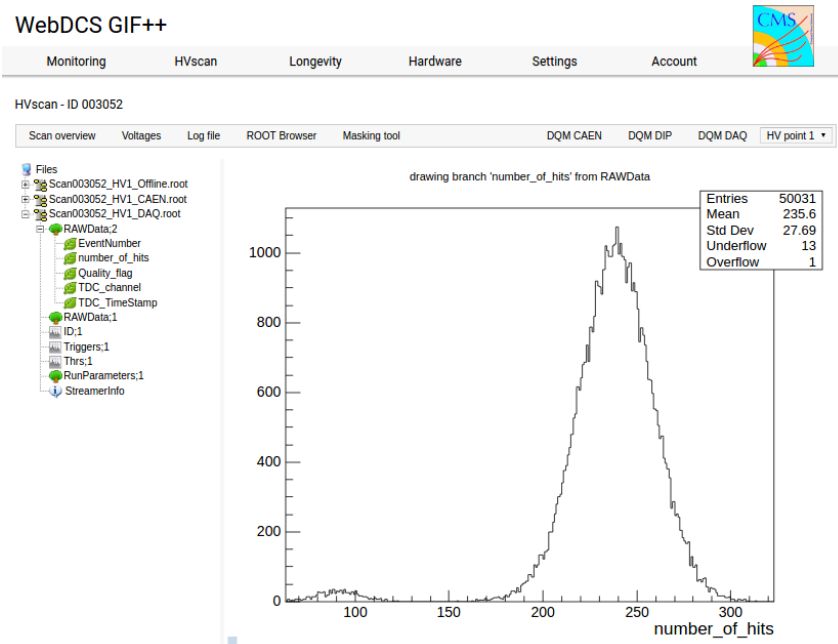


Figure A.3: Structure of the ROOT output file generated by the DAQ. The 5 branches (EventNumber, number_of_hits, Quality_flag, TDC_channel and TDC_TimeStamp) are visible on the left panel of the ROOT browser. On the right panel is visible the histogram corresponding to the variable nHits. In this specific example, there were approximately 50k events recorded to measure the gamma irradiation rate on the detectors. Each event is stored as a single entry in the TTree.

3894 A.4.3 Data quality flag

3895 Among the parameters that are recorded for each event, the quality flag is determined on the fly
 3896 by checking the data recorded by every single TDC. An `enum` called `QualityFlag` was written to
 3897 associate the key `GOOD` to the integer 1 and `CORRUPTED` to 0. From method `v1190a::Read()`, it can
 3898 be understood that the content of each TDC buffer is readout one TDC at a time. Entries are created
 3899 in the data list for the first TDC and then, when the second buffer is readout, events corresponding
 3900 to entries that have already been created to store data for the previous TDC are added to the existing
 3901 list element. On the contrary, when an event entry has not been yet created in the data list, a new
 3902 entry is created.

3903 It is possible that each TDC buffer contains a different number of events. In cases where the first
 3904 element in the buffer list is an event for corresponds to a new entry, the difference in between the
 3905 entry from the buffer and the last entry in the data list is recorded and checked. If it is greater than 1,
 3906 what should never be the case, the quality flag is set to `CORRUPTED` for this TDC and an empty entry
 3907 is created in the place of the missing ones. Missing entries are believe to be the result of a bad hold
 3908 on the TDC buffers at the moment of the readout. Indeed, the software hold is effective only on 1
 3909 TDC at a time and no solution as been found yet to completely block the writting in the buffers when
 3910 an IRQ is received.

3911 At the end of each BLT cycle, the ID of the last entry stored for each TDC buffer is not recorded.
 3912 When starting the next cycle, if the first entry in the pile corresponds to an event already existing
 3913 in the list, the readout will start from this list element and will not be able to check the difference

3914 in between this entry's ID and the one of the last entry that was recorded for this TDC buffer in
 3915 the previous cycle. In the case events were missing, the flag stays at its initial value of 0, which is
 3916 similar to CORRUPTED and it is assumed that then this TDC will not contribute to number_of_hits,
 3917 TDC_channel or TDC_TimeStamp. Finally, since there will be 1 RAWData entry per TDC for each event
 3918 (meaning nTDCs entries, referring to DataReader private attribute), the individual flags of each TDC
 3919 will be added together. The final format is an integer composed nTDCs digits where each digit is the
 3920 flag of a specific TDC. This is constructed using powers of 10 like follows:

3921 TDC 0: QFlag = $10^0 \times \text{QualityFlag}$

3922 TDC 1: QFlag = $10^1 \times \text{QualityFlag}$

3923 ...

3924 TDC N: QFlag = $10^N \times \text{QualityFlag}$

3925 and the final flag to be with N digits:

3926 QFlag = n....3210

3927 each digit being 1 or 0. Below is given an example with a 4 TDCs setup.

3928 If all TDCs were good : QFlag = 1111,

3929 but if TDC 2 was corrupted : QFlag = 1011.

3930 When data taking is over and the data contained in the dynamical RAWData structure is transferred
 3931 to the ROOT file, all the 0s are changed into 2s by calling the method DataReader::GetQFlag().
 3932 This will help translating the flag without knowing the number of TDCs beforehand. Indeed, a flag
 3933 111 could be due to a 3 TDC setup with 3 good individual TDC flags or to a more than 3 TDC setup
 3934 with TDCs those ID is greater than 2 being CORRUPTED, thus giving a 0.

3935 The quality flag has been introduced quite late, in October 2017 only, to the list of GIFT++ DAQ
 3936 parameters to be recorded into the output ROOT file. Before this addition, the missing data, corrupting
 3937 the quality for the offline analysis, was contributing to artificially fill data with lower multiplicity.
 3938 Looking at TBranch number_of_hits provides an information about the data of the full GIFT++
 3939 setup. When a TDC is not able to transfer data for a specific event, the effect is a reduction of the
 3940 total number of hits recorded in the full setup, this is what can be seen from Figure A.4. After offline
 3941 reconstruction detector by detector, the effect of missing events can be seen in the artificially filled
 3942 bin at multiplicity 0 shown in Figure A.5. Nonetheless, for data with high irradiation levels, as it is
 3943 the case for Figure A.5a, discarding the fake multiplicity 0 data can be done easily during the offline
 3944 analysis. At lower radiation, the missing events contribution becomes more problematic as the mul-
 3945 tiplicity distribution overlaps the multiplicity 0 and that in the same time the proportion of missing
 3946 events decreases. Attempts to fit the distribution with a Poisson or skew distribution function were
 3947 not conclusive and this very problem has been at the origin of the quality flag that allows to give a
 3948 non ambiguous information about each event quality.

3949

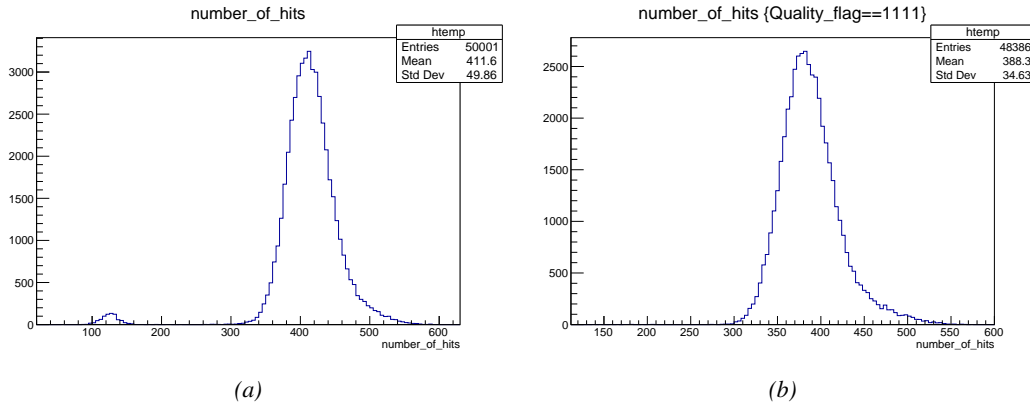


Figure A.4: The effect of the quality flag is explained by presenting the content of TBranch `number_of_hits` of a data file without `Quality_flag` in Figure A.4a and the content of the same TBranch for data corresponding to a `Quality_flag` where all TDCs were labelled as `GOOD` in Figure A.4b taken with similar conditions. It can be noted that the number of entries in Figure A.4b is slightly lower than in Figure A.4a due to the excluded events.

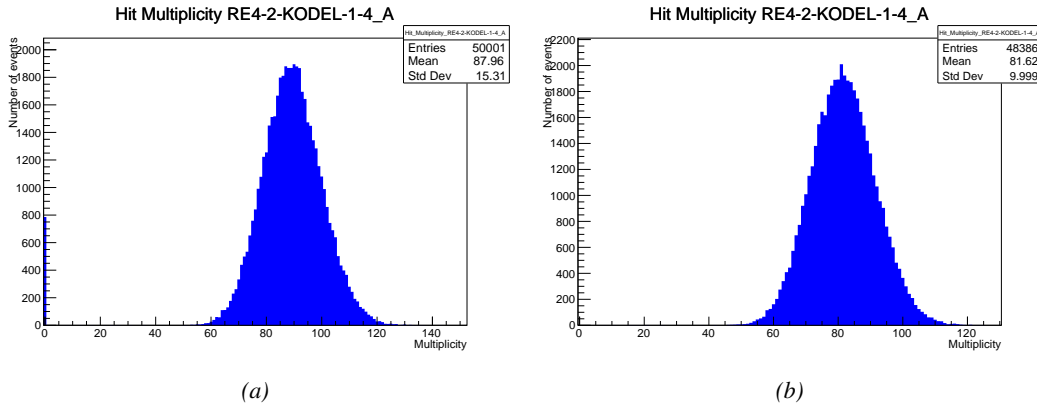


Figure A.5: Using the same data as previously showed in Figure A.4, the effect of the quality flag is explained by presenting the reconstructed hit multiplicity of a data file without `Quality_flag` in Figure A.5a and the reconstructed content of the same RPC partition for data corresponding to a `Quality_flag` where all TDCs were labelled as `GOOD` in Figure A.5b taken with similar conditions. The artificial high content of bin 0 is completely suppressed.

A.5 Communications

3951 To ensure data readout and dialog in between the machine and the TDCs or in between the webDCS
 3952 and the DAQ, different communication solutions were used. First of all, it is important to have a
 3953 module to allow the communication in between the TDCs and the computer from which the DAQ
 3954 operates. When this communication is effective, shifters using the webDCS to control data taking
 3955 can thus send instructions to the DAQ.

3956

3957 A.5.1 V1718 USB Bridge

3958 In the previous section, the data transfer as been discussed. The importance of the `v1718` object
 3959 (Source Code A.5), used as private member of `DataReader`, was not explicited. VME master
 3960 modules are used for communication purposes as they host the USB port that connects the pow-
 3961 ered crate buffer to the computer were the DAQ is installed. From the source code point of view,
 3962 this object is used to control the communication status, by reading the returned error codes with
 3963 `v1718::CheckStatus()`, or to check for IRQs coming from the TDCs through `v1718::CheckIRQ()`.
 3964 To ensure that triggers are blocked at the hardware level, a NIM pulse is sent out of one of the two
 3965 first programmable outputs of the module (`v1718::SendBUSY()`) to the VETO of the coincidence
 3966 module where the trigger signals originate. As long as this signal is ON, no trigger can reach the
 3967 TDCs anymore. Finally, used in the case of noise and background measurements in which the trigger
 3968 needs not to be provided by the muon beam but by an uncorrelated source, a pulse generator
 3969 is enabled with `v1718::RDMTriggerPulse()`. The "random" pulse is sent through the third and
 3970 fourth outputs of the module. Both the BUSY signal and the random pulse are shaped in the method
 3971 `v1718::SetPulsers()` where the number of pulses to be generated, their width, as well as the period
 3972 of the pulse generator is defined.

3973

```
class v1718{
    private:
        int             Handle;
        Data32          Data;           // Data
        CVIRQLevels    Level;         // Interrupt level
        CVAddressModifier AM;          // Addressing Mode
        CVDataWidth     DataSize;      // Data Format
        Data32          BaseAddress;   // Base Address

    public:
        v1718(IniFile *inifile);
        ~v1718();
        long            GetHandle(void) const;
        int             SetData(Data16 data);
        Data16          GetData(void);
        int             SetLevel(CVIRQLevels level);
        CVIRQLevels    GetLevel(void);
        int             SetAM(CVAddressModifier am);
        CVAddressModifier GetAM(void);
        int             SetDataSize(CVDataWidth datasize);
        CVDataWidth     GetDataSize(void);
        int             SetBaseAddress(Data16 baseaddress);
        Data16          GetBaseAddress(void);
        void            CheckStatus(CVErrorCodes status) const;
        bool            CheckIRQ();
        void            SetPulsers(UINT RDM_Frequency);
        void            SendBUSY(PulserLevel level);
        void            RDMTriggerPulse(PulserLevel level);
};
```

3975

Source Code A.5: Description of C++ object v1718.

3976 A.5.2 Configuration file

3977 The DAQ software takes as input a configuration file written using INI standard [277]. This file is
 3978 partly filled with the information provided by the shifters when starting data acquisition using the
 3979 webDCS, as shown by Figure A.6. This information is written in section **[General]** and will later
 3980 be stored in the ROOT file that contains the DAQ data as can be seen from Figure A.3. Indeed,
 3981 another `TTree` called `RunParameters` as well as the 2 histograms `ID`, containing the scan number,
 3982 start and stop time stamps, and `Triggers`, containing the number of triggers requested by the shifter,
 3983 are available in the data files. Moreover, `ScanID` and `HV` are then used to construct the file name
 3984 thanks to the method `DataReader::GetFileName()`.

Chamber	RE2-2-NPD-BARC-8	RE4-2-CERN-105	RE2-2-NPD-BARC-9	RE4-2-CERN-105	RE4-2-KODEL-1-4	Max triggers
HV _{eff} 1	8600	8500	8600	8500	6500	
HV _{eff} 2	8700	8600	8700	8600	6600	
HV _{eff} 3	8800	8700	8800	8700	6700	
HV _{eff} 4	8900	8800	8900	8800	6800	
HV _{eff} 5	9000	8900	9000	8900	6900	
HV _{eff} 6	9100	9000	9100	9000	7000	
HV _{eff} 7	9200	9100	9200	9100	7100	
HV _{eff} 8	9300	9200	9300	9200	7200	
HV _{eff} 9	9400	9300	9400	9300	7300	
HV _{eff} 10	9500	9400	9500	9400	7400	

Figure A.6: WebDCS DAQ scan page. On this page, shifters need to choose the type of scan (Rate, Efficiency or Noise Reference scan), the gamma source configuration at the moment of data taking, the beam configuration, and the trigger mode. These information will be stored in the DAQ ROOT output. Are also given the minimal measurement time and waiting time after ramping up of the detectors is over before starting the data acquisition. Then, the list of HV points to scan and the number of triggers for each run of the scan are given in the table underneath.

3985 The rest of the information is written beforehand in the configuration file template, as explicated
 3986 in Source Code A.6, and contains the hardware addresses to the different VME modules in the
 3987 setup as well as settings for the TDCs. As the TDC settings available in the configuration file are not
 3988 supposed to be modified, an improvement would be to remove them from the configuration file and
 3989 to hardcode them inside of the DAQ code itself or to place them into a different INI file that would
 3990 host only the TDC settings to lower the probability for a bad manipulation of the configuration file
 3991 that can be modified from one of webDCS' menus.

```
3992 [General]
TdcS=4
ScanID=$scanid
HV=$HV
RunType=$runtype
MaxTriggers=$maxtriggers
Beam=$beam
[VMEInterface]
Type=V1718
BaseAddress=0xFF0000
Name=VmeInterface
int_trig_freq=100
[TDC0]
Type=V1190A
BaseAddress=0x00000000
Name=Tdc0
StatusA00-15=1
StatusA16-31=1
StatusB00-15=1
StatusB16-31=1
StatusC00-15=1
StatusC16-31=1
StatusD00-15=1
StatusD16-31=1
[TDC1]
Type=V1190A
BaseAddress=0x11110000
Name=Tdc1
StatusA00-15=1
StatusA16-31=1
StatusB00-15=1
StatusB16-31=1
StatusC00-15=1
StatusC16-31=1
StatusD00-15=1
StatusD16-31=1
3993 [TDC2]
Type=V1190A
BaseAddress=0x22220000
Name=Tdc2
StatusA00-15=1
StatusA16-31=1
StatusB00-15=1
StatusB16-31=1
StatusC00-15=1
StatusC16-31=1
StatusD00-15=1
StatusD16-31=1
[TDC3]
Type=V1190A
BaseAddress=0x44440000
Name=Tdc3
StatusA00-15=1
StatusA16-31=1
StatusB00-15=1
StatusB16-31=1
StatusC00-15=1
StatusC16-31=1
StatusD00-15=1
StatusD16-31=1
[TDCSettings]
TriggerExtraSearchMargin=0
TriggerRejectMargin=0
TriggerTimeSubtraction=0b1
TdcDetectionMode=0b01
TdcResolution=0b10
TdcDeadTime=0b00
TdcHeadTrailer=0b1
TdcEventSize=0b1001
TdcTestMode=0b0
BLTMode=1
```

Source Code A.6: INI configuration file template for 4 TDCs. In section [General], the number of TDCs is explicitated and information about the ongoing run is given. Then, there are sections for each and every VME modules. There buffer addresses are given and for the TDCs, the list of channels to enable is given. Finally, in section [TDCSettings], a part of the TDC settings are given.

3994

```

typedef map< const string, string > IniFileData;

class IniFile{
    private:
        bool          CheckIfComment(string line);
        bool          CheckIfGroup(string line, string& group);
        bool          CheckIfToken(string line, string& key, string& value);
        string         FileName;
        IniFileData   FileData;
        int           Error;

    public:
        IniFile();
        IniFile(string filename);
        virtual      ~IniFile();

    // Basic file operations
    void          SetFileName(string filename);
    int           Read();
    int           Write();
    IniFileData   GetData();
}

// Data readout methods
Data32 addressType(string groupname, string keyname, Data32 defaultvalue);
long intType(string groupname, string keyname, long defaultvalue);
long long longType(string groupname, string keyname, long long
← defaultvalue);
string stringType(string groupname, string keyname, string defaultvalue);
float floatType(string groupname, string keyname, float defaultvalue);

// Error methods
string     GetErrorMsg();
};

3995

```

3996

Source Code A.7: Description of C++ object IniFile used as a parser for INI file format.

3997

In order to retrieve the information of the configuration file, the object `IniFile` has been developed to provide an INI parser, presented in Source Code A.7. It contains private methods returning a boolean to check the type of line written in the file, whether a comment, a group header or a key line (`IniFile::CheckIfComment()`, `IniFile::CheckIfGroup()` and `IniFile::CheckIfToken()`). The key may sometimes be referred to as *token* in the source code. Moreover, the private element `FileData` is a map of `const` string to string that allows to store the data contained inside the configuration file via the public method `IniFile::GetData()` following the formatting (see method `IniFile::Read()`):

3998

3999

4000

4001

4002

4003

4004

4005

4006

```

string group, token, value;
// Get the field values for the 3 strings.
// Then concatenate group and token together as a single string
// with a dot separation.
token = group + "." + token;
FileData[token] = value;

```

4007 More methods have been written to translate the different keys into the right variable format
 4008 when used by the DAQ. For example, to get a **float** value out of the configuration file data, knowing
 4009 the group and the key needed, the method `IniFile::floatType()` can be used. It takes 3 arguments
 4010 being the group name and key name (both `string`), and a default **float** value used as exception in
 4011 the case the expected combination of group and key cannot be found in the configuration file. This
 4012 default value is then used and the DAQ continues on working after sending an alert in the log file for
 4013 further debugging.

4014

4015 A.5.3 WebDCS/DAQ intercommunication

4016 When shifters send instructions to the DAQ via the configuration file, it is the webDCS itself that
 4017 gives the start command to the DAQ and then the 2 softwares use inter-process communication
 4018 through file to synchronise themselves. This communication file is represented by the variable `const`
 4019 `string __runstatuspath`.

4020 On one side, the webDCS sends commands or status that are readout by the DAQ:

- 4021 • INIT, status sent when launching a scan and read via function `CtrlRunStatus(...)`,
- 4022 • START, command to start data taking and read via function `CheckSTART()`,
- 4023 • STOP, command to stop data taking at the end of the scan and read via function `CheckSTOP()`,
 4024 and
- 4025 • KILL, command to kill data taking sent by user and read via function `CheckKILL()`. Note that
 4026 the DAQ doesn't stop before the current ROOT file is safely written and saved.

4027 and on the other, the DAQ sends status that are controled by the webDCS:

- 4028 • DAQ_RDY, sent with `SendDAQReady()` to signify that the DAQ is ready to receive commands
 4029 from the webDCS,
- 4030 • RUNNING, sent with `SendDAQRunning()` to signify that the DAQ is taking data,
- 4031 • DAQ_ERR, sent with `SendDAQError()` to signify that the DAQ didn't receive the expected com-
 4032 mand from the webDCS or that the launch command didn't have the right number of argu-
 4033 ments,
- 4034 • RD_ERR, sent when the DAQ wasn't able to read the communication file, and
- 4035 • WR_ERR, sent when the DAQ wasn't able to write into the communication file.

4036 A.5.4 Example of inter-process communication cycle

4037 Under normal conditions, the webDCS and the DAQ processes exchange commands and status via
 4038 the file hosted at the address `__runstatuspath`, as explained in subsection A.5.3. An example of
 4039 cycle is given in Table A.1. In this example, the steps 3 to 5 are repeated as long as the webDCS tells
 4040 the DAQ to take data. A data taking cycle is the equivalent as what is called a *Scan* in GIFT++ jargon,

4041 referring to a set a runs with several HV steps. Each repetition of steps 3 to 5 is then equivalent to a
 4042 single *Run*.

4043 At any moment during the data taking, for any reason, the shifter can decide that the data taking
 4044 needs to be stopped before it reached the end of the scheduled cycle. Thus at any moment on the
 4045 cycle, the content of the inter-process communication file will be changed to `KILL` and the DAQ will
 4046 shut down right away. The DAQ checks for `KILL` signals every 5s after the TDCs configuration is
 4047 over. So far, the function `CheckKILL()` has been used only inside of the data taking loop of method
 4048 `DataReader::Run()` and thus, if the shifter decides to KILL the data taking during the TDC con-
 4049 figuration phase or the HV ramping in between 2 HV steps, the DAQ will not be stopped smoothly
 4050 and a *force kill* command will be sent to stop the DAQ process that is still awake on the computer.
 4051 Improvements can be brought on this part of the software to make sure that the DAQ can safely
 4052 shutdown at any moment.

4053

step	actions of webDCS	status of DAQ	<code>__runstatuspath</code>
1	launch DAQ ramp voltages ramping over wait for currents stabilization	readout of IniFile configuration of TDCs	INIT
2		configuration done send DAQ ready wait for <code>START</code> signal	DAQ_RDY
3	waiting time over send <code>START</code>		START
4	wait for run to end monitor DAQ run status	data taking ongoing check for <code>KILL</code> signal	RUNNING
5		run over send <code>DAQ_RDY</code> wait for next DCS signal	DAQ_RDY
6	ramp voltages ramping over wait for currents stabilization		DAQ_RDY
3	waiting time over send <code>START</code>		START
4	wait for run to end monitor DAQ run status	update IniFile information data taking ongoing check for <code>KILL</code> signal	RUNNING
5		run over send <code>DAQ_RDY</code> wait for next DCS signal	DAQ_RDY
7	send command <code>STOP</code>	DAQ shuts down	STOP

Table A.1: Inter-process communication cycles in between the webDCS and the DAQ through file string signals.

A.6 Software export

4054 In section A.2 was discussed the fact that the DAQ as written in its last version is not a standalone
 4055 software. It is possible to make it a standalone program that could be adapted to any VME setup

4057 using V1190A and V1718 modules by creating a GUI for the software or by printing the log messages
4058 that are normally printed in the webDCS through the log file, directly into the terminal. This
4059 method was used by the DAQ up to version 3.0 moment where the webDCS was completed. Also, it
4060 is possible to check branches of DAQ v2.X to have example of communication through a terminal.
4061 DAQ v2.X is nonetheless limited in its possibilities and requires a lot of offline manual interventions
4062 from the users. Indeed, there is no communication of the software with the detectors' power
4063 supply system that would allow for a user a predefine a list of voltages to operate the detectors at
4064 and loop over to take data without any further manual intervention. In v2.X, the data is taken for a
4065 single detector setting and at the end of each run, the softwares asks the user if he intends on taking
4066 more runs. If so, the software invites the user to set the operating voltages accordingly to what is
4067 necessary and to manual update the configuration file in consequence. This working mode can be a
4068 very first approach before an evolution and has been successfully used by colleagues from different
4069 collaborations.

4070 For a more robust operation, it is recommended to develop a GUI or a web application to interface
4071 the DAQ. Moreover, to limit the amount of manual interventions, and thus the probability to make
4072 mistakes, it is also recommended to add an extra feature into the DAQ by installing the HV Wrapper
4073 library provided by CAEN of which an example of use in a similar DAQ software developped by a
4074 master student of UGent, and called TinyDAQ, is provided on UGent's github. Then, this HV Wrapper
4075 will help you communicating with and give instructions to a CAEN HV powered crate and can
4076 be added into the DAQ at the same level where the communication with the user was made in DAQ
4077 v2.X. In case you are using another kind of power system for your detectors, it is stringly adviced to
4078 use HV modules or crates that can be remotely controloled via a using C++ libraries.

4079

B

4080

4081

Details on the offline analysis package

4082 The data collected in GIF++ thanks to the DAQ described in Appendix A is difficult to interpret by
4083 a human user that doesn't have a clear idea of the raw data architecture of the ROOT data files. In
4084 order to render the data human readable, a C++ offline analysis tool was designed to provide users
4085 with detector by detector histograms that give a clear overview of the parameters monitored during
4086 the data acquisition [272]. In this appendix, details about this software in the context of GIF++, as
4087 of how the software was written and how it functions will be given.

4088 B.1 GIF++ Offline Analysis file tree

4089 GIF++ Offline Analysis source code is fully available on github at https://github.com/aafagot/GIF_OfflineAnalysis. The software requires ROOT as non-optionnal dependency
4090 as it takes ROOT files in input and write an output ROOT file containing histograms. To compile the
4091 GIF++ Offline Analysis project is compiled with cmake. To compile, first a build/ directory must
4092 be created to compile from there:

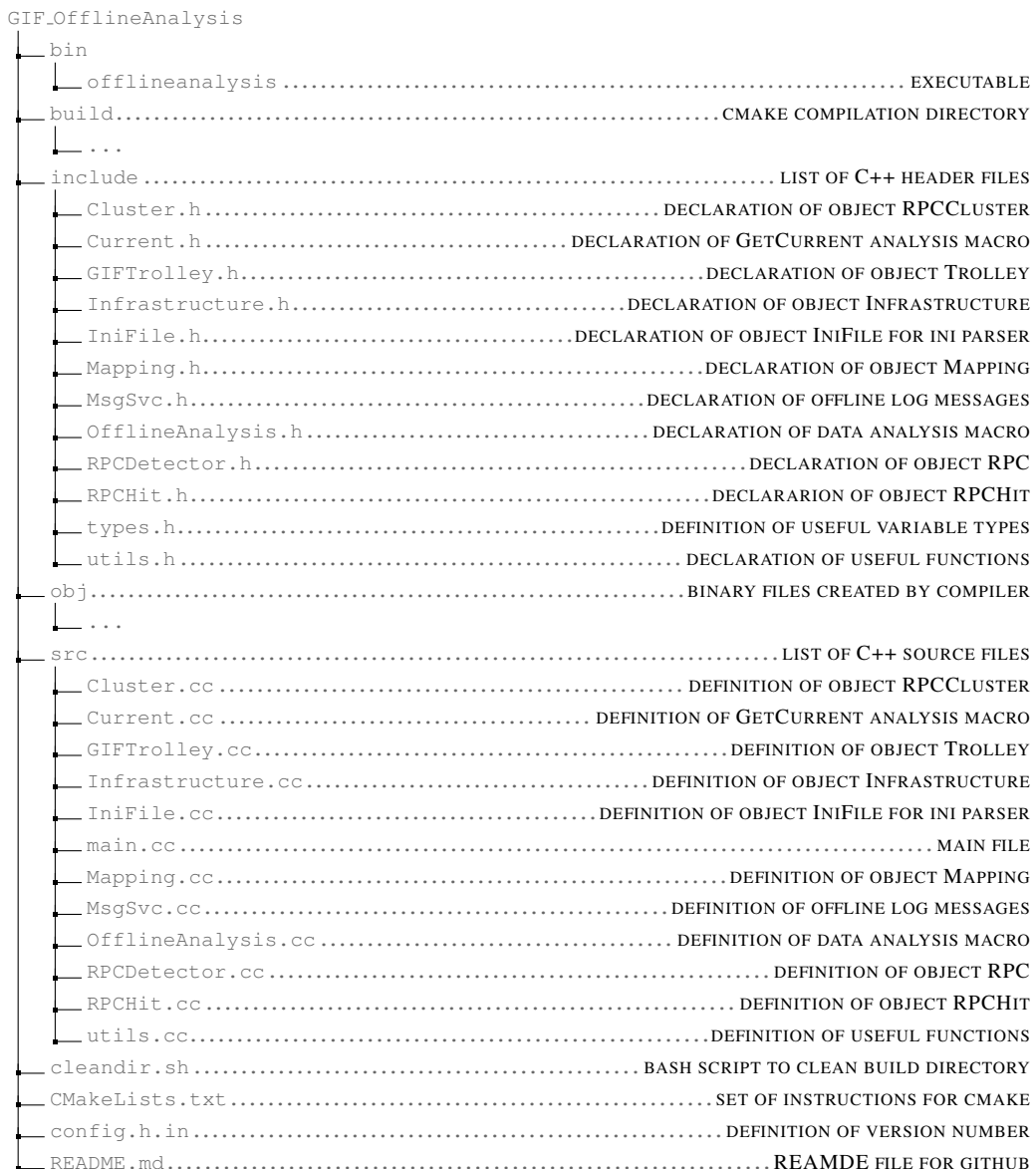
```
4094 mkdir build
4095 cd build
4096 cmake ..
4097 make
4098 make install
```

4096 To clean the directory and create a new build directory, the bash script cleandir.sh can be used:

```
4097
4098 ./cleandir.sh
```

4099 The source code tree is provided below along with comments to give an overview of the files' con-
4100 tent. The different objects created for this project (`Infrastructure`, `Trolley`, `RPC`, `Mapping`, `RPCHit`,
4101 `RPCCluster` and `Inifile`) will be described in details in the following sections.

4102



4103

B.2 Usage of the Offline Analysis

4104

In order to use the Offline Analysis tool, it is necessary to know the Scan number and the HV Step of the run that needs to be analysed. This information needs to be written in the following format:

4106

4107

Scan00XXXX_HVY

4108

4109

where XXXX is the scan ID and Y is the high voltage step (in case of a high voltage scan, data will be taken for several HV steps). This format corresponds to the base name of data files in the database

4110 of the Gif++ webDCS. Usually, the offline analysis tool is automatically called by the webDCS at
 4111 the end of data taking or by a user from the webDCS panel if an update of the tool was brought.
 4112 Nonetheless, an expert can locally launch the analysis for tests on the Gif++ computer, or a user can
 4113 get the code on its local machine from github and download data from the webDCS for its own anal-
 4114 ysis. To launch the code, the following command can be used from the `GIF_OfflineAnalysis` folder:

4115
 4116 `bin/offlineanalysis /path/to/Scan00XXXX_HVY`

4117 where, `/path/to/Scan00XXXX_HVY` refers to the local data files. Then, the offline tool will by itself
 4118 take care of finding all available ROOT data files present in the folder, as listed below:

- 4119 ● `Scan00XXXX_HVY_DAQ.root` containing the TDC data as described in Appendix A.4.2 (events,
 4120 hit and timestamp lists), and
- 4121 ● `Scan00XXXX_HVY_CAEN.root` containing the CAEN mainframe data recorded by the monitor-
 4122 ing tool webDCS during data taking (HVs and currents of every HV channels). This file is
 4123 created independently of the DAQ.

4124 **B.2.1 Output of the offline tool**

4125 **B.2.1.1 ROOT file**

4126 The analysis gives output ROOT datafiles that are saved into the data folder and called using the
 4127 naming convention `Scan00XXXX_HVY_Offline.root`. Inside those, a list of `TH1` histograms can be
 4128 found. Its size will vary as a function of the number of detectors in the setup as each set of histograms
 4129 is produced detector by detector. For each partition of each chamber, can be found:

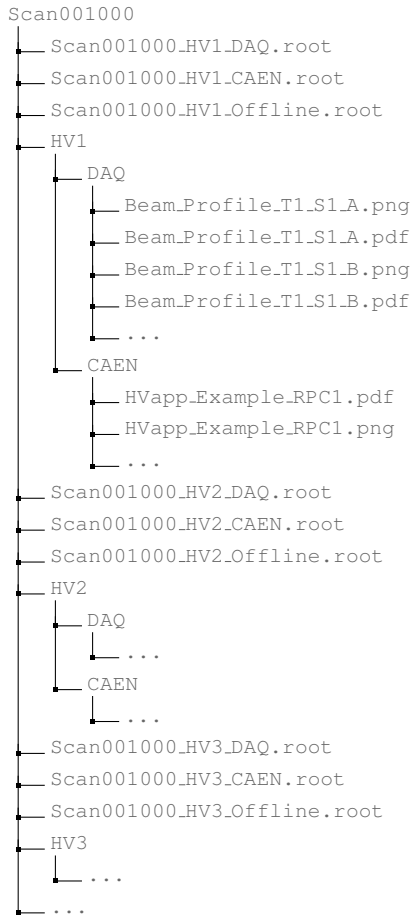
- 4130 ● `Time_Profile_Tt_Sc_p` shows the time profile of all recorded events (number of events per
 4131 time bin),
- 4132 ● `Hit_Profile_Tt_Sc_p` shows the hit profile of all recorded events (number of events per chan-
 4133 nel),
- 4134 ● `Hit_Multiplicity_Tt_Sc_p` shows the hit multiplicity (number of hits per event) of all recorded
 4135 events (number of occurrences per multiplicity bin),
- 4136 ● `Time_vs_Strip_Profile_Tt_Sc_p` shows the 2D time vs strip profile of all recorded events
 4137 (number of events per time bin per strip),
- 4138 ● `Strip_Mean_Noise_Tt_Sc_p` shows noise/gamma rate per unit area for each strip in a se-
 4139 lected time range. After filters are applied on `Time_Profile_Tt_Sc_p`, the filtered version
 4140 of `Hit_Profile_Tt_Sc_p` is normalised to the total integrated time and active detection area
 4141 of a single channel,
- 4142 ● `Strip_Activity_Tt_Sc_p` shows noise/gamma activity for each strip (normalised version of
 4143 previous histogram - strip activity = strip rate / average partition rate),
- 4144 ● `Strip_Homogeneity_Tt_Sc_p` shows the *homogeneity* of a given partition ($\text{homogeneity} = \exp(-\text{strip rates standard deviation}(\text{strip rates in partition}/\text{average partition rate}))$),

- 4146 ● `mask_Strip_Mean_Noise_Tt_Sc_p` shows noise/gamma rate per unit area for each masked
 4147 strip in a selected time range. Offline, the user can control the noise/gamma rate and decide to
 4148 mask the strips that are judged to be noisy or dead. This is done via the *Masking Tool* provided
 4149 by the webDCS,
- 4150 ● `mask_Strip_Activity_Tt_Sc_p` shows noise/gamma activity per unit area for each masked
 4151 strip with respect to the average rate of active strips,
- 4152 ● `NoiseCSize_H_Tt_Sc_p` shows noise/gamma cluster size, a cluster being constructed out of
 4153 adjacent strips giving a signal at the *same time* (hits within a time window of 25 ns),
- 4154 ● `NoiseCMult_H_Tt_Sc_p` shows noise/gamma cluster multiplicity (number of reconstructed
 4155 clusters per event),
- 4156 ● `Chip_Mean_Noise_Tt_Sc_p` shows the same information than `Strip_Mean_Noise_Tt_Scp` us-
 4157 ing a different binning (1 chip corresponds to 8 strips),
- 4158 ● `Chip_Activity_Tt_Sc_p` shows the same information than `strip_Activity_Tt_Scp` using
 4159 chip binning,
- 4160 ● `Chip_Homogeneity_Tt_Sc_p` shows the homogeneity of a given partition using chip binning,
- 4161 ● `Beam_Profile_Tt_Sc_p` shows the estimated beam profile when taking efficiency scan. This
 4162 is obtained by filtering `Time_Profile_Tt_Sc_p` to only consider the muon peak where the
 4163 noise/gamma background has been subtracted. The resulting hit profile corresponds to the
 4164 beam profile on the detector channels,
- 4165 ● `Efficiency_Fake_Tt_Ss_p` shows the efficiency given by fake hits by probing outside the
 4166 peak in an uncorrelated window as wide as the peak window,
- 4167 ● `Efficiency_Peak_Tt_Ss_p` shows the efficiency given by hits contained in the peak window,
- 4168 ● `PeakCSize_H_Tt_Sc_p` shows the cluster size that was estimated using all the hits in the peak
 4169 window,
- 4170 ● `PeakCMult_H_Tt_Sc_p` shows the cluster multiplicity that was estimated using all the hits in
 4171 the peak window,
- 4172 ● `L0_Efficiency_Tt_Sc_p` shows the level 0 muon efficiency that was estimated **without** muon
 4173 tracking after correction,
- 4174 ● `MuonCSize_H_Tt_Sc_p` shows the level 0 muon cluster size that was estimated **without** muon
 4175 tracking after correction, and
- 4176 ● `MuonCMult_H_Tt_Sc_p` shows the level 0 muon cluster multiplicity that was estimated **without**
 4177 muon tracking after correction.

4178 In the histogram labels, *t* stands for the trolley number (1 or 3), *c* for the chamber slot label in
 4179 trolley *t* and *p* for the partition label (A, B, C or D depending on the chamber layout) as explained
 4180 in Chapter 5.3.

4182 In the context of GIF++, an extra script called by the webDCS is called to extract the histograms
 4183 from the ROOT files. The histograms are then stored in PNG and PDF formats into the correspond-
 4184 ing folder (a single folder per HV step, so per ROOT file). An example of histogram organisation is
 4185 given bellow for an hypothetical scan 001000 with at least 3 HV steps and whose chamber located in
 4186 slot 1 of trolley 1 is called *Example_RPC1* and has at least 2 read-out partitions A and B. The goal is
 4187 to then display the histograms graphs on the Data Quality Monitoring (DQM) page of the webDCS,
 4188 as presented in Figure 5.27, in order for the users to control the quality of the data taking at the end
 4189 of data taking.

4190



4191

B.2.1.2 CSV files

4192

Moreover, up to 4 CSV files can be created depending on which ones of the 3 input files were in the data folder:

4194

- Offline-Corrupted.csv , is used to keep track of the amount of data that was corrupted and removed from old data format files that don't contain any data quality flag.

4195

- 4196 ● `Offline-Current.csv`, contains the summary of the currents and voltages applied on each
 4197 RPC HV channel.
- 4198 ● `Offline-L0-EffCl.csv`, is used to write the efficiencies, cluster size and cluster multiplicity
 4199 of efficiency runs. Note that `L0` refers here to *Level 0* and means that the results of efficiency and
 4200 clusterization are a first approximation calculated without performing any muon tracking in
 4201 between the different detectors. This offline tool provides the user with a preliminar calcula-
 4202 tion of the efficiency and of the muon event parameters. Another analysis software especially
 4203 dedicated to muon tracking is called on selected data to retrieve the results of efficiency and
 4204 muon clusterization using a tracking algorithm to discriminate noise or gamma from muons
 4205 as muons are the only particles that pass through the full setup, leaving hits than can be used
 4206 to reconstruct their tracks.
- 4207 ● `Offline-Rate.csv`, is used to write the noise or gamma rates measured in the detector readout
 4208 partitions.

4209 Note that these 4 CSV files are created along with their *headers* (`Offline-[...]-Header.csv`
 4210 containing the names of each data columns) and are automatically merged together when the offline
 4211 analysis tool is called from the webDCS, contrary to the case where the tool is runned locally from
 4212 the terminal as the merging bash script is then not called. Thus, the resulting files, used to make
 4213 official plots, are:

- 4214 ● `Corrupted.csv`,
- 4215 ● `Current.csv`,
- 4216 ● `L0-EffCl.csv`.
- 4217 ● `Rate.csv`.

4218 **B.3 Analysis inputs and information handling**

4219 The usage of the Offline Analysis tool as well as its output have been presented in the previous sec-
 4220 tion. It is now important to dig further and start looking at the source code and the inputs necessary
 4221 for the tool to work. Indeed, other than the raw ROOT data files that are analysed, more information
 4222 needs to be imported inside of the program to perform the analysis such as the description of the
 4223 setup inside of GIFT++ at the time of data taking (number of trolleys, of RPCs, dimensions of the
 4224 detectors, etc...) or the mapping that links the TDC channels to the coresponding RPC channels in
 4225 order to translate the TDC information into human readable data. Two files are used to transmit all
 4226 this information:

4227

- 4228 ● `Dimensions.ini`, that provides the necessary setup and RPC information, and
- 4229 ● `ChannelsMapping.csv`, that gives the link between the TDC and RPC channels as well as the
 4230 *mask* for each channel (masked or not?).

4231 B.3.1 Dimensions file and IniFile parser

4232 GIF++ CMS RPC setup consists in detectors held into trolleys inside of the GIF++ bunker. Each of
 4233 these detector may have a read-out segmented to cover different pseudo-rapidity range once intalled
 4234 in CMS. The segmentation of the read-out is referred to as "partitions". This input file, present in
 4235 every data folder, allows the analysis tool to know of the number of active trolleys, the number of
 4236 active RPCs in those trolleys, and the details about each RPCs such as the number of RPC gaps, the
 4237 number of pseudo-rapidity partitions, the number of strips per partion or the dimensions. To do so,
 4238 there are 3 types of groups in the INI file architecture. Groups are sections of the INI file content
 4239 starting with a title encapsulated in between square brackets. A first general group, appearing only
 4240 once at the head of the document, gives information about the number of active trolleys as well
 4241 as their IDs, as presented in Source Code B.1. For each active trolley, a group similar to Source
 4242 Code B.2 can be found containing information about the number of active detectors in the trolley
 4243 and their IDs. Each trolley group as a `Tt` name format, where `t` is the trolley ID. Finally, for each
 4244 detector stored in slots of an active trolley, there is a group providing information about their names
 4245 and dimensions, as shown in Source Code B.3. Each slot group as a `TtSs` name format, where `s` is
 4246 the slot ID of trolley `t` where the active RPC is hosted.

```
4247
[General]
4248 nTrolleys=2
TrolleysID=13
```

4249 *Source Code B.1: Example of [General] group as might be found in Dimensions.ini. In GIF++, only 2 trolleys are available to hold RPCs and place them inside of the bunker for irradiation. The IDs of the trolleys are written in a single string as "13" and then read character by character by the program.*

```
4250
[T1]
4251 nSlots=4
SlotsID=1234
```

4251 *Source Code B.2: Example of trolley group as might be found in Dimensions.ini. In this example, the file tells that there are 4 detectors placed in the holding slots of the trolley T1 and that their IDs, written as a single string variable, are 1, 2, 3 and 4.*

```
4252
[T1S1]
Name=RE2-2-NPD-BARC-8
Partitions=3
Gaps=3
Gap1=BOT
Gap2=TN
Gap3=TW
AreaGap1=11694.25
AreaGap2=6432
AreaGap3=4582.82
Strips=32
ActiveArea-A=157.8
ActiveArea-B=121.69
ActiveArea-C=93.03
```

4253 *Source Code B.3: Example of slot group as might be found in Dimensions.ini. In this example, the file provides information about a detector named RE2-2-NPD-BARC-8, having 3 pseudo-rapidity readout partitions and stored in slot S1 of trolley T1. This is a CMS RE2-2 type of detector. This information will then be used for example to compute the rate per unit area calculation.*

4254 This information is read-out and stored in a C++ object called `IniFile`, that parses the information
 4255 of the INI input file and stores it into a local buffer for later use. This INI parser is the exact
 4256 same one that was previously developed for the GIF++ DAQ and described in Appendix A.5.2.

4257 **B.3.2 TDC to RPC link file and Mapping**

4258 The same way the INI dimension file information is stored using `map`, the channel mapping and
 4259 mask information making the link in between TDC channels and RPC strips is stored and accessed
 4260 through `map`. First of all, the mapping CSV file is organised into 3 columns separated by tabulations:

4261	RPC_channel	TDC_channel	mask
------	-------------	-------------	------

4263 using as formatting for each field:

4264	TSCCC	TCCC	M
------	-------	------	---

4266 TSCCC is a 5-digit integer where `T` is the trolley ID, `s` the slot ID in which the RPC is held inside
 4267 the trolley `T` and `ccc` is the RPC channel number, or *strip* number, that can take values up to
 4268 3-digits depending on the detector,

4269 TCCC is a 4 digit integer where `T` is the TDC ID to which the RPC is connected, `ccc` is the TDC
 4270 channel number linked to the RPC strip that can take values in between 0 and 127, and

4271 M is a 1-digit integer indicating if the channel should be considered (`M = 1`) or discarded (`M = 0`)
 4272 during analysis. Note that the absence of a third column is interpreted by the mapping file
 4273 parser as `M = 1` by default.

4274 This mapping and masking information is readout and stored thanks to the object `Mapping`, presented
 4275 in Source Code B.4. Similarly to `IniFile` objects, this class has private methods to provide
 4276 with parser rules. The first one, `Mapping::CheckIfNewLine()` is used to find the newline character
 4277 '`\n`' or return character '`\r`' (depending on which kind of operating system interacted with the file).
 4278 Finding and identifying a newline or return character is used for the simple reason that the masking
 4279 information has been introduced only during the year 2017 but the channel mapping files exist since
 4280 2015 and the very beginning of data taking at GIF++. This means that in the older data folders,
 4281 before the upgrade, the channel mapping file only had 2 columns, the RPC channel and the TDC
 4282 channel. For compatibility reasons, this method helps controlling the character following the readout
 4283 of the 2 first fields of a line. In case any end of line character is found, no mask information is present
 4284 in the file and the default `M = 1` is used. On the contrary, if the next character was a tabulation or a
 4285 space, the mask information is present.

4286 Once the 3 fields have been readout, the second private method `Mapping::CheckIfTDCCh()` is
 4287 used to control that the TDC channel is an existing TDC channel by checking its format. Finally,
 4288 the information is stored into 3 different maps (`Link`, `ReverseLink` and `Mask`) thanks to the public
 4289 method `Mapping::Read()`. `Link` allows to get the RPC channel by knowing the TDC channel while
 4290 `ReverseLink` does the opposite by returning the TDC channel by knowing the RPC channel. Finally,
 4291 `Mask` returns the mask associated to a given RPC channel.

```

4292 typedef map<Uint,Uint> MappingData;

4293 class Mapping {
4294     private:
4295         bool          CheckIfNewLine(char next);
4296         bool          CheckIfTDCCh(Uint channel);
4297         string        FileName;
4298         MappingData  Link;
4299         MappingData  ReverseLink;
4300         MappingData  Mask;
4301         int           Error;
4302
4303     public:
4304         Mapping();
4305         Mapping(string baseName);
4306         ~Mapping();
4307
4308         void SetFileName(const string filename);
4309         int  Read();
4310         Uint GetLink(Uint tdcchannel);
4311         Uint GetReverse(Uint rpcchannel);
4312         Uint GetMask(Uint rpcchannel);
4313     };

```

4294 *Source Code B.4: Description of C++ object Mapping used as a parser for the channel mapping and mask file.*

4295 B.4 Description of GIF++ setup within the Offline Analysis tool

4296 In the previous section, the tool input files have been discussed. The dimension file information is
 4297 stored in a map hosted by the `IniFile` object. But this information is then used to create a series of
 4298 new objects that helps defining the GIF++ infrastructure directly into the Offline Analysis. Indeed,
 4299 from the `RPC`, to the more general `Infrastructure`, every element of the GIF++ infrastrucutre is
 4300 recreated for each data analysis based on the information provided in input. All this information
 4301 about the infrastructure will be used to assign each hit signal to a specific strip channel of a specific
 4302 detector, and having a specific active area. This way, rate per unit area calculation is possible.
 4303

4304 B.4.1 RPC objects

4305 `RPC` objects have been developped to represent physical active detectors in GIF++ at the moment
 4306 of data taking. Thus, there are as many `RPC` objects created during the analysis than there were
 4307 active `RPCs` tested during a run. Each `RPC` hosts the information present in the corresponding INI
 4308 slot group, as showed in B.3, and organises it using a similar architecture. This can be seen from
 4309 Source B.5.

4310 To make the object more compact, the lists of gap labels, of gap active areas and strip active
 4311 areas are stored into `vector` dynamical containers. `RPC` objects are always contructed thanks to the
 4312 dimension file information stored into the `IniFILE` and their ID, using the format `TtSs`. Using the
 4313 `RPC` ID, the constructor calls the methods of `IniFILE` to initialise the `RPC`. The other constructors
 4314 are not used but exist in case of need. Finally, some getters have been written to access the different
 4315 private parameters storing the detector information.

4316

4317 **B.4.2 Trolley objects**

4318 Trolley objects have been developped to represent physical active trolleys in GIF++ at the moment
 4319 of data taking. Thus, there are as many trolley objects created during the analysis than there were
 4320 active trolleys hosting RPCs under test during a run. Each Trolley hosts the information present in
 4321 the corresponding INI trolley group, as shown in B.2, and organises it using a similar architecture.
 4322 In addition to the information hosted in the INI file, these objects have a dynamical container of `RPC`
 4323 objects, representing the active detectors the active trolley was hosting at the time of data taking.
 4324 This can been seen from Source Code B.6.

4325 Trolley objects are always contructed thanks to the dimension file information stored into the
 4326 `IniFILE` and their ID, using the format `Tt`. Using the Trolley ID, the constructor calls the methods
 4327 of `IniFile` to initialise the `Trolley`. Retrieving the information of the RPC IDs via `SlotsID`, a new
 4328 `RPC` is constructed and added to the container `RPCs` for each character in the ID string. The other
 4329 constructors are not used but exist in case of need. Finally, some getters have been written to access
 4330 the different private parameters storing the trolley and detectors information.

4331

4332 **B.4.3 Infrastructure object**

4333 The `Infrastructure` object has been developped to represent the GIF++ bunker area dedicated to
 4334 CMS RPC experiments. With this very specific object, all the information about the CMS RPC
 4335 setup within GIF++ at the moment of data taking is stored. It hosts the information present in the
 4336 corresponding INI general group, as shown in B.1, and organises it using a similar architecture. In
 4337 addition to the information hosted in the INI file, this object have a dynamical container of `Trolley`
 4338 objects representing the active tolleys in GIF++ area, themselves containing `RPC` objects. This can
 4339 been seen from Source Code B.7.

4340 The `Infrastructure` object is always contructed thanks to the dimension file information stored
 4341 into the `IniFILE`. Retrieving the information of the trolley IDs via `TrolleysID`, a new `Trolley` is
 4342 constructed and added to the container `Trolleys` for each character in the ID string. By extension,
 4343 it is easy to understand that the process described in Section B.4.2 for the construction of RPCs
 4344 takes place when a trolley is constructed. The other constructors are not used but exist in case of
 4345 need. Finally, some getters have been written to access the different private parameters storing the
 4346 infrastructure, trolleys and detectors information.

```

4347 class RPC{
    private:
        string      name;           //RPC name as in webDCS database
        Uint        nGaps;          //Number of gaps in the RPC
        Uint        nPartitions;    //Number of partitions in the RPC
        Uint        nStrips;         //Number of strips per partition
        vector<string> gaps;       //List of gap labels (BOT, TOP, etc...)
        vector<float> gapGeo;      //List of gap active areas
        vector<float> stripGeo;    //List of strip active areas

    public:
        RPC();
4348    RPC(string ID, IniFile* geofile);
        RPC(const RPC& other);
        ~RPC();
        RPC& operator=(const RPC& other);

        string GetName();
        Uint GetNGaps();
        Uint GetNPartitions();
        Uint GetNStrips();
        string GetGap(Uint g);
        float GetGapGeo(Uint g);
        float GetStripGeo(Uint p);
    };

```

4349 *Source Code B.5: Description of C++ objects RPC that describe each active detectors used during data taking.*

```

class Trolley{
    private:
        Uint      nSlots;   //Number of active RPCs in the considered trolley
        string    SlotsID; //Active RPC IDs written into a string
        vector<RPC*> RPCs; //List of active RPCs

    public:
        Trolley();
        Trolley(string ID, IniFile* geofile);
        Trolley(const Trolley& other);
        ~Trolley();
        Trolley& operator=(const Trolley& other);

        Uint GetNSlots();
        string GetSlotsID();
        Uint GetSlotID(Uint s);
        RPC* GetRPC(Uint r);
        void DeleteRPC(Uint r);

        //Methods to get members of RPC objects stored in RPCs
        string GetName(Uint r);
        Uint GetNGaps(Uint r);
        Uint GetNPartitions(Uint r);
        Uint GetNStrips(Uint r);
        string GetGap(Uint r, Uint g);
        float GetGapGeo(Uint r, Uint g);
        float GetStripGeo(Uint r, Uint p);
    };

```

4351 *Source Code B.6: Description of C++ objects Trolley that describe each active trolley used during data taking.*

```

class Infrastructure {
    private:
        Uint             nTrolleys;   //Number of active Trolleys in the run
        string          TrolleysID;  //Active trolley IDs written into a string
        vector<Trolley*> Trolleys;  //List of active Trolleys (struct)

    public:
        Infrastructure();
        Infrastructure(IniFile* geofile);
        Infrastructure(const Infrastructure& other);
        ~Infrastructure();
        Infrastructure& operator=(const Infrastructure& other);

        Uint    GetNTrolleys();
        string GetTrolleysID();
        Uint    GetTrolleyID(Uint t);

4352        Trolley* GetTrolley(Uint t);
        void      DeleteTrolley(Uint t);

        //Methods to get members of GIFTrolley objects stored in Trolleys
        Uint    GetNSlots(Uint t);
        string GetSlotsID(Uint t);
        Uint    GetSlotID(Uint t, Uint s);
        RPC*   GetRPC(Uint t, Uint r);

        //Methods to get members of RPC objects stored in RPCs
        string GetName(Uint t, Uint r);
        Uint    GetNGaps(Uint t, Uint r);
        Uint    GetNPartitions(Uint t, Uint r);
        Uint    GetNStrips(Uint t, Uint r);
        string GetGap(Uint t, Uint r, Uint g);
        float   GetGapGeo(Uint t, Uint r, Uint g);
        float   GetStripGeo(Uint t, Uint r, Uint p);
    };

```

Source Code B.7: Description of C++ object Infrastructure that contains the full information about CMS RPC experiment in GIF++.

4354 B.5 Handeling of data

4355 As discussed in Appendix A.4.2, the raw data uses a `TTree` architecture where every entry is related
4356 to a trigger signal provided by a muon or a random pulse, whether the goal of the data taking was to
4357 measure the performance of the detector or the noise/gamma background respectively. Each of these
4358 entries, referred also as events, contain a more or less full list of hits in the TDC channels to which
4359 the detectors are connected. To this list of hits corresponds a list of time stamps, marking the arrival
4360 of the hits within the TDC channel.

4361 The infrastructure of the CMS RPC experiment within `GIF++` being defined, combining the raw
4362 data information with the information provided by both the mapping/mask file and the dimension
4363 file allows to build new physical objects that will help in computing efficiency or rates.

4364 **B.5.1 RPC hits**

4365 The raw data stored in the ROOT file as output of the GIFT++ DAQ, is readout by the analysis tool
 4366 using the structure `RAWData` presented in Source Code B.9 that differs from the structure presented
 4367 in Appendix A.4.2 as it is not meant to hold all of the data contained in the ROOT file. In this sense,
 4368 this structure is in the case of the offline analysis tool not a dynamical object and will only be storing
 4369 a single event contained in a single entry of the `TTree`.

4370

```
class RPCHit {
    private:
        Uint Channel;      //RPC channel according to mapping (5 digits)
        Uint Trolley;     //0, 1 or 3 (1st digit of the RPC channel)
        Uint Station;     //Slot where is held the RPC in Trolley (2nd digit)
        Uint Strip;       //RPC strip where the hit occurred (last 3 digits)
        Uint Partition;   //Readout partition along eta segmentation
        float TimeStamp; //Time stamp of the arrival in TDC

    public:
        RPCHit();
        RPCHit(Uint channel, float time, Infrastructure* Infra);
        RPCHit(const RPCHit& other);
        ~RPCHit();
        RPCHit& operator=(const RPCHit& other);

        Uint GetChannel();
        Uint GetTrolley();
        Uint GetStation();
        Uint GetStrip();
        Uint GetPartition();
        float GetTime();
};

typedef vector<RPCHit> HitList;
typedef struct GIFHitList {HitList rpc[NTROLLEYS][NSLOTS][NPARTITIONS];}
    ↪ GIFHitList;

bool SortHitbyStrip(RPCHit h1, RPCHit h2);
bool SortHitbyTime(RPCHit h1, RPCHit h2);
```

4371

Source Code B.8: Description of C++ object `RPCHit`.

4372

```
struct RAWData{
    int iEvent;           //Event i
    int TDCHits;         //Number of hits in event i
    int QFlag;           //Quality flag list (1 flag digit per TDC)
    vector<Uint> *TDCCh; //List of channels giving hits per event
    vector<float> *TDCTS; //List of the corresponding time stamps
};
```

4373

Source Code B.9: Description of C++ structure `RAWData`.

4374 Each member of the structure is then linked to the corresponding branch of the ROOT data tree,
 4375 as shown in the example of Source Code B.10, and using the method `GetEntry(int i)` of the ROOT
 4376 class `TTree` will update the state of the members of `RAWData`.

4377 The data is then analysed entry by entry and to each element of the TDC channel list, a `RPCHit` is
 4378 constructed by linking each TDC channel to the corresponding RPC channel thanks to the Mapping

4380 object. The information carried by the RPC channel format allows to easily retrieve the trolley and
 4381 slot from which the hit was recorded (see section B.3.2). Using these 2 values, the readout partition
 4382 can be found by knowing the strip channel and comparing it with the number of partitions and strips
 4383 per partition stored into the `Infrastructure` object.

```
4384 TTree* dataTree = (TTree*)dataFile.Get("RAWData");
  RAWData data;
  dataTree->SetBranchAddress("EventNumber", &data.iEvent);
  dataTree->SetBranchAddress("number_of_hits", &data.TDCNHits);
  dataTree->SetBranchAddress("Quality_flag", &data.QFlag);
  dataTree->SetBranchAddress("TDC_channel", &data.TDCCh);
  dataTree->SetBranchAddress("TDC_TimeStamp", &data.TDCTS);
```

4386 *Source Code B.10: Example of link in between RAWData and TTree.*

4387 Thus `RPCHit` objects are then stored into 3D dynamical list called `GIFHitList` (Source Code B.8)
 4388 where the 3 dimensions refer to the 3 layers of the readout in `GIF++` : in the bunker there are *trolleys*
 4389 (τ) holding detectors in *slots* (s) and each detector readout is divided into 1 or more pseudo-rapidity
 4390 *partitions* (p). Using these 3 information allows to assign an address to each readout partition and
 4391 this address will point to a specific hit list.

4392

4393 B.5.2 Clusters of hits

4394 All the hits contained in the ROOT file have been sorted into the different hit lists through the
 4395 `GIFHitList`. At this point, it is possible to start looking for clusters. A cluster is a group of adjacent
 4396 strips getting hits within a time window of 25 ns. These strips are then assumed to be part of the same
 4397 physical avalanche signal generated by a muon passing through the chamber or by the interaction of
 4398 a gamma stopping into the electrodes of the RPCs.

4399 To keep the cluster information, `RPCCluster` objects have been defined as shown in Source
 4400 Code B.11. Using the information of each individual `RPCHit` taken out of the hit list, it stores
 4401 the cluster size (number of adjacent strips composing the cluster), the first and last hit, the center for
 4402 spatial reconstruction and finally the start and stop time stamps as well as te time spread in between
 4403 the first and last hit.

4404

4405 To investigate the hit list of a given detector partition, the function `Clusterization()` defined
 4406 in `include/Cluster.h` needs the hits in the list to be time sorted. This is achieved by calling func-
 4407 tion `sort()` of library `<algorithm>` using the comparator `SortHitbyTime(RPCHit h1, RPCHit h2)`
 4408 defined in `include/RPCHit.h` that returns `true` if the time stamp of hit `h1` is lower than that of `h2`.
 4409 A first isolation of strips is made only based on time information. All the hits within the 25 ns win-
 4410 dow are taken separately from the rest. Then, this sub-list of hits is sorted this time by ascending
 4411 strip number, using this time the comparator `SortHitbyStrip(RPCHit h1, RPCHit h2)`. Finally, the
 4412 groups of adjacent strips are used to construct `RPCCluster` objects that are then stored in a temporary
 4413 list of clusters that is at the end of the process used to know how many clusters were reconstructed
 4414 and to fill their sizes into an histogram that will allows to know the mean size of muon or gamma
 4415 clusters. This method to group hits together into clusters is limited as no systematic study of the
 4416 average avalanche time development into TDC hits was performed and that there is no correlation

4417 of both spatial and time information to make the first selection of hits. Due to this, two clusters
 4418 developping consecutively next to each other during a total time longer to 25 ns could be wrongly
 4419 grouped as a cluster composed of the first developed cluster plus a part of the second cluster while
 4420 the rest of the second cluster would be placed in a second truncated cluster. This kind of event
 4421 is not likely but needs to be taken into account nonetheless. A possible improvement would be to
 4422 identify clusters in a 2D space whose dimensions are time and strip. In this 2D space, the cluster
 4423 could be geometrically identified as isolated groups of adjacent strips receiving a hit at a similar time.
 4424

```

4424
4425 class RPCCluster{
4426     private:
4427         Uint ClusterSize; //Size of cluster #ID
4428         Uint FirstStrip; //First strip of cluster #ID
4429         Uint LastStrip; //Last strip of cluster #ID
4430         float Center; //Center of cluster #ID ((first+last)/2)
4431         float StartStamp; //Time stamp of the earliest hit of cluster #ID
4432         float StopStamp; //Time stamp of the latest hit of cluster #ID
4433         float TimeSpread; //Time difference between earliest and latest hits
4434             //of cluster #ID
4435
4436     public:
4437         RPCCluster();
4438         RPCCluster(HitList List, Uint cID, Uint cSize, Uint first, Uint firstID);
4439         RPCCluster(const RPCCluster& other);
4440         ~RPCCluster();
4441         RPCCluster& operator=(const RPCCluster& other);
4442
4443         Uint GetID();
4444         Uint GetSize();
4445         Uint GetFirstStrip();
4446         Uint GetLastStrip();
4447         float GetCenter();
4448         float GetStart();
4449         float GetStop();
4450         float GetSpread();
4451     };
4452
4453 typedef vector<RPCCluster> ClusterList;
4454
4455 //Other functions to build cluster lists out of hit lists
4456 void BuildClusters(HitList &cluster, ClusterList &clusterList);
4457 void Clusterization(HitList &hits, TH1 *hcSize, TH1 *hcMult);
  
```

4458

Source Code B.11: Description of C++ object Cluster.

4459

B.6 DAQ data Analysis

4460 All the ingredients to analyse GIFT++ data have been introduced. This section will focus on the
 4461 different part of the analysis performed on the data, from determining the type of data the tool is
 4462 dealing with to calculate the hit and cluster rate per unit area in each detector or reconstructing
 4463 muon or gamma clusters.

4432 B.6.1 Determination of the run type

4433 In GIF++, both the performance of the detectors in detecting muons in an irradiated environment
 4434 and the gamma or noise background can be independantly measured. These correspond to different
 4435 run types and hence, to different TDC settings giving different data to look at.

4436 In the case of performance measurements, the trigger for data taking is provided by the coin-
 4437 cidence of several scintillators when muons from the beam passing through the area are detected.
 4438 Data is collected in a 600 ns wide window centered around the arrival of muons in the RPCs. The
 4439 expected time distribution of hits is shown in Figure B.1a. The muon peak is clearly visible in the
 4440 center of the distribution and is to be extracted from the gamma background that composes the flat
 4441 part of the distribution.

4442 On the other hand, gamma background or noise measurements are focussed on the non muon
 4443 related physics and the trigger needs to be independant from the muons to give a good measurement
 4444 of the gamma/noise distribution as seen by the detectors. The trigger is then provided by a pulse
 4445 generated by the DAQ at a frequency of 100 Hz whose pulse is not likely to be on time with a muon.
 4446 In order to increase the integrated time without increasing proportionnaly the acquisition time, the
 4447 width of the acquisition windows are increased to 10 μ s. The time distribution of the hits is expected
 4448 to be flat, as shown by Figure B.1b.

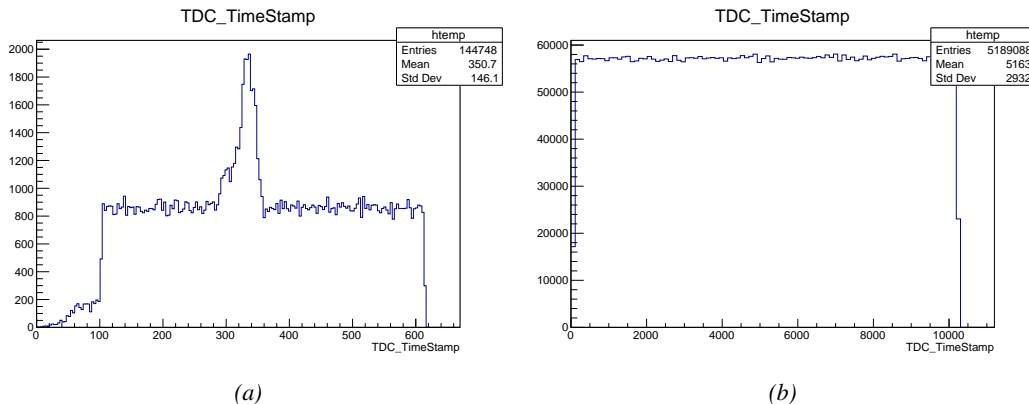


Figure B.1: Example of expected hit time distributions in the cases of efficiency (Figure B.1a) and noise/gamma rate per unit area (Figure B.1b) measurements as extracted from the raw ROOT files. The unit along the x-axis corresponds to ns. The fact that "the" muon peak is not well defined in Figure B.1a is due to the contribution of all the RPCs being tested at the same time that don't necessarily have the same signal arrival time. Each individual peak can have an offset with the ones of other detectors. The inconsistancy in the first 100 ns of both time distributions is an artefact of the TDCs and are systematically rejected during the analysis.

4449 The ROOT files include a `TTree` called `RunParameters` containing, among other things, the infor-
 4450 mation related to the run type. The run type can then be accessed as described by Source Code B.12
 4451 and the function `IsEfficiencyRun()` is then used to determine if the run file is an efficiency run or,
 4452 on the contrary, another type of run (noise or gamma measurement).

4453 Finally, the data files will have a slightly different content whether it was collected before or after
 4454 October 2017 and the upgrade of the DAQ software that brought a new information into the ROOT
 4455 output. This is discussed in Appendix A.4.3 and implies that the analysis will differ a little depending
 4456 on the data format. Indeed, as no information on the data quality is stored, in older data files, the cor-
 4457 rections for missing events has to be done at the end of the analysis. The information about the type

4458 of data format is stored in the variable **bool** `isNewFormat` by checking the list of branches contained
 4459 in the data tree via the methods `TTree::GetListOfBranches()` and `TCollection::Contains()`.

```
4460
4461     TTree* RunParameters = (TTree*)dataFile.Get("RunParameters");
4462     TString* RunType = new TString();
4463     RunParameters->SetBranchAddress("RunType", &RunType);
4464     RunParameters->GetEntry(0);
```

4462 *Source Code B.12: Access to the run type contained in `TTree* RunParameters`.*

4463 **B.6.2 Beam time window calculation for efficiency runs**

4464 Knowing the run type is important first of all to know the width of the acquisition window to be used
 4465 for the rate calculation and finally to be able to seek for muons. Indeed, the peak that appears in the
 4466 time distribution for each detectors is then fitted to extract the most probable time window in which
 4467 the tool should look for muon hits. The data outside of this time window is then used to evaluate the
 4468 noise or gamma background the detector was subjected to during the data taking. Computing the
 4469 position of the peak is done calling the function `SetBeamWindow()` defined in file `src/RPCHit.cc` that
 4470 loops a first time on the data. The data is first sorted in a 3D array of 1D histograms (`GIFH1Array`, see
 4471 `include/types.h`). Then the location of the highest bin is determined using `TH1::GetMaximumBin()`
 4472 and is used to define a window in which a gaussian fit will be applied to compute the peak width.
 4473 This window is a 80 ns defined by Formula B.1 around the central bin.

$$(B.1a) \quad t_{center}(ns) = bin \times width_{bin}(ns)$$

$$(B.1b) \quad [t_{low}; t_{high}] = [t_{center} - 40; t_{center} + 40]$$

4474 Before the fit is performed, the average number of noise/gamma hits per bin is evaluated using
 4475 the data outside of the fit window. Excluding the first 100 ns, the average number of hits per bin
 4476 due to the noise or gamma is defined by Formula B.2 after extracting the amount of hits in the time
 4477 windows $[100; t_{low}]$ and $[t_{high}; 600]$ thanks to the method `TH1::Integral()`. This average number
 4478 of hits is then subtracted to every bin of the 1D histogram, in order to *clean* it from the noise or
 4479 gamma contribution as much as possible to improve the fit quality. Bins where $\langle n_{hits} \rangle$ is greater
 4480 than the actual bin content are set to 0.

$$(B.2a) \quad \Delta t_{noise}(ns) = 600 \overbrace{-t_{high} + t_{low}}^{-80ns} - 100 = 420ns$$

$$(B.2b) \quad \langle n_{hits} \rangle = width_{bin}(ns) \times \frac{\sum_{t=100}^{t_{low}} + \sum_{t=t_{high}}^{600}}{\Delta t_{noise}(ns)}$$

4481 Finally, the fit parameters are extracted and saved for each detector in 3D arrays of **float**
 4482 (`muonPeak`, see `include/types.h`), a first one for the mean arrival time of the muons, `PeakTime`,
 4483 a second for the height or strength of the peak, `PeakHeight`, and a third one for the width of the
 4484 peak, `PeakWidth`. The width is on purpose chosen to be wider than the peak and defined as 6σ of the
 4485 gaussian fit, for a peak range being as given by Formula B.3.

$$(B.3) \quad [t_{low}^{peak}; t_{high}^{peak}] = [t_{center}^{peak} - 3\sigma; t_{center}^{peak} + 3\sigma]$$

4486 For a finer analysis, it is advised to determine more precisely the width of the peak to exclude
 4487 as much noise or background hits as possible. The same settings are applied to every partitions of
 4488 the same detector. To determine which one of the detector's partitions is directly illuminated by the
 4489 beam, the peak height of each partition is compared and the highest one is then used to define the
 4490 peak settings.

4491 It is not possible to identify the particles causing the hits, hence muons, background gamma
 4492 particles or even noise could be responsible of hits within the time window. To be able to account
 4493 for this effect, the peak width extracted from the fit on the peak will also be used to define a fake
 4494 time window, uncorrelated to the muon peak and in which a fake efficiency, contribution from both
 4495 background and noise, will be measured. This window corresponds to the time range described in
 4496 Formula B.4.

$$(B.4) \quad [t_{low}^{fake}; t_{high}^{fake}] = [600 - 6\sigma; 600]$$

4497 B.6.3 Data loop and histogram filling

4498 3D arrays of histogram are created to store the data and display it on the DQM of GIF++ webDCS
 4499 for the use of shifters. The dimensions correspond to the different layers held into the GIF++ infras-
 4500 tructure (trolleys `T` containing RPCs or *slots* `s` each being divided into read-out partitions `p`). These
 4501 histograms, presented in section B.2.1.1, are filled while looping on the data. Before starting the
 4502 analysis loop, it is necessary to control the entry quality for the new file formats featuring `QFlag`. If
 4503 the `QFlag` value for this entry shows that 1 TDC or more have a `CORRUPTED` flag, then this event is
 4504 discarded. The loss of statistics is low enough to be neglected. `QFlag` is controlled using the func-
 4505 tion `IsCorruptedEvent()` defined in `src/utils.cc`. As explained in Appendix A.4.3, each digit of
 4506 this integer represent a TDC flag that can be either 1 or 2. Each 2 is the sign of a `CORRUPTED` state.
 4507 Then, the data is accessed entry by entry in the ROOT `TTree` using `RAWData` and each hit in the hit
 4508 list is assigned to a detector channel and saved in the corresponding histograms. As described in
 4509 Source Code B.13, in the first part of the analysis, in which the loop over the ROOT file's content is
 4510 performed, the different steps are:

4511 **1- RPC channel assignment and control:** a check is done on the RPC channel extracted thanks
 4512 to the mapping via the method `Mapping::GetLink()`. If the channel is not initialised and is 0, or if
 4513 the TDC channel is not contained in a range in between X000 and X127, X being the TDC ID, the
 4514 hit is discarded. This means there was a problem in the mapping. Often a mapping problem leads to
 4515 the failure of the offline tool.

4516 **2- Creation of a `RPCHit` object:** to easily get the trolley, slot and partition in which the hit has
 4517 been assigned, this object is particularly helpful.

4518 **3- General histograms are filled:** the hit is filled into the time distribution, global hit distribution
 4519 and time versus strip histograms, and if the arrival time is within the first 100 ns, it is discarded and
 4520 nothing else happens and the loop proceeds with the next hit in the list, going back to step 1.

4521

```

for(int h = 0; h < data.TDCCh->size(); h++) {
    Uint tdcchannel = data.TDCCh->at(h);
    Uint rpcchannel = RPCChMap->GetLink(tdcchannel);
    float timestamp = data.TDCTS->at(h);
    //Get rid of the hits in channels not considered in the mapping
    if(rpcchannel != NOCHANNELLINK) {
        RPCHit hit(rpcchannel, timestamp, GIFInfra);
        Uint T = hit.GetTrolley();
        Uint S = hit.GetStation()-1;
        Uint P = hit.GetPartition()-1;
        //Fill the time and hit profiles
        TimeProfile_H.rpc[T][S][P]->Fill(hit.GetTime());
        HitProfile_H.rpc[T][S][P]->Fill(hit.GetStrip());
        TimeVSChanProfile_H.rpc[T][S][P]->Fill(hit.GetStrip(), hit.GetTime());
        //Reject the 100 first ns due to inhomogeneity of data
        if(hit.GetTime() >= TIMEREJECT) {
            Multiplicity.rpc[T][S][P]++;
            if(IsEfficiencyRun(RunType)) {
                //Define peak time range for efficiency calculation
                float lowlimit_eff = PeakTime.rpc[T][S][P]
                    - PeakWidth.rpc[T][S][P];
                float highlimit_eff = PeakTime.rpc[T][S][P]
                    + PeakWidth.rpc[T][S][P];
                bool peakrange = (hit.GetTime() >= lowlimit_eff
                    && hit.GetTime() < highlimit_eff);
                //Fill hits inside of the defined peak and noise range
                if(peakrange) {
                    BeamProfile_H.rpc[T][S][P]->Fill(hit.GetStrip());
                    PeakHitList.rpc[T][S][P].push_back(hit);
                } else {
                    StripNoiseProfile_H.rpc[T][S][P]->Fill(hit.GetStrip());
                    NoiseHitList.rpc[T][S][P].push_back(hit);
                }
                //Then define time range for fake efficiency
                float highlimit_fake = BMTDCWINDOW;
                float lowlimit_fake = highlimit_fake
                    - (highlimit_eff-lowlimit_eff);
                bool fakerange = (hit.GetTime() >= lowlimit_fake
                    && hit.GetTime() < highlimit_fake);
                //Fill the hits inside of the fake window
                if(fakerange) {
                    FakeHitList.rpc[T][S][P].push_back(hit);
                }
            } else {
                //Fill the hits inside of the defined noise range
                StripNoiseProfile_H.rpc[T][S][P]->Fill(hit.GetStrip());
                NoiseHitList.rpc[T][S][P].push_back(hit);
            }
        }
    }
}

```

4522

Source Code B.13: For each entry of the raw ROOT data file, the code loops over the list of channels and corresponding time stamps contained in branches `TDC_channel` and `TDC_TimeStamp` and constructs `RPCHit` objects that are filled in the peak, noise and fake hit lists and also fills the time, hit, beam and noise profiles.

4523

4- Multiplicity counter: the hit multiplicity counter of the corresponding detectors is incremented.

4524

4525 **5-a-1 Efficiency runs - Is the hit within the peak window? :** if the hit is contained in the peak
 4526 window previously defined by Formula B.3, it is filled into the beam hit profile histogram of the
 4527 corresponding chamber, added into the list of peak hits and increments the counter of *in time* hits.
 4528 The term *in time* here refers to the hits that are likely to be muons by arriving in the expected time
 4529 window. If the hit is outside of the peak window, it is filled into the noise profile histogram of
 4530 the corresponding detector, added into the list of noise/gamma hits and increments the counter of
 4531 noise/gamma hits.

4532 **5-a-2 Efficiency runs - Is the hit within the fake window? :** if the hit is contained in the fake
 4533 window previously defined by Formula B.4, it is added into the list of fake hits. Counting the fake
 4534 hits outside the peak window allows to estimate the probability to detect in time background or noise.

4535 **5-b- Noise/gamma rate runs - Noise histograms are filled:** the hit is filled into the noise profile
 4536 histogram of the corresponding detector, added into the list of noise/gamma hits and increments the
 4537 counter of noise/gamma hits.

```
4538
  for(UInt tr = 0; tr < GIFInfra->GetNTrolleys(); tr++) {
    UInt T = GIFInfra->GetTrolleyID(tr);
    for(UInt sl = 0; sl < GIFInfra->GetNSlots(tr); sl++) {
      UInt S = GIFInfra->GetSlotID(tr,sl) - 1;
      UInt nStripsPart = GIFInfra->GetNStrips(tr,sl);
      string rpcID = GIFInfra->GetName(tr,sl);
      for (UInt p = 0; p < GIFInfra->GetNPartitions(tr,sl); p++) {
        //Clusterize noise/gamma data
        sort(NoiseHitList.rpc[T][S][p].begin(),
              NoiseHitList.rpc[T][S][p].end(),SortHitbyTime);
        Clusterization(NoiseHitList.rpc[T][S][p],
                       NoiseCSize_H.rpc[T][S][p],NoiseCMult_H.rpc[T][S][p]);
        //Clusterize muon data and fill efficiency histograms based on
        //the content of peak and fake hit vectors if efficiency run
        if(IsEfficiencyRun(RunType)){
          //Peak data
          sort(PeakHitList.rpc[T][S][p].begin(),
                PeakHitList.rpc[T][S][p].end(),SortHitbyTime);
          Clusterization(PeakHitList.rpc[T][S][p],
                         PeakCSize_H.rpc[T][S][p],PeakCMult_H.rpc[T][S][p]);
          if(PeakHitList.rpc[T][S][p].size() > 0)
            EfficiencyPeak_H.rpc[T][S][p]->Fill(DETECTED);
          else EfficiencyPeak_H.rpc[T][S][p]->Fill(MISSED);

          //Fake data
          if(FakeHitList.rpc[T][S][p].size() > 0)
            EfficiencyFake_H.rpc[T][S][p]->Fill(DETECTED);
          else EfficiencyFake_H.rpc[T][S][p]->Fill(MISSED);
        }
        //Save and reinitialise the hit multiplicity
        HitMultiplicity_H.rpc[T][S][p]->Fill(Multiplicity.rpc[T][S][p]);
        Multiplicity.rpc[T][S][p] = 0;
      }
    }
  }
```

4540 *Source Code B.14: Loops to clusterize the hit lists and fill efficiency and multiplicity histograms.*

4541 After the loop on the hit list of the entry is over, the next step is to clusterize the 3D lists filled

4542 in the previous steps, as displayed in Source Code B.14. A 3D loop is then started over the active
4543 trolley, slot and RPC partitions to access these objects. Each `NoiseHitList` and `PeakHitList`, in
4544 case of efficiency run, are clusterized as described in section B.5.2. There corresponding cluster size
4545 and multiplicity histograms are filled at the end of the clustering process.

Then, the peak and fake efficiency histograms are filled in case of efficiency run. The selection is simply made by checking whether the RPC detected signals in the peak window or/and fake window during this event. In the case a hit is recorded in either of both time windows, the histogram is filled with 1. On the contrary, the histogram is filled with 0. Finally, it is useful to remind that at this level, it is not possible yet to discriminate in between a muon hit and noise or gamma hit. the histograms `PeakCSize_H`, `PeakCMult_H` and `EfficiencyPeak_H` are then subjected to noise and background contamination. This contamination is estimated thanks to the fake efficiency histogram `EfficiencyFake_H` and corrected at the moment the results will be written into output CSV files and the histograms `MuonCSize_H`, `MuonCMult_H` and `Efficiency0_H` will be filled. The correction will be explained in Section B.6.4.3.

Finally, the loop ends on the filling of the general hit multiplicity histogram of each detector partitions.

4558 B.6.4 Results calculation

4559 As mentioned in section B.2.1, the analysis of DAQ data provides the user with 3 CSV files and
4560 a ROOT file associated to each and every ROOT data file. The fourth CSV file is provided by the
4561 extraction of the CEAN main frame data monitored during data taking and will be discussed later.
4562 After looping on the data in the previous part of the analysis macro, the output files are created and a
4563 3D loop on each RPC readout partitions is started to extract the histograms parameters and compute
4564 the final results.

4566 B.6.4.1 Rate normalisation

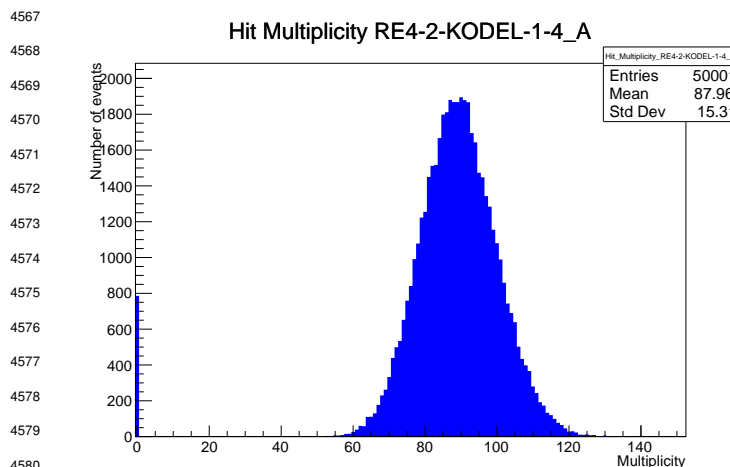


Figure B.2: The effect of the quality flag is explained by presenting the reconstructed hit multiplicity of a data file without `Quality_flag`. The artificial high content of bin 0 is the effect of corrupted data.

The hit rate normalization corresponds to translating a number of hits recorded during the full duration of data taking into a rate per unit area value. In order to achieve such result, it is first needed to know the total integrated time and the active area of the read-out partition on which the hits are counted. The total integrated is simply the noise window used for each event multiplied by the total number of events stored in the data file.

Nevertheless, to analyse old data format files, not containing any quality flag, it is

needed to estimate the amount of corrupted data via a fit as the corrupted data will always fill events with a fake "0 multiplicity". Indeed, as no hits were stored in the DAQ ROOT files, these events artificially contribute to fill the bin corresponding to a null multiplicity, as shown in Figure B.2. In the case the mean of the hit multiplicity distribution is high, the contribution of the corrupted data can easily be evaluated for later correction by comparing the level of the bin at multiplicity 0 and of a skew fit curve that should indicate a value consistent with 0. A skew fit has been chosen over a Poisson fit as it was giving better results for lower mean multiplicity values. Nevertheless, for low irradiation cases, as explained in Appendix A.4.3, the hit multiplicity distribution mean is, on the contrary, rather small and the probability to record events without hits can't be considered small anymore, leading to a difficult and non-reliable estimation of the corruption.

```

4585
4586     needed to estimate the amount of corrupted data via a fit as the corrupted data will always fill events
4587     with a fake "0 multiplicity". Indeed, as no hits were stored in the DAQ ROOT files, these events
4588     artificially contribute to fill the bin corresponding to a null multiplicity, as shown in Figure B.2. In
4589     the case the mean of the hit multiplicity distribution is high, the contribution of the corrupted data
4590     can easily be evaluated for later correction by comparing the level of the bin at multiplicity 0 and
4591     of a skew fit curve that should indicate a value consistent with 0. A skew fit has been chosen over
4592     a Poisson fit as it was giving better results for lower mean multiplicity values. Nevertheless, for
4593     low irradiation cases, as explained in Appendix A.4.3, the hit multiplicity distribution mean is, on
4594     the contrary, rather small and the probability to record events without hits can't be considered small
4595     anymore, leading to a difficult and non-reliable estimation of the corruption.

4595
4596     if(!isNewFormat) {
4597         TF1* GaussFit = new TF1("gaussfit","[0]*exp(-0.5*((x-[1])/[2])**2)",0,Xmax);
4598         GaussFit->SetParameter(0,100);
4599         GaussFit->SetParameter(1,10);
4600         GaussFit->SetParameter(2,1);
4601         HitMultiplicity_H.rpc[T][S][p]->Fit(GaussFit,"LIQR","","0.5,Xmax");
4602
4603         TF1* SkewFit = new TF1("skewfit","[0]*exp(-0.5*((x-[1])/[2])**2) / (1 +
4604         <- exp(-[3]*(x-[4])))",0,Xmax);
4605         SkewFit->SetParameter(0,GaussFit->GetParameter(0));
4606         SkewFit->SetParameter(1,GaussFit->GetParameter(1));
4607         SkewFit->SetParameter(2,GaussFit->GetParameter(2));
4608         SkewFit->SetParameter(3,1);
4609         SkewFit->SetParameter(4,1);
4610         HitMultiplicity_H.rpc[T][S][p]->Fit(SkewFit,"LIQR","","0.5,Xmax");
4611
4612         double fitValue = SkewFit->Eval(1,0,0,0);
4613         double dataValue = (double)HitMultiplicity_H.rpc[T][S][p]->GetBinContent(2);
4614         double difference = TMath::Abs(dataValue - fitValue);
4615         double fitTOdataVSentries_ratio = difference / (double)nEntries;
4616         bool isFitGOOD = fitTOdataVSentries_ratio < 0.01;
4617         double nSinglehit = (double)HitMultiplicity_H.rpc[T][S][p]->GetBinContent(1);
4618         double lowMultRatio = nSinglehit / (double)nEntries;
4619         bool isMultLOW = lowMultRatio > 0.4;
4620         if(isFitGOOD && !isMultLOW){
4621             nEmptyEvent = HitMultiplicity_H.rpc[T][S][p]->GetBinContent(1);
4622             nPhysics = (int)SkewFit->Eval(0,0,0,0);
4623             if(nPhysics < nEmptyEvent)
4624                 nEmptyEvent = nEmptyEvent-nPhysics;
4625         }
4626     }
4627     double corrupt_ratio = 100.*(double)nEmptyEvent / (double)nEntries;
4628     outputCorrCSV << corrupt_ratio << '\t';
4629     float rate_norm = 0.;
4630     float stripArea = GIFInfra->GetStripGeo(tr,sl,p);
4631
4632     if(IsEfficiencyRun(RunType)){
4633         float noiseWindow = BMTDCWINDOW - TIMEREJECT - 2*PeakWidth.rpc[T][S][p];
4634         rate_norm = (nEntries-nEmptyEvent)*noiseWindow*1e-9*stripArea;
4635     } else
4636         rate_norm = (nEntries-nEmptyEvent)*RDMNOISEWDW*1e-9*stripArea;

```

Source Code B.15: Definition of the rate normalisation variable. It takes into account the number of non corrupted entries and the time window used for noise and background calculation, to estimate the total integrated time, and the strip active area to express the result as rate per unit area.

4598 As can be seen in Source Code B.15, conditions have been applied to prevent bad fits and wrong
 4599 corruption estimation in cases where :

- 4600 • The difference in between the data for multiplicity 1 and the corresponding fit value should be
 4601 lower than 1% of the total amount of data : $\frac{|n_{m=1} - sk(1)|}{N_{tot}} < 0.01$ where $n_{m=1}$ is the number
 4602 of entries with multiplicity 1, $sk(1)$ the value of the skew fit, as defined by Formula 5.2, for
 4603 multiplicity 1 and N_{tot} the total number of entries.
- 4604 • The amount of data contained in the multiplicity 0 bin should not exceed 40% of the total
 4605 data content: $\frac{n_{m=0}}{N_{tot}} \leq 0.4$ where $n_{m=0}$ is the number of entries with multiplicity 0. This
 4606 number has been determined to be the maximum to be able to separate the excess of data due
 4607 to corruption from the hit multiplicity distribution.

4608 Those 2 conditions need to be fulfilled to estimate the corruption of old data format files. If the
 4609 fit was successful, the level of corruption is written in `Offline-Corrupted.csv` and the number of
 4610 corrupted entries, refered as the integer `nEmptyEvent`, is subtracted from the total number of entries
 4611 when the rate normalisation factor is computed as explicitated in Source Code B.15. Note that for new
 4612 data format files, the number of corrupted entries being set to 0, the definition of `rate_norm` stays
 4613 valid.

4614 B.6.4.2 Rate and activity

```
int nNoise = StripNoiseProfile_H.rpc[T][S][p]->GetEntries();
float averageNhit = (nNoise>0) ? (float)(nNoise/nStripsPart) : 1.;

for(Uint st = 1; st <= nStripsPart; st++){
    float stripRate =
        StripNoiseProfile_H.rpc[T][S][p]->GetBinContent(st)/rate_norm;
    float stripAct =
        StripNoiseProfile_H.rpc[T][S][p]->GetBinContent(st)/averageNhit;

    StripNoiseProfile_H.rpc[T][S][p]->SetBinContent(st,stripRate);
    StripActivity_H.rpc[T][S][p]->SetBinContent(st,stripAct);
}
```

4616 *Source Code B.16: Description of the loop that allows to set the content of each strip rate and strip activity
 channel for each detector partition.*

4617 At this point, the strip rate histograms, `StripNoiseProfile_H.rpc[T][S][p]`, only contain an
 4618 information about the total number of noise or background rate hits each channel received during the
 4619 data taking. As described in Source Code B.16, a loop on the strip channels will be used to normalise
 4620 the content of the rate distribution histogram for each detector partitions. The initial number of hits
 4621 recorded for a given bin will be extracted and 2 values are computed.

- 4622 • The strip hit rate, defined as the number of hits recorded in the bin normalised like described
 4623 in the previous section, using the variable `rate_norm` and the corresponding bin in histogram
 4624 `StripNoiseProfile_H.rpc[T][S][p]` is updated, and
- 4625 • the strip activity, defined as the number of hits recorded in the bin normalised to the average
 4626 number of hits per bin contained in the partition histogram, using the variable `averageNhit`.
 4627 This value provides an information on the homogeneity of the detector response to the gamma

4628 background or of the detector noise. An activity of 1 corresponds to an average response.
 4629 Above 1, the channel is more active than the average and bellow 1, the channel is less active.
 4630 This value is filled in the histograms `StripActivity_H.rpc[T][S][p]`.

4631 On each detector partitions, which are read-out by a single FEE, all the channels are not pro-
 4632 cessed by the same chip. Each chip can give a different noise response and hence, histograms using
 4633 a chip binning are used to investigate chip related noise behaviours. The average values of the strip
 4634 rate or activity grouped into a given chip are extracted using the using the function `GetChipBin()`
 4635 and stored in dedicated histograms as described in Source Codes B.17 and B.18 respectively.

```
4636 float GetChipBin(TH1* H, Uint chip){  

  4637   Uint start = 1 + chip*NSTRIPSCHIP;  

   int nActive = NSTRIPSCHIP;  

   float mean = 0.;  

   for(Uint b = start; b <= (chip+1)*NSTRIPSCHIP; b++) {  

     float value = H->GetBinContent(b);  

     mean += value;  

     if(value == 0.) nActive--;  

   }  

   if(nActive != 0) mean /= (float)nActive;  

   else mean = 0.;  

   return mean;  

}
```

4638 *Source Code B.17: Function used to compute the content of a bin for an histogram using chip binning.*

```
4639 for(Uint ch = 0; ch < (nStripsPart/NSTRIPSCHIP); ch++) {  

  ChipMeanNoiseProf_H.rpc[T][S][p]->  

    SetBinContent(ch+1,GetChipBin(StripNoiseProfile_H.rpc[T][S][p],ch));  

  ChipActivity_H.rpc[T][S][p]->  

    SetBinContent(ch+1,GetChipBin(StripActivity_H.rpc[T][S][p],ch));  

}
```

4640 *Source Code B.18: Description of the loop that allows to set the content of each chip rate and chip activi-
 tity bins for each detector partition knowing the information contained in the corresponding strip distribution
 histograms.*

4641 The activity variable is then used to evaluate the homogeneity of the detector response to back-
 4642 ground or of the detector noise. The homogeneity h_p of each detector partition can be evaluated
 4643 using the formula $h_p = \exp(-\sigma_p^R / \langle R \rangle_p)$, where $\langle R \rangle_p$ is the partition mean rate and σ_p^R is the
 4644 rate standard deviation calculated over the partition channels. The more homogeneously the rates
 4645 are distributed and the smaller will σ_p^R be, and the closer to 1 will h_p get. On the contrary, if the
 4646 standard deviation of the channel's rates is large, h_p will rapidly get to 0. This value is saved into
 4647 histograms as shown in Source Code B.19 and could in the future be used to monitor through time,
 4648 once extracted, the evolution of every partition homogeneity. This could be of great help to under-
 4649 stand the apparition of eventual hot spots due to ageing of the chambers subjected to high radiation
 4650 levels. The monitored homogeneity information could then be combined with a monitoring of the
 4651 activity of each individual channel in order to have a finer information. Monitoring tools have been
 4652 suggested and need to be developed for this purpose.

```

4653
float MeanPartSDev = GetTH1StdDev(StripNoiseProfile_H.rpc[T][S][p]);
float strip_homog = (MeanPartRate==0)
    ? 0.
    : exp(-MeanPartSDev/MeanPartRate);
StripHomogeneity_H.rpc[T][S][p]->Fill("exp -#left(#frac{\#sigma_{Strip}
    \rightarrow Rate}{\#mu_{(Strip Rate)}}\#right)",strip_homog);
StripHomogeneity_H.rpc[T][S][p]->GetYaxis()->SetRangeUser(0.,1.);

4654
float ChipStDevMean = GetTH1StdDev(ChipMeanNoiseProf_H.rpc[T][S][p]);
float chip_homog = (MeanPartRate==0)
    ? 0.
    : exp(-ChipStDevMean/MeanPartRate);
ChipHomogeneity_H.rpc[T][S][p]->Fill("exp -#left(#frac{\#sigma_{(Chip
    \rightarrow Rate)}\#mu_{(Chip Rate)}}\#right)",chip_homog);
ChipHomogeneity_H.rpc[T][S][p]->GetYaxis()->SetRangeUser(0.,1.);
```

4655 *Source Code B.19: Storage of the homogeneity into dedicated histograms.*

4656 B.6.4.3 Correction of muon performance parameters

4657 By previously filling the peak and fake efficiency histograms as well as the peak and noise cluster
 4658 size and cluster multiplicity it is possible to compute the efficiency of muon detection, the muon
 4659 cluster size, as well as the muon cluster multiplicity. This calculation is based on independant
 4660 event probabilities. The independant events that can be measured in the data are, " μ : A muon was
 4661 detected" and " γ : noise or background was detected". It is trivial to realize that the data in the peak
 4662 window corresponds to the intersection of both events, " $\mu \cup \gamma$: a muon or noise or background was
 4663 detected". This way, the efficiency measured in the peak window is actually the probability of the
 4664 event $\mu \cup \gamma$ while the efficiency in the fake window is then the probability of the event γ alone.
 4665 Assuming that μ and γ are independant, the probability of their intersection can be written as in
 4666 Formula B.5.

$$(B.5) \quad P(\mu \cup \gamma) = P(\mu) + P(\gamma) - P(\mu)P(\gamma)$$

4667 Isolating the probability of the event μ alone, actually corresponding to the muon detection
 4668 efficiency, can be then calculated with the quantities that are contained in the peak and fake histogram
 4669 as in Formula B.6.

$$(B.6) \quad P(\mu) = \frac{P(\mu \cup \gamma) - P(\gamma)}{1 - P(\gamma)} \quad \Leftrightarrow \quad \epsilon_\mu = \frac{\epsilon_{peak} - \epsilon_{fake}}{1 - \epsilon_{fake}}$$

4670 When it comes to the computation of the muon cluster size, a similar reasoning than for the muon
 4671 detection efficiency computation can be used. Indeed, using Formula B.5, out of the total number of
 4672 events where a muon or noise or background can be expressed as a sum of fractions of events μ , γ
 4673 and $\mu \cap \gamma$, the later being the event corresponding to the detection of both events simultaneously, as
 4674 showed in Formula B.7. The fractions can be expressed as a ratio of the probabilities already known,
 4675 using this time the notation $P(\mu \cap \gamma)$ instead of $P(\mu)P(\gamma)$. This choice was made to make the code
 4676 a little clearer.

$$(B.7) \quad 1 = F_\mu + F_\gamma + F_{\mu \cap \gamma} = \frac{P(\mu) - P(\mu \cap \gamma)}{P(\mu \cup \gamma)} + \frac{P(\gamma) - P(\mu \cap \gamma)}{P(\mu \cup \gamma)} + \frac{P(\mu \cap \gamma)}{P(\mu \cup \gamma)}$$

```

if(IsEfficiencyRun(RunType)){  

    //Evaluate the probabilities for each detection case with errors  

    float P_peak = EfficiencyPeak_H.rpc[T][S][p]->GetMean();  

    float P_fake = EfficiencyFake_H.rpc[T][S][p]->GetMean();  

    float P_muon = (P_peak-P_fake)/(1-P_fake);  

    float P_both = P_muon*P_fake;  

    float P_peak_err = sqrt(P_peak*(1.-P_peak)/nEntries);  

    float P_fake_err = sqrt(P_fake*(1.-P_fake)/nEntries);  

    float P_muon_err = sqrt(P_muon*(1.-P_muon)/nEntries);  

    float P_both_err = sqrt(P_both*(1.-P_both)/nEntries);  

    Efficiency0_H.rpc[T][S][p]->Fill("muon efficiency",P_muon);  

    Efficiency0_H.rpc[T][S][p]->Fill("muon efficiency error",P_muon_err);  

    //For each case get the fraction of events it represents  

    float F_both = P_both/P_peak;  

    float F_muon = (P_muon-P_both)/P_peak;  

    float F_fake = (P_fake-P_both)/P_peak;  

    float F_both_err = F_both*(P_both_err/P_both+P_peak_err/P_peak);  

    float F_muon_err = (P_muon_err+F_both_err+F_muon*P_peak_err)/P_peak;  

    float F_fake_err = (P_fake_err+F_both_err+F_fake*P_peak_err)/P_peak;  

    //Get the measured cluster sizes correcting using the fractions  

    float CS_peak = PeakCSIZE_H.rpc[T][S][p]->GetMean();  

    float CS_fake = NoiseCSIZE_H.rpc[T][S][p]->GetMean();  

    float CS_peak_err = 2*PeakCSIZE_H.rpc[T][S][p]->GetStdDev()  

        /sqrt(PeakCSIZE_H.rpc[T][S][p]->GetEntries());  

    float CS_fake_err = 2*NoiseCSIZE_H.rpc[T][S][p]->GetStdDev()  

        /sqrt(NoiseCSIZE_H.rpc[T][S][p]->GetEntries());  

    float CS_muon = (CS_peak-CS_fake*(F_fake+F_both/2.))/(F_muon+F_both/2.);  

    float CS_muon_err = (CS_peak_err  

        +(F_fake+F_both/2.)*CS_fake_err  

        +CS_muon*F_muon_err  

        +CS_fake*(F_fake_err+F_both_err/2.))  

        /(F_muon+F_both/2.);  

    MuonCSIZE_H.rpc[T][S][p]->Fill("muon cluster size",CS_muon);  

    MuonCSIZE_H.rpc[T][S][p]->Fill("muon cluster size error",CS_muon_err);  

    //Finally get the muon cluster multiplicity as peak-fake  

    float noiseWindow = BMTDCWINDOW - TIMEREJECT - 2*PeakWidth.rpc[T][S][p];  

    float peakWindow = 2*PeakWidth.rpc[T][S][p];  

    float CM_peak = PeakCMult_H.rpc[T][S][p]->GetMean();  

    float CM_fake = NoiseCMult_H.rpc[T][S][p]->GetMean()*peakWindow/noiseWindow;  

    float CM_muon = CM_peak-CM_fake;  

    float CM_peak_err = 2*PeakCMult_H.rpc[T][S][p]->GetStdDev()  

        /sqrt(PeakCMult_H.rpc[T][S][p]->GetEntries());  

    float CM_fake_err = 2*NoiseCMult_H.rpc[T][S][p]->GetStdDev()  

        /sqrt(NoiseCMult_H.rpc[T][S][p]->GetEntries())  

        * peakWindow/noiseWindow;  

    float CM_muon_err = CM_peak_err + CM_fake_err;  

    MuonCMult_H.rpc[T][S][p]->Fill("muon cluster multiplicity",CM_muon);  

    MuonCMult_H.rpc[T][S][p]->Fill("muon cluster multiplicity  

    ↳ error",CM_muon_err);  

    //Write in the output CSV file  

    outputEffCSV << P_muon << '\t' << P_muon_err << '\t'  

        << CS_muon << '\t' << CS_muon_err << '\t'  

        << CM_peak << '\t' << CM_peak_err << '\t';
}

```

4678 Source Code B.20: Analysis algorithm to compute muon efficiency, cluster size and multiplicity knowing the peak and fake efficiency, cluster size and multiplicity.

4679 Each ones of these events have an associated cluster size. The cluster size of the noise or back-
 4680 ground already is measured thanks to the clusterization of the noise hit list. In the same way, the
 4681 peak cluster size corresponds to the cluster measured for the event $\mu \cup \gamma$. Nevertheless, the cluster
 4682 of the event $\mu \cap \gamma$ is not known but it can be assumed that the probability of having more than 1
 4683 noise or background cluster contained in the peak window is very low if the peak wondow duration
 4684 is compared to the background rate that rarely seen to go beyond 2000 Hz/cm² [to be confirmed].
 4685 Hence, the cluster size that is likely to be measured in such kind of event where both a muon and a
 4686 background or noise cluster was recorded is the average of the muon cluster size and the background
 4687 cluster size. The cluster size $C_{\mu \cup \gamma}$ probed in the peak can then be written as in Formula B.8 and
 4688 leads to the expression for the muon cluster size C_μ written in Formula B.9.

$$(B.8) \quad C_{\mu \cup \gamma} = C_\mu F_\mu + C_\gamma F_\gamma + \frac{C_\mu + C_\gamma}{2} \times F_{\mu \cap \gamma}$$

$$(B.9) \quad C_\mu = \frac{C_{\mu \cup \gamma} - C_\gamma \times (F_\gamma + F_{\mu \cap \gamma}/2)}{F_\mu + F_{\mu \cap \gamma}/2}$$

4689 Finally, the computation of the muon cluster multiplicity comes quite naturally as the cluster
 4690 multiplicity measured in the peak to which is subtracted the background cluster multiplpicity taken
 4691 in a window of similar width. These calculations, as well as the error propagation that was not
 4692 explicited here, can be seen going through Source Code B.20.

4693 B.6.4.4 Strip masking tool

4694 The offline tool is automatically called at the end of each data taking to analyse the data and offer
 4695 the shifter DQM histograms to control the data quality. After the histograms have been published
 4696 online in the DQM page, the shifter can decide to mask noisy or dead channels that will contribute
 4697 to bias the final rate calculation by editing the mask column of `ChannelsMapping.csv` as can be seen
 4698 in Figure B.3.

4699 From the code point of view, the function `GetTH1Mean()` is used to retrieve the mean rate par-
 4700 tition by partition after the rates have been calculated strip by strip and filled into the histograms
 4701 `StripNoiseProfile_H.rpc[T][S][p]`, as described through Source Code B.21.

4702 Once the mask for each rejected channel has been updated, the shifter can manually run the
 4703 offline tool again to update the DQM plots, now including the masked strips, as well the rate results
 4704 written in the output CSV file `Offline-Rate.csv`. If not done during the shifts, the strip masking
 4705 procedure needs to be carefully done by the person in charge of data analysis on the scans that were
 4706 selected to produce the final results.

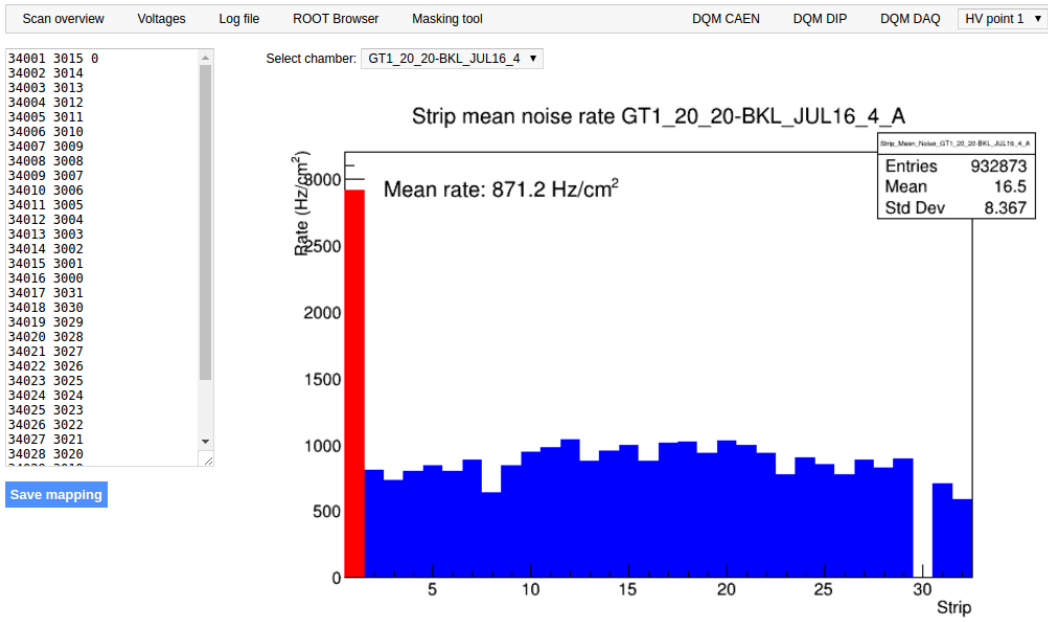


Figure B.3: Display of the masking tool page on the webDCS. The window on the left allows the shifter to edit ChannelsMapping.csv. To mask a channel, it only is needed to set the 3rd field corresponding to the strip to mask to 0. It is not necessary for older mapping file formats to add a 1 for each strip that is not masked as the code is versatile and the default behaviour is to consider missing mask fields as active strips. The effect of the mask is directly visible for noisy channels as the corresponding bin turns red. The global effect of masking strips will be an update of the rate value showed on the histogram that will take into consideration the rejected channels.

```

float GetTH1Mean (TH1* H){
    int nBins = H->GetNbinsX();
    int nActive = nBins;
    float mean = 0.;

    for(int b = 1; b <= nBins; b++){
        float value = H->GetBinContent (b);
        mean += value;
        if(value == 0.) nActive--;
    }

    if(nActive != 0) mean /= (float)nActive;
    else mean = 0.;

    return mean;
}

```

Source Code B.21: The function GetTH1Mean() is used to return the mean along the y-axis of TH1 histograms containing rate information. In order to take into account masked strips whose rate is set to 0, the function looks for masked channels and decrement the number of active channels for each null value found.

4709 **B.6.4.5 Output CSV files filling**

```

for (UInt tr = 0; tr < GIFInfra->GetNTrolleys(); tr++) {
    UInt T = GIFInfra->GetTrolleyID(tr);
    for (UInt sl = 0; sl < GIFInfra->GetNSlots(tr); sl++) {
        UInt S = GIFInfra->GetSlotID(tr,sl) - 1;
        float MeanNoiseRate = 0.;
        float ClusterRate = 0.;
        float ClusterSDev = 0.;

        for (UInt p = 0; p < GIFInfra->GetNPartitions(tr,sl); p++) {
            float MeanPartRate = GetTH1Mean(StripNoiseProfile_H.rpc[T][S][p]);
            float cSizePart = NoiseCSize_H.rpc[T][S][p]->GetMean();
            float cSizePartErr = (NoiseCSize_H.rpc[T][S][p]->GetEntries()==0)
                ? 0.
                : 2*NoiseCSize_H.rpc[T][S][p]->GetStdDev() /
                    sqrt(NoiseCSize_H.rpc[T][S][p]->GetEntries());
            float cMultPart = NoiseCMult_H.rpc[T][S][p]->GetMean();
            float cMultPartErr = (NoiseCMult_H.rpc[T][S][p]->GetEntries()==0)
                ? 0.
                : 2*NoiseCMult_H.rpc[T][S][p]->GetStdDev() /
                    sqrt(NoiseCMult_H.rpc[T][S][p]->GetEntries());
            float ClustPartRate = (cSizePart==0) ? 0.
                : MeanPartRate/cSizePart;
            float ClustPartRateErr = (cSizePart==0) ? 0.
                : ClustPartRate * cSizePartErr/cSizePart;

            outputRateCSV << MeanPartRate << '\t'
                << cSizePart << '\t' << cSizePartErr << '\t'
                << cMultPart << '\t' << cMultPartErr << '\t'
                << ClustPartRate << '\t' << ClustPartRateErr << '\t';

            RPCArea += stripArea * nStripsPart;
            MeanNoiseRate += MeanPartRate * stripArea * nStripsPart;
            ClusterRate += ClustPartRate * stripArea * nStripsPart;
            ClusterSDev += (cSizePart==0)
                ? 0.
                : ClusterRate*cSizePartErr/cSizePart;
        }
        MeanNoiseRate /= RPCArea;
        ClusterRate /= RPCArea;
        ClusterSDev /= RPCArea;
        outputRateCSV << MeanNoiseRate << '\t' << ClusterRate << '\t'
            << ClusterSDev << '\t';
    }
}

```

4711 *Source Code B.22: Description of rate result calculation and writing into the CSV output Offline-Rate.csv. Are saved into the file for each detector, the mean partition rate, cluster size and cluster mutiplicity, along with their errors, for each partition and as well as a detector average.*

4712 All the histograms have been filled. Parameters will then be extracted from them to compute the
 4713 final results that will later be used to produce plots. Once the results have been computed, the very
 4714 last step of the offline macro is to write these values into the corresponding CSV outputs. Aside of
 4715 the file Offline-Corrupted.csv, 2 CSV files are being written by the macro OfflineAnalysis(),
 4716 Offline-Rates.csv and Offline-L0-EffCl.csv that respectively contain information about noise
 4717 or gamma rates, cluster size and multiplicity, and about level 0 reconstruction of the detector effi-
 4718 ciency, muon cluster size and multiplicity. Details on the computation and file writing are respec-

⁴⁷¹⁹ tively given in Sources Codes B.22 and B.20.

⁴⁷²⁰ **Noise/gamma background variables** are computed and written in the output file for each detector
⁴⁷²¹ partitions. A detector average of the hit and cluster rate is also provided, as shown through Sources
⁴⁷²² Code B.22. The variables that are written for each partition are:

- ⁴⁷²³ • The mean partition hit rate per unit area, `MeanPartRate`, that is extracted from the histogram
⁴⁷²⁴ `StripNoiseProfile_H` as the mean value along the y-axis, as described in section B.6.4.4. No
⁴⁷²⁵ error is recorded for the hit rate as this is considered a single measurement. No statistical error
⁴⁷²⁶ can be associated to it and the systematics are unknown.
- ⁴⁷²⁷ • The mean cluster size, `cSizePart`, is extracted from the histogram `NoiseCSize_H` and it's
⁴⁷²⁸ statistical error, `cSizePartErr`, is taken to be 2σ of the total distribution.
- ⁴⁷²⁹ • The mean cluster multiplicity per trigger, `cMultPart`, is extracted from the histogram `NoiseCMult_H`
⁴⁷³⁰ and it's statistical error, `cMultPartErr`, is taken to be 2σ of the total distribution. It is impor-
⁴⁷³¹ tant to point to the fact that this variable gives an information that is dependent on the buffer
⁴⁷³² window width used for each trigger for the calculation.
- ⁴⁷³³ • The mean cluster rate per unit area, `ClustPartRate`, is defined as the mean hit rate normalised
⁴⁷³⁴ to the mean cluster size and it's statistical error, `ClustPartRateErr`, is then obtained using the
⁴⁷³⁵ relative statistical error on the mean cluster size.

⁴⁷³⁶ **Muon performance variables** are computed as discussed in the Section B.6.4.3 and written in
⁴⁷³⁷ the output file for each detector partitions as shown through Sources Code B.20. It is reminded that
⁴⁷³⁸ this offline tool doesn't include any tracking algorithm to identify muons from the beam and only
⁴⁷³⁹ relies on the hits arriving in the time window corresponding to the beam time and is corrected thanks
⁴⁷⁴⁰ to the estimation of the contribution of the background and noise to the efficiency of the detector.
⁴⁷⁴¹ Assuming that the detection of background and muons were independent events, a probabilistic
⁴⁷⁴² approach was then used to correct efficiency, muon cluster size and muon cluster multiplicity. The
⁴⁷⁴³ variables that are written for each partition are:

- ⁴⁷⁴⁴ • The muon efficiency, referred to as the probability to detect a muon in the peak window
⁴⁷⁴⁵ `P_muon`, also filled in histogram `Efficiency0_H`. The statistical error related to the efficiency,
⁴⁷⁴⁶ `P_muon_err`, is computed using a binomial distribution, as the efficiency measures the proba-
⁴⁷⁴⁷ bility of "success" and "failure" to detect muons.
- ⁴⁷⁴⁸ • The mean muon cluster size, `CS_muon`, and its related statistical error, `CS_muon_err`, also filled
⁴⁷⁴⁹ in the histogram `MuonCSize_H`.
- ⁴⁷⁵⁰ • The mean muon cluster multiplicity, `CM_muon`, and its related statistical error, `CM_muon_err`,
⁴⁷⁵¹ also filled in the histogram `MuonCMult_H`.

⁴⁷⁵² In addition to these 2 CSV files, the histograms are saved in ROOT file `Scan00XXXX_HVY_Offline.root`
⁴⁷⁵³ as explained in section B.2.1.1.

4754 B.7 Current information extraction

4755 Detectors under test at GIF++ are connected both to a CAEN HV power supply and to a CAEN
4756 ADC that reads the currents inside of the RPC gaps bypassing the supply cable. During data tak-
4757 ing, the webDCS records into a ROOT file called `Scan00XXXX_HVY_CAEN.root` histograms with the
4758 monitored parameters of both CAEN devices. Are recorded for each RPC channels (in most cases,
4759 a channel corresponds to an RPC gap):

- 4760 • the effective voltage, HV_{eff} , set by the webDCS using the PT correction on the CAEN power
4761 supply,
- 4762 • the applied voltage, HV_{app} , monitored by the CAEN power supply, and the statistical error
4763 related to the variations of this value through time to follow the variation of the environmental
4764 parameters defined as the RMS of the histogram divided by the square root of the number of
4765 recorded points,
- 4766 • the monitored current, I_{mon} , monitored by the CAEN power supply, and the statistical error
4767 related to the variations of this value through time to follow the variation of the environmental
4768 parameters defined as the RMS of the histogram divided by the square root of the number of
4769 recorded points,
- 4770 • the corresponding current density, J_{mon} , defined as the monitored current per unit area,
4771 $J_{mon} = I_{mon}/A$, where A is the active area of the corresponding gap,
- 4772 • the ADC current, I_{ADC} , recorded through the CAEN ADC module that monitors the dark
4773 current in the gap itself. First of all, the resolution of such a module is better than that of
4774 CAEN power supplies and moreover, the current is not read-out through the HV supply line
4775 but directly at the chamber level giving the real current inside of the detector. The statistical
4776 error is defined as the RMS of the histogram distribution divided by the square root of the
4777 number of recorded points.

4778 Once extracted through a loop over the element of GIF++ infrastructure via the C++ macro
4779 `GetCurrent()`, these parameters, organised in 9 columns per detector HV supply line, are written in
4780 the output CSV file `Offline-Current.csv`. The macro can be found in the file `Current.cc`.

References

- [1] K. Ruedenberg & W.H.E. Schwarz. “Three Millennia of Atoms and Molecules”. In: *Pioneers of Quantum Chemistry*. Ed. by Angela K. Wilson E. Thomas Strom. Vol. 1122. ACS Symposium Series, 2013, pp. 1–45.
- [2] A. Lavoisier. *Traité élémentaire de chimie*. Éditions la Bibliothèque Digitale, 2014 (first published 1789).
- [3] J. Dalton. *A New System of Chemical Philosophy*. William Dawson & Sons, 1808.
- [4] J. von Fraunhofer. “Bestimmung des Brechungs- und des Farben-Zerstreuungs - Vermögens verschiedener Glasarten, in Bezug auf die Vervollkommnung achromatischer Fernröhre”. In: *Denkschriften der Königlichen Akademie der Wissenschaften zu München*. Die Akademie, 1817, pp. 193–226.
- [5] J.J. Thomson. “XL. Cathode Rays”. In: *The London, Edinburgh, and Dublin Philosophical Magazine and Journal of Science* 44:269 (1897), pp. 293–316.
- [6] J.B. Perrin. “Nouvelles propriétés des rayons cathodiques”. In: *Comptes Rendus Hebdomadaires des Séances de L'Académie des Sciences*. Vol. 121. Académie des Sciences, 1895, pp. 1130–1134.
- [7] H. Becquerel. “Déviation du rayonnement du radium dans un champ électrique”. In: *Comptes Rendus Hebdomadaires des Séances de L'Académie des Sciences*. Vol. 130. Académie des Sciences, 1900, p. 809.
- [8] J.J. Thomson. “XXIV. On the structure of the atom: an investigation of the stability and periods of oscillation of a number of corpuscles arranged at equal intervals around the circumference of a circle; with application of the results to the theory of atomic structure”. In: *The London, Edinburgh, and Dublin Philosophical Magazine and Journal of Science* 7:39 (1904), pp. 237–265.
- [9] E. Rutherford & T. Royds. “XXIV. Spectrum of the radium emanation”. In: *The London, Edinburgh, and Dublin Philosophical Magazine and Journal of Science* 16:92 (1904), pp. 313–317.
- [10] H. Geiger. “On the scattering of the α -particles by matter”. In: *Proceedings of the Royal Society A* 81 (1908), pp. 174–177.
- [11] H. Geiger & E. Marsden. “On a diffuse reflection of the α -particles”. In: *Proceedings of the Royal Society A* 82 (1909), pp. 495–500.
- [12] H. Geiger. “The scattering of α -particles by matter”. In: *Proceedings of the Royal Society A* 83 (1910), pp. 492–504.
- [13] H. Geiger & E. Marsden. “LXI. The laws of deflexion of a particles through large angles”. In: *The London, Edinburgh, and Dublin Philosophical Magazine and Journal of Science* 25:148 (1913), pp. 604–623.

- 4817 [14] E. Rutherford. "LXXIX. The Scattering of α and β Particles by Matter and the Structure of
4818 the Atom". In: *The London, Edinburgh, and Dublin Philosophical Magazine and Journal of*
4819 *Science* 21:125 (1911), pp. 669–688.
- 4820 [15] E. Rutherford. "LIV. Collision of α particles with light atoms. IV. An anomalous effect in
4821 nitrogen". In: *The London, Edinburgh, and Dublin Philosophical Magazine and Journal of*
4822 *Science* 37:222 (1919), pp. 581–587.
- 4823 [16] O. Masson. "XXIV. The constitution of atoms". In: *The London, Edinburgh, and Dublin*
4824 *Philosophical Magazine and Journal of Science* 41:242 (1921), pp. 281–285.
- 4825 [17] W. Prout. "On the Relation between the Specific Gravities of Bodies in their Gaseous State
4826 and the Weights of their Atoms." In: *Annals of Philosophy* 6 (1815), pp. 321–330.
- 4827 [18] W. Prout. "Correction of a Mistake in the Essay on the Relation between the Specific Gravities
4828 of Bodies in their Gaseous State and the Weights of their Atoms". In: *Annals of Philosophy*
4829 7 (1816), pp. 111–113.
- 4830 [19] E. Rutherford. "Bakerian Lecture: Nuclear constitution of atoms". In: *Proceedings of the*
4831 *Royal Society A* 97 (1920), pp. 374–400.
- 4832 [20] W. Bothe & H. Becker. "Künstliche Erregung von Kern- γ -Strahlen". In: *Zeitschrift für Physik*
4833 66 (1930), pp. 289–306.
- 4834 [21] H. Becker & W. Bothe. "Die in Bor und Beryllium erregten γ -Strahlen". In: *Zeitschrift für*
4835 *Physik* 76 (1932), pp. 421–438.
- 4836 [22] I. Curie & F. Joliot. "Émission de protons de grande vitesse par les substances hydrogenées
4837 sous l'influence de rayons γ très pénétrants". In: *Comptes Rendus Hebdomadaires des Séances*
4838 *de L'Académie des Sciences*. Vol. 194. Académie des Sciences, 1932, pp. 273–275.
- 4839 [23] J. Chadwick. "Possible Existence of a Neutron". In: *Nature* 129 (1932), p. 312.
- 4840 [24] J. Chadwick. "Bakerian lecture. The neutron". In: *Proceedings of the Royal Society A* 142
4841 (1933), pp. 1–25.
- 4842 [25] Max Plank. "Ueber das Gesetz der Energieverteilung im Normalspectrum". In: *Annalen Der*
4843 *Physik* 309 (1901), pp. 553–563.
- 4844 [26] A. Einstein. "Über einen die Erzeugung und Verwandlung des Lichtes betreffenden heuris-
4845 tischen Gesichtspunkt". In: *Annalen Der Physik* 322 (1905), pp. 132–148.
- 4846 [27] N. Bohr. "I. On the constitution of atoms and molecules". In: *The London, Edinburgh, and*
4847 *Dublin Philosophical Magazine and Journal of Science* 26:151 (1913), pp. 1–25.
- 4848 [28] H.G.J. Moseley. "XCIII. The high-frequency spectra of the elements". In: *The London, Edin-
4849 burgh, and Dublin Philosophical Magazine and Journal of Science* 26:156 (1913), pp. 1024–
4850 1034.
- 4851 [29] A. Sommerfeld. "Zur Quantentheorie der Spektrallinien". In: *Annalen Der Physik* 356 (1916),
4852 pp. 1–94.
- 4853 [30] P. Zeeman. "XXXII. On the influence of magnetism on the nature of the light emitted by a
4854 substance". In: *The London, Edinburgh, and Dublin Philosophical Magazine and Journal of*
4855 *Science* 43:262 (1897), pp. 226–239.
- 4856 [31] P. Zeeman. "VII. Doublets and triplets in the spectrum produced by external magnetic forces".
4857 In: *The London, Edinburgh, and Dublin Philosophical Magazine and Journal of Science*
4858 44:266 (1897), pp. 55–60.
- 4859 [32] P. Zeeman. "VII. Doublets and triplets in the spectrum produced by external magnetic forces.—(II.)"
4860 In: *The London, Edinburgh, and Dublin Philosophical Magazine and Journal of Science*
4861 44:268 (1897), pp. 255–259.

BIBLIOGRAPHY

- 4862 [33] P. Zeeman. “XXI. Measurements concerning radiation-phenomena in the magnetic field.—(I.)”
4863 In: *The London, Edinburgh, and Dublin Philosophical Magazine and Journal of Science*
4864 45:273 (1898), pp. 197–201.
- 4865 [34] W. Gerlach & O. Stern. “Der experimentelle Nachweis der Richtungsquantelung im Mag-
4866 netfeld”. In: *Zeitschrift für Physik* 9 (1922), pp. 349–352.
- 4867 [35] W. Pauli. “Über den Einfluß der Geschwindigkeitsabhängigkeit der Elektronenmasse auf den
4868 Zeeman-Effekt”. In: *Zeitschrift für Physik* 31 (1925), 373–385.
- 4869 [36] W. Pauli. “Über den Zusammenhang des Abschlusses der Elektronengruppen im Atom mit
4870 der Komplexstruktur der Spektren”. In: *Zeitschrift für Physik* 31 (1925), 765–783.
- 4871 [37] G.E. Uhlenbeck & S. Goudsmit. “Spinning Electrons and the Structure of Spectra”. In: *Nature*
4872 117 (1926), pp. 264–265.
- 4873 [38] W. Pauli. “Zur Quantenmechanik des magnetischen Elektrons”. In: *Zeitschrift für Physik* 43
4874 (1927), 601–623.
- 4875 [39] L. De Broglie. “Recherches sur la théorie des Quanta”. PhD thesis. University of Paris, 1924.
- 4876 [40] E. Schrödinger. “An Undulatory Theory of the Mechanics of Atoms and Molecules”. In:
4877 *Phys. Rev.* 28 (1927), pp. 1049–1070.
- 4878 [41] P. Dirac. “The quantum theory of the emission and absorption of radiation”. In: *Proceedings
4879 of the Royal Society A* 114 (1928), pp. 243–265.
- 4880 [42] P. Dirac. “The quantum theory of the electron”. In: *Proceedings of the Royal Society A* 117
4881 (1928), pp. 610–624.
- 4882 [43] J. R. Oppenheimer. “On the Theory of Electrons and Protons”. In: *Phys. Rev.* 35 (1930),
4883 pp. 562–563.
- 4884 [44] P. Dirac. “Quantised singularities in the electromagnetic field”. In: *Proceedings of the Royal
4885 Society A* 133 (1931), pp. 60–72.
- 4886 [45] J. R. Oppenheimer. “Note on the Theory of the Interaction of Field and Matter”. In: *Phys.
4887 Rev.* 35 (1930), pp. 461–477.
- 4888 [46] H.A. Bethe. “The Electromagnetic Shift of Energy Levels”. In: *Phys. Rev.* 72 (1947), pp. 339–
4889 341.
- 4890 [47] H.F.J. Dyson. “The Radiation Theories of Tomonaga, Schwinger, and Feynman”. In: *Phys.
4891 Rev.* 75 (1949), pp. 486–502.
- 4892 [48] H. Yukawa. “On the Interaction of Elementary Particles. I”. In: *Proc. Phys. Math. Soc. Jap.*
4893 17 (1935), pp. 48–57.
- 4894 [49] C.D. Anderson & S.H. Neddermeyer. “Cloud Chamber Observations of Cosmic Rays at 4300
4895 Meters Elevation and Near Sea-Level”. In: *Phys. Rev.* 50 (1936), pp. 263–271.
- 4896 [50] S.H. Neddermeyer & C.D. Anderson. “Note on the Nature of Cosmic-Ray Particles”. In:
4897 *Phys. Rev.* 51 (1937), pp. 884–886.
- 4898 [51] J.C. Street & E.C. Stevenson. “New Evidence for the Existence of a Particle of Mass Inter-
4899 mediate Between the Proton and Electron”. In: *Phys. Rev.* 52 (1937), pp. 1003–1004.
- 4900 [52] C.M.G. Lattes et al. “Processes involving charged mesons”. In: *Nature* 159 (1947), pp. 694–
4901 697.
- 4902 [53] C.M.G. Lattes et al. “Observations on the Tracks of Slow Mesons in Photographic Emulsions
4903 (Part 1)”. In: *Nature* 160 (1947), pp. 453–456.

- 4904 [54] C.M.G. Lattes et al. “Observations on the Tracks of Slow Mesons in Photographic Emulsions
4905 (Part 2)”. In: *Nature* 160 (1947), 486–492.
- 4906 [55] R. Blokland et al. “High Energy Photons from Proton-Nucleon Collisions”. In: *Phys. Rev.*
4907 77 (1950), pp. 213–218.
- 4908 [56] G.D. Rochester & C.C. Butler. “Evidence for the Existence of New Unstable Elementary
4909 Particles”. In: *Nature* 160 (1947), 855–857.
- 4910 [57] A. Pais. “Some Remarks on the V-Particles”. In: *Phys. Rev.* 86 (1952), pp. 663–672.
- 4911 [58] M. Gell-Mann. “Symmetries of Baryons and Mesons”. In: *Phys. Rev.* 125 (1962), pp. 1067–
4912 1084.
- 4913 [59] K. Nishijima & T. Nakano. “Charge Independence for V-particles”. In: *Progress of Theoretical
4914 Physics* 10 (1953), 581–582.
- 4915 [60] K. Nishijima. “Charge Independence Theory of V-Particles”. In: *Progress of Theoretical
4916 Physics* 13 (1955), pp. 285–304.
- 4917 [61] M. Gell-Mann. “The interpretation of the new particles as displaced charge multiplets”. In:
4918 *Il Nuovo Cimento* 4 (1956), 848–866.
- 4919 [62] W. Heisenberg. “Über den Bau der Atomkerne. I”. In: *Zeitschrift für Physik* 77 (1932), 1–11.
- 4920 [63] V.E. Barnes et al. “Observation of a Hyperon with Strangeness Minus Three”. In: *Phys. Rev.
4921 Lett.* 12 (1964), pp. 204–206.
- 4922 [64] M. Gell-Mann. “A schematic model of baryons and mesons”. In: *Physics Letters* 8 (1964),
4923 pp. 214–215.
- 4924 [65] G. Zweig. *An SU(3) Model for Strong Interaction Symmetry and its Breaking*. Tech. rep.
4925 CERN-TH-401. CERN, 1964.
- 4926 [66] G. Zweig. *An SU(3) Model for Strong Interaction Symmetry and its Breaking (II)*. Tech. rep.
4927 CERN-TH-412. CERN, 1964.
- 4928 [67] E.D. Bloom et al. “High-Energy Inelastic $e - p$ Scattering at 6° and 10° ”. In: *Phys. Rev. Lett.*
4929 23 (1969), pp. 930–934.
- 4930 [68] M. Breidenbach et al. “Observed Behavior of Highly Inelastic Electron-Proton Scattering”.
4931 In: *Phys. Rev. Lett.* 23 (1969), pp. 935–939.
- 4932 [69] B.J. Bjørken & S.L. Glashow. “Elementary particles and SU(4)”. In: *Physics Letters* 11
4933 (1964), pp. 255–257.
- 4934 [70] J. Iliopoulos & L. Maiani S. Glashow. “Weak Interactions with Lepton-Hadron Symmetry”.
4935 In: *Phys. Rev. D* 2 (1970), pp. 1285–1292.
- 4936 [71] J.H. Christenson et al. “Evidence for the 2π Decay of the K_2^0 Meson”. In: *Phys. Rev. Lett.* 13
4937 (1964), pp. 138–140.
- 4938 [72] M. Kobayashi & T. Maskawa. “CP-Violation in the Renormalizable Theory of Weak Inter-
4939 action”. In: *Progress of Theoretical Physics* 49 (1973), pp. 652–657.
- 4940 [73] H. Harari. “A new quark model for hadrons”. In: *Physics Letters B* 57 (1975), pp. 265–269.
- 4941 [74] B. Richter et al. “Discovery of a Narrow Resonance in e^+e^- Annihilation”. In: *Phys. Rev.
4942 Lett.* 33 (1974), pp. 1406–1408.
- 4943 [75] S. Ting et al. “Experimental Observation of a Heavy Particle J ”. In: *Phys. Rev. Lett.* 33
4944 (1974), pp. 1404–1405.
- 4945 [76] S.W. Herb et al. “Observation of a Dimuon Resonance at 9.5 GeV in 400 GeV Proton-
4946 Nucleus Collisions”. In: *Phys. Rev. Lett.* 39 (1977), pp. 252–255.

BIBLIOGRAPHY

- 4947 [77] S. Abashi et al. “Search for High Mass Top Quark Production in $\bar{p}p$ Collisions at $\sqrt{s} =$
4948 1.8 TeV”. In: *Phys. Rev. Lett.* 74 (1995), pp. 2422–2426.
- 4949 [78] F. Abe et al. “Observation of Top Quark Production in $\bar{p}p$ Collisions with the Collider De-
4950 tector at Fermilab”. In: *Phys. Rev. Lett.* 74 (1995), pp. 2626–2631.
- 4951 [79] F. Tkachov. “A contribution to the history of quarks: Boris Struminsky’s 1965 JINR publi-
4952 cation”. In: (2009).
- 4953 [80] O.W. Greenberg. “Spin and Unitary-Spin Independence in a Paraquark Model of Baryons
4954 and Mesons”. In: *Phys. Rev. Lett.* 13 (1964), pp. 598–602.
- 4955 [81] M.Y. Han & Y. Nambu. “Three-Triplet Model with Double $SU(3)$ Symmetry”. In: *Phys.*
4956 *Rev.* 139 (1965), B1006–B1010.
- 4957 [82] R.P. Feynman. “The behavior of hadron collisions at extreme energies”. In: *Conf. Proc.*
4958 C690905 (1969), pp. 237–258.
- 4959 [83] J.D. Bjorken & E.A. Paschos. “Inelastic Electron-Proton and γ -Proton Scattering and the
4960 Structure of the Nucleon”. In: *Phys. Rev.* 185 (1969), pp. 1975–1982.
- 4961 [84] M. Gell-Mann & H. Leutwyler H. Fritzsch. “Advantages of the color octet gluon picture”.
4962 In: *Physics Letters B* 47 (1973), pp. 365–368.
- 4963 [85] D.J. Gross & F. Wilczek. “Ultraviolet Behavior of Non-Abelian Gauge Theories”. In: *Phys.*
4964 *Rev. Lett.* 30 (1973), pp. 1343–1346.
- 4965 [86] H.D. Politzer. “Reliable Perturbative Results for Strong Interactions?” In: *Phys. Rev. Lett.* 30
4966 (1973), pp. 1346–1349.
- 4967 [87] S. Bethke. “ α_s 2002”. In: *Nuclear Physics B* 121 (2003), pp. 74–81.
- 4968 [88] E. Fermi. “Versuch einer Theorie der β -Strahlen. I”. In: *Zeitschrift für Physik* 88 (1934),
4969 pp. 161–177.
- 4970 [89] W. Pauli. “Dear radioactive ladies and gentlemen”. In: *Phys. Today* 31N9 (1978), p. 27.
- 4971 [90] C.L. Cowan Jr. et al. “Detection of the Free Neutrino: a Confirmation”. In: *Science* 20 (1956),
4972 pp. 103–104.
- 4973 [91] E.J. Konopinski & H.M. Mahmoud. “The Universal Fermi Interaction”. In: *Phys. Rev.* 92
4974 (1953), pp. 1045–1049.
- 4975 [92] J. Steinberger et al. L.M. Lederman M. Schwartz. “Observation of High-Energy Neutrino Re-
4976 actions and the Existence of Two Kinds of Neutrinos”. In: *Phys. Rev. Lett.* 9 (1962), pp. 36–
4977 44.
- 4978 [93] T.D. Lee & C.N. Yang. “Question of Parity Conservation in Weak Interactions”. In: *Phys.*
4979 *Rev.* 104 (1956), pp. 254–258.
- 4980 [94] G. Gamow & E. Teller. “Selection Rules for the β -Disintegration”. In: *Phys. Rev.* 49 (1936),
4981 pp. 895–899.
- 4982 [95] C.S. Wu et al. “Experimental Test of Parity Conservation in Beta Decay”. In: *Phys. Rev.* 105
4983 (1957), pp. 1413–1415.
- 4984 [96] S. Weinberg. “A Model of Leptons”. In: *Phys. Rev. Lett.* 19 (1967), pp. 1264–1266.
- 4985 [97] Y. Nambu & G. Jona-Lasinio. “Dynamical Model of Elementary Particles Based on an Anal-
4986 ogy with Superconductivity. I”. In: *Phys. Rev.* 122 (1961), pp. 345–358.
- 4987 [98] Y. Nambu & G. Jona-Lasinio. “Dynamical Model of Elementary Particles Based on an Anal-
4988 ogy with Superconductivity. II”. In: *Phys. Rev.* 124 (1961), pp. 246–254.

- 4989 [99] & J. R. Schrieffer J. Bardeen L.N. Cooper. “Microscopic Theory of Superconductivity”. In: *Phys. Rev.* 106 (1957), pp. 162–164.
- 4990
- 4991 [100] Y. Nambu. “Quasi-Particles and Gauge Invariance in the Theory of Superconductivity”. In: *Phys. Rev.* 117 (1960), pp. 648–663.
- 4992
- 4993 [101] J. Goldstone. “Quasi-Particles and Gauge Invariance in the Theory of Superconductivity”. In: *Il Nuovo Cimento* 19 (1961), pp. 154–164.
- 4994
- 4995 [102] P.W. Anderson. “Plasmons, Gauge Invariance, and Mass”. In: *Phys. Rev.* 130 (1963), pp. 439–442.
- 4996
- 4997 [103] J. Schwinger. “Gauge Invariance and Mass”. In: *Phys. Rev.* 125 (1962), pp. 397–398.
- 4998 [104] F. Englert & R. Brout. “Broken Symmetry and the Mass of Gauge Vector Mesons”. In: *Phys. Rev. Lett.* 13 (1964), pp. 321–323.
- 4999
- 5000 [105] P.W. Higgs. “Broken Symmetries and the Masses of Gauge Bosons”. In: *Phys. Rev. Lett.* 13 (1964), pp. 508–509.
- 5001
- 5002 [106] & T.W.B. Kibble G.S. Guralnik C.R. Hagen. “Global Conservation Laws and Massless Particles”. In: *Phys. Rev. Lett.* 13 (1964), pp. 585–587.
- 5003
- 5004 [107] Wikipedia. *Standard Model*. 2018. URL: https://en.wikipedia.org/wiki/Standard_Model.
- 5005
- 5006 [108] UA1 Collaboration. “Experimental observation of isolated large transverse energy electrons with associated missing energy at $s = 540 \text{ GeV}$ ”. In: *Physics Letters B* 122 (1983), pp. 103–116.
- 5007
- 5008
- 5009 [109] UA2 Collaboration. “Observation of single isolated electrons of high transverse momentum in events with missing transverse energy at the CERN pp collider”. In: *Physics Letters B* 122 (1983), pp. 476–485.
- 5010
- 5011
- 5012 [110] UA1 Collaboration. “Experimental observation of lepton pairs of invariant mass around $95 \text{ GeV}/c^2$ at the CERN SPS collider”. In: *Physics Letters B* 126 (1983), pp. 398–410.
- 5013
- 5014 [111] UA2 Collaboration. “Evidence for $Z_0 \rightarrow e^+e^-$ at the CERN pp collider”. In: *Physics Letters B* 129 (1983), pp. 130–140.
- 5015
- 5016 [112] ATLAS Collaboration. “Observation of a new particle in the search for the Standard Model Higgs boson with the ATLAS detector at the LHC”. In: *Physics Letters B* 716 (2012), pp. 1–29.
- 5017
- 5018
- 5019 [113] CMS Collaboration. “Observation of a new boson at a mass of 125 GeV with the CMS experiment at the LHC”. In: *Physics Letters B* 716 (2012), pp. 30–61.
- 5020
- 5021 [114] CMS Collaboration ATLAS Collaboration. “Combined Measurement of the Higgs Boson Mass in pp Collisions at $\sqrt{s} = 7$ and 8 TeV with the ATLAS and CMS Experiments”. In: *Physical Review Letters* 114 (2015). 191803.
- 5022
- 5023
- 5024 [115] M. Tanabashi et al. (Particle Data Group). “Review of Particle Physics”. In: *Phys. Rev. D* 98 (2018), p. 030001.
- 5025
- 5026 [116] A.A. Arkhipov. “Proton proton total cross-sections from the window of cosmic ray experiments”. In: *Elastic and diffractive scattering. Proceedings, 9th Blois Workshop, Pruhonice, Czech Republic*. 2001, pp. 293–304.
- 5027
- 5028
- 5029 [117] H. Pointcaré. “The Milky Way and the Theory of Gases”. In: *Popular Astronomy* 14 (1906), pp. 475–488.
- 5030
- 5031 [118] J.C. Kapteyn. “First Attempt at a Theory of the Arrangement and Motion of the Sidereal System”. In: *Astrophysical Journal* 55 (1922), p. 302.
- 5032

BIBLIOGRAPHY

- 5033 [119] F. Zwicky. “Republication of: The redshift of extragalactic nebulae (First published in
5034 1933)”. In: *General Relativity and Gravitation* 41 (2009), pp. 207–224.
- 5035 [120] F. Zwicky. “On the Masses of Nebulae and of Clusters of Nebulae”. In: *Astrophysical Journal* 86 (1937), p. 217.
- 5037 [121] H.W. Babcock. “The rotation of the Andromeda Nebula”. In: *Lick Observatory bulletin* 498
5038 (1939), pp. 41–51.
- 5039 [122] V.C. Rubin & W.K. Ford Jr. “Rotation of the Andromeda Nebula from a Spectroscopic
5040 Survey of Emission Regions”. In: *Astrophysical Journal* 159 (1970), p. 379.
- 5041 [123] D.H. Rogstad & G.S. Shostak. “Gross Properties of Five Scd Galaxies as Determined from
5042 21-CENTIMETER Observations”. In: *Astrophysical Journal* 176 (1972), p. 315.
- 5043 [124] Planck Collaboration. “Planck 2015 results. XIII. Cosmological parameters”. In: *A&A* 594.A13
5044 (2016).
- 5045 [125] N. Jarosik et al. “Seven-year Wilkinson Microwave Anisotropy Probe (WMAP*) observa-
5046 tions: Sky maps, Systematic errors, and Basic Results”. In: *ApJS* 192.14 (2011).
- 5047 [126] E. Verlinde. “Emergent Gravity and the Dark Universe”. In: *SciPost Phys.* 2 (2017), p. 016.
- 5048 [127] A. Maeder. “An alternative to the Λ CDM model: the case of scale invariance”. In: *ApJ*
5049 834.194 (2017).
- 5050 [128] E. Corbelli & P. Salucci. “The extended rotation curve and the dark matter halo of M33”.
5051 In: *Monthly Notices of the Royal Astronomical Society* 311 (2000), pp. 441–447.
- 5052 [129] S. Dimopoulos & H. Georgi. “Softly broken supersymmetry and SU(5)”. In: *Nuclear Physics*
5053 B 193 (1981), pp. 150–162.
- 5054 [130] F. Tanedo. *The Hierarchy Problem: why the Higgs has a snowball’s chance in hell*. 2012.
5055 URL: [https://www.quantumdiaries.org/2012/07/01/the-hierarchy-
5056 problem-why-the-higgs-has-a-snowballs-chance-in-hell/](https://www.quantumdiaries.org/2012/07/01/the-hierarchy-problem-why-the-higgs-has-a-snowballs-chance-in-hell/).
- 5057 [131] M. Kamionkowski & K. Griest G. Jungman. “Supersymmetric dark matter”. In: *Physics*
5058 *Reports* 267 (1996), pp. 10–14.
- 5059 [132] & P. Nath A.H. Chamseddine R. Arnowitt. “Locally Supersymmetric Grand Unification”.
5060 In: *Phys. Rev. Lett.* 49 (1982), pp. 970–974.
- 5061 [133] A. Askew et al. “Searching for dark matter at hadron colliders”. In: *International Journal*
5062 *of Modern Physics A* 29 (2014), p. 1430041.
- 5063 [134] S. Dimopoulos & G. Dvali N. Arkani-Hamed. “The hierarchy problem and new dimensions
5064 at a millimeter”. In: *Physics Letters B* 429 (1998), pp. 263–272.
- 5065 [135] S. Dimopoulos & G. Dvali N. Arkani-Hamed. “Phenomenology, astrophysics, and cosmol-
5066 ogy of theories with submillimeter dimensions and TeV scale quantum gravity”. In: *Phys.*
5067 *Rev. D* 59 (1999), p. 086004.
- 5068 [136] T. Kaluza. “Zum Unitsproblem der Physik”. In: *Sitzungsber. Preuss. Akad. Wiss. Berlin*
5069 (*Math. Phys.*) 1921 (1921), pp. 966–972.
- 5070 [137] O. Klein. “The Atomicity of Electricity as a Quantum Theory Law”. In: *Nature* 118 (1926),
5071 p. 516.
- 5072 [138] L. Randall & R. Sundrum. “Large Mass Hierarchy from a Small Extra Dimension”. In:
5073 *Phys. Rev. Lett.* 83 (1999), pp. 3370–3373.
- 5074 [139] L. Randall & R. Sundrum. “An Alternative to Compactification”. In: *Phys. Rev. Lett.* 83
5075 (1999), pp. 4690–4693.

- 5076 [140] M. Strassler & K. Zurek. “Echoes of a hidden valley at hadron colliders”. In: *Phys. Let. B*
5077 651 (2007), pp. 374–379.
- 5078 [141] A. Sakharov. “Violation of CP i variance, C asymmetry, and baryon asymmetry of the uni-
5079 verse”. In: *JETP Letters* 5 (1967), pp. 24–27.
- 5080 [142] M.E. Shaposhnikov & G. Farrar. “Baryon asymmetry of the Universe in the minimal stan-
5081 dard model”. In: *Phys. Rev. Lett.* 70 (1993), pp. 2833–2836.
- 5082 [143] V.A.Rubakov & M.E. Shaposhnikov V.A. Kuzmin. “On anomalous electroweak baryon-
5083 number non-conservation in the early universe”. In: *Physics Letters B* 155 (1985), pp. 36–
5084 42.
- 5085 [144] M. Drewes & M. Shaposhnikov L. Canetti. “Matter and antimatter in the universe”. In: *New
5086 J. Phys.* 14.095012 (2012).
- 5087 [145] CMS Collaboration. “Search for black holes and sphalerons in high-multiplicity final states
5088 in proton-proton collisions at $\sqrt{s} = 13$ TeV”. In: *Journal of High Energy Physics* 11 (2018).
- 5089 [146] B. Shuve & Y. Cui. “Probing baryogenesis with displaced vertices at the LHC”. In: *Journal
5090 of High Energy Physics* 2 (2015).
- 5091 [147] The ACME Collaboration. “Order of Magnitude Smaller Limit on the Electric Dipole Mo-
5092 ment of the Electron”. In: *Science* 343 (2014), pp. 269–272.
- 5093 [148] N. Neri et al. “On the search for the electric dipole moment of strange and charm baryons
5094 at LHC”. In: *The European Physical Journal C* 77 (2017), p. 181.
- 5095 [149] J. Stevens & M. Sher. “Detecting a heavy neutrino electric dipole moment at the LHC”. In:
5096 *Physics Letters B* 777 (2018), pp. 246–249.
- 5097 [150] D.S. Harmer & K.C. Hoffman R. Davis Jr. “Search for Neutrinos from the Sun”. In: *Physical
5098 Review Letters* 20 (1968), pp. 1205–1209.
- 5099 [151] B. Pontecorvo. “Neutrino Experiments and the Problem of Conservation of Leptonic Charge”.
5100 In: *Sov. Phys. JETP* 26 (1968), pp. 984–988.
- 5101 [152] SNO Collaboration. “Direct Evidence for Neutrino Flavor Transformation from Neutral-
5102 Current Interactions in the Sudbury Neutrino Observatory”. In: *Physical Review Letters*
5103 89.011301 (2002).
- 5104 [153] M. Nakagawa & S. Sakata Z. Maki. “Remarks on the Unified Model of Elementary Parti-
5105 cles”. In: *Progress of Theoretical Physics* 28 (1962), pp. 870–880.
- 5106 [154] P. Minkowski. “ $\mu \rightarrow e\gamma$ at a rate of one out of 10^9 muon decays?” In: *Physics Letters B*
5107 67 (1977), pp. 421–428.
- 5108 [155] R.N. Mohapatra & G. Senjanović. “Neutrino Mass and Spontaneous Parity Nonconserva-
5109 tion”. In: *Phys. Rev. Lett.* 44 (1980), pp. 912–915.
- 5110 [156] CERN. Geneva. LHC Experiments Committee. *CMS Physics Technical Design Report Vol-
5111 ume II: Physics Performance*. Tech. rep. CERN-LHCC-2006-021 ; CMS-TDR-8-2. CMS
5112 Collaboration, 2006.
- 5113 [157] P.W.F. Valle. “Neutrino physics overview”. In: *J. Phys.: Conf. Ser.* 53 (2006), pp. 473–505.
- 5114 [158] T. Massam et al. “Experimental observation of antideuteron production”. In: *Il Nuovo Ci-
5115 mento A* 63 (1965), pp. 10–14.
- 5116 [159] ALEPH Collaboration. “Determination of the number of light neutrino species”. In: *Physics
5117 Letters B* 231 (1989), pp. 519–529.
- 5118 [160] CERN, ed. (1985).

BIBLIOGRAPHY

- 5119 [161] CERN, ed. (1986).
- 5120 [162] CERN, ed. (1994).
- 5121 [163] CERN, ed. (1998).
- 5122 [164] CERN, ed. (1999).
- 5123 [165] CERN. Geneva. LHC Experiments Committee. *Letter of Intent for A Large Ion Collider*
5124 *Experiment [ALICE]*. Tech. rep. CERN-LHCC-93-016. ALICE Collaboration, 1993.
- 5125 [166] CERN. Geneva. LHC Experiments Committee. *ATLAS : technical proposal for a general-*
5126 *purpose pp experiment at the Large Hadron Collider at CERN*. Tech. rep. CERN-LHCC-94-
5127 43. ATLAS Collaboration, 1994.
- 5128 [167] CERN. Geneva. LHC Experiments Committee. *CMS : letter of intent by the CMS Col-*
5129 *laboration for a general purpose detector at LHC*. Tech. rep. CERN-LHCC-92-003. CMS
5130 Collaboration, 1992.
- 5131 [168] CERN. Geneva. LHC Experiments Committee. *LHCb : letter of intent*. Tech. rep. CERN-
5132 LHCC-95-5. LHCb Collaboration, 1995.
- 5133 [169] L. Evans and P. Bryant. “LHC Machine”. In: *JINST* 3 (2008). S08001.
- 5134 [170] LHCb Collaboration. “Observation of $J/\psi p$ Resonances Consistent with Pentaquark States
5135 in $\Lambda_b^0 \rightarrow J/\psi K^- p$ Decays”. In: *Physical Review Letters* 115 (2015). 072001.
- 5136 [171] LHCb Collaboration. “Observation of $J/\psi \phi$ Structures Consistent with Exotic States from
5137 Amplitude Analysis of $B^+ \rightarrow J/\psi \phi K^+$ Decays”. In: *Physical Review Letters* 118 (2017).
5138 022003.
- 5139 [172] ALICE Collaboration. *First results from proton-lead collisions*. URL: <http://aliceinfo.cern.ch/Public/en/Chapter1/results-pPb.html>.
- 5140
- 5141 [173] ATLAS Collaboration. “Observation of a New χ_b State in Radiative Transitions to $\Upsilon(1S)$
5142 and $\Upsilon(2S)$ at ATLAS”. In: *Physical Review Letters* 108 (2012). 152001.
- 5143 [174] LHCb Collaboration. “First Evidence for the Decay $B_s^0 \rightarrow \mu^+ \mu^-$ ”. In: *Physical Review*
5144 *Letters* 110 (2013). 021801.
- 5145 [175] CERN. Geneva. *High-Luminosity Large Hadron Collider (HL-LHC) Technical Design Re-*
5146 *port V. 0.1*. Tech. rep. CERN-2017-007-M. 2017.
- 5147 [176] CERN. Geneva. LHC Experiments Committee. *CMS, the Compact Muon Solenoid : tech-*
5148 *nical proposal*. Tech. rep. CERN-2015-005. 2015.
- 5149 [177] CERN. Geneva. LHC Experiments Committee. *The Phase-2 Upgrade of the CMS Muon*
5150 *Detectors*. Tech. rep. CERN-LHCC-2017-012, CMS-TDR-016. CMS Collaboration, 2017.
- 5151 [178] X. Tata M. Drees. “Signals for heavy exotics at hadron colliders and supercolliders”. In:
5152 *Physics Letters B* 252 (1990), pp. 695–702.
- 5153 [179] D.A. Milstead et al. “Stable massive particles at colliders”. In: *Physics Reports* 438 (2007),
5154 pp. 1–63.
- 5155 [180] Z. Ligeti et al. “Supermodels for early LHC”. In: *Physics Letters B* 690 (2010), pp. 280–
5156 288.
- 5157 [181] CMS Collaboration. “Search for long-lived charged particles in proton-proton collisions at
5158 $\sqrt{s} = 13$ TeV”. In: *Phys. Rev. D* 94 (2016), p. 112004.
- 5159 [182] V. Khachatryan et al. “Search for long-lived charged particles in proton-proton collisions at
5160 $\sqrt{s} = 13$ TeV”. In: *Phys. Rev. D* 94 (2017). 112004.

- 5161 [183] M. Shaposhnikov A. Kusenko. “Supersymmetric Q-balls as dark matter”. In: *Physics Letters B* 418 (1998), pp. 46–54.
- 5162
- 5163 [184] B. Koch et al. “Black holes at LHC?” In: *J. Phys. G: Nucl. Part. Phys.* 34 (2007). S535.
- 5164 [185] J. Schwinger. “Magnetic Charge and Quantum Field Theory”. In: *Phys. Rev.* 144 (1966). 1087.
- 5165
- 5166 [186] M Yu Khlopov et al. “Dark matter with invisible light from heavy double charged leptons of almost-commutative geometry?” In: *Class. Quantum Grav.* 23 (2006). 7305.
- 5167
- 5168 [187] PoS, ed. *Search for Heavy Stable Charged Particles in CMS*. Vol. 084-EPS-HEP2009. 2009, p. 438.
- 5169
- 5170 [188] L.E. Medina Medrano et al. “Studies on Luminous Region, Pile-up and Performance for HL-LHC Scenarios”. In: *Proc. of International Particle Accelerator Conference (IPAC’17), Copenhagen, Denmark, 14-19 May, 2017*. JACoW, 2017, pp. 1908–1911.
- 5171
- 5172
- 5173 [189] CMS Collaboration. *CMS Luminosity - Public Results*. Version 158. 2019. URL: <https://twiki.cern.ch/twiki/bin/view/CMSPublic/LumiPublicResults>.
- 5174
- 5175 [190] CERN. Geneva. LHC Experiments Committee. *Technical Proposal for the Phase-II Upgrade of the CMS Detector*. Tech. rep. CERN-LHCC-2015-010, CMS-TDR-15-02. CMS Collaboration, 2015.
- 5176
- 5177
- 5178 [191] CERN. Geneva. LHC Experiments Committee. *The Phase-2 Upgrade of the CMS Level-1 Trigger - Interim Report to the LHCC*. Tech. rep. CERN-LHCC-2017-013, CMS-TDR-017. CMS Collaboration, 2017.
- 5179
- 5180
- 5181 [192] CERN. Geneva. LHC Experiments Committee. *The CMS muon project : Technical Design Report*. Tech. rep. CERN-LHCC-97-032. CMS Collaboration, 1997.
- 5182
- 5183 [193] CERN. Geneva. LHC Experiments Committee. *High-Luminosity Large Hadron Collider (HL-LHC) Preliminary Design Report*. Tech. rep. CERN-LHCC-94-38. CMS Collaboration, 1994.
- 5184
- 5185
- 5186 [194] F. Sauli. “GEM: A new concept for electron amplification in gas detectors”. In: *Nucl. Instr. Meth. Phys. Res.* 386 (1997), pp. 531–534.
- 5187
- 5188 [195] CERN. Geneva. LHC Experiments Committee. *CMS Technical Design Report for the Muon Endcap GEM Upgrade*. Tech. rep. CERN-LHCC-2015-012, CMS-TDR-013. CMS Collaboration, 2015.
- 5189
- 5190
- 5191 [196] A. Gelmi. *CMS iRPC at HL-LHC: background study*. 2018. URL: https://indico.cern.ch/event/732794/contributions/3021836/attachments/1657792/2654574/iRPC_bkg_study_Upgrade29_05_18.pdf.
- 5192
- 5193
- 5194 [197] A. Gelmi & E. Voevodina. “Background rate study for the CMS improved-RPC at HL-LHC using GEANT4”. In: *Nucl. Instr. Meth. Phys. Res. A* (2018).
- 5195
- 5196 [198] IEEE, ed. *Petiroc, a new front-end ASIC for time of flight application*. Vol. 2013 IEEE Nuclear Science Symposium and Medical Imaging Conference (2013 NSS/MIC). 2014.
- 5197
- 5198 [199] JINST, ed. *Petiroc and Citiroc: front-end ASICs for SiPM read-out and ToF applications*. Vol. Topical Workshop on Electronics for Particle Physics 2013 (TWEPP-13). 2014.
- 5199
- 5200 [200] P.Bortignon. “Design and performance of the upgrade of the CMS L1 muon trigger”. In: *Nucl. Instr. Meth. Phys. Res.* 824 (2016), pp. 256–257.
- 5201
- 5202 [201] The European Parliament and the Council of the European Union. “Regulation (EU) No 517/2014 of 16 April 2014 on fluorinated greenhouse gases and repealing Regulation (EC) No 842/2006”. In: *Official Journal of the European Union* 150 (2014), pp. 195–230.
- 5203
- 5204

BIBLIOGRAPHY

- 5205 [202] R. Santonico and R. Cardarelli. “Development of resistive plate counters”. In: *Nucl. Instr.*
5206 *Meth. Phys. Res.* 187 (1981), pp. 377–380.
- 5207 [203] Yu.N. Pestov and G.V. Fedotovich. *A picosecond time-of-flight spectrometer for the VEPP-*
5208 *2M based on local-discharge spark counter*. Tech. rep. SLAC-TRANS-0184. SLAC, 1978.
- 5209 [204] W.W. Ash, ed. *Spark Counter With A Localized Discharge*. Vol. SLAC-R-250. 1982, pp. 127–
5210 131.
- 5211 [205] I. Crotty et al. “The non-spark mode and high rate operation of resistive parallel plate cham-
5212 bers”. In: *NIMA* 337 (1993), pp. 370–381.
- 5213 [206] I. Crotty et al. “Further studies of avalanche mode operation of resistive parallel plate cham-
5214 bers”. In: *NIMA* 346 (1994), pp. 107–113.
- 5215 [207] R. Cardarelli et al. “Avalanche and streamer mode operation of resistive plate chambers”.
5216 In: *NIMA* 382 (1996), pp. 470–474.
- 5217 [208] R. Cardarelli et al. “Performance of a resistive plate chamber operating with pure CF_3Br ”.
5218 In: *NIMA* 333 (1993), pp. 399–403.
- 5219 [209] M. Abbrescia et al. “Performance of a Resistive Plate Chamber operated in avalanche mode
5220 under ^{137}Cs irradiation”. In: *NIMA* 392 (1997), pp. 155–160.
- 5221 [210] M. Abbrescia et al. “Properties of C2H2F4-based gas mixture for avalanche mode operation
5222 of resistive plate chambers”. In: *NIMA* 398 (1997), pp. 173–179.
- 5223 [211] P. Camarri et al. “Streamer suppression with SF6 in RPCs operated in avalanche mode”. In:
5224 *NIMA* 414 (1998), pp. 317–324.
- 5225 [212] E. Cerron Zeballos et al. “Effect of adding SF6 to the gas mixture in a multigap resistive
5226 plate chamber”. In: *NIMA* 419 (1998), pp. 475–478.
- 5227 [213] E. Cerron Zeballos et al. “A new type of resistive plate chamber: The multigap RPC”. In:
5228 *NIMA* 374 (1996), pp. 132–135.
- 5229 [214] M.C.S. Williams. “The development of the multigap resistive plate chamber”. In: *Nucl.*
5230 *Phys. B* 61 (1998), pp. 250–257.
- 5231 [215] H. Czyrkowski et al. “New developments on resistive plate chambers for high rate opera-
5232 tion”. In: *NIMA* 419 (1998), pp. 490–496.
- 5233 [216] CERN. Geneva. LHC Experiments Committee. *ATLAS muon spectrometer: Technical de-*
5234 *sign report*. Tech. rep. CERN-LHCC-97-22. ATLAS Collaboration, 1997.
- 5235 [217] CERN. Geneva. LHC Experiments Committee. *ALICE Time-Of-Flight system (TOF) : Tech-*
5236 *nical Design Report*. Tech. rep. CERN-LHCC-2000-012. ALICE Collaboration, 2000.
- 5237 [218] The CALICE collaboration. “First results of the CALICE SDHCAL technological proto-
5238 type”. In: *JINST* 11 (2016).
- 5239 [219] PoS, ed. *Density Imaging of Volcanoes with Atmospheric Muons using GRPCs*. International
5240 Europhysics Conference on High Energy Physics - HEP 2011. 2011.
- 5241 [220] C. Lippmann. “Detector Physics of Resistive Plate Chambers”. PhD thesis. Johann Wolf-
5242 gang Goethe-Universität, 2003.
- 5243 [221] W. Riegler. “Induced signals in resistive plate chambers”. In: *NIMA* 491 (2002), pp. 258–
5244 271.
- 5245 [222] M. Abbrescia et al. “Effect of the linseed oil surface treatment on the performance of resis-
5246 tive plate chambers”. In: *NIMA* 394 (1997), pp. 13–20.

- 5247 [223] G.Battistoni et al. “Sensitivity of streamer mode to single ionization electrons”. In: *NIMA*
 5248 235 (1985), pp. 91–97.
- 5249 [224] M.Abbrescia et al. “Cosmic ray tests of double-gap resistive plate chambers for the CMS
 5250 experiment”. In: *NIMA* 550 (2005), pp. 116–126.
- 5251 [225] JINST, ed. *Performance of the Resistive Plate Chambers in the CMS experiment*. The 9th
 5252 International Conference on Positioin Sensitive Detectors. 2012.
- 5253 [226] PoS, ed. *The CMS RPC detector performance during Run-II data taking*. The European
 5254 Physical Society Conference on High Energy Physics (EPS-HEP2017). 2018.
- 5255 [227] Honeywell International Inc. *Solstice(R) ze Refrigerant (HFO-1234ze): The Environmental
 5256 Alternative to Traditional Refrigerants*. Tech. rep. FPR-003/2015-01. 2015.
- 5257 [228] E. Cerron Zeballos et al. “A comparison of the wide gap and narrow gap resistive plate
 5258 chamber”. In: *NIMA* 373 (1996), pp. 35–42.
- 5259 [229] ALICE Collaboration. “A study of the multigap RPC at the gamma irradiation facility at
 5260 CERN”. In: *NIMA* 490 (2002), pp. 58–70.
- 5261 [230] B. Bonner et al. “A multigap resistive plate chamber prototype for time-of-flight for the
 5262 STAR experiment at RHIC”. In: *NIMA* 478 (2002), pp. 176–179.
- 5263 [231] S. Yang et al. “Test of high time resolution MRPC with different readout modes for the
 5264 BESIII upgrade”. In: *NIMA* 763 (2014), pp. 190–196.
- 5265 [232] A. Akindinovg et al. “RPC with low-resistive phosphate glass electrodes as a candidate for
 5266 the CBM TOF”. In: *NIMA* 572 (2007), pp. 676–681.
- 5267 [233] JINST, ed. *Development of the MRPC for the TOF system of the MultiPurpose Detector*.
 5268 RPC2016: XII Workshop on Resistive Plate Chambers and Related Detectors. 2016.
- 5269 [234] M.C.S. Williams. “Particle identification using time of flight”. In: *Journal of Physics G* 39
 5270 (2012).
- 5271 [235] A. Alici et al. “Aging and rate effects of the Multigap RPC studied at the Gamma Irradiation
 5272 Facility at CERN”. In: *NIMA* 579 (2007), pp. 979–988.
- 5273 [236] M. Abbrescia et al. “The simulation of resistive plate chambers in avalanche mode: charge
 5274 spectra and efficiency”. In: *NIMA* 431 (1999), pp. 413–427.
- 5275 [237] JINST, ed. *Description and simulation of physics of Resistive Plate Chambers*. RPC2016:
 5276 XII Workshop on Resistive Plate Chambers and Related Detectors. 2016.
- 5277 [238] V. Francais. “Description and simulation of the physics of Resistive Plate Chambers”. PhD
 5278 thesis. LPC - Laboratoire de Physique Corpusculaire - Clermont-Ferrand, 2017.
- 5279 [239] H. Bethe. “Zur Theorie des Durchgangs schneller Korpuskularstrahlen durch Materie”. In:
 5280 *Annalen der Physik* 397 (1930), pp. 325–400.
- 5281 [240] International Commission on Radiation Units and Measurements. *Stopping Powers for Elec-
 5282 trons and Positions*. Tech. rep. Report 37. 1984.
- 5283 [241] International Commission on Radiation Units and Measurements. *Stopping Power and Ranges
 5284 for Protons and Alpha Particles*. Tech. rep. Report 49. 1994.
- 5285 [242] H. Bichsel. “A method to improve tracking and particle identification in TPCs and silicon
 5286 detectors”. In: *NIMA* 562 (2006), pp. 154–197.
- 5287 [243] W. W. M. Allison and J. H. Cobb. “Relativistic charged particle identification by energy
 5288 loss”. In: *Annual Review of Nuclear and Particle Science* 30 (1980), 253–298.

BIBLIOGRAPHY

- 5289 [244] International Commission on Radiation Units and Measurements. *Average energy to pro-*
5290 *duce an ion pair*. Tech. rep. Report 31. 1994.
- 5291 [245] I.B. Smirnov. “Modeling of ionization produced by fast charged particles in gases”. In: *NIMA* 554 (2005), pp. 474–493.
- 5293 [246] J. Phys.: Conf. Ser., ed. <https://doi.org/10.1088/1742-6596/587/1/012035> *Results of the CAL-*
5294 *ICE SDHCAL technological prototype*. 16th International Conference on Calorimetry in
5295 High Energy Physics (CALOR 2014). 2015.
- 5296 [247] W. Riegler et al. “Detector physics and simulation of resistive plate chambers”. In: *NIMA*
5297 500 (2003), pp. 144–162.
- 5298 [248] I.B. Smirnov. *HEED++ simulation program*. 2010. URL: <http://ismirnov.web.cern.ch/ismirnov/heed>.
- 5300 [249] S.F. Biagi. “Monte Carlo simulation of electron drift and diffusion in counting gases under
5301 the influence of electric and magnetic fields”. In: *NIMA* 421 (1999), pp. 234–240.
- 5302 [250] W. H. Furry. “On Fluctuation Phenomena in the Passage of High Energy Electrons through
5303 Lead”. In: *Phys. Rev.* 52 (1937), pp. 569–581.
- 5304 [251] H. Genz. “Single electron detection in proportional gas counters”. In: *Nucl. Instr. and Meth.*
5305 112 (1973), pp. 83–90.
- 5306 [252] M. Abbrescia et al. “Resistive plate chambers performances at cosmic rays fluxes”. In: *NIMA* 359 (1995), pp. 603–609.
- 5308 [253] M. Abbrescia et al. “Resistive plate chambers performances at low pressure”. In: *NIMA* 394
5309 (1997), pp. 341–348.
- 5310 [254] M. Abbrescia. “Operation, performance and upgrade of the CMS Resistive Plate Chamber
5311 system at LHC”. In: *NIMA* 732 (2013), pp. 195–198.
- 5312 [255] F. Thyssen. “Commissioning, Operation and Performance of the CMS Resistive Plate Cham-
5313 ber System”. PhD thesis. Universiteit Gent, 2014.
- 5314 [256] M. Bianco. “ATLAS RPC certification and commissioning with cosmic rays”. PhD thesis.
5315 Università del Salento, 2007.
- 5316 [257] M. Bianco. “ATLAS RPC certification with cosmic rays”. In: *NIMA* 602 (2009), pp. 700–
5317 704.
- 5318 [258] M. Abbrescia et al. “Study of long-term performance of CMS RPC under irradiation at the
5319 CERN GIF”. In: *NIMA* 533 (2004), pp. 102–106.
- 5320 [259] H.C. Kim et al. “Quantitative aging study with intense irradiation tests for the CMS forward
5321 RPCs”. In: *NIMA* 602 (2009), pp. 771–774.
- 5322 [260] S. Agosteo et al. “A facility for the test of large-area muon chambers at high rates”. In: *NIMA*
5323 452 (2000), pp. 94–104.
- 5324 [261] PoS, ed. *CERN GIF ++ : A new irradiation facility to test large-area particle detectors for*
5325 *the high-luminosity LHC program*. Vol. TIPP2014. 2014, pp. 102–109.
- 5326 [262] D. Pfeiffer et al. “The radiation field in the Gamma Irradiation Facility GIF++ at CERN”.
5327 In: *NIMA* 866 (2017), pp. 91–103.
- 5328 [263] CAEN. *Mod. V1190-VX1190 A/B, 128/64 Ch Multihit TDC*. 14th ed. 2016.
- 5329 [264] CAEN. *Mod. VI718 VME USB Bridge*. 9th ed. 2009.
- 5330 [265] A. Fagot. *GIF Cosmic Muon Monte Carlo Simulation*. 2017. URL: <https://github.com/a-fagot/Cosmics-Simulation>.

- 5332 [266] G. Pugliese et al. “Long-term performance of double gap resistive plate chambers under
5333 gamma irradiation”. In: *NIMA* 477 (2002), pp. 293–298.
- 5334 [267] G. Pugliese et al. “Aging study for resistive plate chambers of the CMS muon trigger detec-
5335 tor”. In: *NIMA* 515 (2003), pp. 342–347.
- 5336 [268] M. Capeans et al. on behalf of the GIF and GIF++ User Communities. “A GIF++ Gamma
5337 Irradiation Facility at the SPS H4 Beam Line”. CERN-SPSC-2009-029 / SPSC-P-339. 2009.
- 5338 [269] R. Guida et al. “Results about HF production and bakelite analysis for the CMS Resistive
5339 Plate Chambers”. In: *NIMA* 594 (2008), pp. 140–147.
- 5340 [270] F. Bellini et al. “Study of HF production in BaBar Resistive Plate Chambers”. In: *NIMA* 594
5341 (2008), pp. 33–38.
- 5342 [271] J. Eysermans. *WebDCS GIF++*. CERN. 2016. URL: <https://www.webdcs.cern.ch>.
- 5344 [272] S. Carrillo A. Fagot. *GIF++ Offline Analysis v6*. 2017. URL: https://github.com/afagot/GIF_OfflineAnalysis.
- 5346 [273] H. Reithler. *Filters for GIF++*. RWTH Aachen University, CMS-CERN. 2013. URL: <https://edms.cern.ch/document/1324028/1>.
- 5348 [274] R. Cardarelli et al. “RPC performance vs. front-end electronics”. In: *NIMA* 661 (2012),
5349 S198–S200.
- 5350 [275] A. Fagot. *GIF++ Data Acquisition Software for CMS RPC*. 2016. URL: https://github.com/afagot/GIF_DAQ.
- 5352 [276] W-Ie-Ne-R. *VME 6021-23 VXI*. 5th ed. 2016.
- 5353 [277] Wikipedia. *INI file*. 2017. URL: https://en.wikipedia.org/wiki/INI_file.